

## REPORT DOCUMENTATION PAGE

AFRL-SR-BL-TR-98-

88

ources, gathering  
this collection of  
s Highway, Suite

Public reporting burden for this collection of information is estimated to average 1 hour per response, including collecting, maintaining, preparing, and reviewing information for this collection. Send comments, including suggestions for reducing this burden, to Washington Headquarters Services, Directorate for Management and Budget, Paperwork Reduction Project, 1204, Arlington, VA 22202-4302, and to the Office of Management and Budget, Paperwork Reduction Project, 1204, Arlington, VA 22202-4302.

1. AGENCY USE ONLY (Leave Blank)	2. REPORT DATE December, 1994	3. Final
----------------------------------	----------------------------------	----------

4. TITLE AND SUBTITLE USAF Summer Research Program - 1994 Summer Faculty Research Program Final Reports, Volume 6, AEDC, FJSRL, and WHMC	5. FUNDING NUMBERS
--	--------------------

6. AUTHORS Gary Moore
--------------------------

7. PERFORMING ORGANIZATION NAME(S) AND ADDRESS(ES) Research and Development Labs, Culver City, CA	8. PERFORMING ORGANIZATION REPORT NUMBER
--	---

9. SPONSORING/MONITORING AGENCY NAME(S) AND ADDRESS(ES) AFOSR/NI 4040 Fairfax Dr, Suite 500 Arlington, VA 22203-1613	10. SPONSORING/MONITORING AGENCY REPORT NUMBER
---	---

11. SUPPLEMENTARY NOTES Contract Number: F49620-93-C-0063
--

12a. DISTRIBUTION AVAILABILITY STATEMENT Approved for Public Release	12b. DISTRIBUTION CODE
---	------------------------

## 13. ABSTRACT (Maximum 200 words)

The United States Air Force Summer Faculty Research Program (USAF- SFRP) is designed to introduce university, college, and technical institute faculty members to Air Force research. This is accomplished by the faculty members being selected on a nationally advertised competitive basis during the summer intersession period to perform research at Air Force Research Laboratory Technical Directorates and Air Force Air Logistics Centers. Each participant provided a report of their research, and these reports are consolidated into this annual report.

14. SUBJECT TERMS AIR FORCE RESEARCH, AIR FORCE, ENGINEERING, LABORATORIES, REPORTS, SUMMER, UNIVERSITIES	15. NUMBER OF PAGES
---	---------------------

16. PRICE CODE

17. SECURITY CLASSIFICATION OF REPORT Unclassified	18. SECURITY CLASSIFICATION OF THIS PAGE Unclassified	19. SECURITY CLASSIFICATION OF ABSTRACT Unclassified	20. LIMITATION OF ABSTRACT UL
--	---	--	----------------------------------

UNITED STATES AIR FORCE  
SUMMER RESEARCH PROGRAM -- 1994  
SUMMER FACULTY RESEARCH PROGRAM FINAL REPORTS

VOLUME 6

ARNOLD ENGINEERING DEVELOPMENT CENTER  
FRANK J. SEILER RESEARCH LABORATORY  
WILFORD HALL MEDCIAL CENTER

RESEARCH & DEVELOPMENT LABORATORIES  
5800 Uplander Way  
Culver City, CA 90230-6608

Program Director, RDL  
Gary Moore

Program Manager, AFOSR  
Major David Hart

Program Manager, RDL  
Scott Licoscos

Program Administrator, RDL  
Gwendolyn Smith

Program Administrator, RDL  
Johnetta Thompson

Submitted to:

AIR FORCE OFFICE OF SCIENTIFIC RESEARCH

Bolling Air Force Base

Washington, D.C.

DTIC QUALITY INSPECTED 4

December 1994

19981204 033

## PREFACE

Reports in this volume are numbered consecutively beginning with number 1. Each report is paginated with the report number followed by consecutive page numbers, e.g., 1-1, 1-2, 1-3; 2-1, 2-2, 2-3.

This document is one of a set of 16 volumes describing the 1994 AFOSR Summer Research Program. The following volumes comprise the set:

<u>VOLUME</u>	<u>TITLE</u>
1	Program Management Report <i>Summer Faculty Research Program (SFRP) Reports</i>
2A & 2B	Armstrong Laboratory
3A & 3B	Phillips Laboratory
4	Rome Laboratory
5A & 5B	Wright Laboratory
6	Arnold Engineering Development Center, Frank J. Seiler Research Laboratory, and Wilford Hall Medical Center <i>Graduate Student Research Program (GSRP) Reports</i>
7	Armstrong Laboratory
8	Phillips Laboratory
9	Rome Laboratory
10	Wright Laboratory
11	Arnold Engineering Development Center, Frank J. Seiler Research Laboratory, and Wilford Hall Medical Center <i>High School Apprenticeship Program (HSAP) Reports</i>
12A & 12B	Armstrong Laboratory
13	Phillips Laboratory
14	Rome Laboratory
15A&15B	Wright Laboratory
16	Arnold Engineering Development Center

## **SFRP FINAL REPORT TABLE OF CONTENTS**

**i-xxi**

<b>1. INTRODUCTION</b>	<b>1</b>
<b>2. PARTICIPATION IN THE SUMMER RESEARCH PROGRAM</b>	<b>2</b>
<b>3. RECRUITING AND SELECTION</b>	<b>3</b>
<b>4. SITE VISITS</b>	<b>4</b>
<b>5. HBCU/MI PARTICIPATION</b>	<b>4</b>
<b>6. SRP FUNDING SOURCES</b>	<b>5</b>
<b>7. COMPENSATION FOR PARTICIPANTS</b>	<b>5</b>
<b>8. CONTENTS OF THE 1994 REPORT</b>	<b>6</b>

### **APPENDICIES:**

<b>A. PROGRAM STATISTICAL SUMMARY</b>	<b>A-1</b>
<b>B. SRP EVALUATION RESPONSES</b>	<b>B-1</b>

### **SFRP FINAL REPORTS**

**SRP Final Report Table of Contents**

<b>Author</b>	<b>University/Institution Report Title</b>	<b>Armstrong Laboratory Directorate</b>	<b>Vol-Page</b>
Dr. James L Anderson	University of Georgia , Athens , GA Determination of the Oxidative Redox Capacity of	AL/EQC	2- 1
Dr. Hashem Ashrafiuon	Villanova University , Villanova , PA ATB Simulation of Deformable Manikin Neck Models	AL/CFBV	2- 2
DR Stephan B Bach	Univ of Texas-San Antonio , San Antonio , TX Pre-Screening of Soil Samples Using a Solids Inser	AL/OEA	2- 3
Dr. Suzanne C Baker	James Madison University , Harrisonburg , VA Rat Pup Ultrasonic Vocalizations: A Sensitive Indi	AL/OER	2- 4
DR Alexander B Bordetsky	Univ of Texas - Dallas , Richardson , TX Knowledge-Based Groupware for Geographically Distr	AL/HRGA	2- 5
DR. Michael J Burke	Tulane University , New Orleans , LA An Empirical Examination of the Effect of Second-O	AL/HRMI	2- 6
DR Yu-Che Chen	University of Tulsa , Tulsa , OK A Study of the Kinematics, Dynamics and Control AI	AL/CFBS	2- 7
DR Shashikala T Das	Wilmington College , Wilmington , OH The Benchmark Dose Approach for Health Risk Assess	AL/OET	2- 8
DR. Donald W DeYoung	University of Arizona , Tucson , AZ Noise as a Stressor: An Assessment of Physiologic	AL/OEBN	2- 9
DR Judy B Dutta	Rice University , Houston , TX Memory for Spatial Position and Temporal Occurrence	AL/CFTO	2- 10
DR Paul A Edwards	Edinboro Univ of Pennsylvania , Edinboro , PA Fuel Identification by Neural Network Analysis of	AL/EQC	2- 11

**SRP Final Report Table of Contents**

<b>Author</b>	<b>University/Institution Report Title</b>	<b>Armstrong Laboratory Directorate</b>	<b>Vol-Page</b>
<b>Dr. Daniel L Ewert</b>	North Dakota State University , Grand Forks , ND Regional Arterial Compliance and Resistance Change	AL/AOCN	2- 12
<b>Dr. Bernard S Gerstman</b>	Florida International Universi , Miami , FL Laser Induced Bubble Formation in the Retina	AL/OEO	2- 13
<b>DR Robert H Gilkey</b>	Wright State University , Dayton , OH Relation Between Detection and Intelligibility in	AL/CFBA	2- 14
<b>Dr. Kenneth A Graetz</b>	University of Dayton , Dayton , OH Using Electronic Brainstorming Tools to Visually R	AL/HRGA	2- 15
<b>Dr. Donald D Gray</b>	West Virginia Unicersity , Morgantown , WV Improved Numerical Modeling of Groundwater Flow an	AL/EQC	2- 16
<b>Dr. Pushpa L Gupta</b>	University of Maine , Orono , ME Regression to the Mean in Half-Life Studies	AL/AOEP	2- 17
<b>Dr. Thomas E Hancock</b>	Grand Canyon University , Phoenix , AZ An Expanded Version of the Kulhavy/Stock Model of	AL/HR2	2- 18
<b>DR. Alexis G Hernandez</b>	University of Arizona , Tucson , AZ Preliminary Results of the Neuropsychiatrically En	AL/AOCN	2- 19
<b>DR P. A Ikomi</b>	Central State University , Wilberforce , OH A Realistic Multi-Task Assessment of Pilot Aptitud	AL/HRMI	2- 20
<b>Dr. Arthur Koblasz</b>	Georgia State University , Atlanta , GA Distributed Sensory Processing During Graded Hemod	AL/AOCI	2- 21
<b>DR Manfred Koch</b>	Florida State University , Tallahassee , FL Application of the MT3D Solute Transport Model to	AL/EQC	2- 22

**SRP Final Report Table of Contents**

<b>Author</b>	<b>University/Institution Report Title</b>	<b>Armstrong Laboratory Directorate</b>	<b>Vol-Page</b>
Dr. Donald H Kraft	Louisiana State University , Baton Rouge , LA An Exploratory Study of Weighted Fuzzy Keyword Bo	AL/CFHD	2- 23
Dr. Brother D Lawless	Fordham University , New York , NY Apoptosis Advanced Glycosylated End Products, Auto	AL/OER	2- 24
Dr. Tzesan Lee	Western Illinois University , Macomb , IL A Statistical Method for Testing Compliance	AL/OEM	2- 25
DR Robert G Main	California State Univ-Chico , Chico , CA A Study of Interaction in Distance Learning	AL/HRTT	2- 26
Dr. Augustus Morris	Central State University , Wilberforce , OH A Novel Design Concept for a Small, Force Reflecti	AL/CFBS	2- 27
DR Mark A Novotny	Florida State University , Tallahassee , FL Computer Calculation of Rate Constants for Biomole	AL/EQS	2- 28
Dr. Joseph H Nurre	Ohio University , Athens , OH A Review of Parameter Selection for Processing Cyl	AL/CFHD	2- 29
DR Edward L Parkinson	Univ of Tennessee Space Inst , Tullahoma , TN Improving the United States Air Force Environmenta	AL/EQS	2- 30
DR Malcom R Parks	University of Washington , Seattle , WA Communicative Challenges Facing Integrated Product	AL/AOE	2- 31
DR David R Perrott	California State Univ-Los Ange , Los Angeles , CA Aurally Directed Search: A Comparison Between Syn	AL/CFBA	2- 32
Dr. Edward H Piepmeier	University of South Carolina , Columbia , SC Dose Response Studies for Hyperbaric Oxygenation	AL/AOHP	2- 33

**SRP Final Report Table of Contents**

<b>Author</b>	<b>University/Institution Report Title</b>	<b>Armstrong Laboratory Directorate</b>	<b>Vol-Page</b>
DR Miguel A Quinones	Rice University , Houston , TX The Role of Experience in Training Effectiveness	AL/HRTE	2- 34
Dr. Ramaswamy Ramesh	SUNY, Buffalo , Buffalo , NY AETMS: Analysis, Design and Development	AL/HRAU	2- 35
DR Gary E Riccio	Univ of IL Urbana-Champaign , Urbana , IL REPORT NOT AVAILABLE AT PRESS TIME	AL/CFHP	2- 36
DR Kandasamy Selvavel	Claflin College , Orangeburg , SC Sequential Estimation of Parameters of Truncation	AL/AOEP	2- 37
DR David M Senseman	Univ of Texas-San Antonio , San Antonio , TX Multisite Optical Recording of Evoked Activity in	AL/CFTO	2- 38
DR Wayne L Shebilske	Texas A&M University , College Station , TX Linking Laboratory Research and Field Applications	AL/HRTI	2- 39
Dr. Larry R Sherman	University of Scranton , Scranton , PA Using The Sem-EDXA System at AL/OEA for Analysis o	AL/OEA	2- 40
Dr. Richard D Swope	Trinity University , San Antonio , TX Regional Arterial Compliance and Resistance Chang	AL/AOCI	2- 41
DR Steven D Tripp	The University of Kansas , Lawrence , KS Representing and Teaching a Discrete Machine: An	AL/HRTC	2- 42
DR Ryan D Tweney	Bowling Green State University , Bowling Green , OH Automated Detection of Individual Response Charact	AL/CFHP	2- 43
Dr. Brian S Vogt	Bob Jones University , Greenville , SC A Multiplexed Fiber-Optic Laser Fluorescence Spect	AL/EQW	2- 44

SRP Final Report Table of Contents

<u>Author</u>	<u>University/Institution</u>	<u>Armstrong Laboratory</u>	<u>Vol-Page</u>
	<u>Report Title</u>	<u>Directorate</u>	
DR Janet M Weisenberger	Ohio State University , Columbus , OH Investigation of the Role of Haptic Movement in Ta	AL/CFBA	2- 45

**SRP Final Report Table of Contents**

<b>Author</b>	<b>University/Institution Report Title</b>	<b>Phillips Laboratory Directorate</b>	<b>Vol-Page</b>
<b>DR Behnaam Aazhang</b>	<b>Rice University , Houston , TX High Capacity Optical Communication Networks</b>	<b>PL/VTPT</b>	<b>3- 1</b>
<b>DR Nasser Ashgriz</b>	<b>SUNY-Buffalo , Buffalo , NY On The Mixing Mechanisms in a Pair of Impinging Je</b>	<b>PL/RKFA</b>	<b>3- 2</b>
<b>Dr. Raymond D Bellem</b>	<b>Embry-Riddle Aeronautical Univ , Prescott , AZ Radiation Characterization of Commerically Process</b>	<b>PL/VTET</b>	<b>3- 3</b>
<b>DR Gajanan S Bhat</b>	<b>Tennessee , Knoxville , TN Polyetherimide Fibers: Production Processing and</b>	<b>PL/RKFE</b>	<b>3- 4</b>
<b>DR Ronald J Bieniek</b>	<b>University of Missouri-Rolla , Rolla , MO Practical Semiquantal Modelling of Collisional Vib</b>	<b>PL/GPOS</b>	<b>3- 5</b>
<b>DR Jan S Brzosko</b>	<b>Stevens Institute of Tech , Hoboken , NJ Conceptual Study of the Marauder Operation in the</b>	<b>PL/WSP</b>	<b>3- 6</b>
<b>DR Ping Cheng</b>	<b>Hawaii at Manoa , Honolulu , HI Determination of the Interfacial Heat Transfer Coe</b>	<b>PL/VTPT</b>	<b>3- 7</b>
<b>DR Meledath Damodaran</b>	<b>University of Houston-Victoria , Victoria , TX Concurrent Computation of Aberration Coefficients</b>	<b>PL/LIMI</b>	<b>3- 8</b>
<b>Dr. Ronald R DeLyser</b>	<b>University of Denver , Denver , CO Analysis to Determine the Quality Factor of a Comp</b>	<b>PL/WSA</b>	<b>3- 9</b>
<b>DR Jean-Claude M Diels</b>	<b>University of New Mexico , Albuquerque , NM Unidirectional Ring Lasers and Laser Gyros with Mu</b>	<b>PL/LIDA</b>	<b>3- 10</b>
<b>Dr. David M Elliott</b>	<b>Arkansas Technology University , Russellville , AR REPORT NOT AVAILABLE AT PRESS TIME</b>	<b>PL/RKFE</b>	<b>3- 11</b>

**SRP Final Report Table of Contents**

<b>Author</b>	<b>University/Institution Report Title</b>	<b>Phillips Laboratory Directorate</b>	<b>Vol-Page</b>
DR Vincent P Giannamore	Xavier University of Louisiana , New Orleans , LA An Investigation of Hydroxylammonium Dinitramide:	PL/RKA	3- 12
DR James E Harvey	University of Central Florida , Orlando , FL A New Mission for the Air Force Phillips Laborator	PL/LIM	3- 13
DR Stan Heckman	Massachusetts Inst of technol , Cambridge , MA REPORT NOT AVAILABLE AT PRESS TIME	PL/GPAA	3- 14
DR. James M Henson	University of Nevada , Reno , NV High Resolution Range Doppler Data and Imagery for	PL/WSAT	3- 15
Dr. San-Mou Jeng	University of Cincinnati , Cincinnati , OH Can Design for Cogging of Titanium Aluminide Alloy	PL/RKFA	3- 16
MR. Gerald Kaiser	University of Mass/Lowell , Lowell , MA Physical Wavelets fo Radar and Sonar	PI/GPOS	3- 17
MR Dikshitulu K Kalluri	University of Mass/Lowell , Lowell , MA Backscatter From a Plasma Plume Due to Excitation	PL/GP	3- 18
Lucia M Kimball	Worcester Polytechnic Inst. , Worcester , MA Investigation of Atmospheric Heating and Cooling B	PL/GPOS	3- 19
MR. Albert D Kowalak	University of Massachusetts/Lo , Lowell , MA Investigations of Electron Interactions with Molec	PL/GPID	3- 20
MR. Walter S Kuklinski	University of Mass/Lowell , Lowell , MA Ionspheric Tomography Using a Model Based Transfor	PL/GP	3- 21
Dr. Min-Chang Lee	Massachusetts Institute , Cambridge , MA Studies of Plasma Turbulence with Versatile Toroid	PL/GPSG	3- 22

**SRP Final Report Table of Contents**

<b>Author</b>	<b>University/Institution Report Title</b>	<b>Phillips Laboratory Directorate</b>	<b>Vol-Page</b>
DR Kevin J Malloy	University of New Mexico , Albuquerque , NM <b>REPORT NOT AVAILABLE AT PRESS TIME</b>	PL/VTRP	3- 23
Dr. Charles J Noel	Ohio State University , Columbus , OH Preparation and Characterization of Blends of Orga	PL/RKA	3- 24
DR Hayrani A Oz	Ohio State University , Columbus , OH A Hybrid Algebraic Equation of Motion-Neural Estim	PL/VTSS	3- 25
DR Sudhakar Prasad	University of New Mexico , Albuquerque , NM Focusing Light into a Multiple-Core Fiber: Theory	PL/LIMI	3- 26
DR Mark R Purtill	Texas A&M Univ-Kingsville , Kingsville , TX Static and Dynamic Graph Embedding for Parallel Pr	PL/WSP	3- 27
DR Krishnaswamy Ravi-Chandar	University of Houston , Houston , TX On the Constitutive Behavior of Solid Propellants	PL/RKAP	3- 28
Dr. Wolfgang G Rudolph	University of New Mexico , Albuquerque , NM Relaxation Processes In Gain Switched Iodine Laser	PL/LIDB	3- 29
DR Gary S Sales	Univof Massachusetts-Lowell , Lowell , MA Characterization of Polar Patches: Comparison of	PL/GPIA	3- 30
DR I-Yeu Shen	University of Washington , Seattle , WA A Study of Active Constrained Layer Damping Treatm	PL/VTSS	3- 31
DR Melani I Shoemaker	Seattle Pacific University , Seattle , WA Frequency Domain Analysis of Short Exposure, Photo	PL/LIMI	3- 32
DR Yuri B Shtessel	University of Alabama-Huntsvil , Huntsville , AL Topaz II Reactor Control Law Improvement	PL/VTPC	3- 33

**SRP Final Report Table of Contents**

<b>Author</b>	<b>University/Institution Report Title</b>	<b>Phillips Laboratory Directorate</b>	<b>Vol-Page</b>
Dr. Alexander P Stone	University of New Mexico , Alburquerque , NM Impedances of Coplanar Conical Plates in a Uniform	PL/WSR	3- 34
DR Charles M Swenson	Utah State University , Logan , UT Reflected Laser Communication System	PL/VTRA	3- 35
Dr. Y. C Thio	University of Miami , Coral Gables , FL A Mathematical Model of Self Compression of Compac	PL/WSP	3- 36
DR Jane M Van Doren	College of the Holy Cross , Worcester , MA Investigations of Electron Interactions with Molec	PL/GPID	3- 37
DR Daniel W Watson	Utah State University , Logan , UT A Heterogeneous Parallel Architecture for High-Spe	PL/VTEE	3- 38
Dr. Wayne J Zimmermann	Texas Woman's University , Denton , TX Determination of Space Debris Flux Based on a Fini	PL/WS	3- 39

**SRP Final Report Table of Contents**

<b>Author</b>	<b>University/Institution Report Title</b>	<b>Rome Laboratory Directorate</b>	<b>Vol-Page</b>
DR Valentine A Aalo	Florida Atlantic University , Boca Raton , FL A Program Plan for Transmitting High-Data-Rate ATM	RL/C3BA	4- 1
DR Moeness G Amin	Villanova University , Villanova , PA Interference Excision in Spread Spectrum Using Ti	RL/C3BB	4- 2
Richard G Barakat	Tufts University , Medford , MA REPORT NOT AVAILABLE AT PRESS TIME	RL/EROP	4- 3
DR David P Benjamin	Oklahoma State University , Stillwater , OK Designing Software by Reformulation Using Kids	RL/C3CA	4- 4
DR Frank T Berkey	Utah State University , Logan , UT The Application of Quadratic Phase Coding to OTH R	RL/OCDS	4- 5
DR Joseph Chaiken	Syracuse University , Syracuse , NY A Study of the Application of Fractals and Kineti	RL/ERDR	4- 6
Dr. Pinyuen Chen	Syracuse University , Syracuse , NY On Testing the Equality of Covariance Matrices Use	RL/OCTS	4- 7
DR Julian Cheung	New York Inst. of Technology , New York , , NY On Classification of Multispectral Infrared Image	RL/OCTM	4- 8
DR Ajit K Choudhury	Howard University , Washington , DC Detection Performance of Over Resolved Targets wit	RL/OCTS	4- 9
Dr. Eric Donkor	University of Connecticut , Stroes , CT Experimental Measurement of Nonlinear Effects in	RL/OCPA	4- 10
DR Frances J Harackiewicz	So. Illinois Univ-Carbondale , Carbondale , IL Circular Waveguide to Microstrip Line Transition	RL/ERA	4- 11

**SRP Final Report Table of Contents**

<b>Author</b>	<b>University/Institution Report Title</b>	<b>Rome Laboratory Directorate</b>	<b>Vol-Page</b>
<b>DR Joseph W Haus</b>	Rensselaer Polytechnic Inst , Troy , NY Simulation of Erbium-doped Fiber Lasers	RL/OCP	4- 12
<b>DR Yolanda J Kime</b>	SUNY College-Cortland , Cortland , NY A Macroscopic Model of Electromigration: Comparis	RL/ERDR	4- 13
<b>DR. Phillip G Kornreich</b>	Syracuse University , Syracuse , NY Semiconductor Cylinder Fibers for Fiber Light Ampl	RL/OCP	4- 14
<b>DR Guifang Li</b>	Rochester Institute of Tech , Rochester , NY Self-Pulsation and Optoelectronic Feedback-Sustain	RL/OCP	4- 15
<b>Dr. Beth L Losiewicz</b>	Colorado State University , Fort Collins , CO Preliminary Report on the Feasibility of Machine S	RL/IR	4- 16
<b>DR. Mohamad T Musavi</b>	University of Maine , Orono , ME Automatic Extraction of Drainage Network from Di	RL/IR	4- 17
<b>DR John D Norgard</b>	Univ of Colorado-Colorado Sprg , Colorado Springs , CO Infrared Images of Electromagnetic Fields	RL/ERPT	4- 18
<b>DR Michael A Pittarelli</b>	SUNY Institute of Technology , Utica , NY Anytime Inference and Decision Methods	RL/C3CA	4- 19
<b>DR Dean Richardson</b>	SUNY Institute of Technology , Utica , NY Ultrafast Spectroscopy of Quantum Heterostructures	RL/OCP	4- 20
<b>DR. Daniel F Ryder, Jr.</b>	Tufts University , Medford , MA Synthesis and Properties of B-Diketonate-Modified	RL/ERX	4- 21
<b>DR Gregory J Salamo</b>	University of Arkansas , Fayetteville , AR Photorefractive Development and Application of InP	RL/ERX	4- 22

SRP Final Report Table of Contents

<u>Author</u>	<u>University/Institution</u>	<u>Rome Laboratory</u>	<u>Vol-Page</u>
	<u>Report Title</u>	<u>Directorate</u>	
Dr. Scott E Spetka	SUNY, Institute of Technology , Utica , NY The TkWWW Robot: Beyond Browsing	RL/IR	4- 23
DR James C West	Oklahoma State University , Stillwater , OK Polarimetric Radar Scattering from a Vegation Can	RL/ERC	4- 24
DR Rolf T Wigand	Syracuse University , Syracuse , NY Transferring Technology Via the Internet	RL/XP	4- 25
Dr. Xi-Cheng Zhang	Rensselaer Polytechnic Institu , Troy , NY Temperature Dependence of THz Emission for <111> G	RL/ERX	4- 26

**SRP Final Report Table of Contents**

<b>Author</b>	<b>University/Institution Report Title</b>	<b>Wright Laboratory Directorate</b>	<b>Vol-Page</b>
DR Sunil K Agrawal	Ohio University , Athens , OH A Study of Preform Design Problem for Metal Deform	WL/MLIM	5- 1
DR Michael E Baginski	Auburn University , Auburn , AL Calculation of Heating and Temperature Distributio	WL/MNMF	5- 2
Dr. William W Bannister	Univ of Massachusetts-Lowell , Lowell , MA Anomalous Effects of Water in Fire Firefighting:	WL/FIVC	5- 3
Mr. Larry A Beardsley	Athens State College , Athens , AL RFSIG Target Model Intergrated With the Joint Mode	WL/MNSH	5- 4
DR Thomas L Beck	McMicken Coll of Arts & Sci , , OH Multigrid Method for Large Scale Electronic Struct	WL/MLPJ	5- 5
DR Victor L Berdichevsky	Wayne State University , Detroit , MI Diffusional Creep in Metals and Ceramics at High T	WL/FIB	5- 6
DR. Steven W Buckner	Colullmbus College , Columbus , GA Quantitation of Dissolved O2 in Aviation Fuels by	WL/POSF	5- 7
DR. James J Carroll	Clarkson University , Potsdam , NY Development of an Active Dynamometer System	WL/POOC	5- 8
Dr. Ching L Chang	Cleveland State University , Cleveland , OH Least-Squares Finite Element Methods for Incompres	WL/FIMM	5- 9
Dr. David B Choate	Transylvania University , Lexington , KY A New Superposition	WL/AAWP	5- 10
DR Stephen J Clarson	University of Cincinnati , Cincinnati , OH Synthesis of Novel Second and Third Order Nonlinea	WL/MLBP	5- 11

**SRP Final Report Table of Contents**

<b>Author</b>	<b>University/Institution Report Title</b>	<b>Wright Laboratory Directorate</b>	<b>Vol-Page</b>
<b>Dr. Milton L Cone</b>	<b>Embry-Riddel Aeronautical Univ , Prescott , AZ The Sensor Manager Puzzle</b>	<b>WL/AAAS-</b>	<b>5- 12</b>
<b>DR Robert W Courter</b>	<b>Louisiana State University , Baton Rouge , LA A Research Plan for Evaluating Wavegun as a Low-Lo</b>	<b>WL/MNAA</b>	<b>5- 13</b>
<b>DR Vinay Dayal</b>	<b>Iowa State University , Ames , IA Longitudinal Waves in Fluid Loaded Composite Fiber</b>	<b>WL/MLLP</b>	<b>5- 14</b>
<b>DR Jeffrey C Dill</b>	<b>Ohio University , Athens , OH Discrete Wavelet Transforms for Communication Sign</b>	<b>WL/AAW</b>	<b>5- 15</b>
<b>DR Vincent G Dominic</b>	<b>University of Dayton , Dayton , OH Electro-Optic Characterization of Poled-Polymer Fi</b>	<b>WL/MLPO</b>	<b>5- 16</b>
<b>DR Franklin E Eastep</b>	<b>University of Dayton , Dayton , OH Influence of Mode Complexity and Aeroseleastci Con</b>	<b>WL/FIBR</b>	<b>5- 17</b>
<b>DR Georges M Fadel</b>	<b>Clemson University , Clemson , SC A Methodology for Affordability in the Design Proc</b>	<b>WL/MTR</b>	<b>5- 18</b>
<b>Dr. Joel R Fried</b>	<b>University of Cincinnati , Cincinnati , OH Computer Modeling of Electrolytes for Battery Appl</b>	<b>WL/POOS-</b>	<b>5- 19</b>
<b>DR Paul D Gader</b>	<b>University of Missouri-Columbi , Columbia , MO Scanning Image Algebra Networks for Vehicle Identi</b>	<b>WL/MNGA</b>	<b>5- 20</b>
<b>DR Philip Gatt</b>	<b>University of Central Florida , Orlando , FL Laser Radar Performance Modelling and Analysis wit</b>	<b>WL/MNGS</b>	<b>5- 21</b>
<b>Dr. Richard D Gould</b>	<b>North Carolina State Univ , Raleigh , NC Analysis of Laser Doppler Velocimetry Data</b>	<b>WL/POPT</b>	<b>5- 22</b>

**SRP Final Report Table of Contents**

<b>Author</b>	<b>University/Institution Report Title</b>	<b>Wright Laboratory Directorate</b>	<b>Vol-Page</b>
Dr. Raghava G Gowda	University of Dayton , Dayton , OH Issues Involved in Developing an Object-oriented S	WL/AAAS-	5- 23
DR Guoxiang Gu	Louisiana State University , Baton Rouge , LA Gain Scheduled Missile Autopilot Design Using Obse	WL/MNAG	5- 24
Dr Venkata S Gudimetla	OGI , Portland , OR Thermal Modeling of Heterojunction Bipolar Transis	WL/ELMT	5- 25
Dr. Raimo J Hakkinen	Washington University , St. Louis , MO Further Development of Surface-Obstacle Instrument	WL/FIMN	5- 26
DR Russell C Hardie	Univsity of Dayton , Dayton , OH Adaptive Quadratic Classifiers for Multispectral T	WL/AARA	5- 27
DR Larry S Helmick	Cedarville College , Cedarville , OH Effect of Humidity on Friction and Wear for Fombl	WL/MLBT	5- 28
DR Alan S Hodel	Auburn University , Auburn , AL Automatic Control Issues in the Development of an	WL/MNAG	5- 29
DR Vinod K Jain	University of Dayton , Dayton , OH Can Design for Cogging of Titanium Aluminide Alloy	WL/MLLN	5- 30
DR Jonathan M Janus	Mississippi State University , Mississippi State , MS Multidemensional Algorithm Development and Analysi	WL/MNAA	5- 31
DR Iwona M Jasiuk	Michigan State University , East Lansing , MI Characterization of Interfaces in Metal Matrix Com	WL/WLL	5- 32
Dr. Jack S Jean	Wright State University , Dayton , OH Reed-Solomon Decoding on Champ Architecture	WL/AAAT-	5- 33

**SRP Final Report Table of Contents**

<b>Author</b>	<b>University/Institution Report Title</b>	<b>Wright Laboratory Directorate</b>	<b>Vol-Page</b>
Dr. Ismail I Jouny	Lafayette College , Easton , PA Modeling and Mitigation of Terrain Scattered Inter	WL/AARM	5- 34
DR Tribikram Kundu	University of Arizona , Tucson , AZ Lamb Wave Scanning of a Multilayed Composite Plate	WL/MLLP	5- 35
DR. Jian Li	University of Florida , Gainesville , FL High Resolution Range Signature Estimation	WL/AARA	5- 36
DR. Chun-Shin Lin	University of Missouri-Columbi , Columbia , MO Prediction of Missile Trajectory	WL/FIPA	5- 37
Dr. Paul P Lin	Cleveland State University , Cleveland , OH Three Dimensional Geometry Measurement of Tire Def	WL/FIVM	5- 38
Dr. Juin J Liou	University of Central Florida , Orlando , FL A Model to Monitor the Current Gain Long-Term Inst	WL/ELRD	5- 39
Dr. James S Marsh	University of West Florida , Pensacola , FL Numerical Reconstruction of Holograms in Advanced	WL/MNSI	5- 40
DR Rajiv Mehrotra	Univ. of Missouri-St. Louis , St. Louis , MO Integrated Information Management for ATR Research	WL/AARA	5- 41
DR Douglas J Miller	Cedarville College , Cedarville , OH A Review of Nonfilled Intrinsically Conductive Ela	WL/MLBP	5- 42
DR Nagaraj Nandbakumar	University of Virginia , Charlottesville , VA Thermophysical Affine Invariants from IR Imagery	WL/AARA	5- 43
Dr. M. G Norton	Washington State University , Pullman , WA Surface Outgrowths on Laser-Deposited YBa <sub>2</sub> Cu <sub>3</sub> O <sub>7</sub> Th	WL/MLPO	5- 44

**SRP Final Report Table of Contents**

<b>Author</b>	<b>University/Institution Report Title</b>	<b>Wright Laboratory Directorate</b>	<b>Vol-Page</b>
DR James F O'Brien	Southwest Missouri State Univ. , Springfield , MO The Importance of Lower Orbital Relaxations in Po	WL/MLBP	5- 45
DR Krishna M Pasala	University of Dayton , Dayton , OH Performance of Music and Monopulse Algorithms in t	WL/AARM	5- 46
DR Robert P Penno	University of Dayton , Dayton , OH An Assessment of the WL/AAAI-4 Antenna Wavefront S	WL/AAAI-	5- 47
DR Marek A Perkowski	Portland State University , Portland , OR A Survey of Literature on Function Decomposition	WL/AAAT-	5- 48
DR Ramachandran Radharamanan	Marquette University , Milwaukee , WI A Study on Virtual Manufacturing	WL/MTI	5- 49
DR Ramu V Ramaswamy	University of Florida , Gainesville , FL Annealed Proton Exchanged (APE) Waveguides in LiTa	WL/MNG	5- 50
DR Stanley J Reeves	Auburn University , Auburn , AL Superresolution of Passive Millimeter-Wave Imaging	WL/MNGS	5- 51
Dr. William K Rule	University of Alabama , Tuscaloosa , AL <RESTRICTED DISTRIBUTION - CONTACT LABORATORY>	WL/MNM	5- 52
DR Arindam Saha	Mississippi State University , Mississippi State , MS Evaluation of Network Routers in Real-Time Paralle	WL/AAAT-	5- 53
DR John J Schauer	University of Dayton , Dayton , OH Turbine Blade Film Jet Cooling with Free Stream Tu	WL/POTT	5- 54
DR Carla A Schwartz	University of Florida , Gainesville , FL Neural Networks Identification and Control in Meta	WL/FIGC	5- 55

**SRP Final Report Table of Contents**

<b>Author</b>	<b>University/Institution Report Title</b>	<b>Wright Laboratory Directorate</b>	<b>Vol-Page</b>
DR. James P Seaba	University of Missouri-Columbi , Columbia , MO Multiple Jet Mixing and Atomization in Reacting an	WL/POSF	5- 56
DR Sivanand Simanapalli	University of NC-Charlotte , Charlotte , NC HRR Radar Based Target Identification	WL/AARA	5- 57
DR. Terrence W Simon	University of Minnesota , Minneapolis , MN Documentation of Boundary Layer Characteristics Fo	WL/POTT	5- 58
DR Marek Skowronski	Carnegie Melon University , Pittsburgh , PA Mechanism for Indium Segregation In In <sub>x</sub> Ga <sub>1-x</sub> As Str	WL/ELRA	5- 59
DR Joseph C Slater	Wright State Univesity , Dayton , OH QFT Control of an Advanced Tactical Fighter Aeroel	WL/FIGS	5- 60
DR John A Tague	Ohio University , Athens , OH Performance Analysis of Quadratic Classifiers for	WL/AARA	5- 61
Dr. Barney E Taylor	Miami Univ. - Hamilton , Hamilton , OH Electroluminescence Studies of the Rigid Rod Polym	WL/MLBP	5- 62
DR Krishnaprasad Thirunarayan	Wright State University , Dayton , OH VHDL-93 Paser in Prolog	WL/ELED	5- 63
DR Robert B Trelease	University of California , Los Angeles , CA Developing Qualitative Process Control Discovery S	WL/MLIM	5- 64
DR. Chi-Tay Tsai	Florida Atlantic University , Boca Raton , FL A Study of Massively Parallel Computing on Epic Hy	WL/MNM	5- 65
DR James M Whitney	University of Dayton , Dayton , OH Stress Analysis of the V-Notch (Iosipescu) Shear T	WL/MLBM	5- 66

**SRP Final Report Table of Contents**

<b>Author</b>	<b>University/Institution Report Title</b>	<b>Arnold Engineering Development Center Directorate</b>	<b>Vol-Page</b>
<b>DR Ben A Abbott</b>	<b>Vanderbilt University , Nashville , TN The Application Challenge</b>	<b>Sverdrup</b>	<b>6- 1</b>
<b>DR Theodore A Bapty</b>	<b>Vanderbilt University , Nashville , TN Development of Large Parallel Instrumentation Syst</b>	<b>Sverdrup</b>	<b>6- 2</b>
<b>Dr. Csaba A Biegl</b>	<b>Vanderbilt University , Nashville , TN Universal Graphic User Interface for Turbine Engine</b>	<b>Sverdrup</b>	<b>6- 3</b>
<b>DR Steven H Frankel</b>	<b>Purdue University , West Lafayette , IN Towards The Computational Modeling of Postall Gas</b>	<b>Sverdrup</b>	<b>6- 4</b>
<b>Dr. Peter R Massopust</b>	<b>Sam Houston State University , Huntsville , TX A Wavelet-Multigrid Approach To Solving Partial Di</b>	<b>Calspan</b>	<b>6- 5</b>
<b>DR Randolph S Peterson</b>	<b>University of the South , Sewanee , TN Infrared Imaging Fourier Transform Spectrometer</b>	<b>Sverdrup</b>	<b>6- 6</b>
<b>DR Roy J Schulz</b>	<b>Univ of Tennessee Space Inst , Tullahoma , TN Design of Soot Capturing Sample Probe</b>	<b>Sverdrup</b>	<b>6- 7</b>
<b>DR S A Sherif</b>	<b>College of Eng-Univ of Florida , Gainesville , FL A Model For Local Heat Transfer &amp; Ice Accretion In</b>	<b>Sverdrup</b>	<b>6- 8</b>
<b>DR. Michael Sydor</b>	<b>University of Minnesota-Duluth , Duluth , MN Dimensional Analysis of ARC Heaters</b>	<b>Calspan</b>	<b>6- 9</b>
<b>Dr. John T Tarvin</b>	<b>CALSPAN</b> <b>Samford University , Birmingham , AL Ultraviolet Flat-Field Response of an Intensified</b>		<b>6- 10</b>

SRP Final Report Table of Contents

<u>Author</u>	<u>University/Institution</u>	<u>Frank J Seiler Research Laboratory</u>	<u>Vol-Page</u>
	<u>Report Title</u>	<u>Directorate</u>	
Dr. Gene O Carlisle	West Texas State University , Canyon , TX REPORT NOT AVAILABLE AT PRESS TIME	FJSRL/ NC	6- 11
DR John R Dorgan	Colorado School of Mines , Golden , CO Fundamental Studies on the Solution and Adsorption	FJSRL/NE	6- 12
DR Mary Ann Jungbauer	Barry University , Miami , FL Non-Linear Optical Properties of a Series of Linea	FJSRL/NC	6- 13
DR. Lawrence L Murrell	Pennsylvania State University , University Park , PA Catalytic Gasification of Pitch Carbon Fibers with	FJSRL/NE	6- 14
DR David E Statman	Allegheny College , Meadville , PA Charge Transport and Second Harmonic Generation in	FJSRL/NP	6- 15

SRP Final Report Table of Contents

<u>Author</u>	<u>University/Institution</u>	<u>Wilford Hall Medical Center</u>	<u>Vol-Page</u>
	<u>Report Title</u>	<u>Directorate</u>	
DR Walter Drost-Hansen	University of Miami , Coral Gables , FL Effects of Temperature on Various Hematological Pa	WHMC/RD	6- 16

## INTRODUCTION

The Summer Research Program (SRP), sponsored by the Air Force Office of Scientific Research (AFOSR), offers paid opportunities for university faculty, graduate students, and high school students to conduct research in U.S. Air Force research laboratories nationwide during the summer.

Introduced by AFOSR in 1978, this innovative program is based on the concept of teaming academic researchers with Air Force scientists in the same disciplines using laboratory facilities and equipment not often available at associates' institutions.

AFOSR also offers its research associates an opportunity, under the Summer Research Extension Program (SREP), to continue their AFOSR-sponsored research at their home institutions through the award of research grants. In 1994 the maximum amount of each grant was increased from \$20,000 to \$25,000, and the number of AFOSR-sponsored grants decreased from 75 to 60. A separate annual report is compiled on the SREP.

The Summer Faculty Research Program (SFRP) is open annually to approximately 150 faculty members with at least two years of teaching and/or research experience in accredited U.S. colleges, universities, or technical institutions. SFRP associates must be either U.S. citizens or permanent residents.

The Graduate Student Research Program (GSRP) is open annually to approximately 100 graduate students holding a bachelor's or a master's degree; GSRP associates must be U.S. citizens enrolled full time at an accredited institution.

The High School Apprentice Program (HSAP) annually selects about 125 high school students located within a twenty mile commuting distance of participating Air Force laboratories.

The numbers of projected summer research participants in each of the three categories are usually increased through direct sponsorship by participating laboratories.

AFOSR's SRP has well served its objectives of building critical links between Air Force research laboratories and the academic community, opening avenues of communications and forging new research relationships between Air Force and academic technical experts in areas of national interest; and strengthening the nation's efforts to sustain careers in science and engineering. The success of the SRP can be gauged from its growth from inception (see Table 1) and from the favorable responses the 1994 participants expressed in end-of-tour SRP evaluations (Appendix B).

AFOSR contracts for administration of the SRP by civilian contractors. The contract was first awarded to Research & Development Laboratories (RDL) in September 1990. After completion of the 1990 contract, RDL won the recompetition for the basic year and four 1-year options.

## 2. PARTICIPATION IN THE SUMMER RESEARCH PROGRAM

The SRP began with faculty associates in 1979; graduate students were added in 1982 and high school students in 1986. The following table shows the number of associates in the program each year.

Table 1: SRP Participation, by Year

YEAR	Number of Participants			TOTAL
	SFRP	GSRP	HSAP	
1979	70			70
1980	87			87
1981	87			87
1982	91	17		108
1983	101	53		154
1984	152	84		236
1985	154	92		246
1986	158	100	42	300
1987	159	101	73	333
1988	153	107	101	361
1989	168	102	103	373
1990	165	121	132	418
1991	170	142	132	444
1992	185	121	159	464
1993	187	117	136	440
1994	192	117	133	442

Beginning in 1993, due to budget cuts, some of the laboratories weren't able to afford to fund as many associates as in previous years; in one case a laboratory did not fund any additional associates. However, the table shows that, overall, the number of participating associates increased this year because two laboratories funded more associates than they had in previous years.

### 3. RECRUITING AND SELECTION

The SRP is conducted on a nationally advertised and competitive-selection basis. The advertising for faculty and graduate students consisted primarily of the mailing of 8,000 44-page SRP brochures to chairpersons of departments relevant to AFOSR research and to administrators of grants in accredited universities, colleges, and technical institutions. Historically Black Colleges and Universities (HBCUs) and Minority Institutions (MIs) were included. Brochures also went to all participating USAF laboratories, the previous year's participants, and numerous (over 600 annually) individual requesters.

Due to a delay in awarding the new contract, RDL was not able to place advertisements in any of the following publications in which the SRP is normally advertised: *Black Issues in Higher Education*, *Chemical & Engineering News*, *IEEE Spectrum* and *Physics Today*.

High school applicants can participate only in laboratories located no more than 20 miles from their residence. Tailored brochures on the HSAP were sent to the head counselors of 180 high schools in the vicinity of participating laboratories, with instructions for publicizing the program in their schools. High school students selected to serve at Wright Laboratory's Armament Directorate (Eglin Air Force Base, Florida) serve eleven weeks as opposed to the eight weeks normally worked by high school students at all other participating laboratories.

Each SFRP or GSRP applicant is given a first, second, and third choice of laboratory. High school students who have more than one laboratory or directorate near their homes are also given first, second, and third choices.

Laboratories make their selections and prioritize their nominees. AFOSR then determines the number to be funded at each laboratory and approves laboratories' selections.

Subsequently, laboratories use their own funds to sponsor additional candidates. Some selectees do not accept the appointment, so alternate candidates are chosen. This multi-step selection procedure results in some candidates being notified of their acceptance after scheduled deadlines. The total applicants and participants for 1994 are shown in this table.

Table 2: 1994 Applicants and Participants

PARTICIPANT CATEGORY	TOTAL APPLICANTS	SELECTEES	DECLINING SELECTEES
SFRP (HBCU/MI)	600 (90)	192 (16)	30 (7)
GSRP (HBCU/MI)	322 (11)	117 (6)	11 (0)
HSAP	562	133	14
TOTAL	1484	442	55

### 4. SITE VISITS

During June and July of 1994, representatives of both AFOSR/NI and RDL visited each participating laboratory to provide briefings, answer questions, and resolve problems for both laboratory personnel and participants. The objective was to ensure that the SRP would be as constructive as possible for all participants. Both SRP participants and RDL representatives found these visits beneficial. At many of the laboratories, this was the only opportunity for all participants to meet at one time to share their experiences and exchange ideas.

## **5. HISTORICALLY BLACK COLLEGES AND UNIVERSITIES AND MINORITY INSTITUTIONS (HBCU/MIs)**

In previous years, an RDL program representative visited from seven to ten different HBCU/MIs to promote interest in the SRP among the faculty and graduate students. Due to the late contract award date (January 1994) no time was available to visit HBCU/MIs this past year.

In addition to RDL's special recruiting efforts, AFOSR attempts each year to obtain additional funding or use leftover funding from cancellations the past year to fund HBCU/MI associates. This year, seven HBCU/MI SFRPs declined after they were selected. The following table records HBCU/MI participation in this program.

Table 3: SRP HBCU/MI Participation, by Year

YEAR	SFRP		GSRP	
	Applicants	Participants	Applicants	Participants
1985	76	23	15	11
1986	70	18	20	10
1987	82	32	32	10
1988	53	17	23	14
1989	39	15	13	4
1990	43	14	17	3
1991	42	13	8	5
1992	70	13	9	5
1993	60	13	6	2
1994	90	16	11	6

## 6. SRP FUNDING SOURCES

Funding sources for the 1994 SRP were the AFOSR-provided slots for the basic contract and laboratory funds. Funding sources by category for the 1994 SRP selected participants are shown here.

Table 4: 1994 SRP Associate Funding

FUNDING CATEGORY	SFRP	GSRP	HSAP
AFOSR Basic Allocation Funds	150	98 <sup>*1</sup>	121 <sup>*2</sup>
USAF Laboratory Funds	37	19	12
HBCU/MI By AFOSR (Using Procured Addn'l Funds)	5	0	0
<b>TOTAL</b>	<b>192</b>	<b>117</b>	<b>133</b>

\*1 - 100 were selected, but two canceled too late to be replaced.

\*2 - 125 were selected, but four canceled too late to be replaced.

## 7. COMPENSATION FOR PARTICIPANTS

Compensation for SRP participants, per five-day work week, is shown in this table.

Table 5: 1994 SRP Associate Compensation

PARTICIPANT CATEGORY	1991	1992	1993	1994
Faculty Members	\$690	\$718	\$740	\$740
Graduate Student (Master's Degree)	\$425	\$442	\$455	\$455
Graduate Student (Bachelor's Degree)	\$365	\$380	\$391	\$391
High School Student (First Year)	\$200	\$200	\$200	\$200
High School Student (Subsequent Years)	\$240	\$240	\$240	\$240

The program also offered associates whose homes were more than 50 miles from the laboratory an expense allowance (seven days per week) of \$50/day for faculty and \$37/day for graduate students. Transportation to the laboratory at the beginning of their tour and back to their home destinations at the end was also reimbursed for these participants. Of the combined SFRP and GSRP associates, 58% (178 out of 309) claimed travel reimbursements at an average round-trip cost of \$860.

Faculty members were encouraged to visit their laboratories before their summer tour began. All costs of these orientation visits were reimbursed. Forty-one percent (78 out of 192) of faculty associates took orientation trips at an average cost of \$498. Many faculty associates noted on their evaluation forms that due to the late notice of acceptance into the 1994 SRP (caused by the late award in January 1994 of the contract) there wasn't enough time to attend an orientation visit prior to their tour start date. In 1993, 58 % of SFRP associates took orientation visits at an average cost of \$685.

Program participants submitted biweekly vouchers countersigned by their laboratory research focal point, and RDL issued paychecks so as to arrive in associates' hands two weeks later.

HSAP program participants were considered actual RDL employees, and their respective state and federal income tax and Social Security were withheld from their paychecks. By the nature of their independent research, SFRP and GSRP program participants were considered to be consultants or independent contractors. As such, SFRP and GSRP associates were responsible for their own income taxes, Social Security, and insurance.

## 8. CONTENTS OF THE 1994 REPORT

The complete set of reports for the 1994 SRP includes this program management report augmented by fifteen volumes of final research reports by the 1994 associates as indicated below:

Table 6: 1994 SRP Final Report Volume Assignments

LABORATORY	VOLUME		
	SFRP	GSRP	HSAP
Armstrong	2	7	12
Phillips	3	8	13
Rome	4	9	14
Wright	5A, 5B	10	15
AEDC, FJSRL, WHMC	6	11	16

AEDC = Arnold Engineering Development Center  
FJSRL = Frank J. Seiler Research Laboratory  
WHMC = Wilford Hall Medical Center

## APPENDIX A – PROGRAM STATISTICAL SUMMARY

### A. Colleges/Universities Represented

Selected SFRP and GSRP associates represent 158 different colleges, universities, and institutions.

### B. States Represented

SFRP -Applicants came from 46 states plus Washington D.C. and Puerto Rico. Selectees represent 40 states.

GSRP - Applicants came from 46 states and Puerto Rico. Selectees represent 34 states.

HSAP - Applicants came from fifteen states. Selectees represent ten states.

### C. Academic Disciplines Represented

The academic disciplines of the combined 192 SFRP associates are as follows:

Electrical Engineering	22.4%
Mechanical Engineering	14.0%
Physics: General, Nuclear & Plasma	12.2%
Chemistry & Chemical Engineering	11.2%
Mathematics & Statistics	8.1%
Psychology	7.0%
Computer Science	6.4%
Aerospace & Aeronautical Engineering	4.8%
Engineering Science	2.7%
Biology & Inorganic Chemistry	2.2%
Physics: Electro-Optics & Photonics	2.2%
Communication	1.6%
Industrial & Civil Engineering	1.6%
Physiology	1.1%
Polymer Science	1.1%
Education	0.5%
Pharmaceutics	0.5%
Veterinary Medicine	0.5%
<hr/> TOTAL	100%

Table A-1. Total Participants

Number of Participants	
SFRP	192
GSRP	117
HSAP	133
<b>TOTAL</b>	<b>442</b>

Table A-2. Degrees Represented

Degrees Represented			
	SFRP	GSRP	TOTAL
Doctoral	189	0	189
Master's	3	47	50
Bachelor's	0	70	70
<b>TOTAL</b>	<b>192</b>	<b>117</b>	<b>309</b>

Table A-3. SFRP Academic Titles

Academic Titles	
Assistant Professor	74
Associate Professor	63
Professor	44
Instructor	5
Chairman	1
Visiting Professor	1
Visiting Assoc. Prof.	1
Research Associate	3
<b>TOTAL</b>	<b>192</b>

Table A-4. Source of Learning About SRP

SOURCE	SFRP		GSRP	
	Applicants	Selectees	Applicants	Selectees
Applied/participated in prior years	26%	37%	10%	13%
	19%	17%	12%	12%
	32%	18%	19%	12%
	15%	24%	9%	12%
	--	--	39%	43%
	8%	4%	11%	8%
TOTAL	100%	100%	100%	100%

Table A-5. Ethnic Background of Applicants and Selectees

	SFRP		GSRP		HSAP	
	Applicants	Selectees	Applicants	Selectees	Applicants	Selectees
American Indian or Native Alaskan	0.2%	0%	1%	0%	0.4%	0%
Asian/Pacific Islander	30%	20%	6%	8%	7%	10%
Black	4%	1.5%	3%	3%	7%	2%
Hispanic	3%	1.9%	4%	4.5%	11%	8%
Caucasian	51%	63%	77%	77%	70%	75%
Preferred not to answer	12%	14%	9%	7%	4%	5%
TOTAL	100%	100%	100%	100%	99%	100%

Table A-6. Percentages of Selectees receiving their 1st, 2nd, or 3rd Choices of Directorate

	1st Choice	2nd Choice	3rd Choice	Other Than Their Choice
SFRP	70%	7%	3%	20%
GSRP	76%	2%	2%	20%

## APPENDIX B – SRP EVALUATION RESPONSES

### 1. OVERVIEW

Evaluations were completed and returned to RDL by four groups at the completion of the SRP. The number of respondents in each group is shown below.

Table B-1. Total SRP Evaluations Received

Evaluation Group	Responses
SFRP & GSRPs	275
HSAPs	116
USAF Laboratory Focal Points	109
USAF Laboratory HSAP Mentors	54

All groups indicate near-unanimous enthusiasm for the SRP experience.

Typical comments from 1994 SRP associates are:

"[The SRP was an] excellent opportunity to work in state-of-the-art facility with top-notch people."

"[The SRP experience] enabled exposure to interesting scientific application problems; enhancement of knowledge and insight into 'real-world' problems."

"[The SRP] was a great opportunity for resourceful and independent faculty [members] from small colleges to obtain research credentials."

"The laboratory personnel I worked with are tremendous, both personally and scientifically. I cannot emphasize how wonderful they are."

"The one-on-one relationship with my mentor and the hands on research experience improved [my] understanding of physics in addition to improving my library research skills. Very valuable for [both] college and career!"

Typical comments from laboratory focal points and mentors are:

"This program [AFOSR - SFRP] has been a 'God Send' for us. Ties established with summer faculty have proven invaluable."

"Program was excellent from our perspective. So much was accomplished that new options became viable "

"This program managed to get around most of the red tape and 'BS' associated with most Air Force programs. Good Job!"

"Great program for high school students to be introduced to the research environment. Highly educational for others [at laboratory]."

"This is an excellent program to introduce students to technology and give them a feel for [science/engineering] career fields. I view any return benefit to the government to be 'icing on the cake' and have usually benefitted."

The summarized recommendations for program improvement from both associates and laboratory personnel are listed below (Note: basically the same as in previous years.)

- A. Better preparation on the labs' part prior to associates' arrival (i.e., office space, computer assets, clearly defined scope of work).
- B. Laboratory sponsor seminar presentations of work conducted by associates, and/or organized social functions for associates to collectively meet and share SRP experiences.
- C. Laboratory focal points collectively suggest more AFOSR allocated associate positions, so that more people may share in the experience.
- D. Associates collectively suggest higher stipends for SRP associates.
- E. Both HSAP Air Force laboratory mentors and associates would like the summer tour extended from the current 8 weeks to either 10 or 11 weeks; the groups state it takes 4-6 weeks just to get high school students up-to-speed on what's going on at laboratory. (Note: this same argument was used to raise the faculty and graduate student participation time a few years ago.)

## 2. 1994 USAF LABORATORY FOCAL POINT (LFP) EVALUATION RESPONSES

The summarized results listed below are from the 109 LFP evaluations received.

### 1. LFP evaluations received and associate preferences:

Table B-2. Air Force LFP Evaluation Responses (By Type)

Lab	Evals Recv'd	How Many Associates Would You Prefer To Get ? (% Response)											
		SFRP				GSRP (w/Univ Professor)				GSRP (w/o Univ Professor)			
		0	1	2	3+	0	1	2	3+	0	1	2	3+
AEDC	10	30	50	0	20	50	40	0	10	40	60	0	0
AL	44	34	50	6	9	54	34	12	0	56	31	12	0
FJSRL	3	33	33	33	0	67	33	0	0	33	67	0	0
PL	14	28	43	28	0	57	21	21	0	71	28	0	0
RL	3	33	67	0	0	67	0	33	0	100	0	0	0
WHMC	1	0	0	100	0	0	100	0	0	0	100	0	0
WL	46	15	61	24	0	56	30	13	0	76	17	6	0
<b>Total</b>	<b>121</b>	<b>25%</b>	<b>43%</b>	<b>27%</b>	<b>4%</b>	<b>50%</b>	<b>37%</b>	<b>11%</b>	<b>1%</b>	<b>54%</b>	<b>43%</b>	<b>3%</b>	<b>0%</b>

**LFP Evaluation Summary.** The summarized responses, by laboratory, are listed on the following page. LFPs were asked to rate the following questions on a scale from 1 (below average) to 5 (above average).

2. LFPs involved in SRP associate application evaluation process:
  - a. Time available for evaluation of applications:
  - b. Adequacy of applications for selection process:
3. Value of orientation trips:
4. Length of research tour:
5. a. Benefits of associate's work to laboratory:  
b. Benefits of associate's work to Air Force:
6. a. Enhancement of research qualifications for LFP and staff:  
b. Enhancement of research qualifications for SFRP associate:  
c. Enhancement of research qualifications for GSRP associate:
7. a. Enhancement of knowledge for LFP and staff:  
b. Enhancement of knowledge for SFRP associate:  
c. Enhancement of knowledge for GSRP associate:
8. Value of Air Force and university links:
9. Potential for future collaboration:
10. a. Your working relationship with SFRP:  
b. Your working relationship with GSRP:
11. Expenditure of your time worthwhile:

(Continued on next page)

12. Quality of program literature for associate:  
 13. a. Quality of RDL's communications with you:  
 b. Quality of RDL's communications with associates:  
 14. Overall assessment of SRP:

Laboratory Focal Point Responses to above questions

	<i>AEDC</i>	<i>AL</i>	<i>FJSRL</i>	<i>PL</i>	<i>RL</i>	<i>WHMC</i>	<i>WL</i>
<i># Evals Recv'd</i>	10	32	3	14	3	1	46
<i>Question #</i>							
2	90 %	62 %	100 %	64 %	100 %	100 %	83 %
2a	<b>3.5</b>	<b>3.5</b>	4.7	4.4	4.0	4.0	<b>3.7</b>
2b	4.0	3.8	4.0	4.3	4.3	4.0	3.9
3	4.2	3.6	4.3	3.8	4.7	4.0	4.0
4	3.8	3.9	4.0	4.2	4.3	NO ENTRY	4.0
5a	4.1	4.4	4.7	4.9	4.3	3.0	4.6
5b	4.0	4.2	4.7	4.7	4.3	3.0	4.5
6a	<b>3.6</b>	4.1	<b>3.7</b>	4.5	4.3	<b>3.0</b>	4.1
6b	3.6	4.0	4.0	4.4	4.7	3.0	4.2
6c	3.3	4.2	4.0	4.5	4.5	3.0	4.2
7a	3.9	4.3	4.0	4.6	4.0	3.0	4.2
7b	4.1	4.3	4.3	4.6	4.7	3.0	4.3
7c	3.3	4.1	4.5	4.5	4.5	5.0	4.3
8	4.2	4.3	5.0	4.9	4.3	5.0	4.7
9	3.8	4.1	4.7	5.0	4.7	5.0	4.6
10a	4.6	4.5	5.0	<b>4.9</b>	4.7	5.0	4.7
10b	4.3	4.2	5.0	4.3	5.0	5.0	4.5
11	4.1	4.5	4.3	4.9	4.7	4.0	4.4
12	4.1	3.9	4.0	4.4	4.7	3.0	4.1
13a	<b>3.8</b>	<b>2.9</b>	4.0	4.0	4.7	<b>3.0</b>	<b>3.6</b>
13b	<b>3.8</b>	<b>2.9</b>	4.0	4.3	4.7	<b>3.0</b>	<b>3.8</b>
14	4.5	4.4	5.0	4.9	4.7	4.0	4.5

### **3. 1994 SFRP & GSRP EVALUATION RESPONSES**

The summarized results listed below are from the 275 SFRP/GSRP evaluations received.

Associates were asked to rate the following questions on a scale from 1 (below average) to 5 (above average)

1. The match between the laboratories research and your field:	4.6
2. Your working relationship with your LFP:	4.8
3. Enhancement of your academic qualifications:	4.4
4. Enhancement of your research qualifications:	4.5
5. Lab readiness for you: LFP, task, plan:	4.3
6. Lab readiness for you: equipment, supplies, facilities:	4.1
7. Lab resources:	4.3
8. Lab research and administrative support:	4.5
9. Adequacy of brochure and associate handbook:	4.3
10. RDL communications with you:	4.3
11. Overall payment procedures:	3.8
12. Overall assessment of the SRP:	4.7
13. a. Would you apply again?	Yes: 85%
b. Will you continue this or related research?	Yes: 95%
14. Was length of your tour satisfactory?	Yes: 86%
15. Percentage of associates who engaged in:	
a. Seminar presentation:	52%
b. Technical meetings:	32%
c. Social functions:	03%
d. Other	01%

16. Percentage of associates who experienced difficulties in:

a. Finding housing:	12%
b. Check Cashing:	03%

17. Where did you stay during your SRP tour?

a. At Home:	20%
b. With Friend:	06%
c. On Local Economy:	47%
d. Base Quarters:	10%

**THIS SECTION FACULTY ONLY:**

18. Were graduate students working with you? Yes: 23%

19. Would you bring graduate students next year? Yes: 56%

20. Value of orientation visit:

Essential:	29%
Convenient:	20%
Not Worth Cost:	01%
Not Used:	34%

**THIS SECTION GRADUATE STUDENTS ONLY:**

21. Who did you work with:

University Professor:	18%
Laboratory Scientist:	54%

#### 4. 1994 USAF LABORATORY HSAP MENTOR EVALUATION RESPONSES

The summarized results listed below are from the 54 mentor evaluations received.

1. Mentor apprentice preferences:

Table B-3. Air Force Mentor Responses

Laboratory	# Evals Recv'd	How Many Apprentices Would You Prefer To Get ?			
		0	1	2	3+
<b>AEDC</b>	6	0	100	0	0
<b>AL</b>	17	29	47	6	18
<b>PL</b>	9	22	78	0	0
<b>RL</b>	4	25	75	0	0
<b>WL</b>	18	22	55	17	6
<b>Total</b>	<b>54</b>	<b>20%</b>	<b>71%</b>	<b>5%</b>	<b>5%</b>

Mentors were asked to rate the following questions on a scale from 1 (below average) to 5 (above average)

2. Mentors involved in SRP apprentice application evaluation process:
  - a. Time available for evaluation of applications:
  - b. Adequacy of applications for selection process:
3. Laboratory's preparation for apprentice:
4. Mentor's preparation for apprentice:
5. Length of research tour:
6. Benefits of apprentice's work to U.S. Air force:
7. Enhancement of academic qualifications for apprentice:
8. Enhancement of research skills for apprentice:
9. Value of U.S. Air Force/high school links:
10. Mentor's working relationship with apprentice:
11. Expenditure of mentor's time worthwhile:
12. Quality of program literature for apprentice:
13.
  - a. Quality of RDL's communications with mentors:
  - b. Quality of RDL's communication with apprentices:
14. Overall assessment of SRP:

	<i>AEDC</i>	<i>AL</i>	<i>PL</i>	<i>RL</i>	<i>WL</i>
<i># Evals Recv'd</i>	<b>6</b>	<b>17</b>	<b>9</b>	<b>4</b>	<b>18</b>
<i>Question #</i>					
<b>2</b>	100 %	76 %	56 %	75 %	61 %
<b>2a</b>	4.2	4.0	<b>3.1</b>	<b>3.7</b>	<b>3.5</b>
<b>2b</b>	4.0	4.5	4.0	4.0	3.8
<b>3</b>	4.3	<b>3.8</b>	<b>3.9</b>	<b>3.8</b>	<b>3.8</b>
<b>4</b>	4.5	<b>3.7</b>	<b>3.4</b>	4.2	<b>3.9</b>
<b>5</b>	<b>3.5</b>	4.1	<b>3.1</b>	<b>3.7</b>	<b>3.6</b>
<b>6</b>	4.3	3.9	4.0	4.0	4.2
<b>7</b>	4.0	4.4	4.3	4.2	3.9
<b>8</b>	4.7	4.4	4.4	4.2	4.0
<b>9</b>	4.7	4.2	3.7	4.5	4.0
<b>10</b>	4.7	4.5	4.4	4.5	4.2
<b>11</b>	4.8	4.3	4.0	4.5	4.1
<b>12</b>	4.2	4.1	4.1	4.8	3.4
<b>13a</b>	<b>3.5</b>	<b>3.9</b>	<b>3.7</b>	4.0	<b>3.1</b>
<b>13b</b>	4.0	4.1	3.4	4.0	3.5
<b>14</b>	4.3	4.5	3.8	4.5	4.1

## 5. 1994 HSAP EVALUATION RESPONSES

The summarized results listed below are from the 116 HSAP evaluations received.

HSAP apprentices were asked to rate the following questions on a scale from 1 (below average) to 5 (above average)

1. Match of lab research to you interest:	3.9
2. Apprentices working relationship with their mentor and other lab scientists:	4.6
3. Enhancement of your academic qualifications:	4.4
4. Enhancement of your research qualifications:	4.1
5. Lab readiness for you: mentor, task, work plan	3.7
6. Lab readiness for you: equipment supplies facilities	4.3
7. Lab resources: availability	4.3
8. Lab research and administrative support:	4.4
9. Adequacy of RDL's apprentice handbook and administrative materials:	4.0
10. Responsiveness of RDL's communications:	3.5
11. Overall payment procedures:	3.3
12. Overall assessment of SRP value to you:	4.5
13. Would you apply again next year?	Yes: 88%
14. Was length of SRP tour satisfactory?	Yes: 78%
15. Percentages of apprentices who engaged in:	
a. Seminar presentation:	48%
b. Technical meetings:	23%
c. Social functions:	18%

The Application Challenge

Ben A. Abbott  
Research Assistant Professor  
Department of Electrical and Computer Engineering

Vanderbilt University  
400 24th Avenue South  
Nashville, TN 37235

Final Report for:  
Summer Faculty Research Program  
Arnold Engineering Development Center

Sponsored by:  
Air Force Office of Scientific Research  
Bolling Air Force Base, Washington, D.C.  
and  
Arnold Engineering Development Center

September 1994

## The Application Challenge

Ben A. Abbott

Research Assistant Professor

Department of Electrical and Computer Engineering

### Abstract

Grand challenge applications test the limits and benefits of high performance computer (HPC) technology applied to problems of great significance. This focus on the development of a handful of pilot applications is necessary for both developers and potential users. However, the development methods employed to achieve the grand challenge goals are not always useful as general application development models for prospective industrial users. One of the critical questions is, what kind of application development technology would enable rapid growth in HPC applications?

This paper argues that in many important industrial application areas the answer is not in the relentless quest for simplified, "easy-to-use" programming models. Rather, it is more efficient to provide rich, domain specific, model-based programming environments that directly support concepts, relations and model composition principles which are routinely used in the particular application field. Further, it highlights our experience using tools of this type to develop high performance applications while participating in the 1994 SFRP at AEDC.

## The Application Challenge

Ben A. Abbott

### Introduction

In recent years, parallel computer architectures have achieved respectable results in high performance computing. Microprocessor-based parallel computers have the potential to offer higher performance/cost ratios than vector multiprocessors. Therefore, significant effort has been invested in their development. Although the peak performance of emerging parallel systems seems to justify this promise, they have not yet delivered this high performance to a large class of applications.

The single most important barrier to the use of highly parallel systems has been the difficulty of programming. The recent convergence in parallel architectures provided the foundation for faster progress in operating systems and parallel languages. Highly portable micro-kernels, modular servers, and data parallel language dialects such as High Performance Fortran and High Performance C++ enable and simplify programming of many applications. While these results are necessary for providing access to the hardware resources, they are far from enough to support the widespread application of high performance parallel computers. Despite the relative simplicity of the HPF and HPC++ parallel programming models, the routine development of applications that can take advantage of four to five orders of magnitude higher computation performance than today's workstations, remains a major challenge.

The current focus on the development of a handful of pilot applications is necessary both for the developers and potential users. Grand challenge applications test the limits and benefits of the technology in problems of great significance. However, the development method used in these unique programs should not be expected to serve as a general application development model for prospective industrial users. One of the critical questions is, what kind of application development technology would enable rapid growth in HPC applications?

This paper argues that in many important industrial application areas the answer is not in the relentless quest for simplified, "easy-to-use" programming models. Rather, it is more efficient to provide rich, domain specific model-based programming environments that directly support concepts, relations and model composition principles which are routinely used in the particular application field. Over the last decade, Vanderbilt University's Measurement and Computing

Systems Laboratory has developed several model-based programming environments for medical instrumentation [19], aerospace [13], process control [11], large-scale signal processing [20] and parallel instrumentation [2] applications. The first part of this paper summarizes the Multigraph Architecture (MGA) which provides a unified framework for model-based programming environments. The second part describes a specific example for an MGA-based model-based programming environment and program synthesis system, which has been developed for large-scale, parallel instrumentation systems, CADDMAS.

### Model-Based Programming Environments

The role and significance of models and modeling in software engineering is well recognized. In a recent paper [8], David Harel described a software development method which utilizes models for representing the function and behavior of the software to be implemented. These models are suggested for use in formal analysis and execution, providing tremendous help in building large-scale, reliable systems. Our approach is closely related to the method described by Harel. In many industrial applications, particularly in the area of embedded and reactive systems, system designers view software as an implementation method of certain functionalities (controllers, monitoring systems, etc.) which are an integral part of a complex environment. The natural way to specify these functionalities is to use the concepts and notions of the domain, independently from the way of their implementation.

In the MGA approach, a model-based programming environment is inherently domain specific; it adopts the concepts, relations, composition principles and constraints of a given domain. In complex domains, for instance in chemical process management where the modeling paradigm is extremely rich [10], the programming environment is necessarily complex. The Multigraph Architecture is a particular solution for building model-based programming environments.

### Multigraph Architecture

The MGA provides the architectural framework for model-based software synthesis in real-time, parallel computing environments. The structure of the MGA, which has been greatly influenced by the need for dynamic program synthesis, includes three main components, the *Modeling Environment*, the *Model Interpreters*, and the *Execution Environment*.

The Modeling Environment includes tools for building, maintaining and storing multiple-

aspect models  $\mathcal{M} = < M_1, M_2, \dots, M_n >$  that represent domain knowledge. The Model Interpreters transform the models into an executable program. A special execution environment is needed to support the program generated. For the past MGA applications, the Execution Environment has been based on a macro-dataflow virtual machine defined by the Multigraph Computational Model (MCM) and implemented by the Multigraph Kernel (MGK). During the SFRP, the execution environment has evolved into what we call “active processes”. “Active processes” fully support the previous abstraction of the Multigraph Kernel as well as being faster, smaller, and supporting hard real-time constraints. Both “active processes” and the MGK execution environments provide support for the MCM along with an application specific “primitive” library whose elements are the lowest-level components of the generated program. The following sections provide details about the Multigraph Architecture components. Details of the new “active processes” execution environment are provided in the final report written by Ted Bapty contained in this volume.

### Modeling Environment

One of the critical issues of model-based program synthesis is the content and structure of model databases. They capture the information needed to generate programs from requirements in a given application domain.

In Multigraph, the application specific knowledge is expressed in the form of *formal models* whose building, verification and maintenance is supported by various tools, which constitute the Modeling Environment. The term *model-based software synthesis* stems from this characteristic of the knowledge-base, and differentiates the approach from other transformational systems where the knowledge base is represented primarily in the form of transformation rules.

### Models and Model Builders

The role and use of system modeling is a fundamental topic in software engineering. Earlier work on structured analysis and design (e.g. [5]), current work on software modeling [8], and object-oriented modeling and design (e.g. [15]) identified basic aspects such as *functional*, *control* (or *behavioral*), and decomposition principles such as *module hierarchy*, *abstraction hierarchy*, and *inheritance hierarchy* that have become part of software engineering practice. Experience with a variety of reactive systems in the fields of instrumentation [18], process control [11], and

signal processing [20] have led to the recognition of the following principles:

1. *Need for multiple-aspect modeling.* A generally accepted approach in modeling reactive systems is to model only specific aspects of the *software to be built* [8]. Although this approach limits the complexity of modeling, it leaves out an essential component of reactive systems, the environment. For example, in process control systems the structure and characteristics of the monitoring and fault diagnostic software are strongly influenced by the model of the plant [14]. This information is usually present in the code only in the form of implicit assumptions and attributes. In large-scale real-time instrumentation systems that are running on parallel hardware configurations, the structure of the signal-flow is directly influenced by the hardware configuration [1]. Therefore, modeling paradigms in Multigraph-based systems typically consist of multiple modeling aspects. These include selected features of the environment, the software system, and their interaction. The software is generated using the information in these models in the *model interpretation process*.
2. *Use of application specific modeling paradigms.* A modeling paradigm includes concepts and relationships that can efficiently represent a domain. Multigraph-based systems use application specific modeling paradigms for two reasons: 1) General-purpose semantic knowledge representation seems to be far in the future [16] and currently it does not promise usable results. 2) Many disciplines use formalized and ad-hoc modeling paradigms for describing the function and behavior of systems, and for communicating design requirements. Process flow-sheets in the chemical industry and signal-flow graphs in electrical engineering are examples of application specific concepts and notations. It is usually inefficient (and maybe impossible) to recast existing, thoroughly understood knowledge in a different framework. Multigraph attempts to provide generality, not on the level of the modeling paradigm, but in the overall framework and the supporting tools. It uses customizable graphic editors for model building [9], modeling paradigm specification languages, and tools for model interpretation.
3. *Use of a unified control discipline.* The control structure is always a considerable part of the complexity of programs. This is particularly true for parallel computing software, where communication and synchronization among the computation units are critical not

only for the correct operation but also for the performance of the system. A basic feature of the MGA is that the execution environment includes a unified processor and architecture independent Multigraph Computation Model (MCM). The significance of the MCM is that models can be transformed into a unified computation-graph. This graph implicitly defines the communication and synchronization among the elementary computation units.

One of the valuable contributions of AI research to modeling is the rich knowledge representation formalism. The two most frequently used solutions are: (1) rule forms possibly augmented with numeric representation schemes; and (2) declarative representation languages defined for the selected problem specific modeling discipline. Experience shows that rule-oriented representation methods are often inefficient, intractable, and, in a number of cases, are not sufficient for general model building problems [6]. It is especially true in system modeling where most of the complexity is expressed in structural relationships. Therefore, the modeling is based on a unified *declarative language framework* and an equivalent *graphic representation formalism* which can be customized to specific modeling paradigms. A detailed description of the underlying software technology can be found in [11]. The general characteristics of the MGA modeling formalism are the following:

1. A declarative language that is a “frame-language” in a LISP-like syntax.
2. The graphic formalism is based on icons, ports, and connections.
3. The model-building is accomplished by using graphic editors. Construction of graphic structures automatically generates the associated textual form, the declarative language representation.

### Execution Environment

The interpretation process transforms the declared models and specifications into a set of communicating executable programs spread across a network of processors. In order to make this program synthesis computation easier to implement, the Multigraph Computational Model (MCM) is used as a unified virtual machine in the Execution Environment. The MCM is a *macro dataflow model*, which defines the run-time structure of the executable program in terms of a control-flow graph (*CG*). *CG* is a directed bipartite graph containing *actor nodes*, *data nodes*,

and their *connections*. An *execution structure* (*tasks* and *environments*) is used for assigning sub graphs of the *CG* to particular computational resources [3], [17]. Components of the MGK based MCM include actornodes, datanodes, environments, tasks, and an interpreter interface.

- *Actornodes* are the computational operators of the dataflow graph. Associated with an actor are: *scheduler state* (inactive, active, ready, or running); *script*, a reentrant algorithm expressed in a procedural/numeric language usually incorporated from a *library of standard operations*; *context*, a static local memory section for state and builder-initialized variables; *input* and *output ports*, the input and output data streams; and *control principle* which determines what criteria will be used to decide when an actor should be executed: *ifall* (data is present), *ifany*, or based on a *real-time* event. MCM kernel *calls* allow actor scripts to receive input tokens, access their context, and propagate output tokens.
- *Datanodes* provide a queuing and asynchronous connection function between actornodes. Any number of actor output ports may be connected to a datanode. A datanode may be connected to any number of actor input ports. Datanodes may be enabled or disabled and have a specified length. Datanodes provide a simple interface for the *model interpreters* to control, build, and monitor an executing graph.
- *Environments* are used to protect system resources and provide a priority mechanism for sections of the dataflow graph. All actors are assigned to an environment. Environments of the same priority are serviced in a round-robin fashion. Only one actor per environment will be executed at any one time, ensuring mutual exclusion within an environment.
- *Tasks* provide a generic interface to the basic computational resources of the underlying machine. In a multitasking environment they are simply the different processing threads available to the MCM kernel. In a multiprocessor system they are the individual processors themselves. Environments are attached to tasks. The *task* and *environment* concepts allow the actual implementation of the underlying system to be hidden from the user.
- The MCM *interpreter interface* provides several functions for the management of the execution environment:
  - Functions to create, destroy, connect input and output ports to datanodes, disconnect from datanodes, activate, deactivate, stop, check the status of, replace, set the context of, and set the script of actornodes.

- Functions to create, destroy, connect to actor input and output ports, disconnect from actors, clear, read, write, enable, disable, check length, set length, and check connections of datanodes.
- Functions to create, destroy, attach to tasks, and set priority of environments as well as to create and destroy tasks.

In summary, the MCM kernel provides an interface to build, modify, monitor, and control an asynchronous macro-dataflow graph. The graph may be partitioned by the concept of environments and tasks. The actual dataflow graph looks slightly different from that of a classic dataflow graph due to the introduction of the passive datanodes providing queuing functions. The use of distinct actornodes and datanodes provides the capability for the model interpreters to build, control, and monitor the dataflow graph.

### Model Interpreters

The model interpreters perform a  $\mathcal{M} \rightarrow CG$  mapping between the models and the executable system specified in terms of the MCM computational model. The interpretation process is dynamic. Complex systems typically include several functional components that form the executable system. For example, a process control system includes the monitoring, control, diagnostic, and operator interface subsystems [11]. A signal monitoring system includes the signal processing system and the message router. These different subsystems are synthesized from the same integrated model database by means of different interpreters. This process, called *multiple-aspect interpretation*, helps to keep the complexity of the individual interpreters low. At the same time, it ensures that the generated subsystems will be consistent with each other. In certain cases, events in the execution environment can cause a model interpreter to begin running again and to cause the currently executing computation graph to be modified. The problems and details of different re-configuration methods and the related synchronization methods are described in [4].

### The APNA Tool

In order to assist in the creation and management of a parallel architecture suitable for a particular application system, the Automatic Parallel Network Analyzer (APNA) tool was developed.

The basic computational blocks of a parallel instrumentation system often allow processor interconnections that are not fixed. For example, transputer architectures with DSP co-processors fit signal processing applications especially well since the hardware connection architecture can be configured to match the structure of the signal flow graph.

As computational requirements increase, so does the need for more processors. When an architecture contains more than a couple of processors, managing hardware complexity becomes a significant problem. Testing to see if the network of processors has been interconnected correctly, searching for hardware errors, generating network information for an application loader, or creating map files for a message passing system by hand is time-consuming for tens of processors and impossible for hundreds.

APNA uses a file containing the declarative description of the hardware architecture to automatically produce load files and maps required by different software components of the system. The APNA tool loads the declarative description files and draws the network in a graphical window. It is capable of loading files of a number of different formats, comparing networks and displaying their differences, generating files for hardware diagnostic programs and network loader, and displaying the attributes of the processors. It can selectively generate message passing maps, handling multiple paths between processors while optimizing the maps for minimum memory usage. [12] provides a detailed description of the APNA tool.

#### A Scalable Parallel Instrumentation Application

The Vanderbilt University Department of Electrical Engineering Measurement and Computing Systems Group in cooperation with the US Air Force at Arnold Engineering Development Center (AEDC), Sverdrup Technology (also at AEDC), and University of Tennessee Space Institute (UTSI) have developed a computer system for on-line data analysis of turbine engine tests in the altitude test cells of AEDC. This new high-speed computer architecture is based on parallel processing concepts. During actual operation, the current 24 channel system *continuously* delivers 200 MFLOPS. This continuous performance index, measured on the actual application program, exceeds the *peak* performance capabilities of many conventional high performance computers.

The Computer Assisted Dynamic Data Analysis and Monitoring System (CADDMAS) uses a heterogeneous architecture including INMOS transputers for communication and general purpose processing, Zoran and Motorola Digital Signal Processors for signal processing operations,

Texas Instruments Graphics Processors for on-line graphic display of calculated data, and an Intel 486 based PC to provide an interactive graphic user interface (GUI). The total processor count of the 24 channel system is 83.

Vanderbilt researchers have been working with AEDC for the past five years. Vanderbilt's role is to develop tools and techniques to manage the software complexity of this large, parallel, real-time instrumentation system. Driving factors concerning the CADDMAS system include:

- A requirement for high performance computing. A 200 channel 2 Giga-Flop **sustained** system is planned.
- A need for interactive monitoring of the processed data requires that some of the computations being performed must be modified on-the-fly.
- Event/Alarm recognition and response time.
- The need for a modular system allowing various components of the hardware to be "plugged" together to build systems of different size and capabilities. The corresponding software must be able to deal with these varying architectures.

In order to address the problems associated with the development of CADDMAS, *model-based* techniques have been applied.

#### Problem Domain

Testing turbine engines involves running an instrumented version of the engine through various operational maneuvers (e.g. Acceleration or Throttle Snap). These tests are typically conducted while the engine is in a test cell (wind tunnel) capable of simulating altitude, atmospheric, and air speed conditions. In order to analyze dynamic vibrations, strain gauges and other stress sensors are attached to the turbine fan blades. A typical aeromechanic stress test instruments the engine with several hundred stress sensors along with a variety of temperature, pressure, flow, and revolution per second sensors. Stress sensors can generate signals with bandwidths in the tens of Kilohertz.

Historically, analysis of turbine engine stress data has been an off line process. On-line capabilities were limited to oscilloscopes showing unprocessed amplitude vs. time information and a small number of signal analyzers for simple spectral analysis on single channels. The bulk

of the raw information was recorded onto analog tapes. Later, the analog tapes were digitized into conventional computers for analysis. The processing of this data was extremely compute intensive, and consequently, only a selected portion of the data was reduced. The analysis imposed a delay of several weeks on the availability of final results. Thus, vital information was not available for on-line test planning and evaluation.

The CADDMAS system was developed to provide these capabilities on-line. The system processes all sensor readings and presents the results in both graphic and in hard copy form, during the test. The immediate availability of results opens the possibility for interactive test planning.

A graphic user interface allows the user to configure various visualization screens interactively. The user can select the number of visible windows on a screen, the contents of each plot window, and the parameters of each plot, such as titles, labels, axis ranges, and plot type, and display window update rate. Stored configurations automate the operation of the user interface. The user can also print any window or all windows on a screen.

#### Computations Performed by CADDMAS

The types of on-line plots generated by the CADDMAS system include:

- Amplitude versus Time. This represents the absolute stress on a blade over time. This calculation involves scaling the sampled A/D counts to engineering units ( $y = Ax + B$ ) and triggering the beginning of a display plot with a once per revolution pulse of the turbine.
- Spectral display with Full-Time Envelope Capture. This shows the energy of vibrations over a range of frequencies. The envelope continuously captures the historical maximum to ensure that no spectral activity is missed. FFT's are used to generate the spectral estimates.
- Frequency Tracking. This display shows the spectrum corrected by engine RPM. This is useful to observe synchronous vibrations over a range of engine speeds.
- Campbell diagrams. These are very important tools in the analysis of engine stress data. The Campbell diagram is a three dimensional scatter plot of stress amplitude vs. frequency vs. RPM. It represents historical information over an entire test maneuver and provides a summary of the blade behavior in a single chart. Generation of a Campbell diagram

involves sorting the peaks of all of the spectral estimates of a strain gauge across a test maneuver and keeping the "interesting" peaks. Interesting is defined per test maneuver and includes: minimum, maximum, and delta RPM of interest, minimum, maximum, and delta frequency of interest, and minimum stress amplitude of interest.

- Phase Campbell diagrams. These show the phase angle relationship between two sensors vs. frequency vs. RPM. They incorporate information from two related sensors and can be used to help determine vibratory modes of an engine component.
- Modified Campbell diagrams. These allow the engineer to visualize the stress behavior of the engine components as a function of any engine or environmental parameter (instead of RPM) such as temperature, pressure, or time.

#### The Hardware Building Blocks

The CADDMAS hardware consists of various computational building blocks. INMOS transputers are used to provide a basic message passing fabric. Each transputer has four high-speed bidirectional serial communication links (20 Mega-bits per second) accessible through independent DMA engines. The current CADDMAS prototype system is capable of the on-line, gap free processing of 24 channels of stress, pressure, accelerometer, and other data at bandwidths up to 20 Kilohertz. The bandwidth can be increased fourfold with a reduction in the number of channels multiplexed by the A/D's. The basic building blocks are modular so as to allow systems of various size and personality to be "plugged" together.

#### Scaling the CADDMAS Models

To build a new CADDMAS system with a different personality, more channels, or different processing capabilities, the following procedure is used.

1. The desired signal flow graph is modeled with the graphical tools. For simply building a larger or smaller CADDMAS, the previously defined compounds may be replicated without change. They simply need to be "plugged" together. Specification changes (such as required channel bandwidth or number of printers needed) are made by simply changing the values of the top level static parameters of the signal flow model to reflect the desired system

specifications. In order to make this process easier for non-programmers, the CADDMAS application uses a separate file, *defaults.lsp*, to define the commonly changed specifications. This file may be edited with a standard text editor. The values defined in it are loaded into the top level compound of the CADDMAS signal flow model before interpretation. Therefore, end users do not have to run the graphical editor to make model supported specification changes. If a new basic processing algorithm is needed, the script must be added to the Multigraph library and the corresponding information added to the signal flow model.

2. The Xgem/GMB MPDL tool is used to model the new hardware architecture resources available. If the resources are already connected into an architecture that is not to be changed (changing the architecture of an 83 processor system can be quite time consuming), then the model must include the fully connected architecture description. Otherwise, the basic building blocks available need to be modeled.
3. The model interpreter synthesizes the *APNA file* and the *builder file* for the selected scenario.
4. The APNA tool uses the automatically generated *APNA file* to produce message passing maps, a network loader description file, and a hardware configuration diagnostic file.
5. The new architecture is physically wired. With a transputer system this involves plugging serial link patch cords into the appropriate sockets on the backplane.
6. The APNA configuration test program (Check) is run with its hardware configuration diagnostic file to find any wiring errors. There are about 100 patch wires in a 50 processor system. Therefore, wiring errors are common.
7. The system is loaded and run. Starting the system causes the following actions to be performed:
  - (a) The APNA produced network loader description file is used to verify and load each of the transputers in the network with its necessary Multigraph kernel.
  - (b) The APNA produced message passing map is transferred down to each of the transputers in order to tell them what routes (including hops) to use to talk with one another.

- (c) The interpreter generated *builder file* is run to create the individual nodes of the macro-dataflow graph, actornodes and datanodes, and interconnect them across their respective processors.
- (d) The graph then begins execution. Once started, the individual processors talk directly with each other as necessary. The user interface can cause different graphs to be plotted at different rates and on different windows by writing various control parameters into particular datanodes of the graph.

### Experience with CADDMAS

The model-based approach has proven to be a very useful tool to help manage the complexity of this large, parallel system.

To date, there have been over 10 different CADDMAS systems developed. The first system was not developed with model-based techniques. Rather, it was programmed using the classic transputer programming approach, communicating sequential processes (CSP) [7].

The first CADDMAS was developed with no model-based techniques or Multigraph tools. It was programmed in Logical Systems C, a transputer C compiler and execution environment. It took two members of the current Vanderbilt team a little over one year to develop the code for the first CADDMAS. However, its development time cannot be directly compared with those using model-based techniques because several of the original basic compute subroutines were wrapped with MCM kernel calls to be used as scripts for the model-based approaches. The modeling tools offer no shortcuts for programming basic subroutines (such as a FFT) on a new compute platform. Rather, they can be employed to reuse libraries of such subroutines to develop and modify systems composed of these routines.

The first CADDMAS system was quite successful with respect to showing the feasibility of combining parallel processing with turbine engine instrumentation problems. It enabled test engineers to get hard copy of plots seconds after a test was performed as opposed to their previous several day waiting period. However, this initial success later led to a flood of system modification requests. In particular the engine testing community began requesting CADDMAS specification changes to match their ever changing testing requirements. Changes requested included varying needs for number and bandwidth of channels, number and type of printer and display changes, additional plot types, accuracy tradeoffs, and varying architectures attempt-

ing to manage the utilization of the small number of processing resources AEDC had initially purchased and manufactured.

Several of these requested changes were made to the original CADDMAS software. Each change typically took a two member Vanderbilt CADDMAS team a week to implement. However, as these requested changes kept coming in, the CADDMAS source code faced a crisis. In the typical C fashion, *IFDEF* preprocessor directives were continually being added to the source code in an attempt to meet varying configuration needs. Over the course of several changes, time to implement a change grew well beyond a week. And some requested changes (scaling to much larger systems in particular) seemed well beyond the reach of the current software. Instead, the difficulty in making these changes demonstrated the need for a complete rewrite of the CADDMAS. Yet, a rewritten set of CSP style code for the new CADDMAS systems would again be doomed to this same crisis if requests for changes continued.

As a result of the initial CADDMAS success, the software crisis it was facing, and the basic research goals of the Measurement and Computing Systems Group at Vanderbilt, a rewrite of the CADDMAS code was cast into the Multigraph Architecture where it could be supported by model-based techniques. It was within this framework that the MBSS tools and techniques arose.

Three CADDMAS systems developed using the model-based *steps to build a new caddmas* procedure outlined above are described below:

- The very first model-based CADDMAS system was a four channel (single FEP), 8 Campbell, 2 graphics displays system. Actual configuration time for that first system could not be measured because the CADDMAS team was still finishing some of the tools along the way.
- The second system was a 24 channel, 48 Campbell, 3 graphics displays, 3 laser printers system. It took the CADDMAS team (at that time 3 full time graduate students working 40 hour weeks) one week to physically wire the network, synthesize the software, find a previously missed bug in the message passing system, and make several new patch cables.
- The third system was a four channel (single FEP), 4 Campbell, 1 graphics display system made from spare parts. It only took one member of the CADDMAS team four hours to physically wire the network and synthesize the software!

While the utilization of the tools and the CADDMAS models by the system developers provides interesting metrics with respect to manipulation of the system by its highly knowledgeable developers, use of the tools by non-programmer end users provides more insight. Since there are several fielded CADDMAS systems that are in actual use, and Vanderbilt is geographically separated from their location, several occasions have arisen that illustrate non-programmer manipulation of the system. In particular, a team of two Arnold Engineering Development Center (AEDC) employees have manipulated the system specifications to generate various CADDMAS scenarios several times.

Both AEDC CADDMAS team members have an intimate understanding of the CADDMAS problem with respect to the signal analysis desired, the usefulness of the output plots, the available input data streams, and the available hardware resources. They did not participate directly in the development of the *actor scripts* or models of the CADDMAS system. However, they did monitor the development of them.

The two AEDC members have successfully used the model-based tools to:

- Change the number and type of available CADDMAS parameters on several occasions by modifying the top-level specifications in the *defaults.lsp* file. In particular, they recently changed accuracy specifications so that only one Campbell diagram would be computed per channel rather than two. However, the one computed had double its original accuracy.
- Regularly change system specifications to increase or decrease the channel bandwidth as needed to support various engine tests.
- Directly modify the hardware architecture. That is, they use the APNA files to verify the architecture changes.
- Change the number of printer devices and display devices in a particular system.

Throughout these changes, the Vanderbilt CADDMAS team has often answered questions (phone calls) about the procedures necessary. However, questions on this level are now quite infrequent. Rather, AEDC just makes the changes they want. For the AEDC team, changes of the magnitude described above are typically accomplished within a 30 minute period.

### CADDMAS Summary

The 24 channel CADDMAS system has been very successful. It has been in use since July

of 1992, supporting about 20 different engine tests. During the Summer of 1994 Vanderbilt is cooperated in the construction of a system based on Texas Instruments' new TMS320C40/C31 parallel digital-signal processors. The main task in that effort was to develop a new MCM for the C40/C31 (called active processes) and the primitive library for the new platform. As well, the hardware models were updated to provide six communication ports instead of four. After those steps were completed, various small versions of CADDMAS systems (1 channel, 2 C40s) were successfully generated. However, as of yet, building a large TI based system has been unsuccessful due to hardware trouble. When the hardware problems are corrected, the generation of the large system is expected to be mainly a modeling and synthesis exercise.

### Conclusions

While the grand challenge problems are extremely useful to the growth of high performance computing, they do not directly reflect the needs of the industrial community. These industrial needs pose yet another challenge, the application challenge. When industrial applications become a major part of high performance computing, overall growth will be tremendously accelerated. Therefore, AEDC has contributed to the growth of the high performance computing community through the CADDMAS project. New techniques are needed to aid in the development of high performance computer applications. Simplification of the programming environment is not always the key to success. The use of domain specific, complex modeling environments is well suited to many industrial applications.

### Acknowledgements

I wish to thank the Air Force Material Command and the Air Force Office of Scientific Research for sponsorship of this research. Research Development Labs must also be commended for their concern and help to us in all administrative and directional aspects of this program. My experience was rewarding and enriching because of many different influences. The help of Tom Tibbals was invaluable in overcoming many technical roadblocks.

### **References**

- [1] Abbott, B., et al.: "Experience Using Model-based Technique for the Development of a Large Parallel Instrumentation system," in *Proc. of the Int. Conf. on Signal Processing*

*Applications and Technology*, Boston, MA., November 1992.

- [2] Abbott, B., Bapty, T., Biegl, C., Karsai, G., Sztipanovits, J.: "Model-Based Approach for Software Synthesis," *IEEE Software*, pp. 42-53, May, 1993.
- [3] Biegl, Cs.: "Design and Implementation of an Execution Environment for Knowledge-Based Systems," Ph.D. Thesis, Electrical Engineering, Vanderbilt University, 1988.
- [4] Blokland, W.: "Structurally Adaptive Systems," Ph.D. Thesis, Electrical Engineering, Vanderbilt University, 1991.
- [5] Constantine, L.L., Yourdon, E.: *Structured Design*, Prentice Hall, Englewood Cliffs, N.J., 1979.
- [6] Davis, R.: "Form and Content in Model-Based Reasoning," *Proc. of the 1989 Workshop on Model-Based Reasoning*, pp. 11-27, 1989.
- [7] Hoare, C.: "Communicating Sequential Processes," *Communications of the ACM*, Vol 21 1978, pp. 666-667.
- [8] Harel, D.: "Biting the Silver Bullet," *IEEE Computer*, pp. 8-20, January, 1992.
- [9] Karsai, G.: "Declarative Programming Using Visual Tools," *Techn. Report #89-003*, Measurement and Computing Systems Laboratory, Vanderbilt University, April, 1989.
- [10] Karsai, G., Sztipanovits, J., Padalkar, S., Debelak, K.: "A Model-Based Approach for Plant-Wide Monitoring Control and Diagnostics," *Proc. of the AIChE Annual Meeting*, (microfilm) Los Angeles, CA, November, 1991.
- [11] Karsai, G., Sztipanovits, Padalkar, S., Biegl, C., J., Okuda, K., Miyasaka, N: "Model-Based Intelligent Process Control for Cogenerator Plants," *Journal of Parallel and Distributed Computing*, Vol. 15, No. 6, pp. 90-102, 1992
- [12] Ledeczi, A., Abbott, B., et. al.: "Parallel DSP system integration," *Microprocessors and Microsystems*, Vol. 17, Num. 8, Oct. 1993, pp. 460-470.
- [13] Misra, A., Sztipanovits, J., Carnes, R.: "Robust Diagnostic System: Structural Redundancy Approach," in *Proc. of the SPIE's International Symposium on Knowledge-Based Artificial*

Intelligence Systems in Aerospace Systems in Aerospace and Industry, Orlando, FL, April 5-6, 1994.

- [14] Padalkar, S., Karsai, G., Biegl, Cs., Sztipanovits, J., Okuda, K., Miyasaka, N.: "Real-time Diagnostic System," *IEEE Expert*, Vol. 6, No. 3, pp. 75-85, June 1991.
- [15] Rumbaugh, J., Blaha, M., Premerlani, W., Eddy, F., Lorensen, W.: "Object-Oriented Modeling and Design," Prentice Hall, Englewood Cliffs, N.J., 1991.
- [16] Setliff, D.: "Knowledge Representation and Reasoning in a Software Synthesis Architecture," *IEEE Transactions on Software Engineering*, pp. 523-533, June 1992.
- [17] Sztipanovits, J., Karsai, K., Biegl, C.: "Graph Model-Based Approach to the Representation, Interpretation and Execution of Signal Processing Systems", *International Journal of Intelligent Systems* V3, pp. 269-280, 1988.
- [18] Sztipanovits, J., Biegl, Cs., Karsai, G., Bourne, J., Mushlin, R., Harrison, C.: "Knowledge-Based Experiment Builder for Magnetic Resonance Imaging (MRI) Systems," *Proc. of the Third IEEE Conference on AI Applications*, pp. 126-133, Orlando, FL, 1987.
- [19] Sztipanovits, J., Karsai, G., Biegl, C.: "Graph Model-Based Approach to the Representation, Interpretation and Execution of Real-Time Signal Processing Systems," *International Journal of Intelligent Systems*, Vol.3., No. 3. pp. 269-280, 1988
- [20] Sztipanovits, J., Wilkes, D., Karsai, G., Biegl, C., Lynd, L: "The Multigraph and Structural Adaptivity," *IEEE Transactions on Signal Processing*, Vol. 41, No. 8., pp. 2695-2716, 1993.

Development of Large Parallel  
Instrumentation Systems

Theodore A. Bapty  
Research Faculty  
Department of Electrical and Computer Engineering

Vanderbilt University  
400 24th Avenue South  
Nashville, TN 37235

Final Report for:  
Summer Faculty Research Program  
Arnold Engineering Development Center

Sponsored by:  
Air Force Office of Scientific Research  
Bolling Air Force Base, Washington, D.C.  
and  
Arnold Engineering Development Center

September 1994

Development of Large Parallel  
Instrumentation Systems

Theodore A. Bapty  
Research Faculty  
Department of Electrical and Computer Engineering

Abstract

Parallel instrumentation systems, such as the AEDC CADDMAS system, are in high demand. Unfortunately, these systems are also very complex and difficult to construct and manage. The combination of parallel processing and real-time constraints force high system complexity. Standard techniques are inadequate to deal with these systems.

Model-based techniques have been proven to deal with large system complexities. We apply model-based techniques to construct large-scale parallel systems in short development times. The abstractions used throughout the entire modeling system are very important to the success of the technique. The work described here deals with the low-level abstractions necessary for a real-time kernel in the modeling approach.

Development of Large Parallel  
Instrumentation Systems  
Theodore A. Bapty

Introduction

The class of high-speed instrumentation presents several problems in system implementation:

1. Applications require high input/output rates to acquire raw data and to display results
2. Conversion of raw data to usable information demands high processing throughput.  
This in turns leads to a parallel processing approach.
3. Systems must operate in a real-time mode. Results must be processed at the same rate or faster than the raw data arrives. The results of processing may be used in a control algorithm or to annunciate alarms, with specific time/latency constraints.
4. Systems are cost-sensitive. If costs are too high, the system will not be implemented.
5. Systems are typically embedded in the operating environment, putting constraints on size and power consumption.
6. Users lack computer engineering experience. Often the potential users are experts in the application domain. They are rarely computer system engineers.

The CADDMAS system is an excellent example of these constraints. The 48 channel, 50 KHz system acquires raw data at a constant 20 Mbyte/second rate. Over 1 GFLOPS(Giga-Floating point Operations Per Second) of sustained processing is necessary to analyze the raw data to produce spectrums and Campbell diagrams. Since there is limited memory in the system, data must be processed through fast enough that memory is not filled. Data alarm detection and annunciation have specified maximum latencies.

The cost constraints on the system force the use of low cost digital signal processors with relatively small memories. The limited space for system deployment also forces small

scale processors. The new CADDMAS numeric processor has only 32,768 words of system memory.

The users of the system are aerospace engineers. They specialize in analyzing the stresses inside a turbine engine to determine the operating conditions. They have little time to learn about computer systems and lack the background to develop real-time instrumentation applications.

#### Software Support for Parallel Real-Time Systems

A great deal of effort has been invested in software development environments in the past 20 years. The concepts of high level languages, top-down, structured programming, object-oriented design, and software environments focus on the development of standard sequential programs. These concepts, while greatly advancing digital computer systems technology, do not address all of the issues necessary to develop parallel real-time instrumentation systems.

More recently, the parallel processing and real-time systems communities have been working on tools for their respective areas. On the parallel processing side, abstractions like message passing have given rise to tools such as Parallel Virtual Machine(PVM) and Message Passing Interface(MPI) libraries. Hardware and software architectures have been designed to implement distributed shared memory systems, such as the KSR1.

In the real-time systems camp, the focus has been on developing scheduling algorithms and real-time kernels. Scheduling algorithms concentrate on the small scale scheduling of tasks on a single processor to ensure specific deadlines are satisfied. Global scheduling technologies attempt to optimize the local schedules of processors for a group of processors.

Real-time kernels abound in the research community. They vary in type, from single processor kernels with no communication, to multiple processors with shared memory assumed (Chimera II), to multiple processors with communications(Spring, MARS). The support for programming is typically at a low level, forcing the programmer to control tasks explicitly.

The parallel processing community tools are insufficient to develop instrumentation systems due to the real-time nature of the application. The objective in “parallel processing” tasks is to maximize throughput. Unfortunately, the time-criticality of responses cannot even be addressed.

The real-time systems community tools are also insufficient to develop instrumentation systems due to the limitations in addressing parallel processing issues and performance. The objective in real-time systems is primarily to meet deadlines. Throughput for any one processor is unimportant. While the basic kernels have the necessary hooks to meet real-time needs, the low level nature requires significant management on the programming level. The abstractions in the tools are not sufficient to deal with large, massively parallel systems.

We therefore need to accumulate the features of both communities, along with other ideas to successfully attack the problems in parallel instrumentation systems. The components developed in these areas, such as scheduling theory, can be used to accelerate development by focusing on the new issues resulting from the combination of these fields.

### Model-Based Systems

The Model-Based approach, as typified in the Multigraph Architecture, has proven to be an extremely useful abstraction for managing complexity. In the case of parallel instrumentation systems, the complexity arises in both the parallel and real-time aspects of the problem.

The Multigraph Architecture (MGA) incorporates many ideas in the areas of modeling, program synthesis, and reactive parallel systems. The framework encourages specification of systems in terms of hierarchical, multiple-aspect models. These models are used to derive executable systems, described in terms of a large grain, directed bipartite dataflow graph. The graphs are executable directly under the Multigraph Execution Environment. The MGA has been developed with real-time, dynamically reconfigurable applications in mind. The system is composed of three main components, the Modeling Environment, the Model Interpreters, and the Execution Environment.

### Modeling Environment

The modeling environment is composed of tools for constructing and maintaining multiple aspect models. The models, represented by  $M = M[1], M[2], \dots M[n]$ , the system specification knowledge. Research has identified several critical areas in modeling, areas which are

supported in the MGA modeling environment:

1. Multiple-aspect, hierarchical modeling, representing not only the structure of the software to be generated, but other environmental aspects, fault diagnostic behavior, system specifications, etc. The environment allows linkages to be created between aspects, to aid in traceability and system generation.
2. Application specific modeling paradigms. Narrowing of details to those of the domain restricts the possibility for areas and aids in the interpretation and checking of the models. MGA supports the specification of domain dependent information. Research work has been done to support meta-level tools for generation of domain-specific modeling environments themselves [6].
3. Unified control discipline. The common systemwide application of control discipline greatly simplifies the modeling process. The MGA specifies the Multigraph Computation Model, which is a large grain graph, defining the communication and triggering of computational units.

The issues of representing real-time constraints has been addressed on the low level by [7]. High level real-time constraints and their impact on systemwide constraints are a topic of this research.

#### Execution Environment

The execution environment implements the macro dataflow model across a set of processors. This set of processors appears as a unified virtual machine. The existence of this environment greatly simplifies the interpretation of the models. Each processor represents one or more *Tasks*. Tasks can, in turn, contain *Environments*. *Actornodes*, the primary computational units, and *Datanodes*, the asynchronous data queues, are assigned within these environments. Tasks allow the management of processors. Within an environment, only one actor executes concurrently, allowing mutual exclusion. Environments are prioritized, allowing some control of execution order. All tasks execute in parallel.

The actornodes have an associated *scheduler state*: active, inactive, ready, and running. A *script* is the reentrant algorithm for the computation, expressed in a procedural language.

Typically these scripts come from a standard library of reusable software. Actornode *contexts* allow local storage of information and allow the builder access to actornode variables. Input and output ports represent the data inflow and outflow from the actornode. The control discipline determines when the actor will be executed: *ifall* when data is present at all input ports or *ifany* when data is present at any of the ports. No provision, however, is included for control based on output queue status. *Real-time* actors allow the execution of the actor to be tied to an event, which is polled by the scheduler between actornode executions. Note that no real-time deadlines are specified or guaranteed. Actor execution is non-preemptive.

The datanodes provide an asynchronous queuing connection between actors. Datanodes have a state (blocked/enabled) and a length. The behavior of datanodes that exceed the maximum length is to discard data. Explicit specification of datanodes allows management of data queuing memory use and some control of communications. Communications is typically implemented in a lower layer of asynchronous message passing, offering hardware independence and portability. (This can, however, lead to inefficiencies due to extra copying of messages.)

The *Interpreter Interface* provides functions to create, monitor, modify, and destroy computational structures on the MVM. Actornodes, datanodes, environments and tasks can be created and destroyed. Priorities can be set for environments, actornodes and datanodes can be placed on tasks and environments. Actornodes and datanodes can be enabled and disabled. Actornodes can be attached to datanodes and datanodes to actornodes. Actornode contexts can be allocated and set, and datanodes can be monitored, read, and written.

### Model Interpreters

The model interpreters perform the mapping from the models  $M$  created in the modeling environment to the computational graph  $CG$  for the execution environment. The interpreter can gather information from several aspects of the model in the process of generating the executable graph. The choice of a consistent graph computational model as the target simplifies the interpretation process.

Multiple interpreters can be used, each responsible for interpreting a specific aspect of the modeling. In this way, the complexity of the individual interpreters can be kept manageable.

During the development of the CADDMAS system, the model-based approach has been applied with significant success. The system has been modeled from the aspects of signal-flow and hardware architecture:

- Signal flow modeling describes the structure of the computations within the system in a large-grain dataflow architecture. The can be represented graphically. Blocks in the model represent computational processes. Data flows and dependencies are represented by arcs and datanodes. (queues)
- Hardware Modeling describes the available hardware components: **Processors**, their properties (memory sizes, CPU speeds, etc); **Communications Links** and their speeds; and **Topology** of the interconnection network.

For the past MGA applications, the Execution Environment has been based on a macro-dataflow virtual machine defined by the Multigraph Computational Model (MCM) and implemented by the Multigraph Kernel (MGK). This environment, while extremely useful as a flexible research platform on large machines for general parallel processing, is too large for the minimal cost, embedded system application. During the SFRP, the execution environment has evolved into what we call “active processes”.

#### Active Processes: a kernel for low-level implementation

None of the Real-time kernels offer the flexibility, portability, and compact structure that are needed for research in software synthesis approaches for dynamic real-time systems. The flexible definition of abstractions for the low level layer will be critical in managing the complexity of the synthesis layers. Consequently, a new kernel is necessary for development of parallel instrumentation systems. The key properties of this kernel are:

- Flexible Scheduling: Static/Dynamic. Processes can monitor the state of queues to control buffering in an application-specific manner. The message streams abstraction can be lossy, lossless, or timed, depending upon the application process handling the

stream. Buffers can be dropped to minimize latency, or compute can be blocked to retain data integrity.

- Structurally Reconfigurable for adaptation to new operating modes. The schedule modifications must be able to be implemented in stages, ensuring system consistency.
- Asynchronous Buffered Communications with Flow Control. Flow control manages communications overload. Communications can be prioritized and/or statically scheduled
- Integrated Memory Management: No buffer copying for message passing optimizes the communication interface. Minimize memory fragmentation and nondeterministic timing for malloc/free.
- Small and Fast: It must fit on 32Kword C31.

“Active processes” fully support the previous abstraction of the Multigraph Kernel as well as being faster, smaller, and supporting hard real-time constraints. Both “active processes” and the MGK execution environments provide support for the MCM along with an application specific “primitive” library whose elements are the lowest-level components of the generated program. Details of the new “active processes” execution environment are summarized below.

#### Active Processes Structure

Active Processes can be viewed as several interoperating systems:

- The Streams provide message queueing with flow control between processes on any processor or logically adjacent(connected by a comm port) processor. Each stream has the following properties:
  1. A queue of messages, whose maximum length is a definable systemwide constant.  
The queue contains pointers to messages.
  2. The acknowledge queue contains a queue of acknowledge packets ready to be transmitted to the neighboring stream.

3. A count of acknowledge packets vs packets transmitted is used in flow control to keep from overflowing a queue.
4. The destination communications port and destination node determine how to transmit the data.
5. The state: Enabled/Disabled. This is useful to block data entry to a stream. The stream can be disabled from the receiving side to prevent data overrun and queueing.

- The Scheduler is a user definable real-time, non-preemptive scheduler. It selects the next process to be executed and calls the process. The scheduler can use any form of logic that fits the application, and any non-preemptive scheduling algorithm. Data dependencies for process execution can be determined here or within the process, again, depending upon the application preference. The current scheduler is a round-robin scheduler, with the application processes determining data dependence. The schedule structure keeps track of the number of inputs and outputs, along with the assigned streams. The input/output stream assignments along with the stream destinations define the application graph topology. The schedule structure also keeps track of the process's local data storage area.
- Messages contain the destination stream, the source stream, the message length, and an error detection signature, and a type. Message types are:
  1. STANDARD-MESSAGE, for regular data transmission
  2. ACK, to acknowledge dequeuing of the data
  3. ACK-DISABLE, to disable the stream
  4. ACK-ENABLE, to enable the stream
- Channels manage the physical channels on a processor. Channels contain queues for messages and ACK's. A key feature with Active Processes is that the channels receive message bodies directly into the destination buffer, eliminating the need for memory copies. The memory manager works in concert with the channels. Memory buffers are freed when the data has been successfully transmitted. The application sees the data

as being automatically freed. Buffers are automatically created while receiving data. These buffers are used directly by the application process. This contrasts other systems where the data is copied to an internal communications buffer before transmission, to ensure that data stays valid. and from a communications buffer into the process. In order to avoid deadlock, the channels remain in a receiving state.

- The Memory Manager keeps track of the dynamic RAM. This mechanism is also configurable by the user. The default manager uses a table based algorithm to avoid the problems of memory fragmentation and nondeterministic garbage collection.

#### Active Processes Interface

The application interface to Active Processes is relatively simple. The functions deal with the streams mechanism of Active Processes. They are as follows:

- **long output-slot-available(long index);**

Determines if there is room for another output data block. **index** is the index of the output slot. This is a result of flow control between processes. This value must be checked before sending out data.

- **void enqueue-output(long out-index, long size, long \*buf\_ptr);**

Sends the message, **buf\_ptr**, to the stream connected to the output, **out-index**. The buffer size is specified. The output buffer will be reclaimed by the memory manager when the message has been successfully transmitted if the stream destination is off-processor. Message buffers may only go to one output stream. If two destinations are needed, the process must duplicate the buffer.

- **void \*get-input-slot-buffer(long index);**

Checks for an input message on slot **index**. The return value is either a pointer to the message or NULL if there is no message currently in the queue. Note that this does not remove the message from the queue, but merely returns a pointer to it. Dequeueing is done explicitly.

- **void dequeue-input(long index);**

Dequeues the input from the queue. Note that no **free** operation is implied. Buffers are managed explicitly by the process.

- **void disable-input-stream(long index);**

Disables the stream so that the source process cannot send output to the stream. This can be used to explicitly disable processes.

- **void enable-input-stream(long index);**

Reenables a disabled stream.

- **void act-comm-tick(void);**

Calls the internal communications routines to ensure that data is received and transmitted. This is necessary when waiting for data on processor without interrupts and DMA.

### Conclusion

The Active Processes system has been implemented on the TMS320C40, the AEDC TMS320C31 quad processor board, and the MSDOS/PC architectures. The implementation supports all of the features above in a flexible manner. The system is written in the C language, in approximately 2500 lines of code.

The system is efficient and has low overhead. The CADDMAS has been implemented under the active, with a uniform interface across all processors, even the tiny memory TMS320C31 fft nodes. System performance exceeds previous implementations of the CAD-DMAS system. This is a result of the low overhead of the kernel and the bandwidth-saving feature of communications with flow-control.

## References

- [1] Abbott, B., et al.: "Experience Using Model-based Technique for the Development of a Large Parallel Instrumentation system," in *Proc. of the Int. Conf. on Signal Processing Applications and Technology*, Boston, MA., November 1992.
- [2] Abbott, B., Bapty, T., Biegl, C., Karsai, G., Sztipanovits, J.: "Model-Based Approach for Software Synthesis," *IEEE Software*, pp. 42-53. May, 1993.
- [3] Biegl, Cs.: "*Design and Implementation of an Execution Environment for Knowledge-Based Systems*," Ph.D. Thesis, Electrical Engineering, Vanderbilt University, 1988.
- [4] Blokland, W.: "*Structurally Adaptive Systems*," Ph.D. Thesis, Electrical Engineering, Vanderbilt University, 1991.
- [5] Abbott, B.: "*Model Based Software Synthesis*," Ph.D. Thesis, Electrical Engineering, Vanderbilt University, 1994.
- [6] Franke, H.: "*Meta-Level Model-Based Environment Generation*," Ph.D. Thesis, Electrical Engineering, Vanderbilt University, 1992.
- [7] Wagnis, P.: "*Hard Real-time Scheduling in Model-Based Programming Environment*," Ph.D. Thesis, Electrical Engineering, Vanderbilt University, 1993.
- [8] Constantine, L.L., Yourdon, E.: *Structured Design*, Prentice Hall, Englewood Cliffs, N.J., 1979.
- [9] Davis, R.: "Form and Content in Model-Based Reasoning," *Proc. of the 1989 Workshop on Model-Based Reasoning*, pp. 11-27, 1989.
- [10] Hoare, C.: "Communicating Sequential Processes," *Communications of the ACM*, Vol 21 1978, pp. 666-667.
- [11] Harel, D.: "Biting the Silver Bullet," *IEEE Computer*, pp. 8-20, January, 1992.
- [12] Karsai, G.: "Declarative Programming Using Visual Tools," *Techn. Report #89-003*, Measurement and Computing Systems Laboratory, Vanderbilt University, April, 1989.

[13] Karsai, G., Sztipanovits, J., Padalkar, S., Debelak, K.: "A Model-Based Approach for Plant-Wide Monitoring Control and Diagnostics," Proc. of the AIChE Annual Meeting, (microfilm) Los Angeles, CA, November, 1991.

[14] Karsai, G., Sztipanovits, Padalkar, S., Biegl, C., J., Okuda, K., Miyasaka, N: "Model-Based Intelligent Process Control for Cogenerator Plants," *Journal of Parallel and Distributed Computing*, Vol. 15, No. 6, pp. 90-102, 1992

[15] Ledeczi, A., Abbott, B., et. al.: "Parallel DSP system integration," *Microprocessors and Microsystems*, Vol. 17, Num. 8, Oct. 1993, pp. 460-470.

[16] Setliff, D.: "Knowledge Representation and Reasoning in a Software Synthesis Architecture," *IEEE Transactions on Software Engineering*, pp. 523-533, June 1992.

[17] Sztipanovits, J, Karsai, K., Biegl, C.: "Graph Model-Based Approach to the Representation, Interpretation and Execution of Signal Processing Systems", *International Journal of Intelligent Systems V3*, pp. 269-280, 1988.

[18] Sztipanovits, J., Biegl, Cs., Karsai. G., Bourne, J., Mushlin, R., Harrison, C.: "Knowledge-Based Experiment Builder for Magnetic Resonance Imaging (MRI) Systems," *Proc. of the Third IEEE Conference on AI Applications*, pp. 126-133, Orlando, FL, 1987.

[19] Sztipanovits, J., Karsai, G., Biegl, C.: "Graph Model-Based Approach to the Representation, Interpretation and Execution of Real-Time Signal Processing Systems," *International Journal of Intelligent Systems*, Vol.3., No. 3. pp. 269-280, 1988

[20] Sztipanovits, J., Wilkes, D., Karsai, G., Biegl, C., Lynd, L: "The Multigraph and Structural Adaptivity," *IEEE Transactions on Signal Processing*, Vol. 41, No. 8., pp. 2695-2716, 1993.

UNIVERSAL GRAPHICAL USER INTERFACE FOR  
TURBINE ENGINE SIMULATION PROGRAMS

Csaba Biegl  
Research Assistant Professor  
Vanderbilt University  
Department of Electrical Engineering  
Box 1649 Station B  
Nashville, TN 37235  
(615) 343 - 8197

Final Report for:  
Summer Faculty Research Program  
Arnold Engineering Development Center

Sponsored by:  
Air Force Office of Scientific Research  
Bolling Air Force Base, Washington, D.C.

and

Arnold Engineering Development Center

September 1994

## UNIVERSAL GRAPHICAL USER INTERFACE FOR TURBINE ENGINE SIMULATION PROGRAMS

Csaba Bieg1  
Research Assistant Professor  
Vanderbilt University  
Department of Electrical Engineering

### Abstract

Simulation of turbine engines is an important part of the engine test process at AEDC. Traditionally, these simulations have been developed in the FORTRAN language with character oriented user interfaces. Increasing demands in terms of simulation performance, accuracy and model development time necessitate the introduction of graphical user interfaces for these simulations. This paper describes two initial attempts to add such user interfaces to existing engine modeling codes. Based on the experience gained with these conversions, a universal graphical user interface is developed which promises to ease the conversion of other, similar FORTRAN engine simulation programs.

---

## UNIVERSAL GRAPHICAL USER INTERFACE FOR TURBINE ENGINE SIMULATION PROGRAMS

Csaba Biegl

### Introduction

An important part of the testing of turbine engines at AEDC is the development of engine models. These are numerical simulation programs which model the behavior of the engine or some of its components under various operating conditions. Some models are based on exact modeling of the physical (transport, thermal and mechanical) processes inside certain engine components. Other models are less detailed component-level simulations which try to infer overall engine parameters from the engine layout and component characteristics.

Turbine engine models can be used for several purposes like design analysis, modeling the interactions between the airframe and the engine, education, etc.. From the point of view of an engine test facility like AEDC, the most beneficial use of the models is to aid the testing operations. The development of accurate engine models is a time-consuming process which uses several possible input data sources:

- Data, component characteristics and sometimes incomplete models from the engine manufacturer
- Parameters inferred based on the geometry (duct diameters, etc..) and operating parameters (RPM, etc..) of various engine components
- Measurement data obtained from engine tests.

Typically, at the beginning of a test sequence the amount of available data does not allow the creation of an accurate engine model. After test runs, some of the measured test parameters are used to verify and to refine the accuracy of the models. Simultaneously, the model is also used to determine some other engine parameters which cannot be measured in the test configuration. Thus the collection of test data and the refinement of the model are two interacting activities which proceed in parallel during the course of a typical engine test sequence.

Once the model has been refined to an acceptable accuracy level it can also be used to validate the test data. A turbine engine test facility is a very complex industrial plant (wind tunnels, compressors, extensively instrumented test cells, etc..) which must be highly reconfigurable in order to support various engine types and operating conditions. The probability of a component failure or a misrouted connection in such a plant is quite high. Most of the time these plant failures will manifest in invalid measurement data. Since running the engine test facility is quite expensive, it is imperative that such plant failures be detected and corrected as early as possible. Accurate engine models play a very important role in the validation of the test data.

To best support the testing operations the engine model has to be available online during the test periods. Ideally, the simulation speed should be real-time or even super real-time so that events in the engine can be analyzed (or even predicted) as they happen. Most currently used engine models do not meet this requirement. On current single processor computers their execution speed is two or more orders of magnitude slower than the real physical process they simulate. This, of course, also depends on the computer platform being used. Future advances in hardware and software technology may narrow the gap. Alternatively, most engine models could be adapted for parallel execution.

. In most test scenarios the models can be quite useful even if they cannot execute in real-time. Typical engine tests proceed with alternating periods of relatively short (few seconds to minutes) engine maneuvers (acceleration, deceleration, throttle snap, etc...) and longer (several ten minutes to few hours) setup periods for the next maneuver. The engine models can be used in the setup periods to analyze and validate the data from the previous maneuver. Many engine models execute fast enough for this kind of usage on today's high performance workstations.

Adequate execution speed of the model is just one requirement for it to be usable in on-line testing. It is also necessary that the simulation be able to interact with the user in an efficient manner. This includes user friendly model input controls and simulation result presentation. These requirements are best satisfied with a well designed integrated graphical user interface for the engine model. The subject of this paper is the development of such an interface. Of course, such a graphical user interface can also aid in the model development process.

#### Current modeling technique

Currently most of the turbine engine modeling work is done in various dialects of FORTRAN. There are several reasons for this:

- *Efficiency*: although there are more modern programming languages available, FORTRAN is still one of the best languages for fast numerical computations. It is exactly the lack of "modern" features like pointers, etc.. which makes it relatively easy to write very good optimizing compilers for it. Additionally, the emerging High Performance Parallel Fortran (HPPF) standard promises a relatively easy way to create parallel Fortran programs.
- *Historical reasons*: most of the existing engine codes were developed on mainframes and later ported to PC-s and workstations. On the mainframe the natural development language was FORTRAN. Later the universal availability of the FORTRAN language made the porting easier.
- *Developers*: most engine models are written by aeromechanical engineers who want to concentrate on the aeromechanical aspects of the problem instead of software engineering issues. Thus the relative simplicity of FORTRAN is again an advantage.

Models are developed based on a few existing code libraries for simulating various components or component interactions. The typical development process involves writing a few engine dependent subroutines and initializing various constants, tables, etc.. with the parameters of the engine. The thus customized FORTRAN library becomes the model of the given engine. In practice there are various versions of the same code library customized for different engines which diverge during the lifetime of the model as changes are implemented.

The input and output of the models is typically done with formatted FORTRAN data files. Most models use the FORTRAN "namelist" construct for parameter input. Output files are mostly just formatted tables of numbers which have to be post-processed with stand-alone plotting programs to generate graphical output.

#### Requirements for the Graphical User Interface

Based on the background information presented above the design of a graphical user interface (GUI) for the existing FORTRAN engine models must satisfy the following requirements:

- *Features*: the main goal of the user interface is to speed up the interaction between the human user and the engine simulation program. This means that the GUI must provide an easy to understand display of simulation data (plots) and it must provide a straightforward interface to control the simulation program. Additionally, in some applications it is desirable that the simulation be interfaced to the on-line engine test data system for providing direct input of measurement data into the model.

- *Universal applicability*: due to the large number of engine models and their variants the user interface must be easily adaptable to any FORTRAN model. Preferably this adaptation should involve only FORTRAN programming because this way the developers of the original models could do it.
- *Portability*: the user interface should be portable to PC-s running DOS and Windows, and to workstations running UNIX and the X Window system

### Software Environment

Although FORTRAN is a very suitable language for writing numerical algorithms, it is not the best choice for writing a graphical user interface. The lack of pointers, dynamic memory allocation and structured data types would make it very hard to code the necessary user interface elements. For this reason the C++ language was chosen to implement the user interface. The C++ interface provides FORTRAN callable interface routines for the model code.

The public domain AT&T FORTRAN to C (F2C) translator was chosen to compile the model codes to C. The resulting C code is then compiled and linked together with the C++ code of the GUI. This solution was chosen for the following reasons:

- *Portability*: the native C and FORTRAN compilers of any computer system typically use different argument passing conventions. Thus if the native compilers were used, the interface between the C++ GUI and the FORTRAN model would have to be re-examined every time the code is ported to a new platform. By compiling the FORTRAN code first to C and observing the F2C translator's parameter passing conventions, the FORTRAN to C++ interface code can be the same for every environment. (Since the C and C++ compilers always use the same parameter passing conventions.)
- *Stability*: the F2C translator is a widely used program, it has been used to compile several large FORTRAN packages successfully. It is actively supported, new versions become available several times every year. It implements the FORTRAN 77 standard with many popular extensions (namelists, etc..).
- *Efficiency*: although it would seem that compiling a FORTRAN program first to C and then using a C compiler to generate machine code would result in less efficient code, it is not necessarily so. Tests on IBM PC 486 platforms have shown that the F2C output when compiled with the DOS port of the GNU C compiler (a well known optimizing portable public domain C compiler) performed almost

identically to the Lahey FORTRAN compiler's output. The only performance disadvantage of using the F2C translator is that the I/O libraries which come with it seem to be less efficient than the I/O libraries of native FORTRAN compilers.

### The DYNTECC User Interface

The graphical user interface for the DYNTECC [1] program was the first interface developed for FORTRAN engine models. Although the development of this interface started before this summer program, it should still be reviewed here because it was completed during this period, and this work influenced the design of future interfaces discussed later. DYNTECC is a one-dimensional compressor simulation program. It divides the compressor into several control volumes and solves the basic transport and continuity equations for each volume.

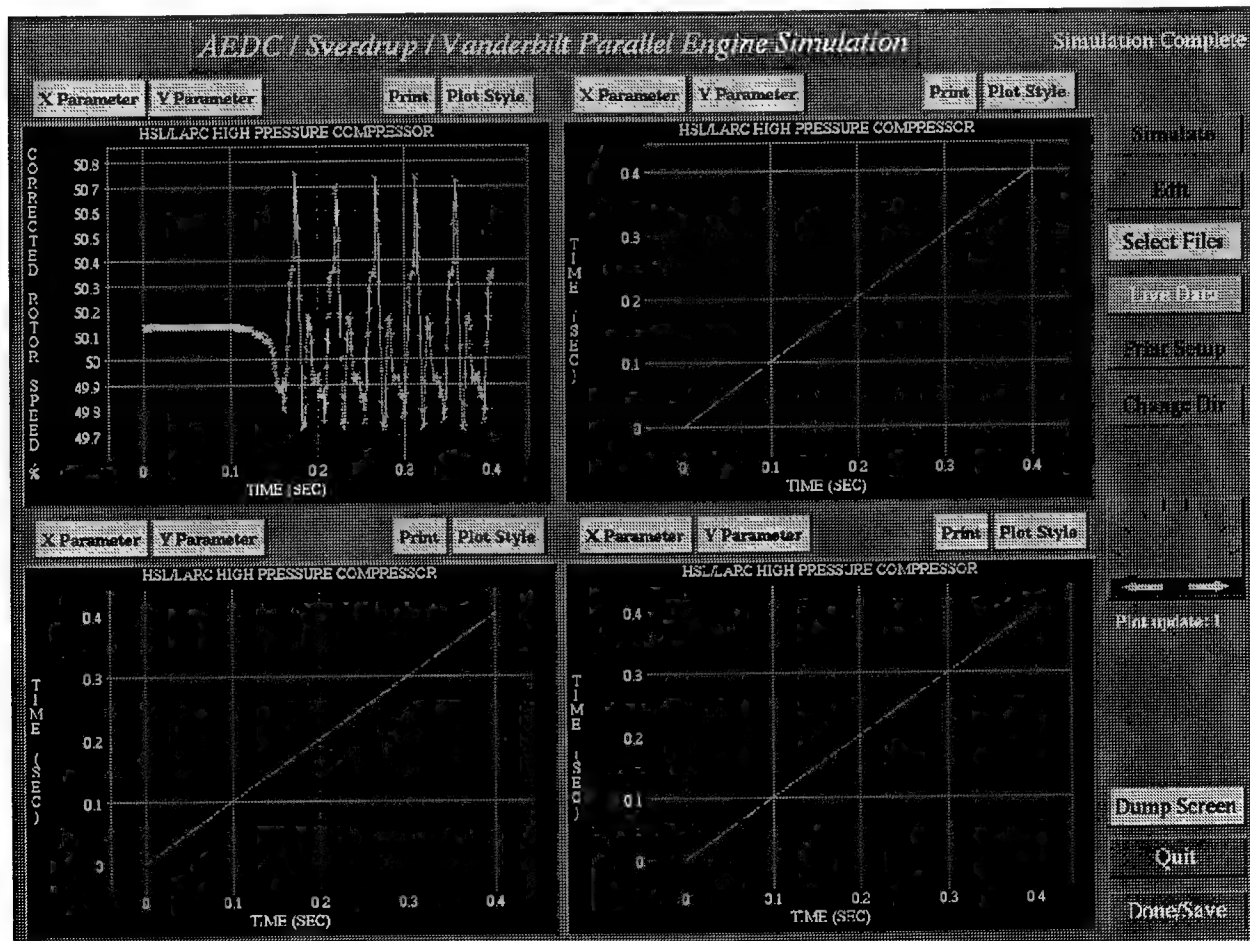


Figure 1. The DYNTECC User Interface

A typical DYNTECC user interface screen can be seen in Figure 1. The interface supports one-dimensional plots of time history data or parameter versus parameter plots. Plots can be created from FORTRAN output files produced during previous runs or interactively, using the DYNTECC code linked into the interface. In the second case the plots are updated on-line as the simulation progresses. The interface supports four on-screen plot regions, each of which can be configured to display any of the available simulation parameters.

The user interface has hard copy capabilities as well. Individual plot regions can be printed on a variety of supported printer types (several laser, ink jet and dot matrix printers), or a dump of the whole user interface screen can be made into a graphics bitmap file (PCX format). The screen dump can later be included into documents or presentations.

On the input side, the user interface supports the editing of the various FORTRAN namelists which make up the input file DYNTECC uses to control the simulation. This is done using a hierarchy of menus, the first of which selects the namelist to edit, and the second selects the edited field. On-line help is available for each of the menu choices.

The DYNTECC user interface has been implemented using SUIT [2], a portable user interface toolkit developed at the University of Virginia. The original DYNTECC FORTRAN code is compiled using F2C when linked with the interface. (Command line versions of DYNTECC are still compiled with the original, native FORTRAN compiler.) The interface is available, and has been used on several platforms, including IBM PC-s running both DOS and Linux and Hewlett Packard workstations.

#### The ATEST/SCIDNT User Interface

The second graphical interface was developed for a modified version of the ATEST [3] engine modeling code. ATEST is a large grain component level simulation of the whole engine which tries to predict overall engine characteristics based on component models and interactions. ATEST models are configured by specifying the engine components and their interactions and parameters (compressor or turbine maps, scale factors, etc.). Typically, the building of an ATEST model is an iterative process in which the parameters of the model components are refined until the desired accuracy is reached. Recently an attempt was made to try to automate this process by integrating the identification package SCIDNT with ATEST. In this setup SCIDNT tries to

adapt a few key engine model parameters based on simulation run results and selected measurement data records.

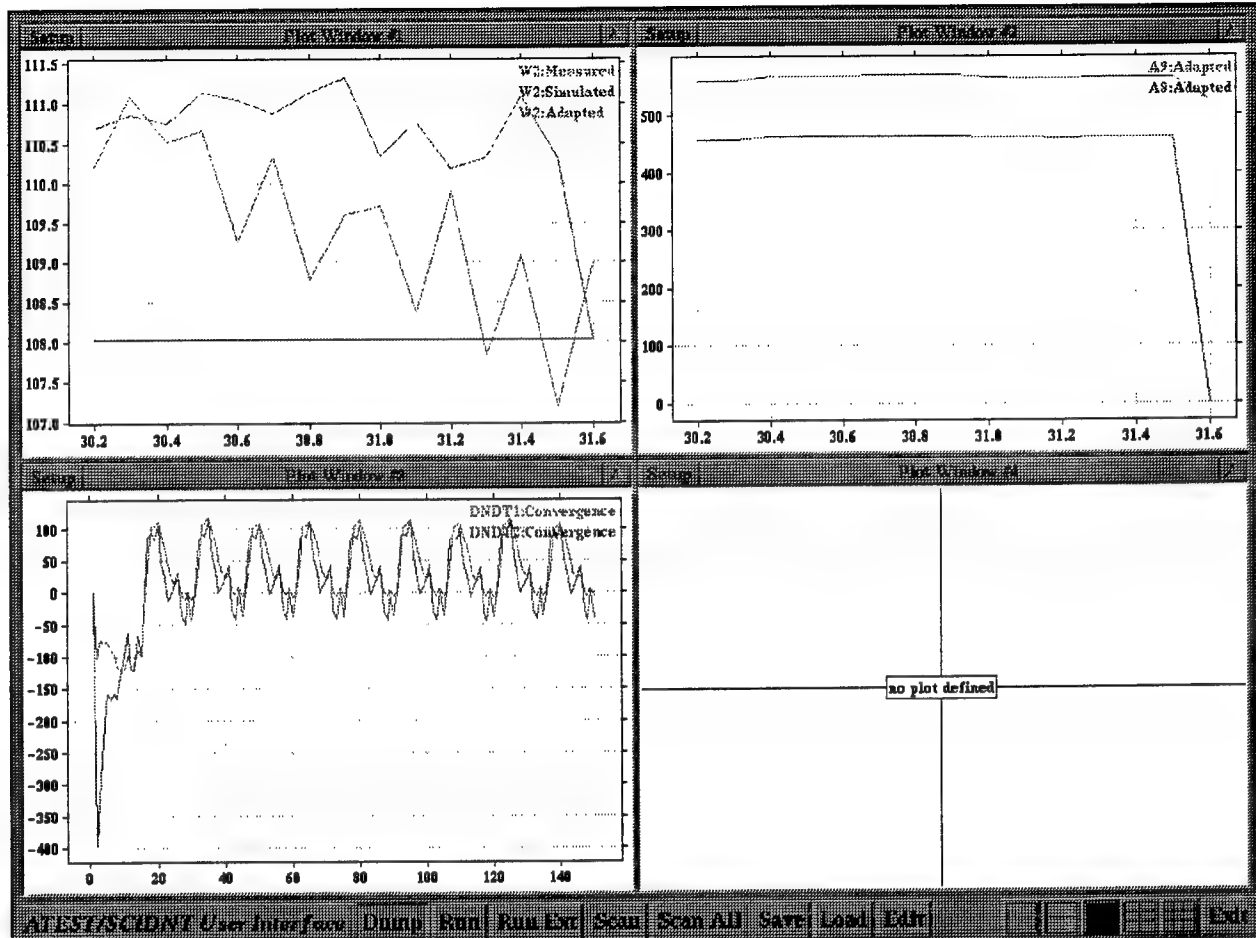


Figure 2. The ATEST/SCIDNT User Interface

A typical ATEST/SCIDNT user interface screen can be seen in Figure 2. The user interface has similar services as the DYNTECC user interface described above, but with a few important additions:

- **Parameter classes:** Unlike the DYNTECC interface which operates with only one kind of data for every parameter (i.e. the current simulation results), the ATEST/SCIDNT interface supports several kinds of values for every parameter. This is necessitated by the adaptation mechanism, since the user may want to examine plots of the same parameter from several sources including measurement data, unadapted and adapted model runs. Additionally to the three parameter classes mentioned above, two more classes are supported: design point values and adaptation histories. Design points are nominal values of certain parameters which are available in the ATEST model. Sometimes their inclusion in

the plots can serve as a reference point. Adaptation histories are records of engine model parameter during the SCIDNT adaptation run. They can be used to analyze the progress of the adaptation process and possibly select more suitable adaptation parameters or gain factors.

- *Multiple plots per plot region:* The ATEST/SCIDNT interface supports plots of multiple parameters or different records of the same parameter in the same plot region. Each parameter will be plotted against the same independent variable (the default is time), but the parameter class of the independent variable will be matched against the class of the variable on the Y axis. For example, if parameters "P1" and "P2" are plotted versus time in the same region, and "P1" is, say, a measured variable while "P2" is a simulated variable, then the X axis will be scaled in time, and the plotted time interval will be the union of the available simulated and measured time points.
- *Handling of custom FORTRAN file formats:* unlike the DYNTECC interface which, when plotting from results of previous runs stored in files, can input only raw FORTRAN output data (i.e. a table of numbers without page, column or row headings), the ATEST/SCIDNT interface can read formatted FORTRAN data. The interface incorporates a set of customizable file scanner library routines which are capable of parsing various formatted FORTRAN output files. This code can also extract parameter names from the files while skipping page headers and other irrelevant information. Adapting this library to a new FORTRAN data file format typically requires writing a short (10 .. 20 lines) subroutine.
- *Minor improvements:* these include support for different screen configurations (instead of the DYNTECC interface's fixed four window configuration, the user can select configurations with one to sixteen plot windows), a simulation screen window to display the messages originally printed by the FORTRAN model on the console and the capability to run external (i.e. not linked into the interface) models and then scan the simulation results from the produced data files.

The ATEST/SCIDNT interface was written in C++, using interface elements (buttons, scrollbars, etc..) which were adapted from public domain toolkits (so called "widget" sets) or implemented from scratch when necessary. The SUIT user interface toolkit used for the DYNTECC interface was not used because of size and efficiency concerns. (SUIT programs, although portable and relatively easy to write and configure, are quite big and slow when compared to user interfaces written using other toolkits.) Writing new widgets was necessary because none of the commercially available "portable" toolkits cover all of the targeted platforms (DOS graphics, Windows and the X Window system) -- at least not without unacceptable restrictions (like limiting the compiler choices under DOS and Windows or requiring a Motif license for workstations).

The first version of the ATEST/SCIDNT interface has been implemented during the summer program. Although it is currently in use by AEDC personnel, it has not been completed to the same level (for example, there is no built-in help) as the DYNTECC interface (which is now used by several other sites besides AEDC). The reason for this is that based on the DYNTECC and initial ATEST interfaces it was possible to identify the requirements for a universal graphical user interface library for engine modeling. It is anticipated that both the DYNTECC and ATEST interfaces will be re-implemented using this library.

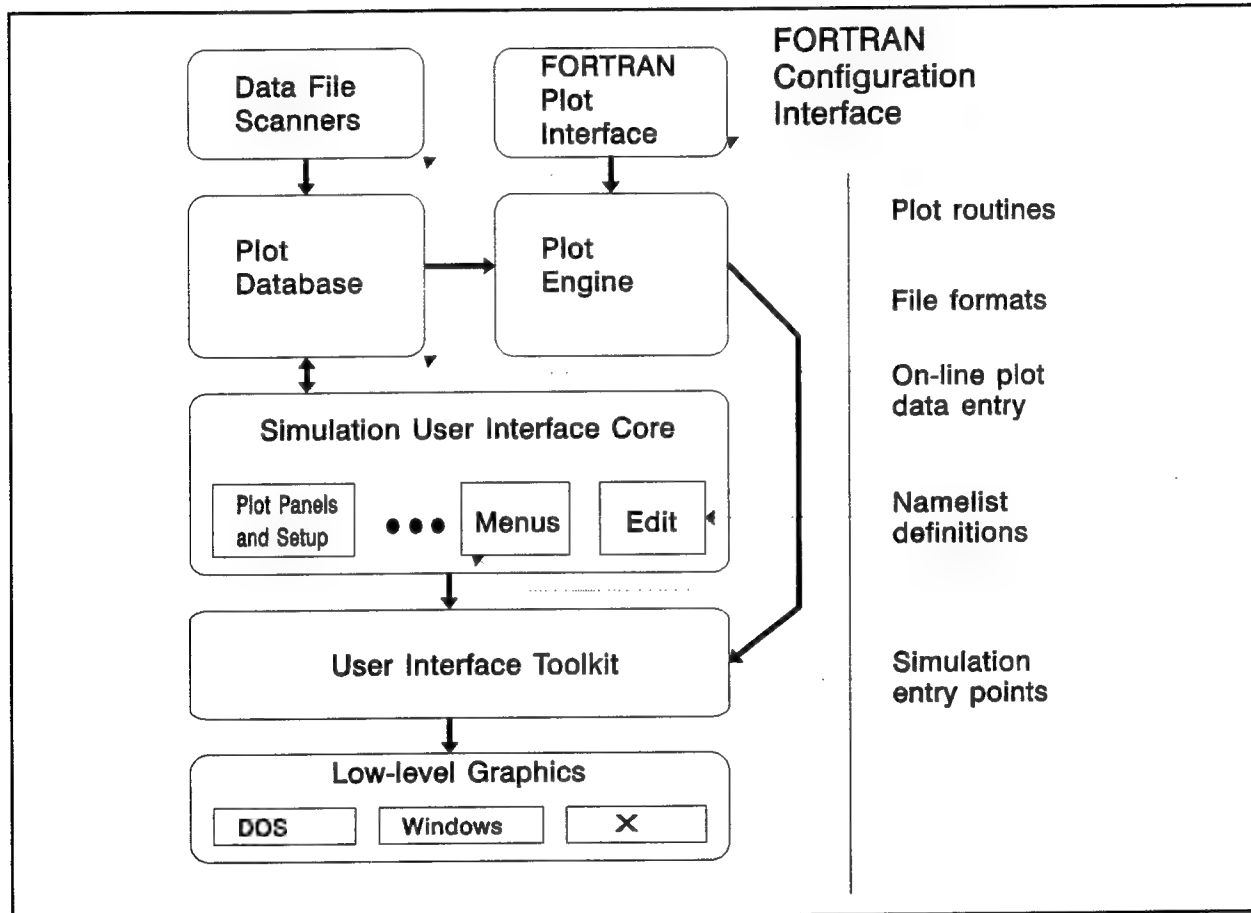


Figure 3. Components of the Universal Interface

#### The Universal Simulation User Interface

Based on the preliminary DYNTECC and ATEST/SCIDNT work a new graphical user interface library for turbine engine modeling was designed whose main goal is to provide universal support for converting existing FORTRAN models. It is anticipated that this conversion will be performed by FORTRAN programmers who write or maintain the models. For this reason the library was designed such that the necessary aspects of the

user interface configuration can be performed from FORTRAN code. Most components of the library originate from the ATEST interface described above. The main components of the new interface design, which can be seen in Figure 3., are:

- *Plot Database*: this data base contains records of simulation variables generated either by loading FORTRAN data files or by running the linked in FORTRAN model code (if any). The data base can be searched by parameter names and classes. Each parameter can have several data records associated with it which are keyed by class. The Plot Database also provide FORTRAN callable subroutines for entering data during a simulation run. In this mode plots are updated on-line as the simulation progresses.
- *Plot Engine and FORTRAN Plot Interface*: this component is responsible for generating the plots which are displayed in the plot windows of the user interface. A slightly modified version of the well-known GNUPLOT plotting program was used for this purpose. The Plot Engine operates in either of two modes: it can plot data from the Plot Database or display data furnished by a FORTRAN subroutine through the FORTRAN Plot Interface routines.
- *Data File Scanners*: the interface provides the capability to scan a few standard FORTRAN data file formats. These include binary data files and horizontally or vertically tabulated formatted tables with or without parameter name headings. Most FORTRAN programs generate output files which are some variants of these formats for printing purposes. For more customized file formats it is possible to write FORTRAN routines for the given file layout using the services of the scanner library.
- *Simulation User Interface Core*: the interface core contains the various screens, panels and menus the user interacts with. The interface core is responsible for coordinating the operations of the other components. It selects the plot window layout, assigns parameters from the Plot Database to the various plot windows for display, configures the plot windows, etc.. Most of the core services can be invoked via the top-level pull-down menu of the interface. The basic layout of the interface can be seen on Figure 4. This layout can be extended by calling FORTRAN entry points from the user interface library during the startup phase of the program. Customization options include:
  - 1) Specifying the title of the application displayed on the top of the screen.

- 2) Registering FORTRAN namelists with the built-in editor of the interface. This editor supports the editing of arbitrary text files. However, when it is used for editing FORTRAN input files which contain namelists whose definition has been registered with the interface, the editor will automatically switch to a namelist editing menu for the corresponding section of the file.
- 3) Registering FORTRAN subroutines which are the entry points of the simulation model. This way these routines can be invoked from the user interface via the "Run" pull-down menu. Initially, this menu contains only one option: to run an external program.
- 4) Registering data file scanner FORTRAN routines. These will appear as new choices under the "Data" pull-down menu. Initially, this menu contains only the file formats for which there is built-in support in the interface.
- 5) Registering the names of the data files which are used by the model. These appear under the "Data" and "Edit" menus and can speed up the usage of the interface, since the user will not be prompted for file names.

- *User Interface Toolkit and Low-level Graphics:* the same components are used as in the ATEST interface. Full screen protected mode DOS and UNIX X Window environments are currently supported. The Windows version will probably be postponed until a true 32 bit Windows (Chicago) is available. Until then the full screen DOS version can be used under Windows as well.

The user interface can be also be used as a stand alone program without integrating it with a FORTRAN model. In this case the simulation can be executed as an external program and the result files are read into the interface and plotted. Only the generic text file editing and plotting capabilities of the interface are available in this case, but even this limited support may be very useful for longer simulation experiments.

The next possible phase of the FORTRAN simulation code integration is the customization of the interface with the namelists, file names and file formats used by the model, but still running the actual model as an external program. This requires a small amount of new FORTRAN code, but allows the creation of a fully customized interface for the model. The advantage of this solution is that the model codes do not have to be recompiled with F2C. The disadvantage is the lack of on-line plots during the simulation run, since plots are available only after the external program terminates and its output files are scanned into the Plot Database.

If on-line plots are needed then the model's FORTRAN code has to be fully integrated into the interface. This requires recompiling with F2C and modifying the FORTRAN code in a few places. Typically, modifications

are necessary because most models were written with the assumption that the code will run only once. This assumption allows shortcuts like not closing files on program exit, overwriting initialized data, etc.. If the model is linked into the user interface then it can be executed several times during the course of a simulation study. In order for the model to run successfully several times and produce identical results, the aforementioned shortcuts have to be identified and fixed.

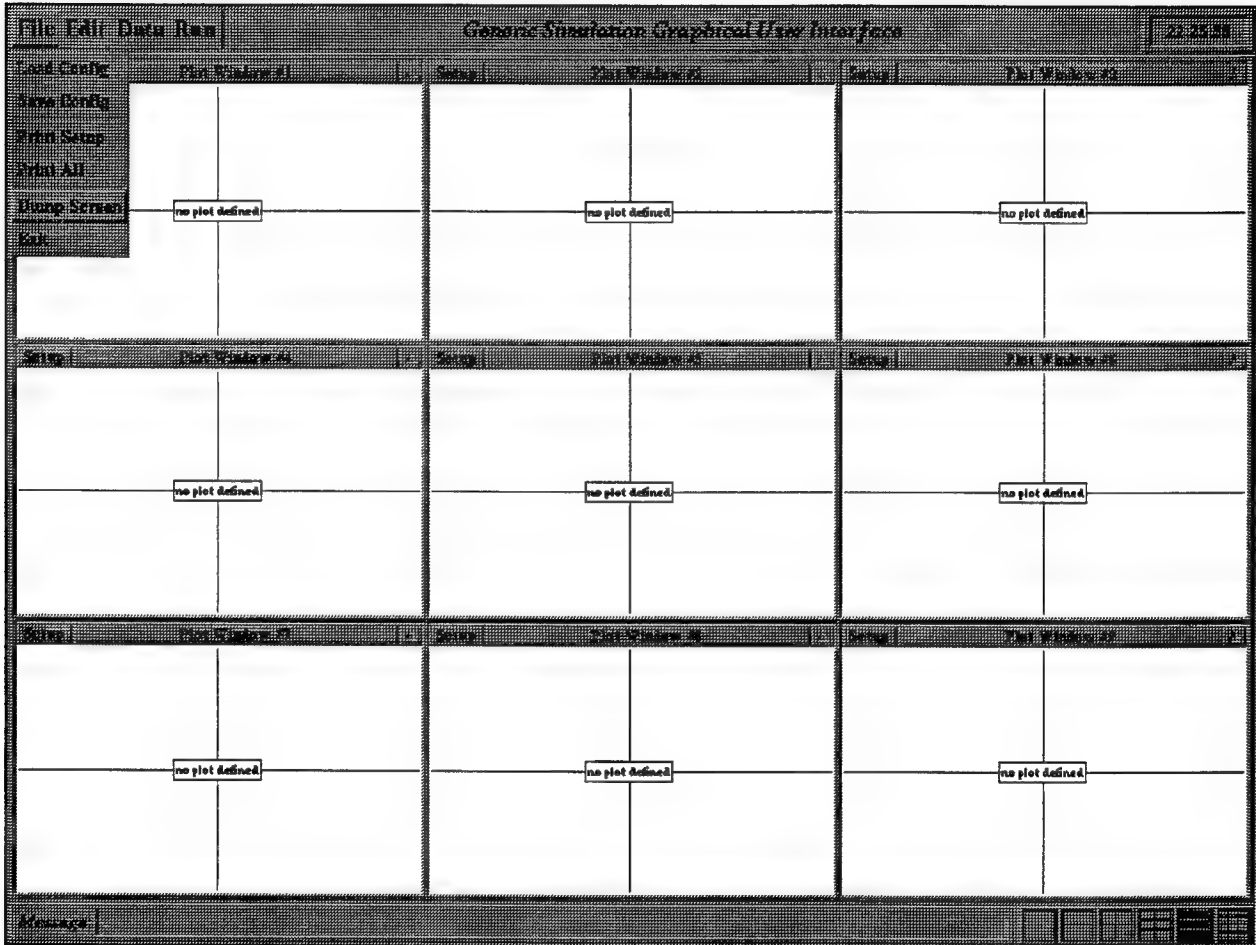


Figure 4. An Example Universal Interface Screen

### Conclusions and Future Work

The interfaces developed during the course of the summer program have significantly enhanced the capabilities of existing FORTRAN turbine engine models. One of the simulations with new a interface (DYNTECC) has actually been distributed to several test sites, and it has been well received. The new universal interface designed during the program promises to unify the existing applications. Its implementation together with the

conversion of the existing DYNTECC and ATEST interfaces is nearing completion. However, the real test of the approach will be when the original FORTRAN programmers of the models will attempt to equip their program with a graphical user interface without the support of a C or C++ programmer.

## References

- [1] Hale, A. A. and Davis, M. W. Jr.: "DYNamic Turbine Engine Compressor Code: DYNTECC -- Theory and Capabilities", AIAA Paper 92-3190, Presented at the 28th Joint Propulsion Conference and Exhibit, Nashville, TN, July 1992.
- [2] Conway, M., Pausch, R. and Passarella, K.: "The SUIT Reference Manual", Department of Computer Science, University of Virginia.
- [3] Chappell, M. A.: "Advanced Turbine Engine Simulation Technique", Society of Automotive Engineers Conference, TOPTEC, Nashville, TN, May 1992.

**TOWARDS THE COMPUTATIONAL MODELING OF  
POSTSTALL GAS TURBINE COMBUSTOR DYNAMICS**

Steven H. Frankel  
Assistant Professor  
School of Mechanical Engineering  
Purdue University  
West Lafayette, IN 47907

Final Report for:  
Summer Faculty Research Program  
Arnold Engineering Development Center

Sponsored by:  
Air Force Office of Scientific Research  
Bolling Air Force Base, DC

and

Sverdrup Technology

August 1994

## **TOWARDS THE COMPUTATIONAL MODELING OF POSTSTALL GAS TURBINE COMBUSTOR DYNAMICS**

Steven H. Frankel  
Assistant Professor  
School of Mechanical Engineering  
Purdue University

### **Abstract**

This report summarizes an eight week investigation aimed at providing suggestions for making improvements to a dynamic engine code called ATEC (Aerodynamic Turbine Engine Code) in the area of modeling the transient behavior of gas turbine combustors during poststall dynamic events. The paper will consist of a brief literature review of computational modeling of gas turbine combustion in general, followed by a discussion of some of the key physical issues dealing with poststall combustor dynamics as well as previous efforts directed towards modeling this phenomena specifically detailing a Pratt & Whitney developed transient combustion code called TRANSI. A summary of the current status of the ATEC project, with particular emphasis on how the combustor is modeled, will be provided. Then a suggested course of action is proposed to improve the combustor model. Preliminary developments on a transient combustion computer code are discussed and future improvements and directions for development and application are outlined.

---

## **TOWARDS THE COMPUTATIONAL MODELING OF POSTSTALL GAS TURBINE COMBUSTOR DYNAMICS**

Steven H. Frankel

### **Introduction**

The gas turbine engine is one of the most reliable and widely used devices for generating mechanical power as evidenced by its successful use in aircraft propulsion, naval power and industrial power technologies. Engine improvements focusing on higher efficiencies and lower pollutant emission levels over the full range of operating conditions, including off-design, continuously present new challenges to the designer. Often, gas turbine engine modeling is done on a component by component basis, ignoring the dynamic interactions between the compressor, combustor and turbine, or if a full engine model is employed it focuses on design operating conditions. Recently, there have been considerable efforts directed towards dynamic modeling of the entire engine (Schobeiri, 1993; Hale and Davis, 1992). These models have been very successful in modeling the compressor and turbine dynamics through the implementation of experimentally obtained maps of component behavior under a variety of operating conditions including off-design. Modeling of the combustor has been restricted to simple heat release models.

Over the past 50 years there have been numerous efforts to model gas turbine combustor behavior (Levebvre, 1983). Physical models and numerical techniques have primarily been developed for the simulation of steady flow in combustors (Correa and Shyy, 1987) with particular emphasis in the past 20 years on engine pollution (Mellor, 1976; Gupta and Lilley, 1994). One of the key stumbling blocks in modeling dynamic engine behavior has been the lack of knowledge of transient combustion phenomena or more specifically poststall combustor dynamics (Przybylko, 1985). This lack of understanding has manifested itself in simple modeling approaches which do not account for the key combustor physics (Davis, 1986; Clark and Green, 1990). Thus there is a strong need for models which can account for some of the transient features of gas turbine combustors.

## Background

Gas turbine combustion chambers involve complicated three-dimensional, two-phase, radiating turbulent reactive flows. As such their modeling is an extremely difficult task and usually many simplifying assumptions are made to make the problem more tractable. These assumptions depend upon the type of information of interest. Computational models have been very useful in complementing experimental studies for engine design (Rizk and Mongia, 1994).

There are two main types of computational modeling approaches that have been used to model steady state combustor behavior. These have been labeled the modular approach and the continuum approach (Mellor, 1976). The modular approach envisions the combustion chamber to consist of a network of chemical reactors. The type of reactor chosen depends on the region of the combustor being modeled. For example, primary zone behavior has been modeled using a well-stirred reactor which assumes that mixing is instantaneous. Detailed kinetics mechanism have been used to determine the composition leaving the reactor. These models have been successful in providing information on pollutant emissions under ideal mixing conditions. Continuum approaches involve the use of Computational Fluid Dynamics (CFD) to solve the equations governing combustion behavior. They typically employ a two-equation turbulent model and a fast chemistry/assumed probability density function combustion model (Correa and Shyy, 1987).

Unsteady combustion is important in several different aspects of gas turbine combustor behavior. This includes the aforementioned poststall combustor dynamics, which is the topic of this study, acoustic interactions in afterburners or ramjet engines (Sterling et al., 1987; Kailasanath, et al., 1987; Jou and Menon, 1986), and flashback phenomena in lean premixed-prevaporized low NO<sub>x</sub> combustors (Mularz, 1979; Tacina, 1990). In order to study unsteady combustion time dependent simulations of the governing equations are necessary. Unfortunately, in order to simulate realistic turbulent reacting flows the computational resources necessary to resolve the wide range of length and time scales that exist in such flows are beyond current computational means (Givi, 1989).

## Poststall Combustor Dynamics

Airflow instabilities occurring within the compressor of a gas turbine engine lead to several important dynamic phenomena. These are called surge and stall. Stall refers to separated flow occurring on one or more of the compressor blades. Typically, stall on a single blade tends to stall the adjacent airfoil which leads to a phenomena termed rotating stall. This localized instability rotates relative to the rotor blades in the opposite direction of the spool rotation. This can occur in several stages of the compressor. Surge, on

the other hand, involves an entire circumferential flow breakdown usually characterized by bulk flow reversal. Both surge and stall phenomena lead to compressor-combustor interactions and some interesting dynamic behavior (Przybylka, 1985).

The purpose of the combustor is to oxidize the fuel in order to provide heat to the airflow raising its kinetic energy to produce thrust. The key objective is to convert all the chemical energy of the fuel to thermal energy with a minimum pressure loss. The combustor receives air from the compressor which has been slowed down by a pre-diffuser, again with minimum pressure loss. The dump region which follows, stabilizes the flow further. The majority of the air enters the primary zone where fuel is injected, vaporized and mixed with the air. Stoichiometric combustion occurs in this zone with most of the fuel being burned. In the secondary zone, which follows the primary zone, additional air is introduced to complete the burning process as well as to cool down the combustion products to temperatures nearer to what the turbine blades can withstand. This may be followed by a dilution zone which, using more air, further adjusts the exhaust gas temperatures to provide a more uniform temperature distribution for the turbine. The design of these zones is dictated by increased combustion efficiency, low pressure loss and minimum pollutant emissions. For further details on gas turbine combustion please see the excellent text by Lefebvre (1983).

The above scenario occurs under normal, steady operating conditions. Compressor dynamic events, such as surge and stall, can affect combustor performance in a variety of ways. During a compressor surge the breakdown of flow leads to a sudden drop in pressure. The combustor feels this pressure drop which may lead to reversal of flow out of the primary zone and into the compressor. Under this scenario the combustor may experience a rich blow out. Relighting of the engine in order to attempt recovery may be difficult due to the fuel rich conditions that may develop during the surge event. The sudden low pressures can also vaporize the liquid fuel in the fuel nozzle resulting in poor spray quality (Przybylka, 1985). Because these compressor instabilities are of an oscillatory nature they may lead to a situation of repeated blowout and reignition in the combustor. Another important consequence of a surge event is that during flow reversal higher compressor inlet temperatures may be experienced which reflect the temperature rise due to compression and work during reversal (Davis, 1986). Then during a reacceleration higher temperature air is now compressed leading to higher combustor inlet temperatures. If reignition occurs before the high temperature air is passed through the combustor, higher combustor exit temperatures may prevail. This will lead to higher turbine blade temperatures which may be beyond the material design temperature and could cause engine failure. It is also possible for fuel to enter the compressor during flow reversal leading to possible autoignition of the fuel. This could lead to flame appearing out the front of the engine. Modeling these dynamic phenomena is important in order to gain a better understanding of turbine engine behavior.

### **Modeling Poststall Combustor Dynamics**

There have been very few reported attempts at modeling poststall combustor dynamics. An effort by Pratt and Whitney, in conjunction with the Air Force, is one of the more recently published attempts (Clark and Green, 1990). Their approach invokes a quasi-steady-state assumption employing empirical correlations to model fuel evaporation, flame stability, autoignition and combustion efficiency (Lefebvre, 1983). A detailed model of the in-nozzle fuel vaporization process was included because one of the main focuses of the study was fuel effects on combustor dynamics. Time dependent data at the entrance to the combustor is provided for total pressure, temperature and mass flow rate. From this input information a combustor loading parameter is computed (see Lefebvre (1983) for discussion of the loading parameter and how it aids in determining combustor efficiency). With the loading parameter determined, combustion efficiency is computed which then determines the heat release and subsequently the combustor pressure and temperature. It is the time dependent behavior of the combustor pressure which is of interest during poststall events. The code constructed based on the above model description is called TRANSI and more details with emphasis on the treatment of the combustor can be found in several references and are summarized in the appendix of this report.

Various tests were conducted with the model which corresponded to an experimental study of transient combustion conducted in conjunction with the model development work (Rosfjord et al., 1988). These tests consisted of providing the model different schedules for air flow, fuel flow, inlet pressure and temperature to simulate different dynamic events, in particular surge and rotating stall. Key quantities such as combustor pressure and temperature are monitored as a function of time for evidence of combustor blowout. When the inlet pre-diffuser pressure is below the combustor pressure a reversed flow condition is specified simulating a compressor surge. Mentioned in the final report are several drawbacks of the current TRANSI model. The most important drawback is the quasi-steady assumption, that is, employing combustion correlations which were developed for steady flow and using them in an unsteady situation. Also the lack of any sort of transport within the combustor, convective or diffusive, laminar or turbulent, leads more or less to a perfectly stirred reactor scenario and limits the type of phenomena that can be simulated (Caron, 1991).

The aim of the current eight week investigation into poststall combustor dynamic modeling was to assess the state-of-the-art in transient combustor modeling in the search for the best approach in order to improve the current combustor modeling capabilities in the dynamic engine simulation code ATEC. A brief description of the ATEC code is provided next with particular emphasis on the current combustion model employed in the code.

## ATEC

The current version of the ATEC code is a modification of a code called DYNTECC (Dynamic Turbine Engine Compressor Code) (Hale and Davis, 1992). The code employ a quasi-one-dimensional, time-dependent compressor modeling technique which involves the solution of the compressible Euler equations with turbomachinery source terms. Basically, the entire engine is divided into a number of individual control volumes along the one-dimensional domain (see Figure 1). Within the compressor each control volume represents a stage of the compressor, that is, a rotor/stator pair. The key feature of the compressor modeling technique is the manner in which the turbomachinery source terms, representing the axial force distribution, the heat transfer and the shaft work, are modeled. This is achieved by employing experimentally and theoretically determined stage characteristics for the compressor under study over its entire range of operating conditions. These stage characteristics take the form of plots of normalized pressure and temperature coefficients versus local mass flow rate. Details of the compressor modeling procedure can be found elsewhere (Davis, 1986). A similar modeling approach has recently been employed for the turbine (Garrard, 1994).

ATEC currently models the combustor by dividing it into a number of control volumes (see Figure 2). A fuel flow rate to the combustor is specified which, together with the air flow rate determined by the solution to the Euler equations, an equivalence ratio is computed. This combustor equivalence ratio, together with the lower heating value of the fuel provides a measure of the total heat release and hence temperature rise through the combustor. This heat release is evenly distributed throughout the combustor control volumes and appears as a source term in the energy equation. Secondary air is brought in downstream of the fuel injection point in order to cool the heated air in preparation for the turbine. Fuel flammability limits taken from empirical data are incorporated as well as autoignition criteria to determine whether combustion is occurring within the chamber. A recent modification to include an empirical correlation which accounts for a reaction rate controlled combustor efficiency was added (Lefebvre, 1983). Previous work has demonstrated the capability of the model to study the effect of combustion on post-stall behavior (Davis, 1986). Simulations were conducted of a nine-stage, high pressure compressor model with a representative combustor. Blowout and reignition of the combustor during surge cycles was observed to actually sustain the surge event (see Figure 3 for a typical result). It was also observed that if a portion of combustor fuel is drawn into the compressor and burned during flow reversal, the compressor inlet will experience a more elevated temperature during this process than would be observed without combustion. If the combustor stays lit during rotating stall, the combustor exit temperature may exceed the design limit of the turbine even if a 50% degradation in combustor efficiency is assumed.

Transport of fuel is not accounted for within the model, thus during surge events, with the accompanying flow reversal, the model is currently not capable of simulating the possibility of flame propagation upstream of the combustor. Previously this was studied by forcibly injecting fuel upstream of the combustor inlet to simulate this backflow phenomena. Also simulations accounting for combustion efficiency degradation during dynamic events are not possible in the context of the current model. The primary goal of the present investigation is to suggest possible ways to improve the current modeling capabilities to be able to dynamically capture the fuel flow reversal and the degradation of combustion efficiency which may accompany a surge event as both these phenomena may lead to combustor blowout (Davis, 1986; Davis, 1994; Garrard, 1994). Discussions along these lines are provided in the next section.

### **Current Transient Combustor Model Development**

In order to improve the combustor modeling capabilities of the ATEC code several factors should be taken into consideration. First, any modifications to improve the combustor model in ATEC should be consistent with the current modeling technique utilized in the rest of the engine, that is, a time-dependent solution of the one-dimensional Euler equations. Second, computational efficiency is a factor as it is desired to run the code on a personal computer. Third, the improvements to the physical model should be guided by the particular physical phenomena of interest. This includes bulk fuel dynamics and combustion efficiency. Thus it does not appear necessary, nor is it possible, to model a complex three-dimensional, viscous, heat conducting turbulent reacting flow in the limited context of a one-dimensional, unsteady, inviscid flow model. Obviously, a great deal of the physics occurring within the combustor must be sacrificed in order to remain computational consistent and tractable within the context of the ATEC code. The physics retained should be just enough to hopefully provide the needed insight. Based on this discussion the course of action outlined in the following paragraphs is suggested.

A transient combustion computer code called TRACC (Transient Combustor Code) is proposed to be developed which solves the quasi-one-dimensional, time-dependent Euler equations coupled with transport equations for the thermochemical variables of interest. A two-step chemical kinetics scheme involving a partial oxidation of the fuel to  $CO$  and  $H_2O$  followed by a  $CO$  oxidation step will be employed (Westbrook and Dryer, 1982). The choice of finite rate chemistry is motivated by the desire to simulate ignition and extinction events, while the choice of two-step chemistry is based on a tradeoff between simulating combustion efficiency degradation and computational efficiency. In the current formulation transport equations for the mass fractions of the fuel and carbon monoxide will be solved as well as an equation for the mixture fraction. These variables, together with atom conservation, are sufficient to determine the mass fractions of the other species. The choice of employing the mixture

fraction approach is motivated by the eventual desire to extend the current formulation to two dimensions together with a turbulent subgrid model (Bilger, 1980). Gaseous propane is selected as the fuel because many of its combustion characteristics are similar to vaporized JP fuels and an adequate reduced kinetics mechanism is available compared to higher hydrocarbons (Lefebvre, 1977; Sloan et al., 1994). Thus an infinitely fast fuel evaporation rate is assumed. In the one-dimensional context we are effectively assuming infinitely fast radial mixing and in the inviscid limit we do not account for molecular diffusion. This is equivalent to treating the turbulent mixing process as quasi-laminar, that is within a computational grid cell, local molecular homogeneity exists. Thus the time required for large-scale turbulent mixing between the fresh air and the recirculating burned products, as well as the time required for the turbulent cascade from the large scale scalar field down to the small scale molecular level, to occur is zero. Since we are not presently interested in making quantitative predictions of pollutant emissions or reacting species profiles within the combustor this gross neglect of mixing is deemed adequate. Note that the current formulation provides a convenient framework in which to make further improvements to account for molecular diffusion, multi-dimensional mixing and turbulent mixing effects through submodel additions.

One of the main difficulties in modeling a gas turbine combustor in one-dimension is related to flame stabilization. In gas turbine engines compressor air flow velocities are usually much larger than combustor flame speeds. In order to stabilize a flame it is necessary that the local flame speed and the local flow velocity be equal at one point in the flow. Typically this is achieved by decreasing the local flow velocity by introducing a recirculation region in the primary combustor zone. This also has the effect of increasing the local turbulence levels which enhances the local flame speed. In actual combustors this recirculation zone is created either through the use of air-flow swirlers, bluff-bodies or opposing jet flows. In a one-dimensional formulation it is needed to mimic this effect otherwise the fuel injected in the primary zone will burn with the air and the flame will blowoff and be swept downstream and carried out the combustor. In stirred reactor modeling efforts this difficulty was alleviated somewhat by employing two reactors in parallel to model the primary zone (Hammond and Mellor, 1971). The first reactor receives the air and fuel. Part of its products are recirculated back through a second reactor mimicking the effects of a recirculation zone. This approach will be investigated in the current model. Another flame stabilization approach which will also be pursued is as follows. A fraction of the mass flow entering the primary zone will be bled off and re-injected just downstream of the fuel injector with zero momentum and thus act to decrease the axial component of momentum. This idea is based on the opposed jet stabilization concept which involves the use of an opposed jet flow to induce a recirculation zone within the primary zone. The amount of stabilizer air will be chosen to create a situation within the primary zone where the primary zone flow velocity is near the laminar flame speed of the mixture leading to a stable flame. This flame stabilization problem is a key issue and introduces some interesting

modeling questions that will require further study during this research project. The geometry of the combustor will now be detailed.

The geometry of the combustion chamber is specified by the area variation along its length. It consists of a prediffuser section followed by the primary and secondary zones of the combustor. The pre-diffuser air flow is split into a primary zone flow and a liner flow which surrounds the main combustor. The liner flow is then split into a stabilizer flow and a secondary air flow. Fuel injection in the primary zone and air injection in primary and secondary flows are achieved by including non-zero source terms in the appropriate transport equations at user-specified locations and with user-provided rates. Ignition is modeled in an approximate manner by adding internal energy to the fluid in a set of control volumes whose location and rate of addition can be specified by the user (Winovich, 1990). It is proposed to test the model in a stand-alone application before implementing it into ATEC. In order to simulate poststall conditions several features of the code are proposed. Time dependent variations of airflow rate, fuel flow rate, inlet temperature and pressure can be specified to simulate rotating stall events. In order to simulate a surge event a valve is located just upstream of the prediffuser section. The purpose of this valve is to induce a reverse flow within the combustor. This is analogous to the surge valve in the transient combustor experiments of Rosfjord et al. (1988). They report that under conditions of high combustor pressure, low air flow rate and the surge valve open, allowing an airstream bleed, reversed flow was induced within the combustor. A similar scenario is expected to be observed in the computer model.

A computer code was written by the PI during his summer 1994 stay at AEDC as part of the AFOSR Summer Faculty Research Program to begin work on the above proposed tasks. A MacCormack's method solver was employed. The code was not completed during the stay but was tested under some simple situations and it was found that the numerical scheme introduced non-physical oscillations in the flow variables and was deemed unsuitable for the current applications. Therefore, it is proposed to modify the solver in the presently underdevelopment transient combustor code as part of this project.

The governing equations will be solved with a flux-difference splitting scheme to be consistent with the current solver employed in ATEC. This scheme is known to avoid spurious oscillations in flow variables near discontinuities (shocks and contact surfaces). In the dynamic engine model there are typically no shocks present, but there are discontinuities across control volumes due to sinks and sources of mass, momentum and energy. These could be caused by bleed flow, compressor work, fuel injection, spark ignition and chemical heat release. A recent study by Lindau and O'Brien (1993), implementing a number of different numerical schemes, found that a Roe flux-difference splitting algorithm with Runge-Kutta time integration was the most robust scheme for incorporation into a ATEC-like compressor flow solver. Since the current transient combustor code will be implemented into ATEC the numerical solvers should be consistent. Recent progress in applying flux-difference splitting schemes to multi-component

chemically reacting flows makes this an attractive research direction to pursue (Larroutrou, 1991; Frankel, 1991; Ton et al., 1994).

TRACC will be exercised in a series of stand-alone tests designed to simulate different dynamic conditions that may be encountered in an actual gas turbine engine. This will be done to characterize and quantify the different combustor behaviors capable of being simulated with the code. These transient combustor tests will mimic the type of combustor rig testing commonly used in dynamic engine test programs (Caron, 1991; Burwell and Grant, 1985). These tests will be summarized here with more details provided in Caron (1991).

1. *Monotonic Transients*: Steady state operation of the combustor is achieved. This is followed by a ramp down of the fuel flow keeping the inlet air flow and temperature constant. The fuel flow rate at which flame extinction occurs is recorded and steady state behavior is resumed at the lower fuel flow. Data from this steady state lean blowout test will be presented in the form of plots of combustor pressure and temperature versus time throughout the engine.

2. *Oscillatory Transients*: Airflow is supplied to the combustor in an oscillatory manner quantified by a mean flow rate, amplitude and frequency. These tests are to simulate rotating stall phenomena. The fuel flow rate during these tests will be held constant.

3. *Surge Transients*: An initial steady state begins this test. The surge valve is opened and closed at some characteristic frequency in an attempt to induce reversed flow within the combustor simulating a deep surge event. Pressure and temperature are monitored for evidence of combustor blowout, reignition or both.

It is felt that these tests will serve several purposes. They will provide stringent tests of the numerical algorithm under the type of conditions likely to be encountered in ATEC. They will highlight the capabilities of TRACC in simulating dynamic engine events in a stand-alone mode while providing insight into how the model will perform when fully implemented into ATEC.

#### **Suggested Improvements and Possible Future Directions**

In any numerical modeling study there are tradeoffs between accuracy and efficiency. There are several advantages and disadvantages to the presently proposed approach for modeling poststall combustor

dynamics. A brief discussion of the tradeoffs involved as well as some suggestions for improvements and future directions is presented next.

There are several advantages of going with time-dependent species equations. One immediate advantage is that some aspects of the unsteady behavior are captured. Accounting for bulk transport of the fuel will also allow for fuel to flow upstream during flow reversals events thereby simulating some of the important dynamic effects of surge on combustor behavior. The effect of combustion efficiency degradation on the amount of heat released is directly affected by poststall dynamic events and through the inclusion of finite-rate chemistry will not have to be treated in an ad hoc manner as in the current ATEC code. There are also several disadvantages of accounting for species transport and chemical kinetics. While the bulk transport of the fuel is accounted for it is done so in only one-dimension and none of the fluid dynamic mixing behavior in the combustor is captured. Obviously at least a two-dimensional formulation is desired to capture some of the mixing effects and to better handle the recirculation zone problem. In the current formulation two additional partial differential equations need to be solved, which if incorporated into ATEC, will substantially increase the overall computational time of the code. Also the coupling between the chemistry and the fluid dynamics requires special numerical treatment as discussed in the previous section. In the inviscid context there is no mixing accounted for so basically the fuel and air assumed mixed at the molecular level if they exist in the same control volume. There is surely no accounting for turbulent mixing effects. Keeping in mind the restrictions placed on the model and the goal of being consistent with the current formulation the above tradeoff is deemed warranted.

In order to numerically simulate the time dependent nature of a complicated gas turbine combustor it is necessary to solve the equations governing the turbulent reacting flow physics employing enough grid points to resolve all the length scales associated with the flow. These length scales range from the largest scales associated with the combustor geometry down to the smallest scales associated with the molecular processes of diffusion and chemical reaction. This is an impossible task with the computational resources currently available and not desirable in the context of the current modeling effort. This approach is often referred to as Direct Numerical Simulation or DNS (Givi, 1989) and is only useful for the study of simple geometry flows at low Reynolds numbers, because under these conditions the range of length scales is resolvable but only on large supercomputers. An alternative approach which attempts to overcome the computational limitations associated with DNS is called Large Eddy Simulation or LES. In the LES approach only the large scale physics are captured on the numerical grid and any physics which occurs at scales smaller than the computational grid scale are modeled. These so called subgrid models must accurately account for the detailed interactions between the three distinctly different physical processes of turbulent convection, molecular diffusion and chemical reaction down to the smallest scales of the flow. This is a difficult task because the behavior of small scale reacting turbulent flows is not well understood.

There have been several attempts recently to account for these processes with different subgrid models (Menon et al., 1993; Frankel et al., 1993; Ryden et al, 1994) each meeting with varying degrees of success.

It is feasible to interpret the inviscid computation of dependent variable transport equations as a pseudo-LES where each flow variable represents a space-filtered value, that is, a local control volume averaged value. In this context an ad hoc turbulent viscosity could be included to represent the enhanced small scale mixing due to turbulence. One of the main difficulties in applying the LES approach to reacting flows stems from the still unresolved issue of closure of the filtered nonlinear chemical source term. One of the more promising approaches which may be applicable here is the use of the Eddy Dissipation Concept (EDC) of Magnussen (1985) which was recently recast in the context of LES and applied to the two-dimensional simulation of a bluff-body stabilized premixed turbulent flame (Ryden et al., 1994). EDC is a general model for dealing with turbulence-chemistry interactions in flames which models the subgrid reacting turbulence as a perfectly stirred reactor. In doing so EDC arrives at an expression for the filtered reaction rates which involves a choice between the smaller of the Arrhenius controlled reaction rate and turbulent mixing controlled reaction rate. Its implementation does require some information in regard to the local turbulent mixing environment which in the context of the current modeling effort would have to be empirically specified. The incorporation of a detailed turbulent mixing model would not be necessary for providing the type of information desired here but would be imperative if one was interested in predicted the effect of engine transient behavior on pollutant emissions such as NO<sub>x</sub>. This issue is addressed next.

Aside from the above suggested improvements, the code as proposed will be capable of simulating some of the important bulk fluid dynamic-thermochemical interactions which are prevalent during poststall events. In particular the qualitative effect of surge on combustor performance can be nicely captured. One potentially important impact that the ATEC code with the new combustor model can make is in the area of flashback in lean-premixed-prevaporized (LPP) combustor (Lefebvre, 1977). As mentioned, during a surge event bulk engine flow reversals may occur which could lead to flame traveling upstream. A fuel-air premixing section could be added to the engine and the mixture ignited in the main combustion zone. The stability of the flame in response to compressor instabilities could then be studied. This code would provide us with an unique tool to actually install an LPP combustor to an already existing engine, say an F100 turbofan, and consider the effect of its integration and interaction with the rest of the engine. Possible design changes could then be investigated. For example diffuser design modifications in order to quell the effect of off-design compressor airflow could be assessed. There have been some experimental studies to investigate the effects of flow transients on LPP combustion systems (Mularz, 1979). These and other experiments would be useful in validating the current formulation.

## Appendix

### TRANSI Combustor Model

The combustor geometry under consideration in the TRANSI computer code includes a pre-diffuser area followed by a shroud volume. Compressor air enters the pre-diffuser and shroud areas and exits the shroud through two locations. The first exit extracts some air for turbine cooling with the rest going through to the combustor. These different mass flows manifest themselves in a shroud pressure rise that appears to be computed based on a steady Bernoulli's equation. The user may specify time-dependent conditions for inlet total temperature and either inlet total pressure or inlet airflow rate. The combustor receives air from the shroud. Fuel flow is determined by the detailed treatment of the fuel nozzle which will not be discussed here (for more details see Caron, 1991). The heated air leaves the combustor through an outflow which simulates the inlet guide vanes of the turbine and either a choked or subsonic flow condition is specified depending upon the burner pressure to ambient pressure ratio. Again mass flow differences result in a change in combustor pressure. Within the combustor a number of physical processes are modeled by semi-empirical correlations. These are discussed next.

Combustor efficiency in gas turbine combustors is often defined as the ratio of the actual heat released during the combustion process over the maximum amount of heat stored as chemical energy in the fuel. It is important for reasons of fuel economy, low emissions of UHCs and CO, and for engine restart at high altitudes for relight (Lefebvre, 1983). The combustion process occurs mainly in the primary zone of the combustor. This process traditionally depends on the injection of liquid fuel into the region of flame stabilization. After a short time evaporation of the liquid fuel occurs and combustion commences. The key to efficient combustion depends on having sufficient time, temperature and turbulence (as well as pressure) to burn the fuel. Thus the combustor efficiency can be related to the various time scales of these different processes (Lefebvre, 1983).

If one assumes that the process of liquid fuel evaporation and fuel-air turbulent mixing both occur very fast then the combustion efficiency is determined by the airflow rate and the rate of chemical reaction between the fuel and air molecules. Based on the assumption that the primary zone can be modeled as a turbulent flame brush an expression can be derived for combustion efficiency. In this context combustion efficiency is related to the amount of fuel that passes through the flame brush unburnt. The form of the expression as used in the TRANSI code is provided in Clark and Green (1990) and Caron (1991).

For the situation where evaporation and chemical reaction rates are both fast then efficiency depends only of the residence time and the turbulent mixing times. Based on an eddy viscosity concept and simple relations for turbulent velocity and length scale an expression for combustion efficiency can be derived and is given in Caron (1991).

With mixing and reaction rates fast enough the fuel evaporation process will be the key factor controlling combustor efficiency. Based on simple mass transfer relations an expression for combustion efficiency can be derived and the form used in TRANSI is given in Caron (1991).

As a general rule under low pressure conditions evaporation and reaction rates exert the predominant influence whereas under conditions of high pressure mixing is the key influence on combustor efficiency. All three of the above expressions are used in TRANSI in order to compute the combustion efficiency.

Two other key physical processes are also modeled employing semi-empirical relations. These are ignition and flame stabilization. Ignition of a combustible mixture can occur in several ways. A supply of energy, either by an electric spark or by contact with a hot surface, is usually sufficient to achieve ignition of a fuel-air mixture. Spontaneous ignition is also a possibility if the local pressure and temperature are sufficient for autoignition to occur. Spark ignition is the traditional mode for gas turbine combustors. In the TRANSI model autoignition is assumed to occur depending on temperature, pressure and fuel type which together gives an ignition delay time. Based on characteristic time theory this ignition delay time is compared with the primary zone residence time. When the ignition delay time is less than the residence time autoignition is assumed to occur.

The basic principle behind flame stabilization is for the gas velocity to be equal to the flame speed. If the gas velocity is greater than the flame speed the flame will move downstream, a condition often referred to as blowoff. If the gas velocity is less than the flame speed the flame will move upstream, a condition often referred to as flashback (Lefebvre, 1983). Thus it is desired to increase the burning velocity and decrease the main flow velocity. Most primary zones contain some sort of flame holder whose purpose is to create a highly turbulent region where the flow velocity is less than the burning velocity of the mixture. Flame stability in the TRANSI code is determined from a empirical plot of equivalence ratio versus primary zone loading parameter. Thus equivalence ratio is computed based on the air and fuel flow rates and the loading parameter depends on the airflow rate, the pressure and the temperature which gives a measure of primary zone flow velocity. This stability plot determines the maximum airflow rate which can support a stable flame. Beyond this velocity the fresh mixture does not spend enough time in the shear layer to be ignited by the hot recirculation zones. This velocity is often referred to as the blowout velocity. This plot also sets the rich and lean blowout limits. When the flame stability and autoignition criteria are satisfied a flame is assumed to exist.

### References

Bilger, R.W., 'Turbulent Flows with Nonpremixed Reactants', in Turbulent Reacting Flows, eds. Libby, P.A. and Williams, F.A., 44, Springer-Verlag, (1980).

Burwell, A.E. and Patterson, G.T., 'Dynamic Engine Behavior During Post Surge Operation of a Turbofan Engine', AIAA-85-1430, (1985).

Caron, T.J., 'Fuel Effects on Gas Turbine Combustor Dynamics', Pratt & Whitney Final Report for Naval Air Propulsion Center, FR-21669, (1991).

Clark, J. and Green, J., 'Modeling Gas Turbine Combustor Performance Under Transient Conditions', AIAA-90-2161, (1990).

Correa, S.M. and Shyy, W., 'Computational Models and Methods for Continuous Gaseous Turbulent Combustion', *Prog. Energy Combust. Sci.*, **13**, 249-292, (1987).

Davis, M.W., 'A Stage-by-Stage Post-Stall Compression System Modeling Technique: Methodology, Validation, and Application', PhD Dissertation, Virginia Polytechnic Institute and State University, (1986).

Davis, M.W., Personal Communication, (1994).

Frankel, S.H., 'A Second Order Roe Scheme for the Multi-Species Euler Equations with Chemistry', unpublished report, (1991).

Frankel, S.H., 'Large Eddy Simulation of Turbulent Reacting Flow by Assumed PDF Methods', *Fluids Engineering Conference on Engineering Applications of Large Eddy Simulations*, FED 162, 81-101, (1993).

Garrard, D., Personal Communication, (1994).

Gupta, A.K. and Lilley, D.G., 'Combustion and Environmental Challenges for Gas Turbines in the 1990's', *Journal of Propulsion and Power*, **10**, No. 2, 137-147, (1994).

Hale, A.A. and Davis, M.W., 'DYNAMIC Turbine Engine Compressor Code DYNTECC - Theory and Capabilities', AIAA-92-3190, (1992).

Jou, W.H. and Menon, S., 'Numerical Simulation of the Vortex-Acoustic Wave Interaction in a Dump Combustor', AIAA-86-0002, (1986).

Kailasanath, K. and Gardner, J.H. and Boris, J.P., 'Acoustic-Vortex Interactions and Low Frequency Oscillations in Axisymmetric Combustors', AIAA-87-1065, (1985).

Larroutuou, B., 'How to Preserve the Mass Fraction Positivity when Computing Compressible Multi-Component Flows', *Journal of Comput. Phys.*, **95**, 59-84, (1991)

Lefebvre, A.H., 'Lean Premixed/Prevaporized Combustion', NASA CP-2016, (1977).

Lefebvre, A.H., Gas Turbine Combustion, Taylor & Francis, (1983).

Lindau, J.W. and O'Brien, W.F., 'Solution Schemes for Stage by Stage Dynamic Compression System Modeling', AIAA-93-0154, (1993).

Magnussen, B.F., 'Heat Transfer in Gas Turbine Combustors - A Discussion of Mathematical Modeling of Combustion, Heat and Mass Transfer with Emphasis on Heat Transfer in Gas Turbine Combustors', AGARD CP No. 390, *Heat Transfer and Cooling in Gas Turbines*, Paper No. 23, (1985).

Mellor, A.M., 'Gas Turbine Engine Pollution', *Prog. Energy Combust. Sci.*, **1**, 111-133, (1976).

Menon, S. and McMurtry, P.A. and Kerstein, A.K., 'A Linear Eddy Subgrid Model of Turbulent Combustion', in Large Eddy Simulations of Complex Engineering and Geophysical Flows, eds. Galperin, B. and Orszag, S.A., Cambridge University Press, (1994).

Przybylka, S.J., 'Application of System Identification Techniques to Poststall Combustor Dynamics', AIAA-85-1353, (1985).

Rosfjord, T.J., and Haley, J., and Bonnell, J.M., 'Unique Transient Combustor Test Capability', AIAA 88-3197 (1988).

Rizk, N.K. and Mongia, H.C., 'Emissions Predictions of Different Gas Turbine Combustors', AIAA-94-0118, (1994).

Ryden, R., and Eriksson, L., Olovsson, S., 'Large Eddy Simulation of Bluff Body Stabilized Turbulent Premixed Flames', ASME Paper NO. 93-GT-157, presented at the International Gas Turbine and Aeroengine Congress and Exposition, Cincinnati, Ohio, May 24-27, (1993).

Schobeiri, T. and Lippke, C. and Abouelhkeir, M., 'Nonlinear Dynamic Simulation of Single- and Multi-spool Core Engines', AIAA-93-2580, (1993).

Sloan, D.G., and Sturgess, G.J., 'Modeling Local Extinction in Turbulent Flames', ASME Paper NO. 94-GT-433, presented at the International Gas Turbine and Aeroengine Congress and Exposition, The Hague, Netherlands, June 13-16, (1994).

Sterling, J.D. and Zukowski, E.E., 'Longitudinal Mode Combustion Instabilities in a Dump Combustor', AIAA-87-0220, (1987).

Ton, V.T., and Karagozian, A.R., and Marble, F.E. and Osher, S.J. and Engquist, B.E., 'Numerical Simulations of High-Speed Chemically Reacting Flow', *Theoret. Comput. Fluid Dynamics*, **6**, 161-179, (1994).

Westbrook, C.K., and F.L. Dryer, 'Simplified Reaction Mechanisms for the Oxidation of Hydrocarbon Fuels in Flames', *Combust. Sci. Tech.*, **27**, 31-43, (1981).

Winowich, N.S., 'Numerical Prediction of Turbulent Flame Stability in Premixed/Prevaporized (HSCT) Combustors', NASA-CR-188991, (1990).

## Figures

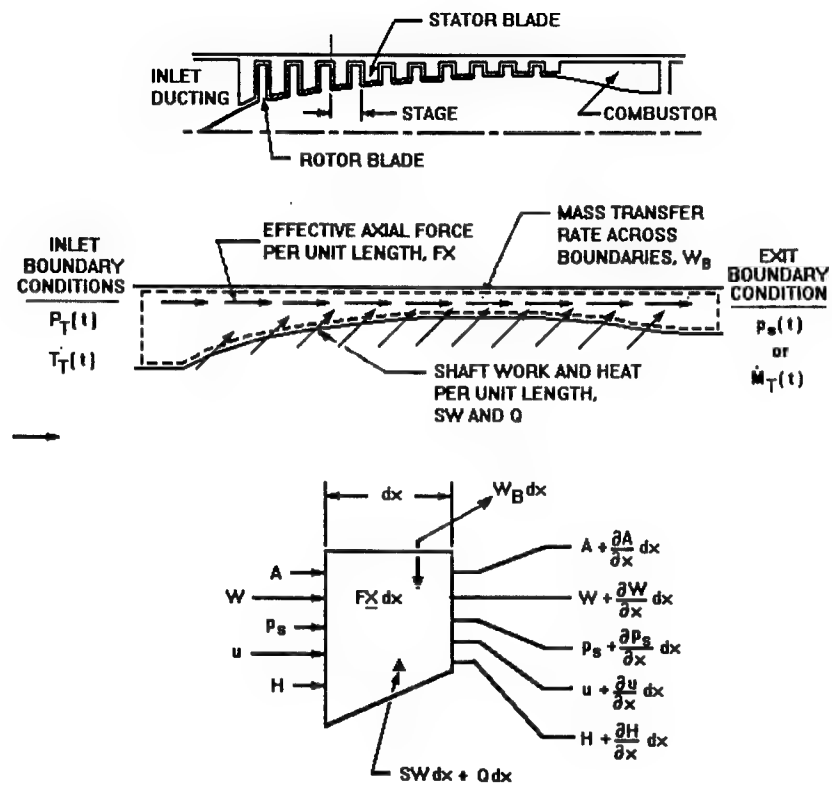


Figure 1: Physical compression system modeled and control volume concept illustrated (used with permission).

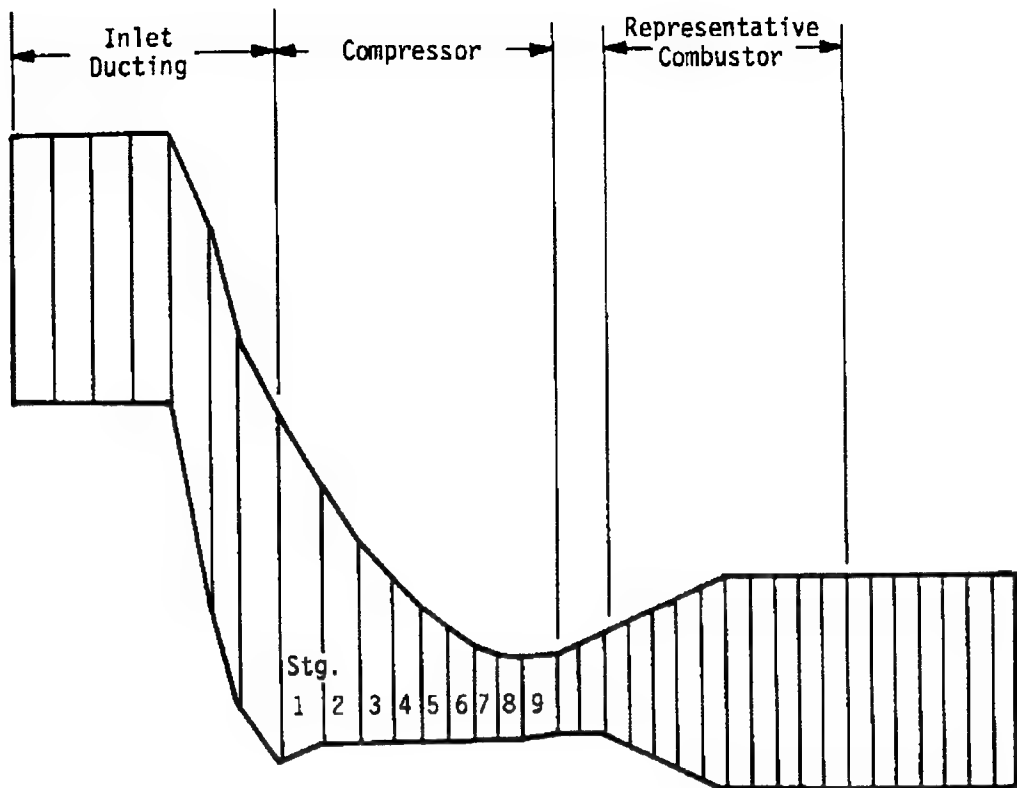


Figure 2: Control volume schematic of nine-stage compressor with representative combustor (used with permission).

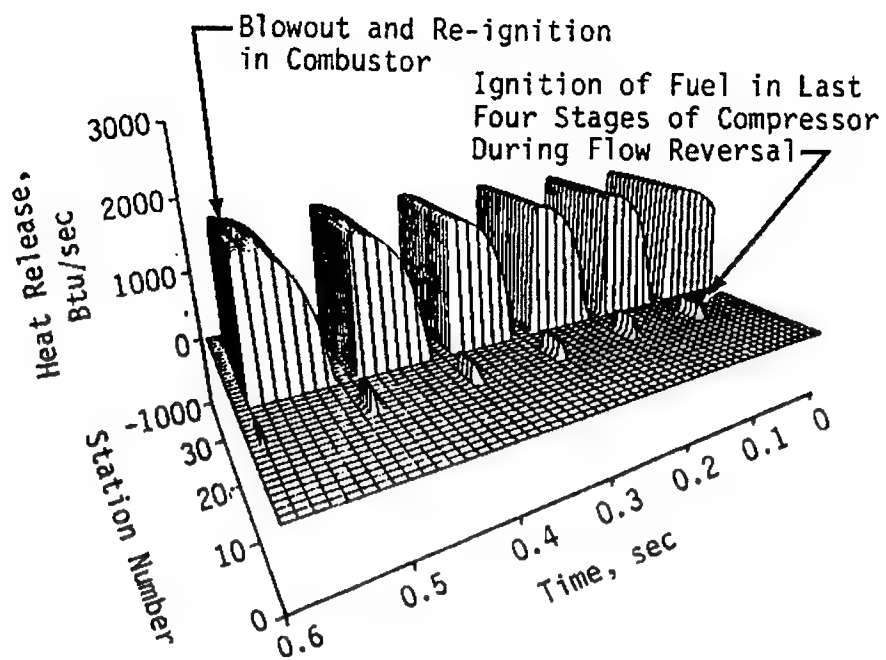


Figure 3: Heat release in the compressor due to 10 percent of the combustor fuel flow being ingested during flow reversal of a surge cycle (used with permission).

**A WAVELET-MULTIGRID APPROACH  
TO SOLVING PARTIAL DIFFERENTIAL EQUATIONS  
BASED ON FRACTAL FUNCTIONS**

**Peter R. Massopust  
Assistant Professor  
Department of Mathematics**

**Sam Houston State University  
Huntsville, Texas 77341**

**Final Report for:  
Summer Faculty Research Program  
Arnold Engineering Development Center**

**Sponsored by:  
Air Force Office of Scientific Research  
Bolling Air Force Base, DC**

**and**

**Arnold Engineering Development Center**

**August 1994**

**A WAVELET-MULTIGRID APPROACH  
TO SOLVING PARTIAL DIFFERENTIAL EQUATIONS  
BASED ON FRACTAL FUNCTIONS**

**Peter R. Massopust  
Assistant Professor  
Department of Mathematics  
Sam Houston State University**

**Abstract**

A Wavelet-Multigrid approach to solving partial differential equations based on fractal functions is presented. The scaling functions and wavelets in this method are piecewise  $C^1$  fractal functions supported on intervals of length at most 1. This new approach is ideal for solving boundary value problems and gives exact formulas for inner products of the form  $\int_{\mathbb{R}} \eta' \eta' dx$ ,  $\int_{\mathbb{R}} \eta \eta' dx$ , and  $\int_{\mathbb{R}} \eta^2 \eta' dx$ , where  $\eta$  represents a fractal scaling function or fractal wavelet. Furthermore, the preconditioner for the algebraic system, derived from the weak formulation of the differential equation, is obtained via a recursive and exact procedure that is based upon properties of the underlying fractal scaling functions and fractal wavelets.

---

A WAVELET-MULTIGRID APPROACH  
TO SOLVING PARTIAL DIFFERENTIAL EQUATIONS  
BASED ON FRACTAL FUNCTIONS

Peter R. Massopust

Introduction

In recent years, wavelets, in particular those constructed by I. Daubechies [5], have been used in Galerkin-type schemes to obtain numerical solutions for partial differential equations. Wavelets yield highly localized bases of approximation spaces for Galerkin methods and their superior approximation properties promise computationally efficient algorithms. There are, however, three important issues that have to be resolved before the Daubechies scaling functions and wavelets can be applied to Galerkin-type methods:

- The scaling functions and wavelets are primarily constructed for functions supported on  $\mathbb{R}$  and their restriction to compact intervals causes “boundary effects”. It is possible to construct wavelets on a compact interval  $I$  but this adds new scaling functions to those already supported on  $I$ . A second approach that avoids boundary effects is based upon periodizing the scaling functions and wavelets. Both methods, however, lead to, for instance, large bandwidths in the stiffness matrix.
- There are no explicit formulas for the scaling functions and wavelets (with the exception of the discontinuous Haar basis). Therefore, integrals of the form  $\int_{\mathbb{R}} \eta \eta' dx$ ,  $\int_{\mathbb{R}} \eta' \eta' dx$ , and  $\int_{\mathbb{R}} \eta^2 \eta' dx$ , where  $\eta$  is either a scaling function or wavelet, have to be evaluated either numerically, or by solving an associated eigenvalue problem that employs the refinement equation for scaling functions and wavelets. In [4], conditions are given under which this latter approach gives unique solutions.
- The stiffness matrix is ill-conditioned. The condition number  $\kappa$  is proportional to  $m \log m$  for a grid of size  $2^{-m}$ . This ill-conditioning is due to the fact that the stiffness matrix resolves *all* the scales. This problem can be overcome by *multilevel preconditioning*. In [3], a multilevel preconditioner is constructed and it is shown that the condition number of the stiffness matrix of the preconditioned algebraic system is asymptotically independent of the mesh size.

We have developed a Wavelet-Multigrid method based upon fractal functions that is, by construction, well-suited for boundary value problems and, using properties of fractal functions, allows the exact evaluation of the aforementioned integrals without any additional conditions. This approach employs the multiresolution analyses constructed in [7,8,9,10]. There, dilation- and translation-invariant subspaces of  $L^2(\mathbb{R})$  were constructed whose elements are piecewise

fractal functions, and in [8] it is shown that there exists a set of fractal scaling functions  $\{\phi^1, \phi^2, \phi^3\}$  and fractal wavelets  $\{\psi^1, \psi^2, \psi^3\}$  with the following properties:

- $D\phi^i$  and  $D\psi^i$  exist on  $\mathbb{R} \setminus \mathbb{Z}/2$ , and  $D^\pm\phi^i$  and  $D^\pm\psi^i$  are bounded on  $\mathbb{Z}/2$ . (Here  $D$  denotes the ordinary derivative and  $D^\pm$  the ordinary right and left derivative, respectively.)
- $\text{supp } \phi^1 = \text{supp } \phi^2 = [0, 1/2]$  and  $\text{supp } \phi^3 = \text{supp } \psi^i = [0, 1]$ ,  $i = 1, 2, 3$ .
- For all  $i, j \in \{1, 2, 3\}$  and  $k, \ell, m, n \in \mathbb{Z}$ :

$$(\phi_{mk}^i, \phi_{m\ell}^j) = \delta_{ij, k\ell}, \quad (\psi_{mk}^i, \psi_{n\ell}^j) = \delta_{ij, k\ell, mn}, \quad (\phi_{mk}^i, \psi_{n\ell}^j) = 0.$$

Here  $(\cdot, \cdot)$  denotes the  $L^2$ -inner product and  $\eta_{m\ell} := 2^{m/2}\eta(2^m \cdot - \ell)$ .

We employed the above fractal scaling functions  $\phi^i$  and wavelets  $\psi^i$ ,  $i = 1, 2, 3$ , to define a multiresolution analysis of  $L^2(I)$  such that

$$V_m := \overline{\text{span} \{ \phi^i(2^m \cdot - \ell_i) : \ell_i \in \Lambda_i, i = 1, 2, 3 \}}^{H_0^1(I)} \subset H_0^1(I),$$

where  $I := [0, 1]$ ,  $\Lambda_1 = \Lambda_2 := \{0, 1, \dots, 3 \cdot 2^{m+1} - 2\}$ ,  $\Lambda_3 := \{0, 1, \dots, 3 \cdot 2^{m+1} - 3\}$ , and  $H_0^1(I)$  is the Sobolev space consisting of all  $L^2$ -functions  $f$  with compact support in  $I$  closed under the norm  $\|f\|_{L^2(\mathbb{R})} + \|f'\|_{L^2(\mathbb{R})}$ . (Here “ $\prime$ ” denotes the weak derivative.) The spaces  $V_m$ ,  $m \in \mathbb{N}$ , are taken as approximation spaces for a Wavelet-Galerkin method. Since the scaling functions  $\phi^i$  and the wavelet  $\psi^i$  are fractal functions, inner products of the type mentioned earlier can be calculated *exactly*! (See Section 2.) We also derived the preconditioner and showed that it can be obtained via a recursive and exact procedure using the properties of the underlying fractal scaling functions and wavelets.

The structure of this report is as follows: Wavelets and some of their properties are presented in Section 1. Because of the limited scope of this report, the interested reader is referred to the references for a more complete introduction to wavelets. In Section 2, we briefly review some of the theory of fractal functions concentrating on the issues that are of importance for our purposes. We again refer to the references for more detail. Section 3 deals with the main issues addressed in this introduction. We present the Wavelet-Multigrid method, derive the preconditioner and discuss our findings.

## Section 1

A finite collection of  $L^2$ -functions  $\psi := \{\psi^j : j = 1, \dots, B\}$ , is called a *wavelet vector* if the two-parameter family  $\{2^{m/2}\psi(2^m \cdot - \ell) : m, \ell \in \mathbb{Z}\}$  forms an orthonormal, or more generally, an unconditional basis of  $L^2(\mathbb{R})$ . One way to construct such a vector wavelet is through multiresolution analysis (see [11]), which consists of a nested sequence  $V_m \subset V_{m+1}$ ,  $m \in \mathbb{Z}$ , of closed subspaces

of  $L^2(\mathbb{R})$  such that the closure of their union is  $L^2(\mathbb{R})$  and their intersection is the trivial subspace  $\{0\}$ . Furthermore, each subspace  $V_m$  is spanned by the dyadic dilates and integer translates of a finite set of *scaling functions*, sometimes also called the generators of the multiresolution analysis. Typically, this scaling vector  $\phi := \{\phi^i : i = 1, \dots, A\}$  has compact support or decays rapidly enough at infinity. The condition that the spaces  $V_m$  be nested implies that the scaling vector  $\phi$  satisfies the following *two-scale matrix dilation equation* or *matrix refinement equation*

$$\phi(x) = \sum_{i=1}^A \sum_{\ell \in \mathbb{Z}} C_\ell \phi(2x - \ell), \quad (1)$$

where the  $\{C_\ell\}_{\ell \in \mathbb{Z}}$  are  $A \times A$  matrices satisfying  $\sum_{\ell \in \mathbb{Z}} \|C_\ell\|_{\ell^2(\mathbb{R}^A)} < \infty$ . If the  $L^2$ -orthogonal complement of  $V_m$  in  $V_{m+1}$  is denoted by  $W_{m+1}$ , then there exists a wavelet vector  $\psi$  such that  $W_{m+1}$  is spanned by the dyadic dilates and integer translates of  $\psi$ . Moreover, the wavelet vector satisfies a two-scale matrix dilation equation of the form

$$\psi(x) = \sum_{j=1}^A \sum_{\ell \in \mathbb{Z}} D_\ell \phi(2x - \ell), \quad (2)$$

where the  $A \times A$  matrices  $\{D_\ell\}_{\ell \in \mathbb{Z}}$  are in  $\ell^2(\mathbb{R}^A)$ . (Since we consider dyadic dilates, the number of scaling functions equals the number of wavelets.) Since  $V_{m+1} = V_m \oplus W_{m+1}$ , every function  $f_{m+1} \in V_{m+1}$  can be *decomposed* into an “averaged” or “blurred” component  $f_m \in V_m$  and a “difference” or “fine-structure” component  $g_{m+1} \in W_{m+1}$ :

$$f_{m+1} = f_m + g_{m+1}.$$

This decomposition can be continued until  $f_{m+1}$  is decomposed into a coarsest component  $f_0$  and  $m$  difference components  $g_k$ ,  $k = 1, \dots, m+1$ :

$$f_{m+1} = f_0 + g_1 + \dots + g_m + g_{m+1}. \quad (3)$$

This *decomposition algorithm* can be reversed to give a *reconstruction algorithm*: Given the coarse components together with the fine structure components one reconstructs any  $f_m \in V_m$  via reversal of Eqn. 3. Let us note that both algorithms are usually applied to the expansion coefficients (in terms of the underlying basis) of  $f$  and  $g$  and that they involve the matrices  $C_\ell$  and  $D_\ell$ . The reader is referred to the references for more details.

Scaling vectors and vector wavelets are to satisfy three conditions:

1. Both  $\phi$  and  $\psi$  should have compact support. (This implies that the sums in Eqns. 1 and 2 are finite).

2. The scaling and wavelet vectors should be fully  $L^2$ -orthogonal in the following sense:

$$\begin{aligned} (\phi(2^m \cdot -k), \phi(2^m \cdot -\ell)) &= \delta_{k\ell} I_A, \\ (\psi(2^m \cdot -k), \psi(2^m \cdot -\ell)) &= \delta_{mn, k\ell} I_A, \\ (\phi(2^m \cdot -k), \psi(2^m \cdot -\ell)) &= O_A, \end{aligned} \quad (4)$$

where  $I_A$  and  $O_A$  denotes the  $A \times A$  identity and zero matrix, respectively. (This guarantees that the reconstruction and the decomposition algorithm is finite.)

3. The scaling vector and thus the wavelet vector should have a certain degree of smoothness. (For second order boundary values it suffices for  $\phi$  to in  $BV$  or  $H^1$ .)

It was shown in [9] that the preceding three conditions imply

$$\phi(2^m x - \ell) = \sum_{\ell'} C_{\ell-2\ell'}^\dagger \phi(2^{m-1} x - \ell') + D_{\ell-2\ell'}^\dagger \psi(2^{m-1} x - \ell'). \quad (5)$$

(Here  $\dagger$  denotes the Hermitian conjugate.) If we define

$$\begin{aligned} \Phi_m &:= (\phi^1(2^m \cdot), \phi^1(2^m \cdot -1), \dots, \phi^1(2^m \cdot -2^m + 1), \phi^2(2^m \cdot), \\ &\dots, \phi^2(2^m \cdot -2^m + 1), \dots, \phi^A(2^m \cdot), \dots, \phi^A(2^m \cdot -2^m + 1))^t, \end{aligned} \quad (6)$$

with  $t$  denoting the transpose, and in a similar fashion  $\Psi_m$  and  $\Phi_{m-1}$ , then the preceding equation can be written in a more compact form:

$$\Phi_m = L_m \begin{pmatrix} \Phi_{m-1} \\ \Psi_m \end{pmatrix}, \quad (7)$$

where  $L_m$  is the  $A \cdot 2^m \times A \cdot 2^m$  matrix whose entries are given by

$$(L_m)_{i(\ell+1), \ell'+1+(j-1)2^{m-1}} = (K_{\ell-2\ell'}^\dagger)_{ij}, \quad (8)$$

with  $i = 1, \dots, A$ ;  $j = 1, \dots, 2A$ ;  $\ell' = 0, 1, \dots, 2^{m-1} - 1$ ;  $\ell = 0, 1, \dots, 2^m - 1$ , and

$$(K_\alpha^\dagger)_{ij} := \begin{cases} (C_\alpha^\dagger)_{ij} & j = 1, \dots, A \\ (D_\alpha^\dagger)_{ij} & j = A + 1, \dots, 2A. \end{cases}$$

We will encounter Eqn. 8 again in Section 3 where the preconditioner is constructed.

## Section 2

In this section we briefly introduce fractal functions and indicate how they can be used to construct multiresolution analyses of  $L^2(\mathbb{R})$  and  $L^2(I)$ .

Throughout this section,  $N$  denotes an integer greater than 1 and  $s$  a real number in  $(-1, 1)$ .

Fractal (interpolation) functions were first constructed in [1]. The graph of such a function is made up of a finite number of images of itself. For example, if we work on  $I := [0, 1]$  with given interpolation points  $(0, y_0)$ ,  $(1/2, y_1)$ , and  $(1, y_2)$ , then we define a fractal function as follows: Let  $(C^*(I), \|\cdot\|_\infty)$  denote the Banach space of all continuous functions passing through the preceding set of interpolation points endowed with the sup-norm. Define the contractive operator  $T$  on  $C^*(I)$  by

$$Tf(x) := \lambda_i \circ u_i^{-1}(x) + sf \circ u_i^{-1}(x), \quad (9)$$

for all  $x \in u_i(I)$ ,  $i = 1, 2$ . Here  $u_i(x) := (x + i - 1)/2$  and  $\lambda_i(x) := a_i x + b_i$  is chosen so that  $Tf(0) = y_0$ ,  $Tf(1/2) = y_1$ , and  $Tf(1) = y_2$ , whenever  $f(0) = y_0$ ,  $f(1/2) = y_1$ , and  $f(1) = y_2$ . The fixed point  $f^*$  of  $T$  is continuous and passes through the given interpolation points, and is called a *fractal (interpolation) function*. Let  $w_i(x, y) := (u_i(x), \lambda_i(x))$ . Then the graph  $G^*$  of  $f^*$  satisfies  $G^* = w_1 G^* \cup w_2 G^*$ . Let us note that this is not the most general construction of a fractal function. We refer the interested reader to [12] for more detail. Furthermore, the functions  $\lambda_i$  need not be affine. As a matter of fact, for our Wavelet-Multigrid method we need them to be quadratic functions. Choosing the  $\lambda_i$  to be quadratic functions and  $|s| < 1/2$  guarantees that the fixed point  $f^*$  of  $T$  is  $C^1$ . We also note that the fixed point equation for  $f^*$  can be written as a *nonhomogenous two-scale dilation equation*:

$$f^*(x) = \lambda(x) + \sum_{\ell} s f(2x - \ell), \quad (10)$$

with

$$\lambda(x) := \begin{cases} \lambda_1(x) & 0 \leq x < 1/2, \\ \lambda_2(x) & 1/2 \leq x \leq 1 \end{cases}$$

For our purposes, the most important characteristic of fractal functions is that  $f^*(\cdot/2)$  restricted to  $I$  is also a fractal function. Just as polynomials are pieced together to form splines, these fractal functions can be pieced together to generate a linear space  $V_0$  of continuous piecewise fractal functions with integer knots such that if  $f \in V_0$ , then both  $f(\cdot/2)$  and  $f(\cdot + 1)$  are also in  $V_0$  (see Fig. 1). The space  $V_0$  is spanned by the integer translates of a finite number of scaling functions  $\{\phi^1, \dots, \phi^4\}$ . The space  $V_0$  depends on the free parameter  $s$  and can be thought of as a parametrized spline space. It can be shown (see [7,8,9,10]) that for a proper choice of  $s$  a scaling vector  $\phi$  and an associated vector wavelet  $\psi$  can be constructed so that the aforementioned properties 1, 2, and 3 are satisfied. As mentioned in the Introduction, one can even construct a compactly supported, piecewise  $C^1$  scaling vector  $\phi$  and associated wavelet vector  $\psi$  that are fully orthogonal. In Figs. 2 and 3 the graphs of the three scaling functions and the three associated wavelets are shown. The value for

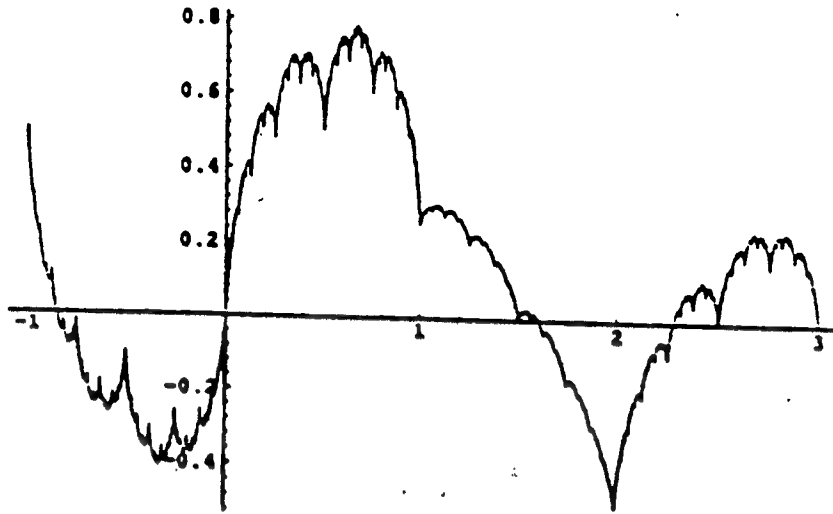


Figure 1: A piecewise fractal function

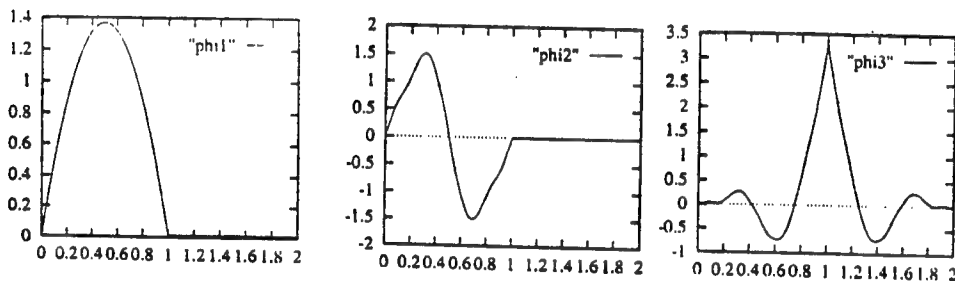


Figure 2: Piecewise  $C^1$  fractal scaling functions

$s$  in this case is given by  $(2 - \sqrt{10})/6$ . By their construction, fractal scaling functions and fractal wavelets can be used to define multiresolution analyses of  $L^2(I)$ . The procedure is as follows: Let  $\tilde{V}_m := V_m \cap L^2(I)$  and  $\tilde{W}_m := W_m \cap L^2(I)$ . If we set  $\tilde{\phi}_{ml}^i := \phi_{ml}^i|_I$  and  $\tilde{\psi}_{ml}^i := \psi_{ml}^i|_I$ , then  $\{\tilde{\phi}_{ml}^i : i = 1, \dots, A; m \in \mathbb{N} \cup \{0\}; -i \leq l \leq 2^m - 1\}$  is an orthonormal basis for  $\tilde{V}_m$  and  $\{\tilde{\psi}_{ml}^i : i = 1, \dots, A; m \in \mathbb{N}; i-1 \leq l \leq 2^{m-1} - (i+1)\}$  is an orthonormal basis for  $\tilde{W}_m$ . Moreover,

$$L^2(I) = \bigoplus_{m \in \mathbb{N}} \tilde{W}_m.$$

Employing essentially the same strategy one can assure that all the approximation spaces  $V_m$  are in  $H_0^1(I)$ : All those functions in  $V_m$  that are not in  $H_0^1(I)$  are deleted. For the piecewise  $C^1$  scaling functions and wavelets mentioned earlier, we obtain the following bases for  $V_m$ : (In order to ease notation we will from

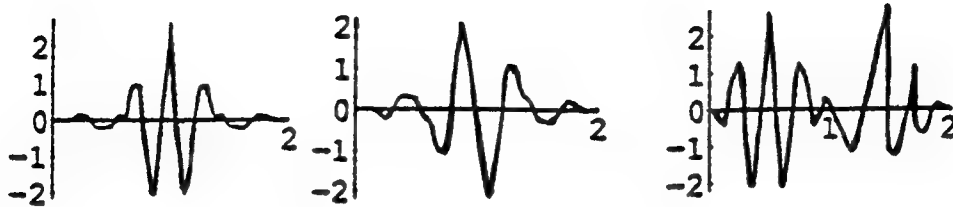


Figure 3: The associated wavelets

now on omit the  $\sim$  from the spaces  $V_m$  and  $W_m$  since our emphasis is entirely on a multiresolution analysis of  $L^2(I)$ .)

$$V_0 = \overline{\text{span}\{\phi^1(x), \phi^1(x-1), \phi^2(x), \phi^2(x-1), \phi^3(x)\}}^{H_0^1(I)} \subset H_0^1(I). \quad (11)$$

For general  $m \in \mathbb{N}$ , the spaces  $V_m$  were already given in the Introduction. Since  $V_m$  contains the piecewise quadratic functions  $\phi^1(2^m \cdot -\ell_1)$  and since these functions are dense in  $H_0^1$ , it follows immediately that

$$\overline{\bigcup_{m=0}^{\infty} V_m}^{H_0^1(I)} = H_0^1(I). \quad (12)$$

Since there are  $3 \cdot 2^{m+1} - 1$  scaling functions in  $V_m$ , there are  $3 \cdot 2^{m+1}$  wavelets in  $W_{m+1}$ . The six wavelets in  $W_1$  are:  $\psi^i(x), \psi^i(x+1)|_I + \psi^i(x-1)|_I$ ,  $i = 1, 2, 3$ . The basis for  $W_m$  then consists of the dilates and appropriate integer translates of these six wavelets.

For our later purposes we need the following results from the theory of fractal functions (see, for instance, [12]).

**Theorem 1** *Let  $f$  be a fractal function supported on  $I = [0, 1]$  generated by the two maps  $\lambda_1$  and  $\lambda_2$ . Let  $p \in \mathbb{N} \cup \{0\}$ . Then the moment  $\int_I x^p f(x) dx$  can be recursively and explicitly calculated in terms of the lower order moments:*

$$\int_I x^p f(x) dx = \frac{\int_I [x^p \lambda_1(x) + (x+1)^p \lambda_2(x)] dx + s \sum_{q=0}^{p-1} \binom{p}{q} \int_I x^q f(x) dx}{2(2^p - s)}. \quad (13)$$

**Theorem 2** *Let  $f$  and  $g$  be two fractal functions generated by  $\lambda_i$  and  $\mu_i$ ,*

$i = 1, 2$ , respectively. Then the  $L^2$ -inner product  $(f, g)$  is given by

$$(f, g) = \frac{\sum_i (\lambda_i, \mu_i) + s[(\lambda_i, g) + (\mu_i, f)]}{2(1 - s^2)}. \quad (14)$$

If  $f$  and  $g$  are in  $H^1$ , then

$$(f', g') = \frac{2 \sum_i (\lambda'_i, \mu'_i) + s[(\lambda'_i, g') + (\mu'_i, f')]}{1 - 4s^2}. \quad (15)$$

Note that, if  $\lambda_i$  and  $\mu_i$ ,  $i = 1, 2$ , are polynomials, then the  $L^2$ -inner product between fractal functions  $f$  and  $g$  is given in terms of the moments of  $f$  and  $g$ . In our Wavelet-Multigrid Method, the scaling functions  $\phi^i$ ,  $i = 1, 2, 3$ , are generated by quadratic  $\lambda$ 's and, thus, any  $L^2$ -inner product between these scaling functions and their derivatives can be explicitly and recursively calculated. This produces exact answers for the inner products appearing in the weak formulation of the differential equation. More precisely, the scaling functions  $\phi^i$  are generated by the following maps:

$$\begin{aligned} \phi^1 : \quad & \lambda_1^1(x) = (1/2 - s)x + (s - 1/4)x^2, \\ & \lambda_2^1(x) = 1/4 - sx + (s - 1/4)x^2, \\ \phi^2 : \quad & \lambda_1^2(x) = (1/2 - s)x + (s - 1/2)x^2, \\ & \lambda_2^2(x) = (s - 1/2)x + (1/2 - s)x^2, \\ \phi^3|_{[0,1/2]} : \quad & \lambda_1^3(x) = \alpha(1/2 - s)x + [1/2 - (3\alpha + \beta)/8 + (\alpha - 1)s]x^2, \\ & \lambda_2^3(x) = (4 + \alpha - \beta)/8 + [1 - (\alpha + \beta)/4 + (\beta - 2)s]x \\ & \quad + [-1/2 + (\alpha + 3\beta)/8 + (1 - \beta)s]x^2, \\ \phi^3|_{[1/2,1]} : \quad & \lambda_1^4(x) = (1 - s) + \beta(s - 1/2)x \\ & \quad + [-1/2 + (\alpha + 3\beta)/8 + (1 - \beta)s]x^2, \\ & \lambda_2^4(x) = (4 + \alpha - \beta)/8 - s + [-1 + (\alpha + \beta)/4 + (2 - \alpha)s]x \\ & \quad + [(1/2 - (3\alpha + \beta)/8 + (\alpha - 1)s]x^2, \end{aligned}$$

where  $\alpha := (\sqrt{10} - 3)/2$  and  $\beta := (7 + \sqrt{10})/2$ . Using Theorems 1 and 2, one can easily obtain the following  $L^2$ -inner products between the scaling functions:

$$\begin{aligned} (\phi^{1'}, \phi^{1'}) &= (20 - 7\sqrt{10})/3, & (\phi^{1'}, \phi_1^{1'}) &= 0, \\ (\phi^{1'}, \phi^{2'}) &= 0, & (\phi^{1'}, \phi_1^{2'}) &= 0, \\ (\phi^{1'}, \phi^{3'}) &= -5(10\sqrt{2} + 7\sqrt{5})/3, & (\phi_1^{1'}, \phi_1^{1'}) &= (\phi^{1'}, \phi^{1''}), \\ (\phi_1^{1'}, \phi^{2'}) &= 0, & (\phi_1^{1'}, \phi_1^{2'}) &= 0, \\ (\phi_1^{1'}, \phi^{3'}) &= -(\phi^{1'}, \phi^{3'}) & (\phi^{2'}, \phi^{2'}) &= 4(5 + \sqrt{10}), \\ (\phi^{2'}, \phi_1^{2'}) &= 0, & (\phi^{2'}, \phi^{3'}) &= 3^8\sqrt{30}(4 + \sqrt{10})/\gamma, \\ (\phi_1^{2'}, \phi_1^{2'}) &= (\phi^{2'}, \phi^{2'}), & (\phi_1^{2'}, \phi^{3'}) &= -(\phi^{2'}, \phi^{3'}), \\ (\phi^{3'}, \phi^{3'}) &= 43\,046\,721(1160 + 367\sqrt{10})/(10\gamma^2), \end{aligned}$$

where

$$\gamma := \sqrt{10615782653 - 3334494410\sqrt{10}}.$$

Nonlinearities of polynomial type or polynomial coefficients in differential operators lead to triple  $L^2$ -inner products of the form  $\int_I f g h dx$ , where  $f$ ,  $g$ , and  $h$  are fractal functions. The next theorem shows that these triple inner product can also be calculated exactly.

**Theorem 3** Suppose that  $f$ ,  $g$ , and  $h$  are fractal functions, generated by polynomial maps  $\lambda_i$ ,  $\mu_i$ , and  $\nu_i$ , respectively. Then

$$\begin{aligned} (f g, h) = & \frac{1}{2} \sum_i \{(\lambda_i \mu_i, \nu_i) + s[(\lambda_i \mu_i, h) + (\lambda_i \nu_i, g) + (\mu_i \nu_i, f)] \\ & + s^2[(\lambda_i, g h) + (\mu_i, f h) + (\nu_i, f g)]\}, \end{aligned} \quad (16)$$

where inner products of the form  $(\lambda_i, g h)$  are given by

$$(\lambda_i, g h) = \frac{\sum_i \{(\tilde{\lambda}_i, \mu_i \nu_i) + s[(\tilde{\lambda}_i \mu_i, h) + (\tilde{\lambda}_i \nu_i, h)]\}}{2(1 - s^2)}. \quad (17)$$

The coefficients in the polynomials  $\tilde{\lambda}_i(x) = \sum_{j=0}^d \tilde{b}_j^i x^j$  are related to the coefficients of the polynomials  $\lambda_i(x) = \sum_{j=0}^d b_j^i x^j$  via

$$b_j^i = \tilde{b}_j^i - \sum_i \sum_{k=0}^{d-j} \binom{j+k}{k} \frac{\tilde{b}_{j+k}}{2^{j+k}} i^k. \quad (18)$$

Finally, let us remark that the matrices  $C_\ell$  and  $D_\ell$  in the two-scale dilation equations satisfied by  $\phi^i$  and  $\psi^i$ ,  $i = 1, 2, 3$ , are known exactly.

### Section 3

In this section we introduce our Wavelet-Multigrid method, derive the preconditioner and briefly discuss our findings.

Suppose that  $L$  is a self-adjoint elliptic differential operator of even degree. We are interested in solving the Dirichlet problem

$$Lu = f \quad \text{on } (0, 1), \quad u(0) = u(1) = 0, \quad (19)$$

where  $f \in L^2(I)$ . The weak formulation of Eqn. 19 is to find a  $u \in H_0^1(I)$  so that

$$B(u, v) = (f, v), \quad v \in H_0^1(I). \quad (20)$$

Here,  $B(u, v)$  is the bilinear form induced by  $L$ :  $B(u, v) = (L^{1/2}u, L^{1/2}v)$ . The finite-dimensional spaces  $V_m$  defined earlier are used to define a Galerkin method for the Dirichlet problem Eqn. 19. To this end, let

$$u_m^n := u^n|_{V_m}, \quad m \in \mathbb{N}_0,$$

i.e., for a set of constants  $\{a_{m;\ell_i}^n : m, n \in \mathbb{N}_0; \ell_i \in \Lambda_i; i = 1, 2, 3\}$ , where  $\Lambda_1 = \Lambda_2 = \{0, 1, \dots, 3 \cdot 2^{m+1} - 1\}$  and  $\Lambda_3 = \{0, 1, \dots, 3 \cdot 2^{m+1} - 2\}$ , we set

$$u_m^n = \sum_{i=1}^3 a_{m;\ell_i}^n \phi^i(2^m \cdot -\ell_i), \quad (21)$$

or, using Eqn. 6,

$$u_m = \mathbf{a}^t \Phi_m. \quad (22)$$

By definition of  $V_m$ ,  $\lim_{m \rightarrow \infty} u_m = u$  (in the norm of  $H_0^1(I)$ ). Substituting Eqn. 22 into Eqn. 20 we obtain

$$D_m \mathbf{a}_m = \mathbf{f}_m, \quad (23)$$

where  $D_m$  is a positive definite self-adjoint operator and where we set

$$\mathbf{f}_m := ((f, \phi^1), (f, \phi_1^1), \dots, (f, \phi_{2^{m+1}-1}^1), (f, \phi^2), \dots, (f, \phi_{2^{m+1}-2}^3))^t.$$

In the case where  $L := -\frac{\partial^2}{\partial x^2} + \sigma$ ,  $\sigma > 0$ , the preceding equation becomes

$$(D_m + \sigma I) \mathbf{a}_m = \mathbf{f}_m,$$

and the  $(3 \cdot 2^{m+1} - 1) \times (3 \cdot 2^{m+1} - 1)$  matrix  $D_m$ , the stiffness matrix, is given by

$$D_m := \begin{pmatrix} D_{11} & D_{12} & D_{13} \\ D_{12} & D_{22} & D_{23} \\ D_{13} & D_{23} & D_{33} \end{pmatrix},$$

where

$$D_{ij} = \text{diag}((\phi^{i'}, \phi^{j'})), \quad i, j = 1, 2,$$

$$D_{i3} = \begin{pmatrix} (\phi^{i'}, \phi^{3'}) & \phi_1^{i'}, \phi^{3'} & 0 & \dots & 0 \\ 0 & (\phi^{i'}, \phi^{3'}) & \phi_1^{i'}, \phi^{3'} & \ddots & \vdots \\ \vdots & 0 & \ddots & \ddots & 0 \\ \vdots & & \ddots & \ddots & (\phi_1^{i'}, \phi^{3'}) \\ 0 & \dots & \dots & 0 & (\phi^{i'}, \phi^{3'}) \end{pmatrix},$$

and similarly for  $D_{3j}$ . The matrices  $D_{ij}$ ,  $i, j = 1, 2$ , are of size  $2^{m+1} \times 2^{m+1}$ , whereas the matrices  $D_{i3}$  and  $D_{3j}$  are of size  $(2^{m+1} - 1) \times (2^{m+1} - 1)$ . The entries in the preceding matrices can be calculated exactly using Theorems 1 and 2.

**Remark.** Even when the coefficient functions in the differential operator  $L$  are polynomials, the inner products in  $B(u, v) = (D_m, v)$  can be calculated exactly using Theorems 1 and 2.

An equation like 23 is usually solved by means of an iteration of the form

$$\mathbf{a}_m^k := (I - \omega C_m D_m) \mathbf{a}_m^{k-1} + \omega C_m f_m, \quad k \in \mathbb{N}, \quad (24)$$

with some relaxation parameter  $\omega \in (0, 1)$  and a preconditioner  $C_m$ . It is shown in [3] that the preconditioner for a Wavelet-Galerkin method is obtained as follows: Consider the basis  $\mathcal{B}_m := \{\Phi_m : m \in \mathbb{N}_0\}$  of  $V_m$  and let  $L_m$  be the operator that takes  $\mathcal{B}_m$  onto the basis  $\mathcal{B}_{m-1} := \{(\Phi_{m-1}, \Psi_m) : m \in \mathbb{N}\}$  of  $V_{m-1} \oplus W_m$ . (Compare with Eqn. 8 !) The preconditioner  $C_m$  is then given by

$$C_m = L_m^2 (L_m^t)^2. \quad (25)$$

If one would like to relax on more than one level, the preconditioner has to be a product of operators of the preceding form. More precisely, consider

$$\Phi_m = L_m^{(1)} \begin{pmatrix} \Phi_{m-1} \\ \Psi_m \end{pmatrix},$$

and, analogously,

$$\Phi_{m-1} = L_{m-1}^{(1)} \begin{pmatrix} \Phi_{m-2} \\ \Psi_{m-1} \end{pmatrix}.$$

Then,

$$\begin{pmatrix} \Phi_{m-1} \\ \Psi_m \end{pmatrix} = \begin{pmatrix} L_{m-1}^{(1)} & 0 \\ 0 & I \end{pmatrix} \begin{pmatrix} \Phi_{m-2} \\ \Psi_{m-1} \end{pmatrix},$$

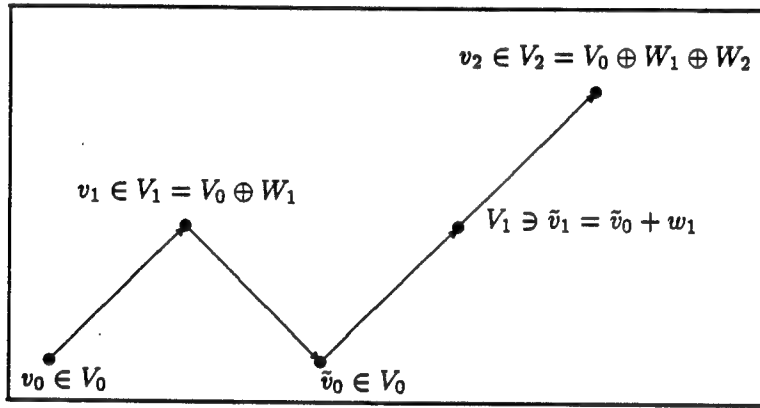
and, if we denote the above matrix by  $L_m^{(2)}$ , we have the preconditioner for going from  $V_m$  to  $V_{m-2} \oplus W_{m-1} \oplus W_m$

$$\Phi_m = L_m^{(1)} L_m^{(2)} \begin{pmatrix} \Phi_{m-2} \\ \Psi_{m-1} \\ \Psi_m \end{pmatrix}.$$

Hence, if we resolve all the levels, we obtain

$$\begin{aligned} \Phi_m &= L_m^{(1)} L_m^{(2)} \dots L_m^{(m)} \begin{pmatrix} \Phi_0 \\ \Psi_1 \\ \Psi_2 \\ \vdots \\ \Psi_m \end{pmatrix}, \quad m \in \mathbb{N}, \\ &\in V_m \quad \in V_0 \oplus \bigoplus_{j=1}^m W_j \end{aligned} \quad (26)$$

Next, we show the structure of the preconditioner when a full multigrid cycle is used to obtain successively better approximations to  $u_m$ . The figure below shows part of a typical full multigrid cycle. With each approximation space  $V_m$  we associate a grid  $G_m := \mathbb{Z}/2^m \mathbb{Z}$ ,  $m \in \mathbb{N}_0$ . Related to this multigrid cycle are the following mappings: An injection mapping  $j_m : V_m \rightarrow V_{m+1}$ ,  $v_m \mapsto j(v_m)$ , a decomposition mapping  $p_m : V_{m+1} \rightarrow V_m$ ,  $v_{m+1} = v_m + w_{m+1} \mapsto v_m$ , and a reconstruction mapping  $r_m : (V_m, W_{m+1}) \rightarrow V_{m+1}$ ,  $(v_m, w_{m+1}) \mapsto v_m + w_{m+1}$ .



The space  $V_0$  corresponds to the coarsest grid  $G_0$ . On this grid an initial guess solution  $v_0$  is relaxed (employing Eqn. 24 with  $m = 0$ ). Using the injection mapping  $j_0$ , the relaxed solution, which we again denote by  $v_0$ , is embedded into  $V_1$ . On the grid  $G_1$  the system in Eqn. 24 (with  $m = 1$ ) is relaxed and the thus-obtained approximate solution  $v_1$  projected onto  $V_0$ . Let  $\tilde{v}_0 := p_1(v_1)$ . We again relax on the grid  $G_0$  producing an up-dated solution. To ease notation, we denote this solution again by  $\tilde{v}_0$ . Now we reconstruct to get  $\tilde{v}_1 := r_1(\tilde{v}_0, w_1)$ , where  $w_1 := v_1 - \tilde{v}_0$ . Preconditioning and relaxing on the grid  $G_1$  produces an up-dated solution to  $\tilde{v}_1$  which is via  $j_2$  embedded into  $V_2$ . On the corresponding grid we precondition and relax again to obtain  $v_2$ . The multigrid cycle now continues, proceeding in a completely analogous fashion, until a predetermined finest level is reached. The solution on this grid is then the sought-after approximation for  $u_m$ .

Finally, let us present the structure of the matrices  $L_m$  used to define the preconditioner  $C_m$ . To this end, consider the equation

$$\Phi_1 = \begin{pmatrix} C_U^{(1)} & D_U^{(1)} \\ C_L^{(1)} & D_L^{(1)} \end{pmatrix} \begin{pmatrix} \Phi_0 \\ \Psi_1 \end{pmatrix}. \quad (27)$$

The  $11 \times 11$  matrix in the preceding expression is known explicitly from Eqn. 7 (with  $m = 1$ ) and was divided into the  $5 \times 5$  matrix  $C_U^{(1)}$ , the  $5 \times 6$  matrix  $D_U^{(1)}$ , the  $6 \times 5$  matrix  $G_L^{(1)}$ , and the  $6 \times 6$  matrix  $D_L^{(1)}$ . It is clear from earlier

arguments that the matrix in Eqn. 27 is nothing but the matrix  $L_1 = L_1^{(1)}$ . Moreover,

$$L_2 = L_2^{(1)} L_2^{(2)} = \begin{pmatrix} C_U^{(2)} & D_U^{(2)} \\ C_L^{(2)} & D_L^{(2)} \end{pmatrix} \begin{pmatrix} L_1 & 0 \\ 0 & I \end{pmatrix},$$

or,

$$L_2 = \begin{pmatrix} C_U^{(2)} L_1 & D_U^{(2)} \\ C_L^{(2)} L_1 & D_L^{(2)} \end{pmatrix},$$

and, thus, in general,

$$L_{m+1} = \begin{pmatrix} C_U^{(m+1)} L_m & D_U^{(m+1)} \\ C_L^{(m+1)} L_m & D_L^{(m+1)} \end{pmatrix}, \quad m \in \mathbb{N}. \quad (28)$$

Since the matrices

$$\begin{pmatrix} C_U^{(m)} & D_U^{(m)} \\ C_L^{(m)} & D_L^{(1)} \end{pmatrix}$$

are the matrices in Eqn. 5, they can be obtained from  $L_1$  by insertion of zeros and shifting of row blocks and are, therefore, very sparse. (The structure of these matrices is essentially contained in Eqn. 5.)

**Remark.** The Wavelet-Multigrid method described above is also well-suited for nonlinear problems such as the one-dimensional Burgers' Equation

$$\frac{\partial u}{\partial t} = -u \frac{\partial u}{\partial x} + \sigma \frac{\partial^2 u}{\partial x^2}, \quad (29)$$

together with appropriate boundary and/or initial conditions. We like to find a weak solution in some subspace  $H_*^1(I)$  of  $H^1(I)$ . Using an explicit time discretization scheme, Eqn. 29 gives

$$\frac{u^{n+1} - u^n}{\Delta t} = -u^{n+1} \frac{\partial u^n}{\partial x} + \sigma \frac{\partial^2 u^{n+1}}{\partial x^2}, \quad (30)$$

where  $n \in \mathbb{N}_0$ ,  $u^n(x) := u(n\Delta t, x)$ , and  $\Delta t > 0$ . Employing the preceding scaling functions  $\phi^i$  and wavelets  $\psi^i$  but with the spaces  $V_m$  now in  $H_*^1(I)$ , we determine, for a fixed  $n$  and  $k$ , a solution  $u_m^{n,k} := u^{n,k}|_{V_m}$  by iterating the system

$$a_m^{n,k+1} = a_m^{n,k} - \omega C_m \mathbf{R}_m^{n,k}, \quad (31)$$

where  $a_m^{n,k}$  are the expansion coefficients of  $u_m^n$  in terms of the basis of  $V_m$ ,  $C_m$  is the preconditioner described earlier, and  $\mathbf{R}_m^{n,k}$  is the residual of Eqn. 30. Under the assumption that the spectral radius of  $I - \omega C_m \partial \mathbf{R}_m^{n,k} / \partial u_m^{n,k}$  is less than 1, we have the following convergence results:

$$u^{n+1} = \lim_{k \rightarrow \infty} u^{n,k} \quad \text{and} \quad u^{n,k} = \lim_{m \rightarrow \infty} u_m^{n,k}.$$

Notice that the weak formulation of Eqn. 30 contains the symmetric quadratic form  $\mathbf{Q}(\mathbf{a}_m^{n,k}) = (Q_{il} : i = 1, 2, 3; l = 0, 1, \dots, 3 \cdot 2^{m+1} - 1)$  with

$$Q_{il} := \sum_{p,q=1}^3 (\phi^p \phi^q, \phi^{i'}) a_{m;p\ell}^{n,k}, a_{m;q\ell_q}^{n,k},$$

with  $\ell_i \in \Lambda_i$ . The inner product in this quadratic form can again be calculated exactly using Theorem 3.

### Summary

We have developed a new Wavelet-Multigrid Method for solving partial differential equations which is

- well-suited for boundary value problems;
- gives exact answers for integrals appearing in the weak formulation without imposing further conditions;
- uses a preconditioner that can be obtained from a recursive and exact procedure that is based upon properties of the underlying fractal scaling functions and fractal wavelets.

Furthermore, this method promises to be computationally efficient.

## References

- [1] M. F. Barnsley, "Fractal Functions and Interpolation," *Constr. Approx.* **2** (1986), 303–329.
- [2] C. Chui, *An introduction to Wavelets*, Academic Press, San Diego, 1992.
- [3] W. Dahmen and A. Kunoth, "Multilevel Preconditioning," *Numer. Math.* **63** (1992), 315–344.
- [4] W. Dahmen and C. Micchelli, "Using the Refinement Equation for Evaluating Integrals of Wavelets," *SIAM J. Numer. Anal.* **30**(2) (1993), 507–537.
- [5] I. Daubechies, "Orthonormal Bases of Compactly Supported Wavelets," *Commun. Pure and Applied Math.* **41**(1988), 909–996.
- [6] I. Daubechies, *Ten Lectures on Wavelets*, SIAM, Vol. 61, Philadelphia, 1992.
- [7] G. Donavan, J. S. Geronimo, D. P. Hardin, and P. R. Massopust, "Construction of Orthogonal Wavelets Using Fractal Functions," *to appear in SIAM J. Math. Anal.*

- [8] J. S. Geronimo, *Personal Communication*.
- [9] J. S. Geronimo, D. P. Hardin, and P. R. Massopust, "Fractal Functions and Wavelet Expansions Based Upon Several Scaling Functions," *to appear in J. Approx. Th.*.
- [10] D. P. Hardin, P. Kessler, and P. R. Massopust, "Multiresolution Analyses Based on Fractal Functions," *J. Approx. Th.* **71** (1992), 104-120.
- [11] S. Mallat, "Multiresolution Approximation and Wavelet Orthonormal Bases of  $L^2(\mathbb{R})$ ," *Trans. Amer. Math. Soc.* **315** (1989), 68-88.
- [12] P. R. Massopust, *Fractal Functions, Fractal Surfaces, and Wavelets*, Academic Press, San Diego, 1994.

FINAL REPORT SUMMER 1994  
INFRARED IMAGING FOURIER TRANSFORM SPECTROMETER  
(IRIFTS)

Randolph S. Peterson  
Associate Professor  
Physics Department

The University of the South  
Sewanee, TN 37383

Final Report for:  
Summer Faculty Research Program  
Arnold Engineering Laboratory

Sponsored by:  
Air Force Office of Scientific Research  
Bolling Air Force Base, Washington, D.C.

and

Arnold Engineering Laboratory

November 1994

INFRARED IMAGING FOURIER TRANSFORM SPECTROMETER  
(IRIFTS)

Randolph S. Peterson  
Associate Professor  
Physics Department  
The University of the South

Abstract

Infrared spectra were obtained using a commercial Fourier Transform Infrared Spectroscopy (FTIR) spectrometer that was stripped for use with available imaging optics. This allowed a detector array to be used in the place of the usual single detector. Both an image and the IR spectrum at each image point were observed with this IR system. Demonstration of the high throughput concept was successful, with an IR spectrum from all detectors of the array yielding a spectrum identical in detail with the IR spectrum from any individual detector of the array.

INFRARED IMAGING FOURIER TRANSFORM SPECTROMETER  
(IRIFTS)

Randolph S. Peterson

Introduction

Remote sensing, dynamic plume analysis need the capabilities of an imaging infrared spectrometer, known as hyperspectral imaging. This project is the beginning and re-establishment<sup>1</sup> of a research and development effort in dynamic, infrared hyperspectral imaging, and an important related technique, superthroughput FTIR spectroscopy.

In the time available for this project, a commercial BOMEM FTIR spectrometer was adapted (stripped) for use with an external imaging system and multidetector array. Image tests were successfully conducted and FTIR spectra were obtained from the multidetector array. Tests of superthroughput spectroscopy were conducted. Results of these tests and an overview of the general theory of these ideas are described in this report.

Some previous experimental and theoretical studies of the IRIFTS concept exist<sup>1</sup>, and those reports have been retested for this report. This work represents an extension of previous work through the use of a 2D detector instead of the 1D detector.

Theory

The basis of most FTIR spectrometers is the Michelson interferometer<sup>2</sup>, which is similar to the interferometer used in this study. A schematic diagram of the unfolded optics of an interferometer is shown in Figure 1. Parallel light enters the interferometer and is split into two beams by the

beamsplitter. The two beams travel to and are reflected from separate mirrors back to the beamsplitter where they recombine. If the phases of the two beams are identical upon recombination, the radiation combines and interferes constructively. Otherwise there is some degree of destructive recombination, through total destructive interference, depending upon the phase differences. As the translating mirror is displaced, the phase difference upon recombination changes continuously. The resulting interference swings from complete constructive to complete destructive as the translating mirror is displaced a quarter of a wavelength of the infrared radiation.

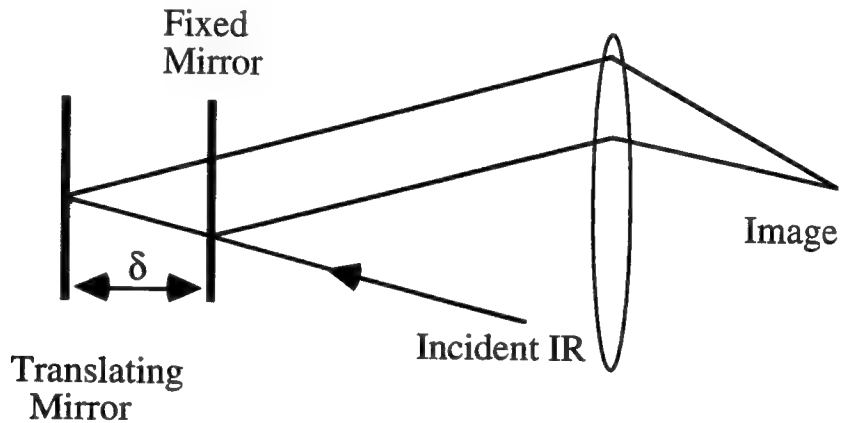


**Figure 1.** Schematic diagram of IR paths in interferometer.

If the light incident upon the beamsplitter is not parallel to the optical axis but at an angle  $\theta$ , the phase difference upon recombination is

$$\phi = (4\pi\delta\sigma) \cos\theta$$

where  $\delta$  is the mirror displacement and  $\sigma$  is the IR wavenumber. The irradiance,  $E(\delta, \theta)$ , is simply

$$E(\delta, \theta) = C \int B(\sigma) \{1 + \cos(4\pi\delta\sigma \cos\theta)\} d\sigma$$

where  $B(\sigma)$  is the monochromatic intensity and  $C$  is an integration constant. This function is shown in Figure 2 for monochromatic light and several mirror displacements. The irradiance for an extended source subtending a solid angle,  $\Omega$ ,

$$\Omega = 2\pi(1 - \cos\theta),$$

is known<sup>1</sup> to be

$$E(\delta, \theta) = C \int B(\sigma) \{1 + \text{sinc}(\Omega_{\max}\sigma\delta)\cos(4\pi\sigma\delta - 2\Omega_{\max}\sigma\delta)\}d\sigma$$

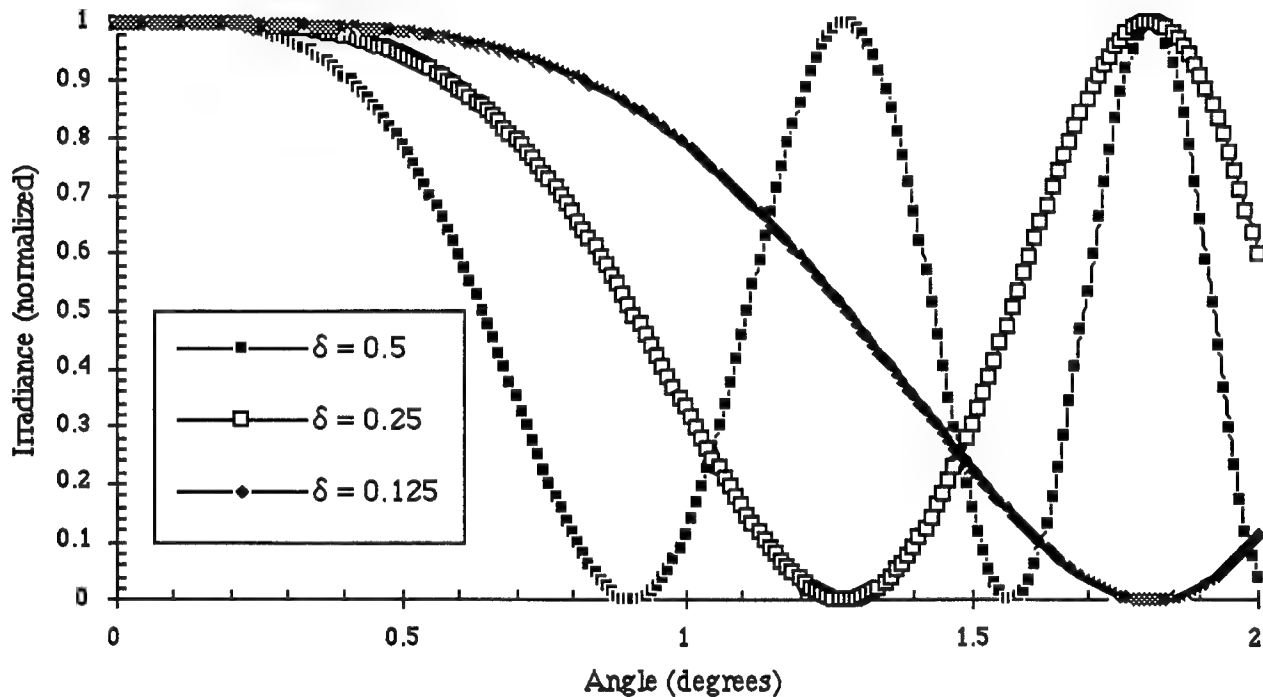


**Figure 2.** Irradiance for off-axis rays with mirror displacements,  $d$  (cm). The radiation is monochromatic, 2.5  $\mu\text{m}$  wavelength IR.

The width of the central image of Figure 2 limits the size of a single, on-axis detector to a value traditionally taken as half the angular size of the first minimum. This translates into an angular size of

$$\theta = (2\delta\sigma_{\max})^{-0.5}$$

which is referred to as the half angle obliquity limit. This limit assures that for all observed wavelengths the phase difference integrated over the detector area is less than 180°.

Overcoming this limit is the driving force behind the research conducted for this report. Using an array of detectors with areas small enough that phase changes over any detector element are less than 180° can allow for more of the total radiation passing through the interferometer (superthroughput) and allow for imaging along with the spectroscopy (hyperspectral imaging).

Hyperspectral imaging spectrometers with 32 detectors in a rectangular array are being developed commercially by BOMEM, but no other research efforts in this type of hyperspectral imaging spectrometers are known by this author. No current research in superthroughput with multiple detectors is known by this author. Earlier work was done by Johnson<sup>3</sup> at Block Engineering in the late 1970's.

#### Experimental Technique

A BOMEM model 100 FTIR spectrometer was stripped of all its optical system, except the interferometer, and used as the foundation of these experimental studies. A schematic of the optical system used is shown in Figure 3. The BOMEM computer software developed

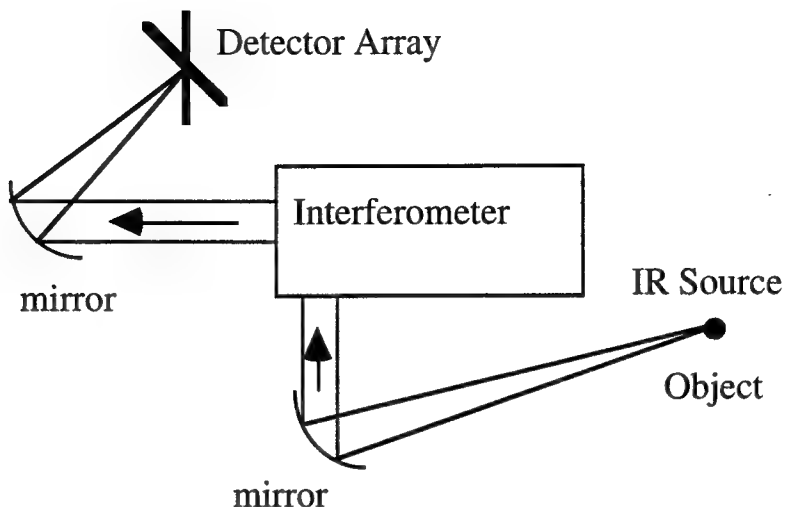


**Figure 3.** Experimental optical plan used in these experiments.

for this model FTIR was used for acquisition and analysis of most of the infrared radiation. This software was not ideally suited to the experimental needs of this study, but there was no available time to develop appropriate software. Some data remains partially analyzed as a result.

An indium antimonide (InSb) detector with seventeen individual detector elements in a symmetric cross pattern was used as a 2D detector array. Tests with large blackbody sources allowed for adjustment and confirmation of a uniform image and nearly identical center burst intensities for all the detectors. As only one amplifier and ADC system were available for these tests, each detector was polled separately by physically connecting and disconnecting cables to the detector array. This was a very time consuming data analysis technique.

Various spectral resolutions (corresponding to a range of  $2\delta$  values) were used in a variety of imaging tests. Resolutions of  $16 \text{ cm}^{-1}$  were used for the final tests of imaging and phases changes, as this allowed for the

greatest amount of data to be acquired in the least amount of time. This relatively low resolution results in all elements of the detector system used for these studies lying inside the half angle obliquity limit. This means that phases are reasonably constant across each detector as well as across the entire detector array.

A blackbody source was used for the final tests. Imaging was performed with simple objects that simply blocked part of the IR source or were selective absorbers of the IR radiation. Aluminum tape was used to block part of the IR radiation, and clear plastic replaced the tape to provide both partial blocking and selective absorption of the incident IR radiation.

### Results

Results from the various tests are studied in the time or spatial domain as interferograms (Igrams) and in the spectral domain in the form of their Fourier transform power spectra, corrected for beamsplitter phase shifts and digital sampling effects. Reproducibility of the Igrams was of great concern because of the ever present possibility that the physical disconnecting and reconnecting of the detector cable would displace the detectors, moving them out of the focal plane. In Figure 4 the intensities of two Igrams are shown, correlated by time (or phase from center burst). The excellent linearity over the entire range of observation, and in this expanded view over part of that range, is evidence of the reproducibility of the data. The two Igrams were separated in time by one hour of data taking and seventeen connects and disconnects of the data cable.

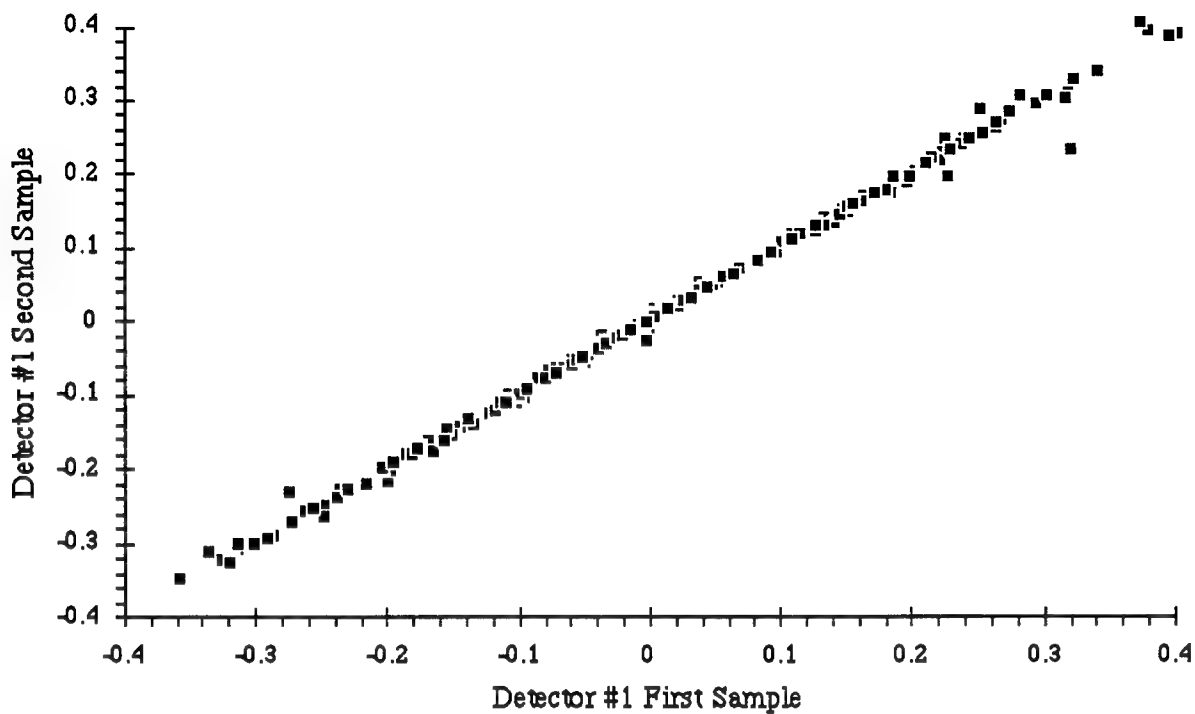


**Figure 4.** Correlation of two interferogram intensities from the same detector used as a check for reproducibility under the prevailing experimental conditions.

A piece of plastic was used as an object for imaging by this optical system. The plastic partially blocked and absorbed (most strongly in the 2,800 to 3,000  $\text{cm}^{-1}$  band) IR radiation from an 800  $^{\circ}\text{C}$  blackbody radiation source. The image on the 2D detector array is sketched in Figure 5. The image is inverted, as it should be for the optical layout, and little absorption is observed in the lower detectors, while strong absorption is observed in the other detectors. The fact that some absorption due to the plastic is observed in all the spectra indicates that the system was somewhat out of focus. Sample power spectra are shown in Figure 6.

The spectra in Figure 6 are blackbody curves attenuated at the high and low frequencies by the detector efficiency. No radiation is detected below a frequency of about  $1700\text{ cm}^{-1}$ . Strong absorption bands<sup>4</sup> due to  $\text{CO}_2$  are visible near  $2350\text{ cm}^{-1}$  and bands from  $\text{H}_2\text{O}$  are seen near  $1900\text{ cm}^{-1}$  and  $3700\text{ cm}^{-1}$ . These are expected since the spectra were obtained with samples in air. Absorption bands due to the plastic sheet are visible in both detectors, with the absorption much stronger in detector #14. Note that the  $\text{CO}_2$  and  $\text{H}_2\text{O}$  absorption bands are of the same relative strength in each detector.

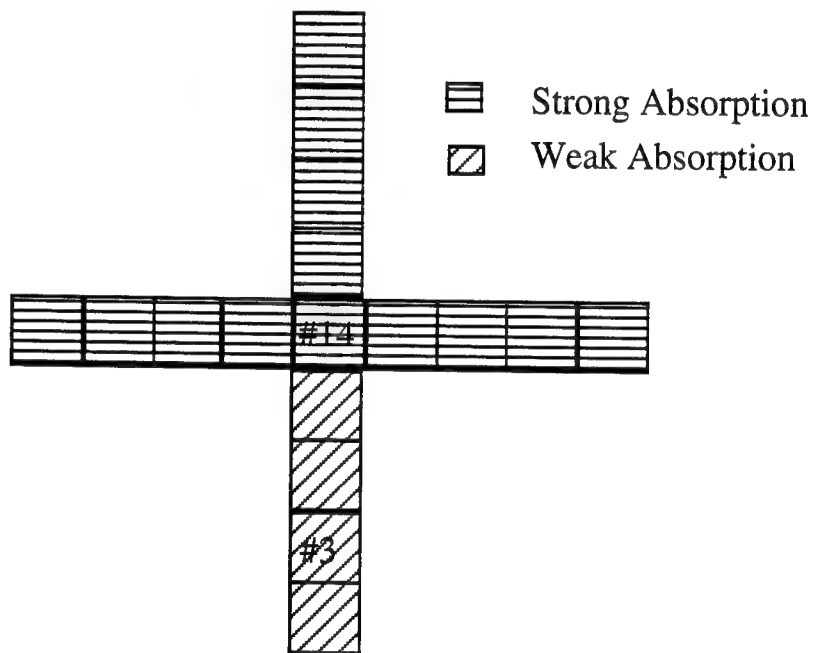


**Figure 5.** Detector array and observed strength of absorption in object plastic film.

Since all the detectors used for the optical layout employed in this experiment lay well within the classical obliquity limit, the phase difference between the signals at each detector were much less than  $180^\circ$ . Comparison of the individual Igrams showed some small phase differences over the time of the Igram. Igrams from each detector were added, ignoring the small phase

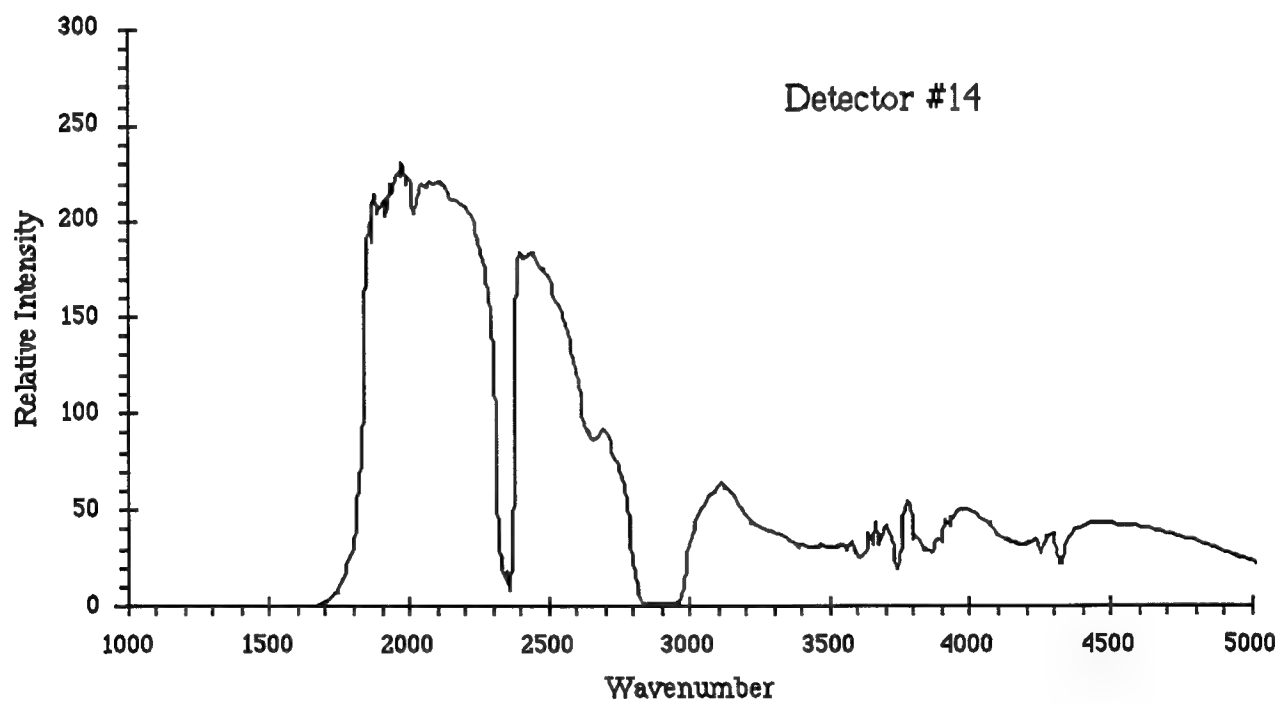
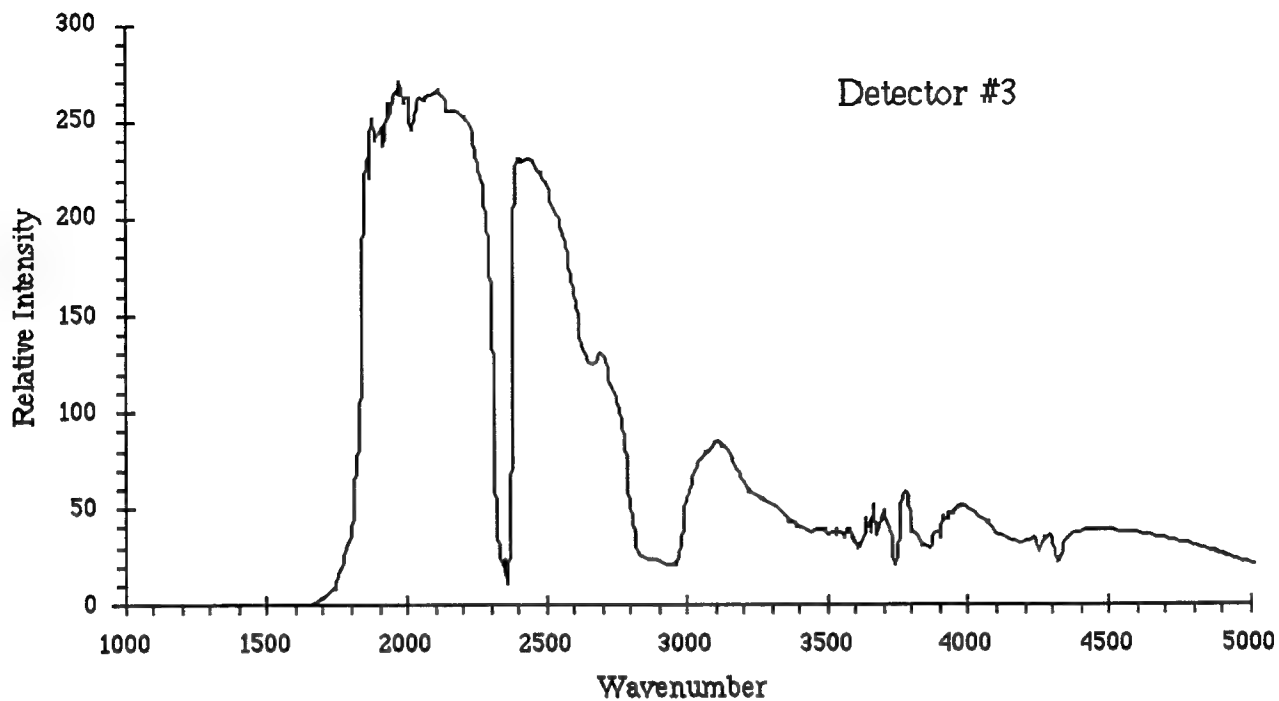


**Figure 6.** Power spectra from indicated detectors, exhibiting strong absorption in the 2,800 to 3,000 cm<sup>-1</sup> band in detector #14, and weak absorption in detector #3.

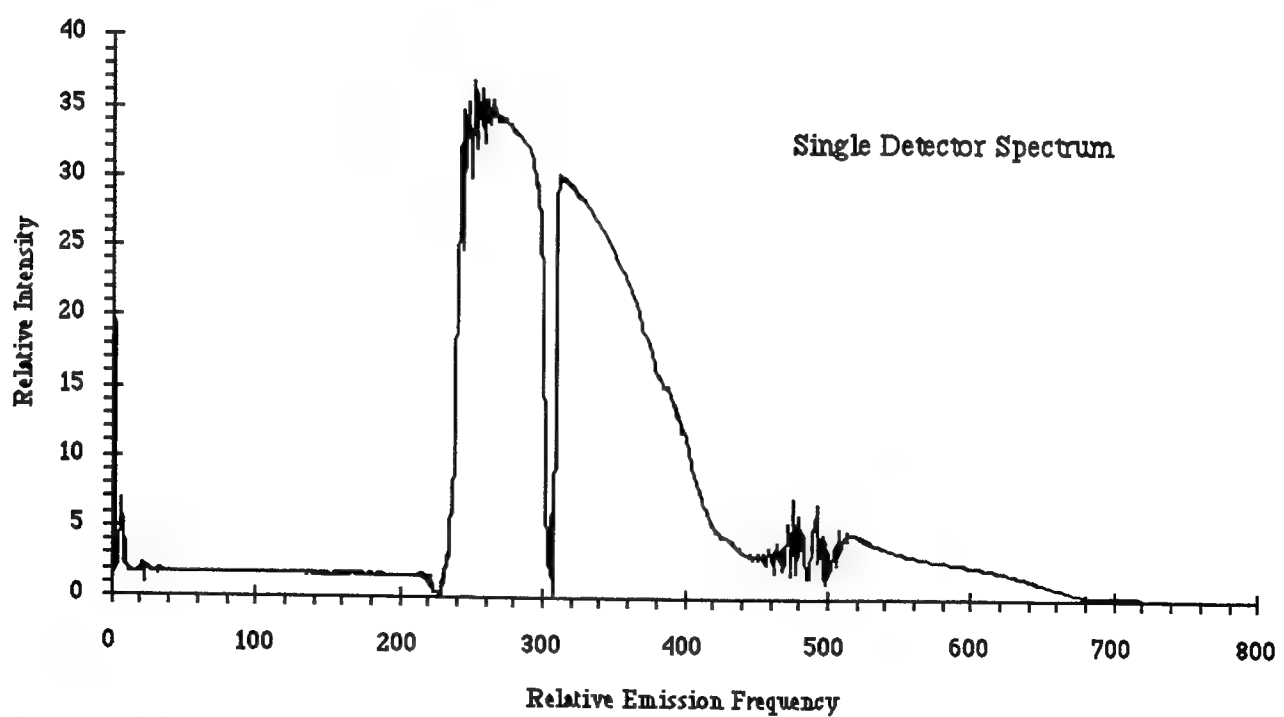
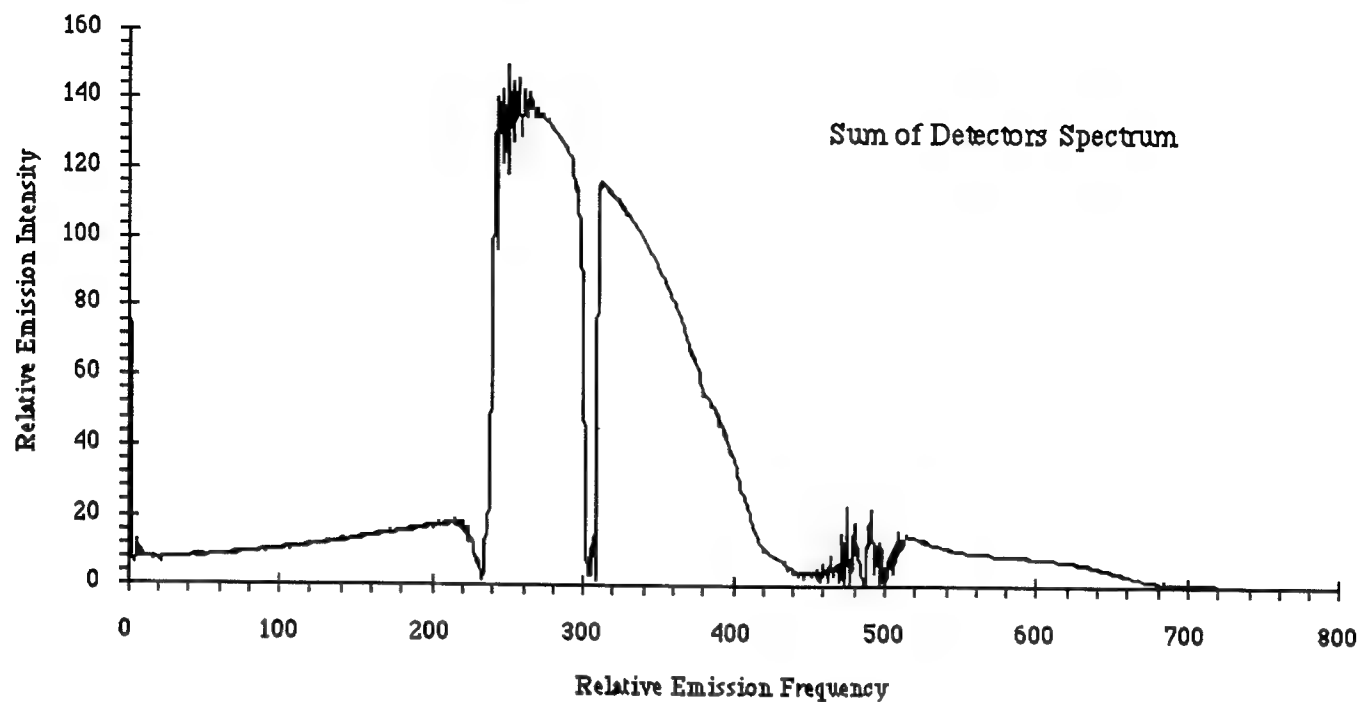


**Figure 7.** Spectra from a single detector and a sum of all detectors.

differences and the resulting Igram was Fourier transformed to give the power spectrum of Figure 7. The power spectrum derived from a single detector is also shown in Figure 7. Note that the sum spectrum is identical in all details, but is more intense than the single-detector spectrum. The only noticeable difference is for the low frequency region. The detector cannot detect this frequency IR and that which is present in the sum spectrum is "computational noise". The source of the radiation was an unattenuated, 800°C blackbody IR source.

The quality of the sum spectrum of Figure 7 indicates the advantage in using all the light that passes through the interferometer. Greater signal strengths result with a resolution as good as the single-detector spectrum. If the detectors extend out to and past the obliquity limit, phase corrections must be made to the individual Igrams before they are combined to produce a sum spectrum.

#### Conclusions

Tests of imaging and superthroughput with an FTIR spectrometer adapted for imaging use have been started. Results from these tests are consistent with theoretical expectations and previous experimental results. Imaging was achieved and high throughput observed from the experiments performed.

References

1. Charles W. Pender, Jr., "Development of an Imaging Fourier Transform Spectrometer," AEDC-TR-86-17, May 1986.
2. John Robert Bell, *Introductory Fourier Transform Spectroscopy*, Academic Press, New York, 1972.
3. N. J. E. Johnson, "Spectral Imaging with the Michelson Interferometer," *Proceedings of SPIE*, p.2, v.226, Washington, D.C., April 1980.
4. Stadtler Research Laboratories, *Stadtler Standard Spectra, Gasses and Vapors*, Philadelphia, PA, 1972.

## DESIGN OF SOOT CAPTURING SAMPLE PROBE

Roy J. Schulz

Professor of Mechanical and Aerospace Engineering

University of Tennessee Space Institute

B. H. Goethert Parkway

Tullahoma, TN 37388-8897

Final Report for:

AFOSR Summer Faculty Research Program

Arnold Engineering Development Center

Arnold Air Force Station, TN 37389

Sponsored by:

Air Force Office of Scientific Research

Bolling Air Force Base, DC

September 1994

## Design of Soot Capturing Sampling Probe

Roy J. Schulz

Professor of Mechanical and Aerospace Engineering

University of Tennessee Space Institute

Tullahoma, TN 37388-8897

### Abstract

Extractive gas sampling probes have been used for many years to acquire samples of process streams, of atmospheric aerosols, and of effluent streams from power generation and chemical process industry plants, for chemical and particulate analyses. The design and application of these probes to extract samples from rocket exhaust streams is complicated by the high temperature of the exhaust and by the fact that the exhaust flow is supersonic, which means that a bow shock wave can be formed standing in front of the probe inlet tip. Bow shock waves are strong compression waves that can raise the static temperature and pressure of the sampled gas stream, thus disturbing its chemical state, as well as cause the breakup of suspended particles in the captured gas stream, thus changing the particle size distribution in the captured sample stream.

The purpose of the task undertaken during the summer faculty research program was to develop a concept and a potential design for an extractive gas and soot particle sampling probe (GSSP) to capture soot-containing exhaust gas samples from supersonic exhaust flows of liquid hydrocarbon-fueled rocket engines. The design of the probe must minimize the effects of the sample extraction process on the chemistry of the gas and soot particles extracted, as well as minimize the effects of the sampling procedure on the soot particle size distribution. The GSSP must survive the severe thermal environment, and if possible, not create too big a disturbance in the rocket exhaust flow.

## Design of Soot Capturing Sampling Probe

Roy J. Schulz

### **1.0 Technical Details of Research Project**

The problem is illustrated schematically in Fig. 1, where a thermally-protected, intrusive sample extraction probe is shown inserted into the exhaust flow of a rocket motor, fairly near the exit plane of the nozzle. The hydrocarbon-fueled engine is expected to be operated fuel-rich, with suspended soot particles being carried in the exhaust gas. Soot particles are submicron sized (.1-.2 micron, typical) particles of nearly pure carbon form, each particle basically being an agglomeration of sub-submicron sized spherical carbon particles (.01 micron, typical) connected in partially twisted, folded, or knotted strings and chain-like structures. These particles form in fuel-rich combustion zones, where gas temperatures are in the 1400-1600 C range, from the products of hydrocarbon fuel pyrolysis and thermal decomposition. In the combustion or cracking process, soot precursor species are formed. These precursors are aromatic ring compounds, and acetylene (C<sub>2</sub>H<sub>2</sub>). A significant amount of research has been done to formulate the global or overall mechanism by which soot is formed in specific flames from these chemical precursors, including ions. The overall soot formation mechanism has been found to be affected by:

- 1) fuel type, and both local and overall flame stoichiometry
- 2) flame( laminar, turbulent, premixed or diffusion) type
- 3) turbulence levels, and intermittency
- 4) burner or combustor design(global flow patterns)
- 5) temperature profile along and/or across the flame zones
- 6) flame heat loss due to radiation (by soot and by molecular species)
- 7) types of aromatic ring radical species produced in the cool fuel-rich zones(geometry of the reaction site locations on the rings)
- 8) kinetic mechanisms for ring and multi-ring formation by reaction of C<sub>2</sub>H<sub>2</sub> with the ring radical compounds
- 9) coagulation and/or condensation processes which layer the multi-ring dimers and multimers into sub-submicron spherical carbon particles
- 10) temperatures and oxidant concentrations that the carbon particle strings/chains experience before and after leaving the flame or hot zones, which determines whether the formations of the soot particles and deposits are amorphous, "puffy", "soft", and loosely-bonded, or are "hard", "platelet-type", and tightly bonded on surfaces.

Besides soot characteristics, it is necessary to first introduce the significant problems utilizing intrusive, extractive gas and particle sampling probes.

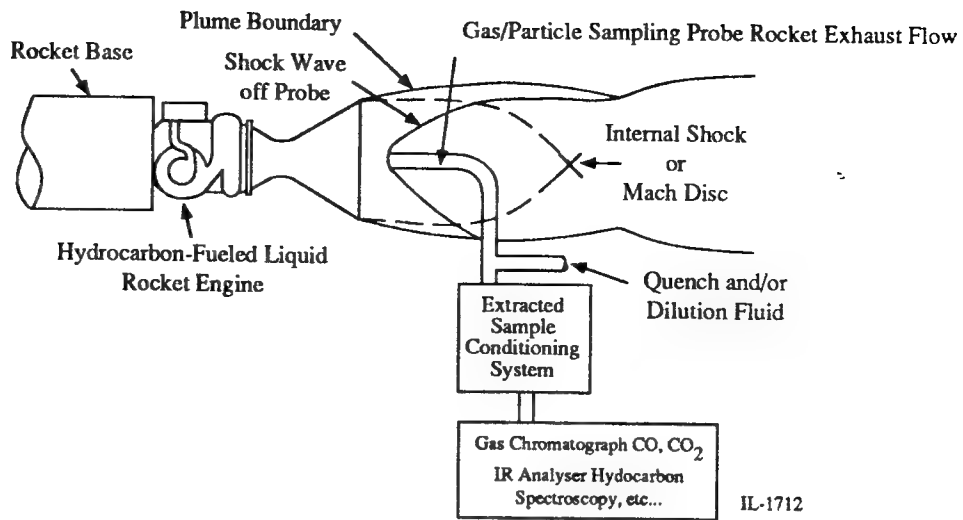


Figure 1. Schematic of Thermally Protected, Extractive, Intrusive, Gas Sampling Probe System in Rocket Exhausted

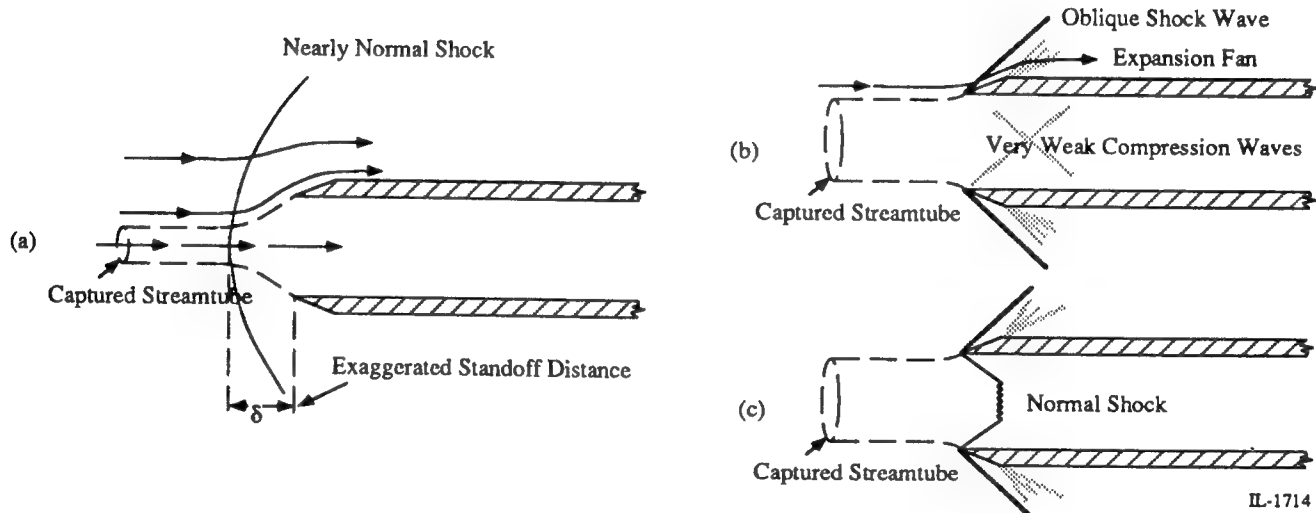


Figure 2. Schematic of Possible Aerodynamic Behavior in Inlet Gas - Particle Sampling Probe in Supersonic Flow

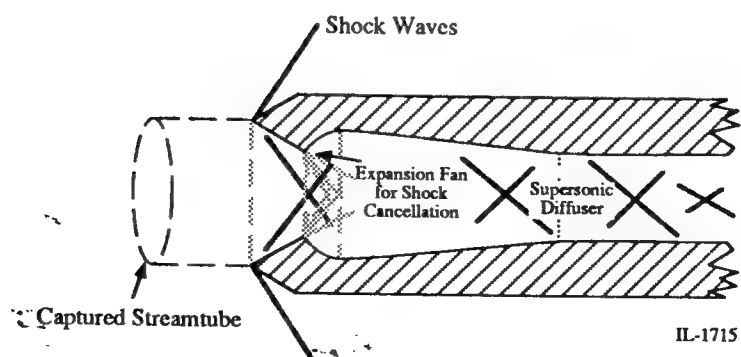


Figure 3. Schematic of Shock-Cancellation Inlet Design for Gas-Particle Sampling Probe in Supersonic Flow

The sampled stream tube or gas flow starts out as an undisturbed flow in the freestream, upstream of the probe. The streamtube geometry for the sampled, extracted flow can pass from the freestream to the interior of the sampling probe in several different ways in supersonic flow. Figures 2 and 3 show three different ways this can occur. The flow to be sampled can be spilled at the probe inlet tip, it can be perfectly matched to the probe inlet conditions, or it can be swallowed by the probe. The controlling factor is the back pressure that the probe operates with, or alternately, the mass flow the probe was designed to pump from the freestream. For the perfectly matched case, and the swallowed case, all of the flow covered by the projected cross-sectional area of the probe inlet is ingested by the probe. For the spilled case, the probe pumps less mass flow than is delivered to its cross-sectional flow area by the freestream, and some of this flow is directed to flow around the probe inlet tip. Thus, the probe acts somewhat as a blunt, solid body in the flow, creating a bow shock wave standing in front of the probe. The deflection of the fluid streamlines upstream of the inlet causes inertial separation of the particle sizes, and even reductions in measured particle number densities or concentrations, compared to freestream levels. Generally, the very smallest particle sizes follow the gas streamlines, and the larger particles tend to follow deflected, but much less curved, trajectories up and into the probe tip, based on a geometrical scaling of the process by the ratio of particle size to characteristic dimension of the capturing body. Therefore, the probe tip acts like some equivalent (but *a priori* unknown) solid body in the sense that it has a capture efficiency for particles of a given size. Also, as stated, the flow has its static temperature and pressure raised in passing through the bow shock wave, thus causing a shift in the gas chemical composition entering the probe inlet. This compression process can initiate soot formation by raising the temperature of an initially somewhat cool, fuel-rich sample, or, it can initiate soot oxidation and destruction in an O<sub>2</sub>- and/or OH radical-rich gas sample carrying soot. Strictly at the probe tip inlet, it is obvious that the flow situation in Fig 2(b) illustrates the desired flow capturing aerodynamics: the entire freestream streamtube is captured (hence, all particle sizes) and, there is no disturbing shockwave across the inlet flow. It is presumed that a process of deceleration and cooling of the flow can be achieved farther downstream in the tubing that carries the extracted sample flow to the gas composition and particle sizing analyzers. In fact, design of the process of decelerating and cooling the sample flow in the delivery tubing of the probe system without changing either gas or soot chemical composition, or soot particle sizes, can be considered as the definitive problem of the probe design project undertaken during the summer research project, in addition, of course, to the thermal protection design of the probe system.

## **2.0 Some Previous Work on Sample Probe Design**

Early work on aerosol sampling probe design and isokinetic sampling and aerodynamic misalignment, on probe capture efficiency for particles, was reported by Watson, ref. 2-1. Other factors affecting the capture efficiency of isokinetic sampling probes, such as particle de-entrainment and deposition in the sample collection feed lines, and probe aerodynamic shape, were discussed by Parker, ref. 2-2. Parker derived equations, based on assumed statistical measures of aerosol size distributions, that indicate when a sample line has an internal diameter large enough to ensure capture of all particle sizes in the sampled stream, based on stream velocity, sampling time, and other

parameters.

Some of the most recent work on the theoretical description of aerosol sampling probe capture efficiency and particle aerodynamics in the capture or sampling process in supersonic streams has been reported by Forney, et al., ref. 2-3.

The aerodynamic inlet conditions of an ideal thin-walled cylindrical sample extraction probe were analyzed by Forney, et al, ref. 3-4, based on numerical and analytical methods. The mechanism by which an ideal probe could capture freestream particles when the probe in a supersonic flow operated in the spillage mode was shown by Forney, et al, to be a function of a generalized particle Stokes number that accounts for particle drag as a function of a slip flow Reynolds number. Because soot particles are so extremely small, their Knudsen number is unity and greater, hence they can experience non-continuum flow (slip-flow) conditions. The use of a generalized Stokes number to characterize solid body (cylinder) particle capture efficiencies was also demonstrated by Israel and Rosner, ref. 2-5. One of the significant problems of the use of intrusive probes to capture samples of particles borne by flowing streams is that in the capture process, drag and inertial forces can disrupt the particle structures. Estimates of these forces on the particle motion during the capture process have been made by Forney, et al, ref. 2-6,2-7, although particle breakup by deceleration and aerodynamic forces was not addressed.

Experimentally, studies have been done to address the sampling error in measuring freestream particle number density due to probe-induced particle size separation, segregation, or "classification". This may be generally called the effect of probe capture efficiency for different particle sizes on sampled size distributions, that occurs when the probe is operated in the spillage mode, Martone, et al, ref. 3-8. These authors showed a significant reduction in sampled particle concentrations (number densities), compared to freestream concentrations, when the probe is operated anisokinetically (in the spillage mode) in sonic and supersonic flows. The particles sampled were submicron in diameter, .8 micron. The authors showed that anisokinetic sampling errors followed trends reported for purely subsonic flows, and that the results of supersonic experiments could be correlated to subsonic experiments by using the subsonic Mach number immediately downstream of the nearly normal bow shock wave standing off the inlet of the anisokinetically operated probes in the supersonic flows.

Hack, et al., ref. 2-9, have compared soot particle sizes and concentrations obtained with extractive probes to optically made measurements of the sizes and concentrations. These measurements were made in a research combustor designed to provide all of the flow features of a gas turbine combustor, including recirculation in the primary, swirling flame zone. Both hot and cold measurements were made, and many interesting and important results were obtained. One result of significance was that, in hot flows, the morphology or forms of the soot particles sampled were affected by the sampling conditions, or, specifically, the probe operating conditions. The authors reported "platelet-like" soot particles (structures) and "tightly packed, puff-like" structures, depending on the sample transport temperature and its cooling rate in the sample delivery tubing (hereinafter called the sample flow

train) connecting the probe tip to the gas/soot analyzers, specifically, to the filters used to strain the soot particles from the sample stream. The "puff-like" structures or soot particles occurred with higher temperatures along the extraction flow train. The authors concluded that "large particles" (5 micron) with puff-like structures could be formed in the extractive sample flow train, specifically, on the filters. Although there were occasions when large particles were observed optically in the freestream combustion gases, they were always present on the filters, and, their number densities or concentrations were always greater on the filters. The formation of the larger particle sizes on the filters was thought to occur from the deposition of pyrolyzing fuel fragments that form the microspheroids of carbon particles in the chain-like structures. Basically, these structures fill up the 5 micron filter pores, and then they continue to grow into the puff-like structures seen under microscopy. This soot-forming process in the extractive sampling flow occurred when the flow temperatures were maintained along the flow train, that is, were not rapidly quenched in the flow train by nitrogen dilution, for example. The authors conclude that the platelet-like structures formed on the filters under conditions of "high cooling rates", and were "likely as a product of rapidly condensing heavily concentrated fuel pockets extracted in early stages of pyrolysis". This implies that what these researchers were sampling was immature soot particles, that is, they were extracting soot in the process of being formed, and it was not completely thermally conditioned nor partially oxidized by the combustion flow, as would be in a laboratory burner, for example, where soot is sampled above the flame tip. This also has implications for sampling in substoichiometric, fuel-rich flames and rocket plumes, because it implies that the rate of sample cooling and quenching will affect the age of the captured soot, or, perhaps more appropriately, the stage of the soot in the soot forming, chemical- kinetically controlled processes. Soot-sampling using intrusive probes in gas turbine combustor exhaust flow has also been done by D. W. Netzer and his colleagues and students at the U. S. Naval Postgraduate School in Monterey, California. Lohman, ref. 3-10, for example, also observed larger (up to 25 micron) agglomerated particles made from myriads of submicron (0.1 micron) diameter carbon particles. Lohman discusses the observations of Hack, et al., ref. 3-9, who also reported such agglomerations. The effects of the probe design, the sample cooling rate of non-intrusive, optical, laser-based gas-particle diagnostic methods. For example, by Samuelson, et al, ref. 2-11, using purely optical techniques, to determine soot particle sizes and concentrations in the research combustor for different fuels and fuel blends. Apparently, extractive probe sampling was not done. However, this raises the question: what is measured by the optical method? Is it mature soot, or soot-like complexes on their way to becoming soot, or what? The point here is that the optical method must also provide information about the chemical and agglomeration state of the surveyed "soot" particle. Such measurements may be possible combining simultaneous scattering, absorption, and spectroscopic signal analysis, based on multi-beam, multi-frequency laser systems. However, it also seems possible and attractive to develop ultra-rapid-quench sample extraction probes, based on aerodynamically optimized shock-swallowing designs, with nitrogen dilution. Such extractive probes should freeze the soot or the pre-soot particulates in their freestream state, and hopefully, not cause either agglomeration/growth nor fragmentation of the captured particles. This is objective of the GSSP design sought in the summer research project.

In a very closely related area, there has been sustained interest in the rocket propulsion community to

sample the particulate stream in the exhaust flow produced by burning aluminized propellants in solid-fueled rocket motors. Misener and Kessel, ref. 2-12 discussed measurements and characterization of particulate-laden solid-rocket motor exhaust flows including a new design for an intrusive, particle-sampling probe based on isokinetic sampling of supersonic exhaust by shock-swallowing methods. This probe design was implemented for use in particle sampling studies for rocket exhaust at the U. S. Naval Postgraduate School, and its performance and results reported by Laredo, et al., ref. 2-13, Eno, ref. 2-14, Kellman, ref. 2-15, Kim, ref. 2-16, and Racine, ref. 2-17. This probe design confirmed the need to do isokinetic sampling in supersonic flows, and, it demonstrated that this kind of sampling can be achieved with an internal jet-ejector system, Fig. 3, that essentially pumps the probe inlet flow, thus swallowing the nose or inlet shock wave. In addition, by operating the jet-ejector system with dry nitrogen, the sampled stream is inerted and cooled down by mixing with the ejector flow, on its way to the sample diagnostics apparatus downstream in the sample flow train. Therefore, this aspect of the Phillips Lab isokinetic sampling probe will be adopted for use in the design of the soot-sampling probe considered in the present summer faculty project.

## References - Section 2.0

- 2-1. Watson, H. H., "Errors Due to Anisokinetic Sampling of Aerosols", American Industrial Hygiene Assoc. Quarterly, V.15, N.1, pp. 21-25, March, 1954.
- 2-2. Parker, G. J., "Some Factors Governing the Design of Probes for Sampling in Particle-and Drop-Laden Streams", Atmospheric Environment, V.2, pp. 477-490, Pergamon Press, 1968.
- 2-3. Forney, L. J., McGregor, W. K., and Van Dyke, D. B., "Computation of Gas Flowfields in Supersonic Particle Probes", Trans. ASME Journal of Fluids Engineering, V. 108, pp. 77-81, March, 1986.
- 2-4. Forney, L. J., and McGregor, W. K., "Particle Sampling in Supersonic Streams with a Thin-Walled Cylindrical Probe", AIAA Journal, V. 25, N. 8, pp. 1100-1104, August, 1987.
- 2-5. Israel, R., and Rosner, D. E., "Use of a Generalized Stokes Number to Determine the Aerodynamic Capture Efficiency of Non-Stokesian Particles from a Compressible Flow", Aerosol Science and Technology, V. 2, pp. 45-51, January, 1983.
- 2-6. Forney, L. J., Van Dyke, D. B., and McGregor, W.K., "Dynamics of Particle-Stoke Interactions: Part I: Similitude", Aerosol Science and Technology, V. 6, pp. 129-141, 1987.
- 2-7. Forney, L. J., Walker, A. E., and McGregor, W. K., "Dynamics of Particle-Shock Interactions: Part II: Effect of the Basset Term", Aerosol Science and Technology, V. 6, pp. 143-152, 1987.
- 2-8. Martone, J. A., Daley, P. S., and Boubel, R. W., "Sampling Submicrometer Particles Suspended in Near Sonic and Supersonic Free Jets", Journal of the Air Pollution Control Assoc., V. 30, N. 8, pp. 898-903, August, 1980.
- 2-9. Hack, R. L., Samuelson, G. S., Poon, C. C., and Bachelo, W. D., "An Exploratory Study of Soot Sample Integrity and Probe Perturbation in a Swirl-Stabilized Combustor", Trans. ASME Journal of Engineering for Power, V. 103, pp. 759-770, October, 1981.
- 2-10. Lohman, A. L., "An Investigation into the Soot Production Processes in a Gas Turbine Engine", Master of

Science Thesis, Aeronautical Engineering, the Naval Postgraduate School, Monterey, California, September, 1984.

2-11. Samuelson, G. S., Wood, C. P., and Jackson, T. A., "Optical Measurements of Soot Size and Number Density in a Complex Flow, Swirl-stabilized Combustor", pp. 21-1 to 21-15, AGARD Conference Proceedings No. 353, Combustion Problems in Turbine Engines, AGARD CP-353, 1983.

2-12. Misener, J. A., and Kessel, P. A., "Current AFRPL Measurements and Characterization of Particulates in Solid Rocket Motor Plumes", Proc. 15th JANNAF Plume Technology Meeting, CPIA Publication 426, May, 1985.

2-13. Laredo, D., Kellman, L., Eno, T., and Netzer, D. W., "Particulate Behavior in Exhaust Nozzles and Plumes", (to be found).

2-14. Eno, T. J., "A Combined Optical and Collection Probe for Solid Propellant Exhaust Particle Analysis", Thesis, Master of Science, Engineering Science, Naval Postgraduate School, Monterey, California, December, 1989.

2-15. Kellman, L. J., "Modification and Experimental Validation of a Combined Optical and Collection Probe for Solid Propellant Exhaust Analysis", Thesis, Master of Science, Aeronautical Engineering, Naval Postgraduate School, Monterey, California, March, 1991.

2-16. Kim, H., "Multiple-Wavelength Transmission Measurements in Rocket Motor Plumes", Thesis, Master of Science, Naval Postgraduate School, Monterey, CA, September, 1991.

2-17. Racine, J. A., "Subscale Solid Rocket Motor Infrared Signature and Particle Behavior", Thesis, Master of Science, Aeronautical Engineering, Naval Postgraduate School, Monterey, CA, December, 1991.

### **3.0 A Brief Discussion on the Nature of Soot Particles**

Lack of space (page count) precludes inclusion of a discussion of soot formation. A very brief list of references the author found informative is presented below.

### **References - Section 3.0**

3-1. Schalla, R., and Hibbard, R. R., "Smoke and Coke Formation in the Combustion of Hydrocarbon-Air Mixtures", Chapter IX of Basic Considerations in the Combustion of Hydrocarbon Fuels with Air, NACA Report 1300, Lewis Flight Propulsion Laboratory, Cleveland, OH, (1958).

3-2. Migaridis, C. M. and Dobbins, R. A. "Morphological Description of Flame-Generated Materials", Combustion Science and Technology, Vol. 71, pp. 95-109, (1990).

3-3. Lahaye, J., and Prado, G., "Formation of Carbon Particles from a Gas Phase: Nucleation Phenomenon", Water, Air and Soil Pollution, Vol. 3, pp. 473-481, (1974).

3-4. Mulholland, G. W., Samson, R. J., Mountain, R. D., and Ernst, M. H., "Cluster Size Distribution for Free Molecular Agglomeration", J. Energy and Fuels, American Chemical Society, Vol. 2, No. 4, pp. 481-486, (1988).

- 3-5. Sorensen, C. M., Cai, J. and Lu, N., "Light-Scattering Measurements of Monomer Size, Monomers per Aggregate, and Fractal Dimension for Soot Aggregates in Flames", *Applied Optics*, Vol. 31, No. 30, pp. 6547-6557, 20 October, (1992).
- 3-6. Glassman, I., *Combustion*, Second Edition, Academic Press, Inc., Orlando, FL, (1987).
- 3-7. Hamins, A., "Soot", Chapter 3, pp. 71-95, in *Environmental Applications of Combustion Processes*, I. K. Puri, Editor, CRC Press, Boca Raton, FL, (1993).
- 3-8. Ikegama, M. (editor), "Soot Formation Fundamentals", Chapter 5, in *Advanced Combustion Science*, T. Someya, General Editor, Springer-Verlag, Inc., Tokyo, Japan, (1993).

#### 4.0 Design Approach to Thermal Protection of the GSSP

Data on the thermal environment of the operational soot-capturing probe have been provided by Heirs, III, ref. 4-1, on output sheets from the VIPER code, ref. 4-2. Equilibrium and kinetic nozzle expansions were provided. The parameters of importance are the stagnation and exit plane static flow conditions. The heat flow and heat flux estimates can be based on equilibrium flow for convenience. The calculated data was tabularized to provide the stagnation and exit plane static flow properties of the exhaust gas. These properties formed the basis for heat transfer and gas dynamic design calculations.

Although the soot-capturing probe is designed as a shock-swallowing, isokinetic sampling probe, there will be stagnation points and bow shock waves at various places on the probe. The heat flux of the probe tip will result from stagnation point heat transfer. Therefore, probe tip stagnation point properties were also required as reference values. These were calculated from perfect gas supersonic flow relations.

The preliminary design calculations for heat transfer indicated high values for stagnation point heat fluxes, of the order of 4 kw/cm<sup>2</sup> for a 1/4" nose tip radius. In fact, manipulation of the equations showed that there was a fundamental relationship between the wall thickness at the probe stagnation point and the stagnation point radius of curvature, R<sub>n</sub>. For example, the stagnation point heat flux can be represented symbolically as:

$$q_{ws} = \frac{A}{\sqrt{R_n}}$$

where A is a dimensional constant that involves all the other factors such as enthalpy difference, etc. This heat flux must be conducted through the nose wall thickness and then convected away by the cooling water flowing in cooling channels behind the stagnation point or line. On the other hand, a general equation for the overall heat transfer process of the watercooling of the leading edge or stagnation point is given by:

$$q_{ws} = \frac{B}{\delta_w}$$

where  $B$  is a dimensional constant that incorporates the temperature difference across the nose cooling circuit, the overall heat transfer coefficient, etc.  $\delta_w$  is the wall thickness at the stagnation point or leading edge. By setting the expressions for  $q_{ws}$  equal one has

$$\frac{A}{\sqrt{R_N}} = \frac{B}{\delta_w}$$

or alternately

$$R_N = C \delta_w^2$$

where  $C$  is a combined dimensional constant. This equation means that as the nose or stagnation wall thickness increases, the nose radius of curvature increases as the square of this thickness. To put it another way, a small nose radius of curvature will require very thin walls to conduct away the applied heat flux. Thus, small models, sharp leading edges, small blunt noses, etc., will require very thin-walled construction, or face thermal destruction. If the rocket exhaust carries particulates, the sandblast effect on thin walled probes could also be a crucial factor in the probe survivability. Special surface hardening or coatings on the probe outer surface may be required to assist the thin-walled probes to survive. The analysis showed that, under the given conditions, a 1/4" nose radius would require wall thickness of about 0.06", in copper, to handle the stagnation heat flux. This is pretty thin for a structurally weak material such as copper. Therefore, an alternate means of nose tip and stagnation line thermal protection was needed.

An alternate method to ensure survivability of the probe in high heat flux and particulate-laden flows is to use the cooling water as a thermal barrier by spraying it out of ports at the nose and stagnation line. In actuality, that is the design approach recommended by the author for thermal and sand-blast protection of the soot capturing sample probe: water sprays out of nose and stagnation line ports for evaporative cooling and particulate protection. It will be necessary to account for, and in fact design for, some ingestion of the sprayed water by the soot capturing probe. This is a design detail that can partly be designed using engineering principles and rules of thumb, or engineering estimates, and partly, it will require experimental testing and development. Thus, test, modification, and development of the soot capturing sample probe will be necessary.

## References - Section 4.0

- 4-1. Heirs, III, R.S. Private Communication, May 1994.
- 4-2. Annon. "Viscous Interaction Performance Routine (Viper) - Version 3", Release date MAR 94, Written by Software and Engineering Associates (SEA) Inc., For the USAF Astronautics Laboratory. SEA, Inc., 1000 E. William St., STE 200, Carson City, NV, 89701.
- 4-3. Anon "Equations, Tables, and Charts for Compressible Flow", NACA Report 1135, Ames Aeronautical Laboratory, Moffett Field, California, (1953).
- 4-4. Fay, J., and Riddell, F., "Theory of Stagnation Point Heat Transfer in Dissociated Air", J. Aeronautical

Sciences, 25, pp. 73-85, (1958).

4-5. Rose, P., and Stark, W., "Stagnation Point Heat Transfer Measurements in Dissociated Air", J. Aeronautical Sci., 25, pp. 86-97, (1958).

4-6. Fay, J. A., "Hypersonic Heat Transfer in the Air Laminar Boundary Layer", paper in Chapter 30 of The High Temperature Aspects of Hypersonic Flow, AGARDograph 68, W. C. Nelson, editor, the Macmillen Co., pp. 583-605, (1964).

4-7. Tauber, M. E., "A Review of High-Speed, Convective, Heat-Transfer Computation Methods", NASA Technical Paper 2914, Ames Research Center, Moffett Field, California, (1989).

4-8. Love, E. S., "Prediction of Inviscid Induced Pressures from Round Leading Edge Blunting at Hypersonic Speeds", ARS Journal, pp. 792-793, October, (1959).

## 5.0 Estimates of Soot Flow Rate, Particle Number Densities, Particle Capture Rates, Probe Flow Rates, Etc., in Hydrocarbon-Fueled Rocket Motor Exhaust

The thermal analysis of section 5 was done to obtain estimates of the heat loads expected on the probe as a function of the probe geometry and size-scale. It is obvious that the amount of material ingested by the isokinetic sampling probe will depend on the probe inlet area or probe size, and the exhaust flow conditions. Therefore, in order to get ball park estimates of the amount of material ingested by the probe, and perhaps deposited upon filters, the following equations and numerical evaluations were derived.

The calculations in this section are based on estimated exhaust flow exit static conditions. The relevant theoretical estimates of important design variables are calculated below in the following subsections.

### 5.1) Rocket Exhaust Gas Mixture Flow Rate Per Unit Flow Area

$$g = \rho_e u_e = (0.167)(2571) = 459.4 \text{ kg/m}^2\text{-s}$$

### 5.2) Soot Mass Flow Rate Per Unit Flow Area

Using an estimated<sup>1</sup> nominal soot mass fraction of 1% by mass in the rocket exhaust,

$$g_s = \rho_s u_e = Y_s g = (0.01)(459.4) = 4.59 \frac{\text{kg}}{\text{m}^2\text{-s}}$$

### 5.3) Soot Particle Cloud Density

From 5.2.) we compute the soot particulate cloud density

$$\rho_s u_e = Y_s \rho_e u_e$$

$$\rho_s = Y_s \rho_e = (0.01)(0.167)$$

$$\rho_s = 1.67 \times 10^{-3} \frac{\text{kg - soot}}{\text{m}^3 \text{ mixture}}$$

#### 5.4) Soot Number Density

The number density of the soot particles in the rocket exhaust can be determined as follows. The soot mass flow can be written

$$g_s = \rho_s u_e = m_s N_s u_e$$

where  $m_s$  is the mass of a single soot particle, and  $N_s$  is the number of soot particles per  $m^3$  of space.

Thus, by equating the expressions for  $g_s$ , get

$$g_s = m_s N_s u_e = Y_s g = Y_s \rho_e u_e$$

Therefore,

$$N_s = Y_s \frac{\rho_e}{m_s}$$

Since

$$m_s = C_s V_s = C_s \frac{\pi}{6} D_s^3$$

where  $C_s$  is the density of a single particle, then, by substitution

$$N_s = \frac{6 Y_s \rho_e}{\pi C_s D_s^3}$$

For the assumed diameter of the nominal soot particle size, of

$$D_s = 0.01 \mu\text{m} = 1 \times 10^{-8} \text{m}$$

and, based on the density of amorphous carbon as

$$C_s = 1950 \text{ kg/m}^3$$

then, the computed number density,  $N_s$ , is

$$N_s = \frac{6(0.01)(0.167)}{(3.14)(1950)(1 \times 10^{-8})^3} = 1.64 \times 10^{18} \frac{\text{part.}}{\text{m}^3}$$

On a per  $\text{cm}^3$  basis

$$N_s = \frac{1.64 \times 10^{18}}{(100)^3} = 1.64 \times 10^{12} \frac{\text{part.}}{\text{cm}^3}$$

This value is certainly within range of measured soot particle densities in exhaust gas flows, specifically in the range

$$N_s \sim \left( 10^8 - 10^{12} \frac{\text{part.}}{\text{cm}^3} \right)$$

in a propane/O<sub>2</sub> flame.

Note that the volume of a single soot particle is

$$V_s = \frac{\pi}{6} D_s^3 = 5.23 \times 10^{-25} \text{ m}^3$$

and has a surface area of

$$A_{s\rho} = \pi D_s^2 = 3.14 \times 10^{-16} \text{ m}^2$$

A characteristic length for a soot particle is then

$$L_c = V_s/A_s = 1.67 \times 10^{-9} \text{ m}$$

for use in analyzing a soot particle thermally by a lumped system analysis.

### 5.5) Capture Rate for Number of Soot Particles in Isokinetic Sampling System

The volume of gas, per unit area, per second, in the exhaust flow is

$$\frac{V}{A} = u_e$$

The number of particles sampled as a particle flux is then given by

$$\dot{N}_s'' = N_s \frac{V}{A} = N_s u_e$$

Numerically, for the rocket exhaust conditions specified this is

$$\dot{N}_s'' = (1.64 \times 10^{18})(2571) = 4.216 \times 10^{21} \frac{\text{part.}}{\text{m}^2 \cdot \text{s}}$$

This, of course, must yield the same mass flow rate per unit area as obtained from the particle continuity equation

$$g_s = \dot{N}_s'' m_s = (4.216 \times 10^{21})(1950) \left( \frac{3.14}{6} \right) (1 \times 10^{-8})^3$$

$$g_s = 4.303 \text{ kg/m}^2 \cdot \text{s}$$

which is reasonably close to the previously computed value of 4.59 kg/m<sup>2</sup> · s. Note also, that the mass of a single soot particle is

$$m_s = C_s V_s = (1950) \left(\frac{3.14}{6}\right) (1 \times 10^{-8})^3 = 1.02 \times 10^{-21} \text{ kg}$$

### 5.6) Operation Times to Fill Up Porous Filters with Captured Soot

Assume that a soot capturing filter is a porous sheet comprised of identical pores, with a porosity of

$$\epsilon = A_p / A_F$$

The number of pores is then given by

$$N_p = A_p / a_p$$

where  $a_p$  is the open area of a single pore. Then, by substitution

$$A_p = \epsilon A_F$$

and

$$N_p = \frac{\epsilon A_F}{a_p}$$

Hence, with the porosity of the filter and its pore sizes specified, the number of pores is determined. Assuming that each pore will fill up with  $n_p$  soot particles, then the number of soot particles filling the filter pores is

$$N_{SF} = n_p N_p = \frac{n_p \epsilon A_F}{a_p}$$

$N_{SF}$  is the number of soot particles sampled from beginning of the sampling process to the end, when the filter clogs up. Therefore,

$$N_{SF} = \dot{N}_s'' b A_{pr} t$$

where  $A_{pr}$  is the capture area of the sampling probe inlet,  $\beta$  is the capture efficiency of the probe, overall, and  $t$  is the sample period. By equating the expressions for  $N_{SF}$

$$N_{SF} = n_p N_p = \frac{n_p \epsilon A_F}{a_p} = \dot{N}_s'' \beta A_{pr} t$$

Therefore, the sample period time, for operating the sampling probe is

$$t = \frac{n_p \epsilon A_F}{N_s \beta A_{pr} a_p}$$

Thus, this equation is a system scaling equation, to assist in estimating how long the sample probe can be operated (or for selecting the size ( $m^2$ ) of filter required, etc.

#### 5.7) Soot Surface Area in Sample Flow

The soot surface area in the sample flow can be determined on the basis of the sample rate. The surface area per unit volume of mixture is given by

$$A_{SS} = N_s A_{sp} = (1.64 \times 10^{18}) (3.14 \times 10^{-16})$$

$$A_{SS} = \frac{515 \text{ m}^2 \text{ soot surface}}{\text{m}^3 \text{ of sample collected}}$$

Because this surface area is quite large, it is apparent that even a small fraction of it can result in complete coverage of the soot deposition filters.

This is again an indication that the gas/soot sampling probe system may have to be quite large in volume, and/or that the sampling times,  $t$ , will be rather short.

#### 5.8) Estimates of Sample Time, $t$ Based on Estimated Parametric Values for System Components

Based on an SEM photo of Nuclepore filters having  $5\mu\text{m}$  pore sizes, the porosity of the filter was estimated at  $\epsilon = 0.1$

That is, it appears that particle capturing filters are not very porous. Assuming a nominal size for the sampling probe inlet (cross-sectional) capture area diameter of one inch, or

$$D_{pr} = 1'' = 2.54^{-2}\text{m}$$

then the capture area for a shock-swallowing probe is

$$A_{pr} = \frac{\pi}{4} D_{pr}^2 = 5.067^{-4} \text{ m}^2$$

Assuming a filter size of 1m by 1m, or a filter-area of

$$A_F = 1 \text{ m}^2$$

then the sample capturing times can be estimated as follows, based on the computed sampling flux rate,  $\dot{N}_s''$ , calculated as

$$\dot{N}_s'' = 4.216 \times 10^{21} \frac{\text{part.}}{\text{m}^2 \cdot \text{s}}$$

Although the number of particles required to "fill up a pore",  $n_p$ , will be difficult to estimate with accuracy, a very simplistic value is given by

$n_p$  times a projected particle area =  $a_p$  (the pore area)

where,  $a_p$  is the pore open area. For a "5μm" pore size

$$a_p = \frac{\pi}{4} (d_p)^2 = 0.7854 (5 \times 10^{-6})^2$$

or,

$$a_p = 1.963 \times 10^{-11} \text{ m}^2$$

The particle projected area for single 0.01 μm particles

$$\text{particle projected area} = A_{sp_p} = A_{sp}/4$$

or,

$$A_{sp_p} = 7.85 \times 10^{-17} \text{ m}^2$$

Therefore, we obtain

$$n_p = a_p / A_{sp_p} = 1.963^{-11} / 7.85 \times 10^{-17}$$

or, at a minimum,

$$n_p = 250127 \text{ particles of } 0.01\mu\text{m diameter, to clog a } 5\mu\text{m pore.}$$

We have all the information required to compute  $t$  except  $\beta$ , the probe overall capture efficiency, which we take as unity. Therefore, computing the sampling time  $t$  as the time taken to clog up a filter, we get

$$t = \frac{n_p \cdot \epsilon \cdot A_F}{\dot{N}_s'' \beta \cdot A_{pr} \cdot a_p} = \frac{\epsilon \cdot A_F}{\dot{N}_s'' \beta \cdot A_{pr} \cdot A_{sp_p}} = \frac{4 \cdot \epsilon \cdot A_F}{\dot{N}_s'' \beta \cdot A_{pr} \cdot A_{sp}}$$

Hence  $t$  is given by

$$t = \frac{(0.10)(1.0)(2.5 \times 10^5)}{(4.21 \times 10^{21})(1.0)(5.067^{-4})(1.963^{-11})}$$

$$t = 5.97 \times 10^{-4} = 6 \times 10^{-4} \text{ sec} = 0.6 \text{ millisecond}$$

Therefore, the  $1\text{m}^2$  sample-capturing filter will clog up in less than a millisecond of gas/soot sample probe operation time, for a 1"-diameter probe inlet in the rocket exhaust stream. If the probe inlet diameter is reduced to 1/4", then

$$A_{pr} = 3.17 \times 10^{-5} \text{ m}^2$$

For this probe size,  $t$  is computed as

$$t = \frac{(0.1)(1.0)(2.5 \times 10^5)}{(4.21 \times 10^{21})(1.0)(3.17 \times 10^{-5})(1.963 \times 10^{-11})}$$

$$t = 9.5 \times 10^{-3} \text{ seconds} \approx 10\text{ms}$$

Thus, the sample or operation time increased from less than a millisecond to about 10 milliseconds. However, this too is a very short sampling time. A quick calculation based on a 1/10th inch diameter soot sampling probe yields a 60 millisecond sampling time. Therefore, it is apparent that the soot sampling probe must be designed with a large filter area, and also, it must be a dual operating mode probe. This dual operating mode design is outlined and discussed in the following section.

## **6.0 Design Concept for Dual Operating Mode Soot Capturing Probe**

The results of the heat transfer analysis and the capture rate calculations of sections 5 and 6, respectively, indicated conflicting design requirements. To reduce heat flux maxima, the size of the probe should be relatively large with relatively large nose and leading edge radius. of curvature. However, these cause the aerodynamics to become a problem with detached shock waves, etc., and also, the mass ingestion rate by the probe becomes quite large.

Even with the use of water spray cooling through spray ports to permit aerodynamically sharp leading edges, small nose radii, etc., the problem of significant mass ingestion and filter clogging remains a concern, unless, the probe has a dual mode of operation. Basically, the dual mode of operation is this: the probe can be designed to ingest a rocket exhaust flow isokinetically, using the concepts of the AFRPL and Naval Post-graduate School designs for shock-swallowing, internal jet-ejector pumping and flow dilution, etc. This ingested stream is then sampled isokinetically by a very much smaller internal sample tube that provides the much smaller sample to a filter apparatus for microscopic analysis. Thus, the main part of the isokinetically sampled stream is captured, diluted, partly water quenched and the considerable masses collected. From this stream, however, a very much smaller stream is withdrawn and sent to filters of appropriate dimension.

Figure 4 shows a schematic of the dual mode concept for a soot sampling probe for rocket exhaust applications. The concept utilizes the water spray thermal protection for the nose tip and the leading edge of the support sting of the probe. Internally, dry N<sub>2</sub> is supplied to an internal, backward-facing ejector-jet system to help pump the sampled stream and ensure shock swallowing operation. This N<sub>2</sub> flow mixes with the sampled stream and dilutes and partially quenches it. In the center of the probe is a much smaller isokinetic sampling tube that extracts a very small part of the sample flow and delivers it to some type of filter arrangement. This tube can be 1/10" or smaller in diameter, according to calculations made using the theory of reference 2-2, section 2.

Note that the sketch of Figure 4 shows that the nose tips or probe inlets are detachable. Therefore, nose damage can be quickly repaired, or, alternate nose tip designs (geometry) can be quickly installed for experimental development testing. Further, because of the spray cooling thermal protection arrangement, the probe can be fabricated from thin-walled stainless steel for relative strength.

Details of the design concept shown in Figure 4 have been developed by the author and with the assistance of a design engineer, work can begin on the engineering design and fabrication of this probe concept. A test plan for this probe or one of even smaller scale, can be prepared so that experimental validation and development of the probe may begin.

As a final remark, it should be noted that analytical models can be developed of the aerodynamic flow up to, over, and internally in the probe. These models can range from one-dimensional stream tube flow with soot-oxidation chemical kinetics, to elaborate, parabolized Navier-Stokes calculations, with shock-capturing, particle dynamics and different real-gas or chemical kinetic composition models. Such models can help to analyze the probe performance. However, the author recommends small-scale experimental probes be built and tested first, to justify the practicality of the design, before elaborate analytical models are developed.

## **7.0 Summary**

From the results of the present study, the author believes that requirement for a practical, soot sampling probe for surveying hydrocarbon-fueled liquid rocket exhaust flows can be satisfied by a probe of the type illustrated in Figure 4 of this study. The need to sample soot in such an environment had been established by R. S. Heirs, III, among others, and the author was given the opportunity to try to develop a potentially viable probe design with the support of a 1994 Summer Faculty Project Research Position at the USAF Arnold Engineering Development Center, Arnold AFB, Tennessee. A dual-mode probe design concept is suggested based on shock-swallowing, isokinetic sampling probe designs that have been reported in the literature. The dual-mode probe concept is an extension and modification, or adaptation of these designs. It is suggested that a prototype probe be built to a small scale that can be affordably tested and the design verified. Following the experimental development, larger scale probes could be designed and built with confidence, together with analytical models of such probes.

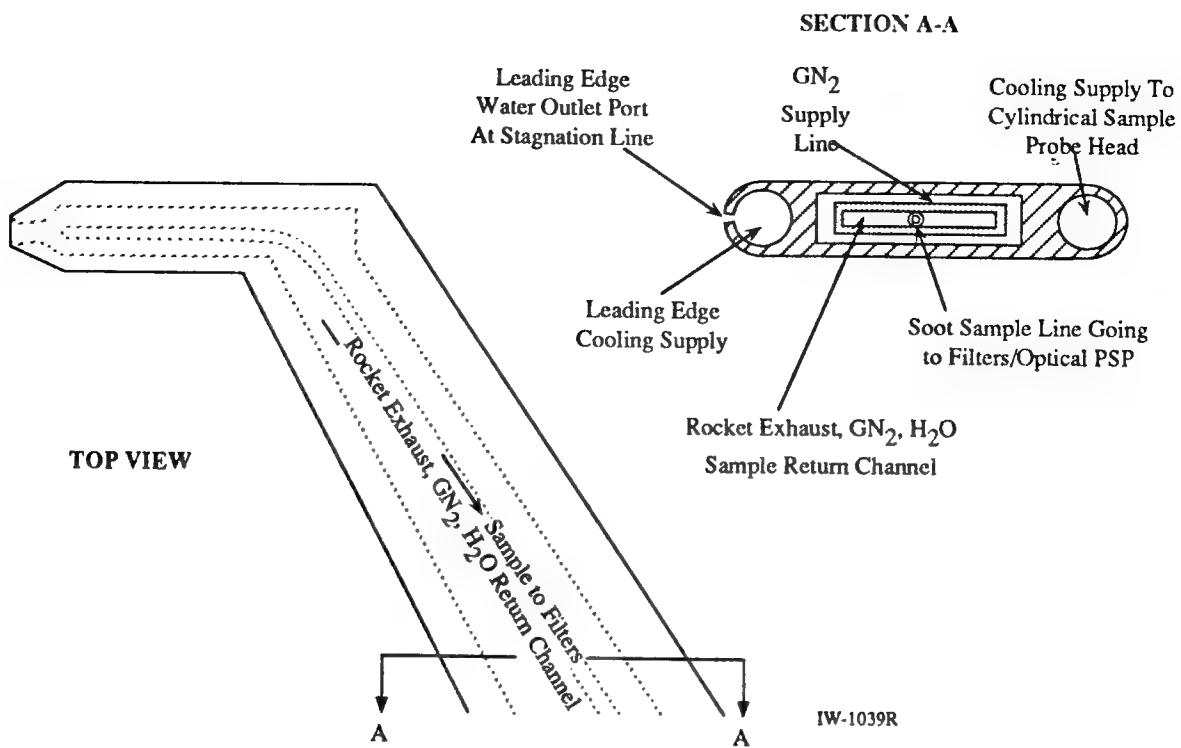


Figure 4. Simplified Configuration Schematic of Dual Soot Sampling Probe: Part 1 - General Configuration

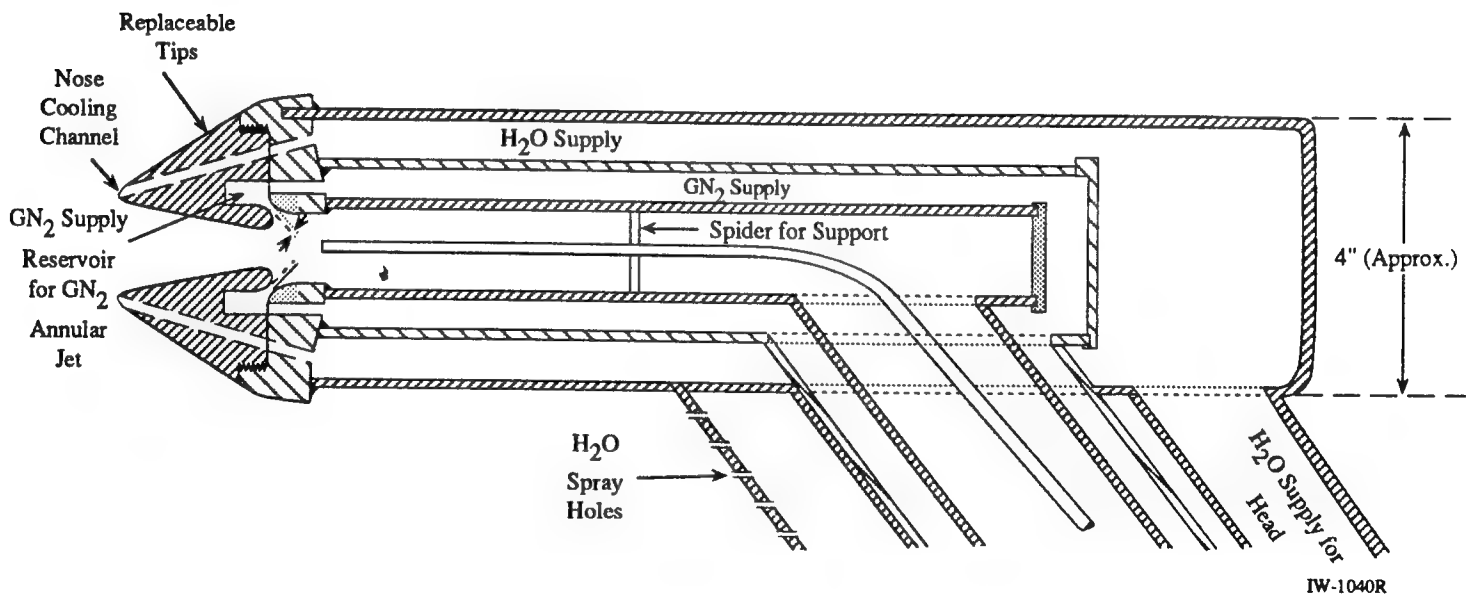


Figure 4 (Continued). Schematic of Dual Soot Sampling Probe: Part 2 - Details of Sample Probe Head

A MODEL FOR LOCAL HEAT TRANSFER AND ICE ACCRETION  
IN HIGH SPEED SUBSONIC FLOW OVER AN AIRFOIL

S.A. Sherif  
Associate Professor  
Department of Mechanical Engineering

University of Florida  
228 MEB  
Gainesville, Florida 32611

Final Report for:  
Summer Faculty Research Program  
Arnold Engineering Development Center

Sponsored by:  
Air Force Office of Scientific Research  
Bolling Air Force Base, DC

and

Arnold Engineering Development Center

September 1994

A MODEL FOR LOCAL HEAT TRANSFER AND ICE ACCRETION  
IN HIGH SPEED SUBSONIC FLOW OVER AN AIRFOIL

S.A. Sherif  
Associate Professor  
Department of Mechanical Engineering  
University of Florida

Abstract

Icing occurs on the forward-facing surfaces of aircraft when they encounter clouds of supercooled water droplets. The rate and nature of the ice accreting on the surface are functions of the flight speed and altitude, aircraft configuration, cloud liquid water content, water droplet size and distribution, and ambient temperature. Icing clouds can either be stratus or cumulus. The former type has a large horizontal extent and depth, a moderate liquid water content, and an altitude of 5,000 ft. Cumulus clouds, on the other hand, have a small horizontal extent, a large liquid water content, and an altitude of 10,000 ft. Temperature and droplet size are similar for both types of clouds, however.

The object of this research effort is to develop a semi-empirical model for determining the local heat transfer and ice accretion rates on the surface of an airfoil under a host of scenarios that involve changing the flight speed and altitude, cloud liquid water content, water droplet size and distribution and ambient temperature. The model is general enough to handle both the leading edge and aft regions of the airfoil under laminar and turbulent flow conditions. The model is also capable of handling conditions that involve equilibrium surface temperatures near the freezing point so that freezing, condensation, sublimation, and evaporation can occur simultaneously.

# A MODEL FOR LOCAL HEAT TRANSFER AND ICE ACCRETION IN HIGH SPEED SUBSONIC FLOW OVER AN AIRFOIL

S. A. Sherif

## Introduction

Icing of an aircraft occurs when it flies through a cloud of small supercooled water droplets. A portion of the water droplets impinges on the aircraft components and results in ice formation. The growth of ice on an aircraft wing results in a sharp increase in drag and a reduction in lift. This causes a deterioration in the aerodynamic performance of the aircraft. From a thermodynamics stand point, however, two types of ice accretion mechanisms have been identified, resulting in two physically and geometrically different formations. For low liquid water content, air temperature, and flight speed, the accreting ice is characterized by a white opaque color and a low density (less than  $1 \text{ gm/cm}^3$ ). This formation is called rime ice and is more likely to occur on relatively streamlined shapes extending into the incoming air. Rime ice forms upon impact of the water droplets with the surface and is characterized by a freezing fraction of unity. When both the liquid water content and the flight speed are high, while the air temperature is near freezing, the resulting ice formation will be characterized by a clear color and a density near  $1 \text{ gm/cm}^3$ . This mechanism of formation results in glaze ice which is usually associated with the presence of liquid water and a freezing fraction less than one.

Early work on aircraft icing was characterized by disagreement on the physical processes responsible for ice formation. Taylor (1940) was the first to develop the differential equation governing droplet trajectories for the special cases of constant drag coefficient and Stokes low drag. Glauret (1940) determined the local collection efficiencies by combining the droplet trajectories obtained by Taylor (1940). Extensive research on aircraft icing began during World War II and continued through the mid 1950's. For example, Langmuir and Blodgett (1946) presented their landmark work in the area of droplet trajectory calculation shortly after the end of the War. However, research slowed down significantly towards the end of the 1950's and throughout the 1960's. In the early 1970's, Japan and Canada began an ambitious program with a particular emphasis on the thermodynamics of the ice accretion process. Recent work on the subject includes that of Kirby and Hansman (1986), Van Fossen et al. (1984), Pais et al. (1988), Lozowski and Olsekiw (1981), Bragg and Gregorek (1983), Bartlett and Foster (1990), Wright

et al. (1988), Newton et al. (1988), and Cebeci and Besnard (1994).

The objective of this effort is to develop a generalized model capable of describing the local heat transfer and ice accretion rates on an airfoil surface under a host of environmental conditions. Heat transfer and ice accretion rates are influenced by the air speed and temperature, liquid water content, droplet size and distribution, and body geometry. The model presented here permits a parametric analysis of the local heat transfer and ice accretion rates for different scenarios of freezing/sublimation/evaporation combinations for both laminar and turbulent flow conditions along the airfoil surface.

### Analysis

The analysis described in this section is based on the assumption that the rate of energy added to a section of an airfoil equals the rate of energy removed from the same section. This analysis can later be used in a quasi-steady state context in which steady state conditions are allowed to exist for sufficiently small time intervals. Computing future values can then proceed utilizing those values computed from the previous time step.

The energy added comprises terms which are due to freezing, aerodynamic heating, droplet kinetic energy, and external sources (such as the deicing heater). The energy removed, on the other hand, includes terms which are due to convection, evaporation, sublimation, droplet warming, and aft conduction. The analysis will be carried out for an airfoil for both the leading edge and the after body regions. In general, either the flat plate approximation or the wedge flow approximation may be used for purposes of computing the heat and mass transfer rates. This analysis utilizes the flat plate approximation for the two extreme cases of laminar and turbulent flow. The analysis will be general enough to handle both low speed flows as well as high speed subsonic compressible flow conditions.

Figure 1 illustrates the different modes of energy transfer to and from an accreting ice surface which is representative of the leading edge of an airfoil. The steady state energy balance can be expressed as:

$$\dot{q}_f + \dot{q}_{aero} + \dot{q}_{drop} + \dot{q}_{ext} = \dot{q}_c + \dot{q}_e + \dot{q}_{sub} + \dot{q}_{warm} + \dot{q}_{aft} \quad (1)$$

The heat flux to the surface due to the freezing of the impinging water may be expressed by:

$$\dot{q}_f = \dot{m}_f'' [\lambda_f + c_i(t_{fz} - t_s)] \quad (2)$$

where  $\dot{m}_f''$  is the mass flux of the fraction of water impinging on the surface and freezing into ice. Assuming that the freezing fraction,  $n_f$ , is defined by:

$$n_f = \dot{m}_f'' / \dot{m}_i'' \quad (3)$$

then the local mass flux of water impinging on the surface and freezing into ice may be expressed by:

$$\dot{m}_f'' = n_f \beta W V_\infty \quad (4)$$

The local collection efficiency,  $\beta$ , is defined as the ratio between the locally impinging droplet flux and the freestream droplet flux. This efficiency is governed by the ratio of the inertia of the impinging droplets and their aerodynamic drag. Aerodynamic drag exists because of the freestream flow field disturbance created by the airfoil. The local collection efficiency is primarily a function of the droplet size and distribution, water density and viscosity, freestream velocity, airfoil geometry, and angle of attack. This local collection efficiency may actually be viewed as a dimensionless mass flux of the water impinging at a particular location on the airfoil surface. Bragg (1982) reports that the nondimensionalization of the local collection efficiency is done with respect to the mass flux in the freestream. Thus, a collection efficiency of unity may simulate the dimensionless mass flux on an imaginary flat plate (that does not alter the freestream flow) placed perpendicular to the freestream.

Computing the local collection efficiency can be accomplished in a number of ways. For example, Brun et al. (1953 a,b) presented  $\beta$  for three types of airfoils at a  $4^\circ$  angle of attack as a function of the droplet Reynolds number, the profile distance  $s/L$ , and the reciprocal of the inertia parameter  $K_T^{-1}$ . The inertia parameter has been reported in the literature according to the following equation:

$$K_T = \frac{2}{9} \frac{a^2 \rho_w V_\infty}{L \mu} \quad (5)$$

However, this method requires that the droplet Reynolds number and inertia parameter be computed everytime there is a need to compute the local collection efficiency. Langmuir (1946)

used a modified inertia parameter,  $K_{T,o}$  to scale the local collection efficiency data to be applicable for any Reynolds number. The modified inertia parameter is defined as:

$$K_{T,o} = K_T (\eta/\eta_s) \quad (6)$$

Here  $\eta/\eta_s$  represents the ratio of the trajectory of a droplet in still air with an initial Reynolds number and no gravity divided by the same droplet trajectory if the drag is assumed to obey Stokes law. In general, closed form expressions for the modified inertia parameter can be found if an integrable form of the droplet drag coefficient is available (Bragg, 1982). Putnam (1961) developed such an equation for the drag coefficient and used it to obtain the following algebraic expression for the modified inertia parameter:

$$K_{T,o} = 18K_T [Re_{drop}^{-2/3} - \sqrt{6} Re_{drop}^{-1} \tan (\frac{Re_{drop}^{1/3}}{\sqrt{6}})] \quad (7)$$

The above equation is valid up to a droplet Reynolds number of 1000. An alternative approximate equation for  $K_{T,o}$  was given by Bowden et al. (1964) according to:

$$K_{T,o} = 1.87 \times 10^{-7} \left[ \frac{1.15 V_\infty}{\mu g} \right]^{0.6} \left[ \frac{d_{drop}^{1.6}}{12 \rho_\infty^{0.4} L} \right] \quad (8)$$

where the units of the variables given in Equation (8) are knots for the velocity,  $lb_f \cdot s / ft^2$  for the dynamic viscosity, ft for the chord length,  $lb_m / ft^3$  for the density, and  $ft/s^2$  for the gravitational constant. Equation (8) gives values within  $\pm 5\%$  for droplet Reynolds numbers ranging from 25 to 1000. The modified inertia parameter will be computed using Equation (8) for purposes of the model described here. The local collection efficiency can then be computed employing the graphical relationships given in several references for a number of airfoils at different angles of attack as a function of the distance along the airfoil surface and the modified inertia parameter (see Brun et al., 1953b for the NACA 65A004 airfoil, and Brun et al., 1953a for the NACA 65-208 and 65-212 airfoils).

The heat flux to the surface due to aerodynamic heating may be expressed by:

$$\dot{q}_{\text{aero}} = \frac{rh_c V_1^2}{2gJc_p} \quad (9)$$

where the boundary layer recovery factor,  $r$ , is given by Hardy (1946) as:

$$r = [1 - (V_1^2 / V_\infty^2) (1 - Pr^{n_1})] \quad (10)$$

The constant  $n_1$  is equal to 1/2 for laminar boundary layers and 1/3 for turbulent boundary layers. The local velocity at the outer edge of the boundary layer is usually given as a function of the chordwise distance of the airfoil. For example, Bowden et al. (1964) gives the ratio of the boundary layer edge velocity to the freestream velocity as a function of the ratio between the chordwise station to the airfoil chord length for the NACA 65<sub>1</sub>-208 and 65<sub>1</sub>-212 airfoils. Knowledge of the boundary layer edge velocity enables computing the pressure, temperature, and density of air at the outer edge. This can be accomplished employing the following relations which are particularly applicable for high speed flows where the freestream Mach number is larger than 0.3 (Johnson, 1947):

$$\frac{p_1}{p_\infty} = \left[ 1 + \sqrt{\frac{\gamma-1}{2}} M_\infty \left\{ \sqrt{\frac{\gamma-1}{2}} M_\infty - \left( \frac{V_1}{V_\infty} \right) \right\} \right]^{\frac{\gamma}{\gamma-1}} \quad (11)$$

$$\frac{T_1}{T_\infty} = \left( \frac{p_1}{p_\infty} \right)^{\frac{\gamma-1}{\gamma}} \quad (12)$$

$$\frac{\rho_1}{\rho_\infty} = \left( \frac{p_1}{p_\infty} \right)^{\frac{1}{\gamma}} \quad (13)$$

For some airfoils, the coefficient of pressure along the surface may be available in lieu of the velocity ratio  $V_1/V_\infty$  (see for example Abbott et al., 1945). In this case the pressure ratio should first be computed using the following expression:

$$\frac{p_1}{p_\infty} = 1 + \frac{\gamma}{2} M_\infty^2 C_p \quad (14)$$

The velocity at the outer edge of the boundary layer should then be found using the equation:

$$\frac{V_1}{V_\infty} = \sqrt{\frac{2}{\gamma-1}} \frac{1}{M_\infty} \left[ 1 + \left( \frac{\gamma-1}{2} \right) M_\infty^2 - \left( \frac{p_1}{p_\infty} \right)^{\frac{\gamma-1}{\gamma}} \right] \quad (15)$$

The temperature and density outside the boundary layer can still be determined employing Equations (12) and (13).

The convective heat transfer coefficient,  $h_c$ , is usually evaluated using empirical formulas appropriate for the geometry and the flow regime. Two approximations are commonly employed for purposes of computing the heat transfer coefficient for airfoils. The first is known as the flat plate approximation whereby the leading edge of the airfoil is replaced with a cylinder while the afterbody is replaced with a flat plate (Boelter et al., 1948 and Martinelli et al., 1943). This approximation is most accurate for full-scale thin airfoils in high-speed flows with long heating lengths (Sogin, 1954). The second approximation is the wedge flow approximation which is particularly useful for the entire laminar flow regime including both the leading edge and aft regions. The fluid properties are usually evaluated at the average temperature between the surface and the freestream,  $t_f$  (unless otherwise stated).

Schmidt and Wenner (1943) presented the following equation for computing the local convective heat transfer coefficient at angle  $\phi$  from the stagnation point on a heated cylinder:

$$Nu_d = 1.14 Re_d^{0.5} Pr^{0.4} \left[ 1 - \left| \frac{\phi}{90} \right|^3 \right] \quad (16)$$

where  $0 \leq \phi \leq 90^\circ$ . When applying Equation (16) to an airfoil, the leading edge having a radius of curvature of  $d/2$ , is replaced by the cylinder diameter,  $d$ . The latter quantity is commonly expressed as the ratio  $d/L$ . The angle  $\phi$  can be expressed as:

$$\phi = \frac{360 s}{\pi d} \quad (17)$$

Substituting the expression for  $\phi$  from Equation (17) into the Nusselt number expression of Equation (16) and replacing the cylinder diameter by the chord length as the characteristic distance in the Nusselt and Reynolds number terms, the following expression can be obtained:

$$Nu_L = Re_L^{0.5} Pr^{0.4} \left[ 1.14 \left( \frac{L}{d} \right) - 2.353072 \left( \frac{L}{d} \right)^{3.5} \left( \frac{s}{L} \right)^3 \right] \quad (18)$$

For the after region of the airfoil, two possibilities exist depending on the flow regime. For laminar flow, Martinelli et al. (1943) proposed the following equation:

$$Nu_L = 0.286 Re_L^{0.5} \left( \frac{V_1}{V_\infty} \right)^{0.5} \left( \frac{L}{s} \right)^{0.5} \quad (19)$$

For turbulent flow, the Nusselt number expression in the after region may be written as:

$$Nu_L = 0.0296 Pr^{1/3} Re_L^{0.8} \left( \frac{V_1}{V_\infty} \right)^{0.8} \left( \frac{L}{s} \right)^{0.2} \quad (20)$$

Once the Nusselt number has been computed, the convective heat transfer coefficient may be determined for a given air thermal conductivity. Bowden et al (1964) gave the following expression for the thermal conductivity:

$$k = \frac{0.001533 (T/1.8)^{1.5}}{T/1.8 + 245.4 (10^{-12/(T/1.8)})} \quad (21)$$

where  $T$  is in  $^{\circ}R$  and  $k$  is in Btu/hr.ft.  $^{\circ}F$ . The heat flux to the surface due to droplet kinetic energy can be expressed as follows:

$$\dot{q}_{drop} = \frac{\dot{m}_i V_1^2}{2gJc_p} \quad (22)$$

Terms included in the above equation have been described earlier in the analysis. External sources of input energy to the airfoil (such as the deicing heater) are incorporated in the analysis

in the interest of making the model more general. This term has to be specified *a priori*.

The analysis described so far covered all terms contributing to increasing the energy content of the airfoil. As mentioned earlier, there are primarily five mechanisms that contribute to energy losses from an airfoil; convection, evaporation, sublimation, droplet warming, and aft conduction. Since the analysis presented here is intended to treat both the leading edge and afterbody regions, the aft conduction term will be ignored. This term is more relevant to analyses pertaining to the leading edge region only.

The convective heat flux from the airfoil surface may be written as:

$$\dot{q}_c = h_c (t_s - t_l) \quad (23)$$

Terms in Equation (23) have all been described earlier. The temperature  $t_l$  at the outer edge of the boundary layer can be computed from Equation (12). Evaporation and sublimation from the airfoil surface are unlikely to occur simultaneously unless the surface temperature is in the vicinity of the freezing point and both ice and water are simultaneously present. Messinger (1953) provided a detailed analysis of the equilibrium temperature of an unheated icing surface for several scenarios of dry and wet icing conditions. The model described here deals with the general case of partial freezing (as expressed by the freezing fraction  $n_f$ ) as well as partial evaporation and partial sublimation. In other words, the analysis takes into account the possibility that evaporation and sublimation would occur simultaneously.

Liquid water present on the airfoil surface may be a direct result of water impinging on the surface or it may be due to melting of some of the ice already in existence. Ice melting may occur due a variety of reasons such as aerodynamic heating, droplet kinetic energy, or the deicing heater. In order to contain the complexity of this model, liquid water present on the surface will be assumed to result solely from direct impinging. Since the freezing fraction represents the portion of the impinging water freezing into ice, the remaining amount should represent the portion that remains as liquid. This may be mathematically expressed by the following equation:

$$\dot{m}_l'' = \dot{m}_i'' - \dot{m}_f'' \quad (24)$$

In general, some of the liquid present on the surface would evaporate, while some of the ice would sublimate. In order to account for these two possibilities, two additional quantities

will be defined; an evaporation fraction  $n_e$  and a sublimation fraction  $n_s$ . These terms may be mathematically expressed as follows:

$$n_e = \frac{\dot{m}_e''}{\dot{m}_{e,\max}''} = \frac{\dot{m}_e''}{\dot{m}_l''} = \frac{\dot{m}_e''}{\dot{m}_i'' - \dot{m}_f''} = \frac{\dot{m}_e''}{\dot{m}_i''(1 - n_f)} \quad (25)$$

$$n_s = \frac{\dot{m}_s''}{\dot{m}_{s,\max}''} = \frac{\dot{m}_s''}{\dot{m}_f''} = \frac{\dot{m}_s''}{\dot{m}_i'' n_f} \quad (26)$$

The maximum amount of water that can be evaporated (or the evaporation potential) is equal to the amount of liquid water present on the surface and can be expressed by the following equation according to Sogin (1954):

$$\dot{m}_{e,\max}'' = \dot{m}_l'' = \frac{h_v p_1}{R_a T_f} \left[ \frac{M_v}{M_a} \left\{ \frac{p_{v,w}}{p_1 - p_{v,w}} - \left( \frac{p_{v,\infty}}{p_\infty} \right) \frac{p_1}{p_1 - p_{v,w}} \right\} \right] \quad (27)$$

The above equation assumes that the water vapor behaves like a thermally perfect gas which allows the thermodynamic properties of the vapor to be calculated as though the air were not present. It also allows the densities of the water vapor at the airfoil surface and at the boundary layer edge ( $\rho_{v,w}$  and  $\rho_{v,1}$ , respectively) to be evaluated in terms of the partial pressures of the vapor (so that  $\rho_v = p_v/(R_v T)$ ). Equation (27) also accounts for the influence of induced convection. Since the sum of the partial pressures of the air and water vapor is virtually uniform across the boundary layer, along any normal to the surface, a decrease in the vapor partial pressure would increase the air partial pressure and cause the air to diffuse toward the surface. However, since the air cannot penetrate the surface, a counter convection of air takes place, thus resulting in removing additional vapor from the vicinity of this surface.

The water vapor pressure terms appearing in Equation (27) can be computed using empirical correlations. For the temperature range  $492 \leq T \leq 672^\circ R$ , Pelton and Willbanks (1972) provided the following equation:

$$p_{v,w} = 2117 \left( \frac{672}{T} \right)^{5.19} \exp \left[ -9.06 \left( \frac{\lambda_e}{T} - 1.4525 \right) \right] \quad (28)$$

where  $T$  is in  $^{\circ}\text{R}$ ,  $p_{v,w}$  is in  $\text{lb}_f/\text{ft}^2$  absolute, and  $\lambda_e$  is the latent heat of vaporization which can be expressed by:

$$\lambda_e = 1352.3 - 0.5696 T + 0.0839 \times 10^{-4} T^2 + 0.0927 \times 10^{-7} T^3 \quad (29)$$

For a supercooled liquid at a temperature less than  $492^{\circ}\text{R}$ , Dorsey (1940) provided the following correlation:

$$p_{v,w} = 2117 \exp \left[ 2.3 \left\{ A_1 + \frac{A_2}{(T/1.8)} + \frac{A_3((T/1.8)^2 - A_7)}{(T/1.8)} (10^{[A_4((T/1.8)^2 - A_7)^2]} - 1) + A_5(10^{[A_6(374.11 - (T/1.8))^{5/4}]} \right\} \right] \quad (30)$$

where the constants are as follows:  $A_1 = 5.4266514$ ,  $A_2 = -2005.1$ ,  $A_3 = 1.3869 \times 10^{-4}$ ,  $A_4 = 1.1965 \times 10^{-11}$ ,  $A_5 = -4.4 \times 10^{-3}$ ,  $A_6 = -5.7148 \times 10^{-3}$ , and  $A_7 = 2.937 \times 10^5$ .

The mass transfer coefficient,  $h_v$ , may be related to the heat transfer coefficient,  $h_c$ , employing the Lewis analogy. This gives:

$$h_v = h_c / (\rho c_p Le^{2/3}) = h_c / [\rho c_p (\frac{\alpha}{D})^{2/3}] \quad (31)$$

The coefficient of mass diffusion of water vapor in air,  $D$ , may be computed using the following empirical relationship (ASHRAE, 1993):

$$D = \frac{0.00215}{p} [ T^{2.5} / (T + 441) ] \quad (32)$$

where the pressure is in psia, the temperature is in  $^{\circ}\text{R}$ , and the diffusion coefficient is in  $\text{ft}^2/\text{hr}$ . The specific heat at constant pressure of air,  $c_p$ , may be computed using the following correlation (Keenan and Kaye, 1961):

$$c_p = 0.2318 + 0.1040 \times 10^{-4} T + 0.7166 \times 10^{-8} T^2 \quad (33)$$

Again,  $T$  is in  $^{\circ}\text{R}$ , while  $c_p$  is in  $\text{Btu}/\text{lb}_m \cdot ^{\circ}\text{F}$ . The above correlation is valid in the range

$400 \leq T \leq 1700^{\circ}\text{R}$ . The heat flux leaving the surface due to evaporation may, thus, be expressed by:

$$\dot{q}_e = \lambda_e \dot{m}_e'' \quad (34)$$

Similarly, the maximum amount of ice that can be sublimated (or the sublimation potential) is equal to the amount of ice present on the surface and can be expressed by:

$$\dot{m}_{s,\max}'' = \dot{m}_f'' = \frac{h_v p_1}{R_a T_f} \left[ \frac{M_v}{M_a} \left\{ \frac{p_{v,i}}{p_1 - p_{v,i}} - \left( \frac{p_{v,\infty}}{p_\infty} \right) \frac{p_1}{p_1 - p_{v,i}} \right\} \right] \quad (35)$$

where the partial vapor pressure at the surface over ice was given by Dorsey (1940) as:

$$p_{v,i} = 2.7845 \exp \left[ 2.3 \left\{ \frac{B_1}{(T/1.8)} + 0.4343 B_2 \log_e (T/1.8) + B_3 (T/1.8) + B_4 (T/1.8)^2 + B_5 \right\} \right] \quad (36)$$

and the constants are:  $B_1 = -2.4455646 \times 10^3$ ,  $B_2 = 8.2312$ ,  $B_3 = 1.677006 \times 10^{-2}$ ,  $B_4 = 1.20514 \times 10^{-5}$ , and  $B_5 = -6.757169$ . The resulting vapor pressure is in  $\text{lb}_f/\text{ft}^2$  absolute.

It is important to note, in applying Equation (35) to compute the rate of sublimation, that the mass and heat transfer coefficients were assumed to remain unchanged vis-a-vis ice and water. This assumption, although not exact, is not totally inaccurate based on experimental evidence. The heat flux due to sublimation can similarly be expressed by:

$$\dot{q}_{\text{sub}} = \dot{m}_s'' \lambda_s \quad (37)$$

The heat flux leaving the surface due to droplet warming may be determined using the equation:

$$\dot{q}_{\text{warm}} = \dot{m}_i'' c_w (t_{fz} - t_i) \quad (38)$$

The equilibrium surface temperature can, in principle, be determined by solving Equation (1) after substituting the corresponding expressions for the different heat flux terms. Since it is difficult to solve the resulting equation for  $t_s$  in closed form, an iterative procedure may be used. This procedure can proceed by assuming a trial value for  $t_s$  and solving for the net heat flux and continuing the iteration until the net heat flux becomes zero. The model presented may also be

used by specifying a value for the equilibrium surface temperature *a priori* and determining the conditions necessary to satisfy that equilibrium temperature.

### Method of Solution

The model described above requires knowledge of the following variables *a priori*: Freestream static pressure (altitude pressure)  $p_\infty$ , freestream static temperature  $t_\infty$ , flight speed  $V_\infty$  or flight Mach number  $M_\infty$ , cloud liquid water content  $W$ , volume median droplet diameter  $d_{\text{drop}}$ , airfoil configuration and angle of attack, equilibrium surface temperature  $t_s$ , evaporation fraction  $n_e$ , and sublimation fraction  $n_s$ .

For a given airfoil, the ratio of the boundary layer outer edge velocity to the freestream velocity  $V_1/V_\infty$  may be obtained as a function of the nondimensional chordwise distance  $x/L$ . Knowledge of  $V_1/V_\infty$  and the freestream Mach number can then be used to compute  $p_1/p_\infty$ ,  $T_1/T_\infty$ , and  $\rho_1/\rho_\infty$  from Equations (11), (12), and (13), respectively, as functions of the chordwise distance. The velocity, pressure, temperature, and density profiles can be converted to their counterparts in terms of the nondimensional profile distance  $s/L$  using the method described by Falkner (1953). The modified inertia parameter  $K_{T,0}$  can be obtained from Equation (8) knowing the flight speed  $V_\infty$ , volume median droplet diameter  $d_{\text{drop}}$ , airfoil chord length  $L$ , and freestream air density  $\rho_\infty$  and dynamic viscosity  $\mu$ . The local collection efficiency  $\beta$  can be computed for the airfoil in question knowing the modified inertia parameter, angle of attack, and nondimensional profile distance  $s/L$  (see for example Brun et al., 1953 a,b). Knowledge of the local liquid water content  $W$  enables computing the local impinging droplet flux as a function of the nondimensional profile distance  $s/L$ .

The evaporation potential (or the maximum rate of evaporation) can be determined using Equation (27) as follows. First, the coefficient of mass diffusion of water vapor in air  $D$  is obtained from Equation (32) at the average boundary layer film temperature  $t_f$ . The convective heat transfer coefficient  $h_c$  is then found for both the airfoil leading edge and aft regions. For the leading edge region,  $h_c$  is determined from Equation (16) as a function of the angular position from the stagnation point,  $\phi$ , and for the aft region from either Equations (19) or (20) based on the flow regime. The mass transfer coefficient  $h_v$  is then determined using the Lewis analogy [Equation (31)] and the knowledge of  $h_c$  and  $c_p$ . The air specific heat is found from Equation (33) at the film temperature  $t_f$ . The vapor pressure over water at the surface

temperature  $t_s$  can then be found from Equation (28) if  $t_s \geq 32^\circ\text{F}$  or from Equation (30) if  $t_s < 32^\circ\text{F}$ . The vapor pressure at the freestream  $p_{v,\infty}$  can be found in a similar manner employing either Equation (28) or (30) depending on the value of  $t_\infty$ . The evaporation potential (also equal to the mass flux impinging on the surface and remaining as liquid) is then determined employing Equation (27). The actual evaporative mass flux is computed from Equation (25) knowing the evaporation fraction  $n_e$ . The evaporative heat flux leaving the surface can be computed using Equation (34) knowing the latent heat of vaporization  $\lambda_e$ . This latter quantity is, in turn, found from Equation (29) at the surface temperature  $t_s$ .

In a similar manner, the sublimation potential (also equal to the mass flux impinging on the surface and freezing into ice) can be found using Equation (35) knowing the vapor pressure over ice  $p_{v,i}$ . This latter quantity can, in turn, be found employing Equation (36) at the surface temperature  $t_s$ . The actual mass flux subliming, can be determined from Equation (26) with the knowledge of the sublimation fraction  $n_s$ . The heat flux due to sublimation can be found from Equation (37) knowing the latent heat of sublimation  $\lambda_s$ .

Since the mass flux impinging on the surface and freezing into ice is assumed equal to the sublimation potential, the freezing fraction  $n_f$  can now be determined employing Equation (3). The heat flux due to freezing is found from Equation (2) knowing the latent heat of fusion of ice  $\lambda_f$  and the specific heat of ice  $c_i$ .

Determination of the heat flux due to aerodynamic heating may be accomplished using Equation (9) knowing the boundary layer recovery factor  $r$ . This factor is, in turn, found from Equation (10) with the knowledge of the velocity ratio  $V_i/V_\infty$  and the Prandtl number. Naturally, the recovery factor is a function of the local position on the airfoil surface. The Prandtl number depends in part on the thermal conductivity of air which can, in turn, be determined from Equation (21) at the boundary layer film temperature  $t_f$ . Determination of the heat flux due to droplet kinetic energy is relatively straightforward using Equation (22). Also, the convective heat flux can easily be determined from Equation (23) knowing  $h_c$  and  $t_s$ . And finally, the heat flux due to droplet warming is found from Equation (38) knowing and the liquid water specific heat  $c_w$ .

After all the heat flux quantities have been determined, the heat balance at every position on the airfoil surface should be checked to ensure that Equation (1) is always satisfied. If that is not the case, another value of  $t_s$  should be assumed and the procedure repeated until

Equation (1) is satisfied.

### Conclusions

The preceding analysis provides the basis of a relatively general semi-empirical model capable of analyzing the energy and mass balances over the surface of any airfoil in high speed subsonic compressible flow for both laminar and turbulent conditions. The model determines the different mass and energy fluxes by assuming *a priori* knowledge of an evaporation fraction  $n_e$  and a sublimation fraction  $n_s$ . Based on the assumption that evaporation and sublimation may occur simultaneously and that the only source of liquid water present on the surface is direct impinging (as opposed to ice melting), the freezing fraction  $n_f$  is computed. The model allows for a continuous check on whether the surface temperature selected upfront is indeed the equilibrium temperature. This check is possible for every point on the airfoil surface and thus leaves the door open for the variability of the surface temperature along the surface. The model does not account for chordwise conduction, however.

### Nomenclature

A	surface area, $\text{ft}^2$
$A_1-A_7$	constants defined by Equation (30)
a	droplet radius, ft or microns
$B_1-B_5$	constants defined by Equation (36)
$c_i$	specific heat of ice, $0.485 \text{ Btu/lb}_m \cdot {}^\circ\text{F}$
$c_p$	specific heat at constant pressure of air, $\text{Btu/lb}_m \cdot {}^\circ\text{F}$
$C_p$	pressure coefficient, dimensionless
$c_v$	specific heat at constant volume of air, $\text{Btu/lb}_m \cdot {}^\circ\text{F}$
$c_w$	specific heat of liquid water, $1 \text{ Btu/lb}_m \cdot {}^\circ\text{F}$
D	coefficient of diffusion of water vapor in air, $\text{ft}^2/\text{hr}$
d	diameter, ft
$d_{\text{drop}}$	volume median droplet diameter, ft or microns
g	gravitational constant, $32.17 \text{ lb}_m \cdot \text{ft/lb}_f \text{s}^2$
$h_c$	local convective heat transfer coefficient, $\text{Btu/hr.ft}^2 \cdot {}^\circ\text{F}$
$h_v$	local mass transfer coefficient, $\text{ft/hr}$
J	mechanical equivalent of heat = $778.26 \text{ ft.lb}_f/\text{Btu}$
k	thermal conductivity of air, $\text{Btu/hr.ft.}^\circ\text{F}$
$K_T$	inertia parameter, dimensionless
$K_{T,0}$	modified inertia parameter, dimensionless
L	airfoil chord length, ft
Le	Lewis number, $\text{Sc}/\text{Pr}$ or $\alpha/\text{D}$ , dimensionless
$M_\infty$	freestream Mach number

$M_a$	molecular weight of dry air, 28.966 lb/lb <sub>mole</sub>
$M_v$	molecular weight of water vapor, 18.0160 lb/lb <sub>mole</sub>
$\dot{m}_e$	local mass flux evaporating from the surface, lb <sub>m</sub> /ft <sup>2</sup> .hr
$\dot{m}_{e,max}$	evaporation potential, lb <sub>m</sub> /ft <sup>2</sup> .hr
$\dot{m}_f$	local mass flux of water impinging on the surface and freezing into ice, lb <sub>m</sub> /hr.ft <sup>2</sup>
$\dot{m}_i$	local mass flux of water impinging on the surface, lb <sub>m</sub> /ft <sup>2</sup> .hr
$\dot{m}_l$	local mass flux impinging on the surface and remaining as liquid water, lb <sub>m</sub> /ft <sup>2</sup> .hr
$\dot{m}_s$	local mass flux subliming from the surface, lb <sub>m</sub> /ft <sup>2</sup> .hr
$\dot{m}_{s,max}$	sublimation potential, lb <sub>m</sub> /ft <sup>2</sup> .hr
$n_e$	evaporation fraction, dimensionless
$n_f$	freezing fraction, dimensionless
$n_s$	sublimation fraction, dimensionless
$n_l$	constant equal to 1/2 for laminar and 1/3 for turbulent boundary layers
$Nu_d$	Nusselt number based on cylinder diameter, $h_c d / \kappa$ , dimensionless
$Nu_L$	Nusselt number based on chord length, $h_c L / \kappa$ , dimensionless
$Pr$	Prandtl number = $\mu c_p / \kappa$ , dimensionless
$p_1$	local static pressure at the outer edge of the boundary layer, psia
$p_{v,i}$	water vapor pressure over ice, psia
$p_{v,w}$	water vapor pressure at the surface, psia
$p_{v,1}$	water vapor pressure at the outer edge of the boundary layer, psia
$p_{v,\infty}$	water vapor pressure at the freestream, psia
$p_\infty$	static pressure at the freestream (altitude pressure), psia
$\dot{q}_{aft}$	local heat flux from surface due to aft conduction, Btu/hr.ft <sup>2</sup>
$\dot{q}_{aero}$	local heat flux to surface due to aerodynamic heating, Btu/hr.ft <sup>2</sup>
$\dot{q}_c$	local heat flux from surface due to convection, Btu/hr.ft <sup>2</sup>
$\dot{q}_{drop}$	local heat flux to surface due to droplet kinetic energy, Btu/hr.ft <sup>2</sup>
$\dot{q}_e$	local heat flux from surface due to evaporation, Btu/hr.ft <sup>2</sup>
$\dot{q}_{ext}$	local heat flux to surface due to external sources, Btu.hr.ft <sup>2</sup>
$\dot{q}_f$	local heat flux to surface due to water freezing, Btu/hr.ft <sup>2</sup>
$\dot{q}_{sub}$	local heat flux from surface due to sublimation, Btu/hr.ft <sup>2</sup>
$\dot{q}_{warm}$	local heat flux from surface due to droplet warming, Btu/hr.ft <sup>2</sup>
$r$	boundary layer recovery factor, dimensionless
$R_v$	gas constant of water vapor, 85.778 ft.lb <sub>f</sub> /lb <sub>m</sub> .°R
$R_a$	gas constant of dry air, 53.352 ft.lb <sub>f</sub> /lb <sub>m</sub> .°R
$Re_d$	Reynolds number based on cylinder diameter, $\rho V_\infty d / \mu$
$Re_{drop}$	Reynolds number based on droplet diameter, $\rho V_\infty d_{drop} / \mu$
$Re_L$	Reynolds number based on chord length, $\rho V_\infty L / \mu$
$s$	distance along airfoil surface measured from leading edge, ft
$s_u$	upper surface impingement limit, ft
$s_l$	lower surface impingement limit, ft
$Sc$	Schmidt number, $\nu / D$ , dimensionless
$t_f$	average temperature between surface and freestream, °F
$t_{fz}$	freezing temperature of water, 32°F

$t_s$	equilibrium surface temperature, °F
$t_1$	local static temperature at the outer edge of the boundary layer, °F
$t_\infty$	freestream temperature, °F
T	absolute temperature, °R
$V_\infty$	freestream velocity, ft/s
$V_1$	local velocity at the outer edge of the boundary layer, ft/s or knots
W	cloud liquid water content, gm/m <sup>3</sup>
$\alpha$	thermal diffusivity, ft <sup>2</sup> /hr
$\beta$	local collection efficiency, dimensionless
$\gamma$	ratio of specific heats $c_p/c_v$ , 1.405 dimensionless
$\mu$	dynamic viscosity of air, slug/ft.s or lb <sub>m</sub> /ft.hr
$\nu$	kinematic viscosity of air, ft <sup>2</sup> /hr
$\lambda_e$	latent heat of vaporization of water, Btu/lb <sub>m</sub>
$\lambda_f$	latent heat of fusion of ice, 144 Btu/lb <sub>m</sub> , °F
$\lambda_s$	latent heat of sublimation of ice, Btu/lb <sub>m</sub>
$\eta$	trajectory of a droplet in still air with no gravity
$\eta_s$	trajectory of a droplet assuming drag to obey Stokes law
$\rho_w$	density of liquid water, lb <sub>m</sub> /ft <sup>3</sup> or slug/ft <sup>3</sup>
$\rho_1$	local air density at the outer edge of the boundary layer, slug/ft <sup>3</sup> or lb <sub>m</sub> /ft <sup>3</sup>
$\rho_\infty$	freestream air density, slug/ft <sup>3</sup> or lb <sub>m</sub> /ft <sup>3</sup>
$\phi$	angle from the stagnation point of airfoil, degrees

## References

Abbott, I.H., Van Doenhoff, A.E., and Stivers, L.S., Jr., "Summary of Airfoil Data," NACA ACR L5C05.

ASHRAE, 1989, *Handbook of Fundamentals*, The American Society of Heating, Refrigerating and Air-Conditioning Engineers, Inc. Atlanta, Georgia.

Bartlett, C.S. and Foster, R.G., 1990, "The Effect of Experimental Uncertainties on Icing Test Results," *28th Aerospace Sciences Meeting*, Reno, NV, January 8-11, AIAA Paper 90-0665.

Boelter, L.M.K., Grossman, L.M., Martinelli, R.C., and Morrin, E.H., 1948, "An Investigation of Aircraft Heaters, XXIX - Comparison of Several Method of Calculating Heat Losses from Airfoils," NACA Technical Note 1453.

Bowden, D.T., Gensemer, A.E., and Skeen, C.A., 1964, "Engineering Summary of Airframe Icing Technical Data," Federal Aviation Agency, Technical Report No. ADS-4, Contract FA-WA-4250, Washington, D.C., March.

Bragg, M.B., 1982, "Rime Ice Accretion and Its Effect on Airfoil Performance," NASA Contractor Report 165599, Lewis Research Center, Grant NAG 3-28, March.

Bragg, M.B. and Gregorek, G.M., 1983, "An Analytical Evaluation of the Icing Properties of Several Low and Medium Speed Airfoils," *21st Aerospace Sciences Meeting*, Reno, NV, January 10-13, AIAA Paper 83-0109.

Brun, R.J., Gallagher, H.M., and Vogt, D.E., 1953a, "Impingement of Water Droplets on NACA 65-208 and 65-212 Airfoils at 4° Angle of Attack," NACA Technical Note 2952.

Brun, R.J., Gallagher, H.M., and Vogt, D.E., 1953b, "Impingement of Water Droplets on NACA 65A004 Airfoil and Effect of Change in Airfoil Thickness from 12 to 4 percent at 4° Angle of Attack," NACA Technical Note 3047.

Cebeci, T. and Besnard, E., 1994, "Prediction of the Performance Degradation of an Aircraft in Natural Icing Conditions," *32nd Aerospace Sciences Meeting*, Reno, NV, January 10-13, AIAA Paper 94-0487.

Dorsey, N.E., 1940, *Properties of Ordinary Water Substance*, American Chemical Society Monograph, Series 81, Reinhold Publishing Company, NY.

Falkner, V.M., "The Length of Aerofoil Curved Surfaces," *Aircraft Engineering*, March, pp.72-73.

Glauret, M., 1940, "A Method of Constructing the Path of Raindrops of Different Diameters Moving in the Neighborhood of (1) a Circular Cylinder, (2) an Airfoil Placed in a Uniform Stream of Air, and a Determination of the Rate of Deposit of the Drops on the Surface and the Percentage of Drops Caught," British Aeronautical Research Council, R&M No. 2025

Hardy, J.K., 1946, "Protection of Aircraft Against Ice," Report No. S.M.E. 3380, British Royal Aircraft Establishment, July.

Howarth, L., 1953, *Modern Developments in Fluid Dynamics - High Speed Flow*, Vol. II, Oxford University Press, United Kingdom.

Johnson, H.A., 1947, "A Design Manual for Determining the Thermal Characteristics of High Speed Aircraft," AAF Technical report 5632.

Keenan, J.H. and Kaye, J., 1961, *Gas Tables*, John Wiley & Sons, Inc., NY.

Kirby, M.S. and Hansman, R.J., 1986, "Experimental Measurements of Heat Transfer from an Iced Surface During Artificial and Natural Cloud Icing Conditions," *Fourth AIAA/ASME Thermophysics and Heat Transfer Conference*, Boston, MA, June 2-4, AIAA Paper 86-1352.

Langmuir, I. and Blodgett, K.B., 1946, "A Mathematical Investigation of Water Droplet Trajectories," Army Air Forces Technical Report No. 5418, Contract No. W-33-038-ac-9151

Lozowski, E.P. and Oleskiw, M.M., 1981, "Computer Simulation of Airfoil Icing Without Runback," *19th Aerospace Sciences Meeting*, St. Louis, MO, January 12-15, AIAA Paper 81-0402.

Martinelli, R.C., Guibert, A.G., Morrin, E.H., and Boelter, L.M.K., 1943, "An Investigation of Aircraft Heaters, VIII - A Simplified Method for the Calculations of the Unit Thermal Conductance Over Wings," NACA ARR (WR W-14).

Messinger, B.L., 1953, "Equilibrium Temperature of an Unheated Icing Surface as a Function of Air Speed," *Journal of the Aeronautical Sciences*, January, pp. 29-42.

Newton, J.E., Van Fossen, G.T., Poinsatte, P.E., and DeWitt, K.J., 1988, "Measurement of Local Convective Heat Transfer Coefficients from a Smooth and Roughened NACA-0012 Airfoil: Flight Test Data," *26th Aerospace Sciences Meeting*, Reno, NV, January 11-14, AIAA Paper 88-0287.

Pais, M.R., Singh, S.N., and Zou, L., 1988, "Determination of the Local Heat-Transfer characteristics on Simulated Smooth Glaze Ice Accretions on a NACA 0012 Airfoil," *26th Aerospace Sciences Meeting*, Reno, NV, January 11-14, AIAA Paper 88-0292.

Pelton, J.M. and Willbanks, C.E., 1972, "A Kinetic Model for Two-Phase Flow in High Temperature Exhaust Gas Coolers," AEDC-TR-72-89 (AD744514), Arnold Engineering Development Center, TN, June.

Putnam, A., 1961, "Integrable Form of Droplet Drag Coefficient," *ARS Journal*, Vol. 33, pp. 1467-1468.

Sogin, H.H., 1954, "A Design Manual for Thermal Anti-Icing Systems," WADC Technical Report 54-313, Wright Air Development Center, Air Research and Development Command, Wright-Patterson Air Force Base, OH.

Taylor, G.I., 1940, "Notes on Possible Equipment and Technique for Experiments on Icing on Aircraft," British Aeronautical Research Council, R&M No. 2024, January.

Van Fossen, G.J., Simoneau, R.J., Olsen, W.A., Jr., and Shaw, R.J., 1984, "Heat Transfer Distributions Around Nominal Ice Accretion Shapes Formed on a Cylinder in the NASA Lewis Icing Research Tunnel," *22nd Aerospace Sciences Meeting*, Reno, NV, January 9-12, AIAA Paper 84-0017, Also, NASA Technical Memorandum 83557.

Wright, W.B., Keith, T.G., and De Witt, K.J., 1988, "Transient Two-Dimensional Heat Transfer Through a Composite Body with Application to Deicing of Aircraft Components," *26th Aerospace Sciences Meeting*, Reno, NV, January 11-14, AIAA Paper 88-0358.

## DIMENSIONAL ANALYSIS OF ARC HEATERS

Michael Sydor

Professor

Department of Physics

University of Minnesota-Duluth

Duluth, Minnesota 55812

Final Report for:

Summer Faculty Research Program

Calspan Corporation/AEDC Corporations

Arnold Air Force Base, Tennessee

Sponsored by:

Air Force Office of Scientific Research

Bolling Air Force Base, DC

and

Calspan Corporation

August 1994

## DIMENSIONAL ANALYSIS OF ARC HEATERS

Michael Sydor  
Professor of Physics  
Department of Physics  
University of Minnesota-Duluth

### Abstract

A predictive equation for the operation of arc heaters was developed using non-dimensional Pi parameters. It was shown that the gross efficiency of a heater can be expressed in terms of heater length, its throat diameter, and the effective length of the air column heated by the arc's discharge path. This together with non-dimensional expressions for sonic flow and centerline enthalpy allows us to predict the voltage and the current necessary to operate a heater at a given pressure and desired heat output.

## DIMENSIONAL ANALYSIS OF ARC HEATERS

Michael Sydor

### Introduction:

In a complex physical system we often know the trends between physical variables but lack their precise relationship. Dimensional analysis helps establish these relationships by using non dimensional Pi relations.<sup>1</sup> Here, we consider data for several segmented arc heaters and attempt to characterize their operation independent of physical size.

The heaters ranged from 8.85 inch length and 0.9 inch diameter, to 64 inch length and 2 inch diameter. Power drawn by the heaters ranged from 0.8 to 32 megawatts. All arcs operated using air. A consistent data base for the heaters and the theoretical formulation of the problem was developed by Horn, Felderman and MacDermott of AEDC. We broaden the problem to include data on the lateral excursion of the arc from the heater centerline.<sup>2</sup> Data on arc excursions shows that heaters lack longitudinal uniformity because confinement characteristics of the arc change with the distance from the anode. The data also shows that in long heaters, tangential injection of mass tends to confine the arc's excursions to a cylinder with a diameter equivalent to the heater throat diameter. Both of these effects appear to play an important role in heater efficiency and suggest that an analytical description of arc heaters should include terms that describe the effects of the arc's longitudinal instability and account for its hydrodynamic confinement. We use this information to guide us in the construction and selection of Pi parameters.

### Methodology:

We begin by considering the Buckingham Pi theorem.<sup>1</sup> The theorem requires that the number of non-dimensional Pi terms equal the number of variables less the number of fundamental dimensions. In our case, we have nine variables: thermodynamic variables of pressure, mass flow, and enthalpy, P,  $m'$  and  $H$ ; physical variables of heater length, heater diameter and throat diameter, L, D and  $D^*$ ; electrical variables of voltage, current, and resistance, V, I, and R. There are four fundamental dimensions: mass, length, time and electric charge. Thus we require five Pi terms. The first eight variables are explicit in the data base. The electrical resistance is implicit through Ohm's law. Calculation of R involves integration over some internal distribution of enthalpy and electrical conductivity. Thus, the description of R in terms of Pi parameters will have to include an internal property such as the centerline enthalpy.

In our search for fundamental Pi parameters, we rely on physical relations and processes pertinent to arc heaters.

To begin with, there are three length measurements. These can provide two Pi terms from a choice of  $L/D$ ,  $D/D^*$ , and  $L/D^*$ . We will see that for reasons of confinement mentioned above,  $L/D^*$  will be most useful.

Classical thermodynamics suggests a variety of Pi terms based on turbulent mass flow. Felderman and MacDermott identified a sonic flow parameter,  $Pi_m$ , as the most useful. The parameter is given by:

$$Pi_m = PD^*^2 / (m' H_0^{1/2})$$

where  $H_0$  is the average enthalpy of a heater, and the remaining variables are defined above. For ideal gas  $Pi_m$  is constant and specifies the state of dynamic equilibrium for ideal gas flow. In arc heaters  $Pi_m$  is a weak function of enthalpy. Felderman and MacDermott found a pressure independent correlation of  $Pi_m$  with the average enthalpy. They show that for operation in air:

$$PD^*{}^2/(m' H_0{}^{1/2}) = (H_r/H_0)^{0.0837} \quad (2.18\%)$$

where  $H_r$  (494.2 Btu/lbm) is the reference enthalpy for air.

Another correlation for  $Pi_m$  comes from the dimensionless ratio  $P/\rho_0 H_0$ . This ratio is derived from the definition of enthalpy:

$$H = U + P/\rho$$

where  $U$  is the internal energy per unit mass, and  $\rho$  denotes the density of air. For ideal gas,  $U$  is a function of temperature only, and  $P/\rho H$  is constant. For heaters,  $P/\rho_0 H_0$  correlates with the average temperature to within 6%, while  $P/\rho_0$  tracks the average temperature of heaters to within 1.5%. The ratio  $P/\rho_0 H_0$  can be used in correlation with sonic flow because  $m' = D^2 \rho v$  and  $m H_0 \sim mv^2/2$ , where  $v$  is the mass flow velocity. We found a correlation of sonic flow parameter and  $P/\rho_0 H_0$  according to:

$$PD^*{}^2/(m' H_0{}^{1/2}) = 1.67(P/\rho_0 H_0)^{0.4} \quad (2.13\%)$$

Felderman and MacDermott further identify a voltage  $Pi$  parameter they needed in the solution of Ohm's law. The voltage parameter is given by:

$$Pi_V = (V/L)(D\sigma/PH_C)^{1/2}$$

where  $\sigma$  is the average electric conductivity, and  $H_C$  is the corresponding centerline enthalpy. Centerline enthalpy is derived from a mass weighted integration of an internal distribution of enthalpy in a heater. The integration procedure chosen assumes the square enthalpy profile shown below, and is carried out under the condition that the integral

must yield the average enthalpy  $H_o$ , and that a concurrent integration for  $\sigma$  satisfies Ohm's law:

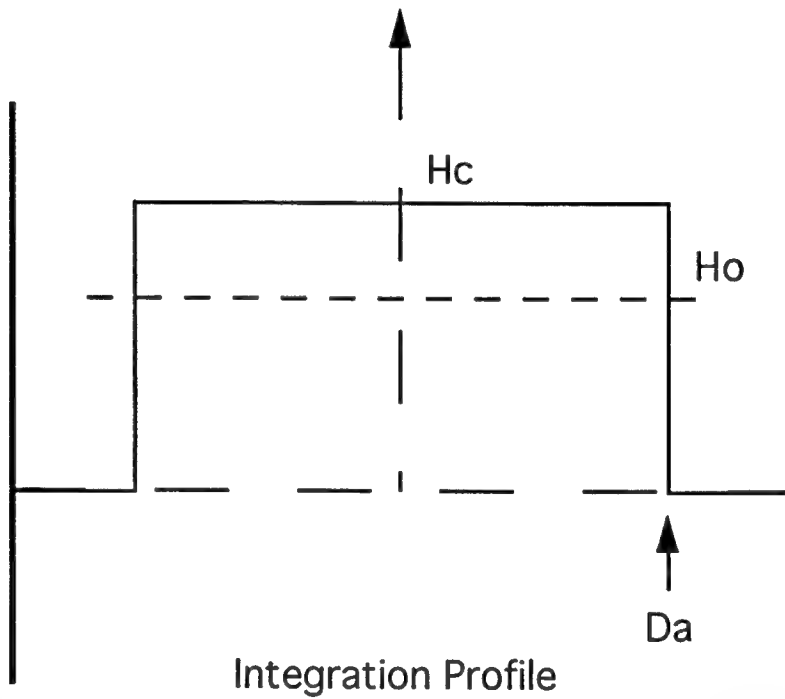
$$\int \rho(r, P, H) vH(r) 2\pi r dr = \pi D^2 \rho_o v H_o / 4$$

and

$$4/\pi D^2 \int \sigma(r, H, P) 2\pi r dr = \sigma$$

such that

$$V/I = 4L/\pi D^2 \sigma$$



The integration profile allows for a variable boundary layer  $Da$ , at the heater wall. The boundary layer is adjusted until the above integration conditions are met. Using this integration procedure, the subsequently calculated  $P_{iy}$  correlates with the actual voltage to within  $\sim 10\%$ . However, the corresponding correlation for current  $I$  shows a  $\sim 14\%$  r.m.s error. Furthermore,  $P_{iy}$  was somewhat sensitive to data subsets, possibly because

one data subset contained a preponderance of short heaters. We questioned the dependence of  $P_{iv}$  on data subsets. Was it due to longitudinal non uniformity of heaters? Longitudinal non uniformity would demand that above integrals include a dependence in length, else the variability of  $H(r)$  with length should be included as a dependence in the  $P_i$  parameters.

Continuos photographic records were available for the arc's position at 8.6, 30, and 51 inch distance from the anode in a 64 inch long heater. The arc was viewed through narrow slits and its position was recorded on a moving film. Examination of film data showed that long arcs become unstable in the center section of the heater, indicating that the distribution of Joule heating changed with the distance from the anode. The enthalpy profile and the distribution of electrical conductivity should be related to the discharge path that creates current carriers and Joule heating. Thus, we suspect that  $H$  and  $\sigma$  are both functions of heater length and behave in a fashion similar to the distribution of the arc's intensity with length, as shown in Fig. 1.

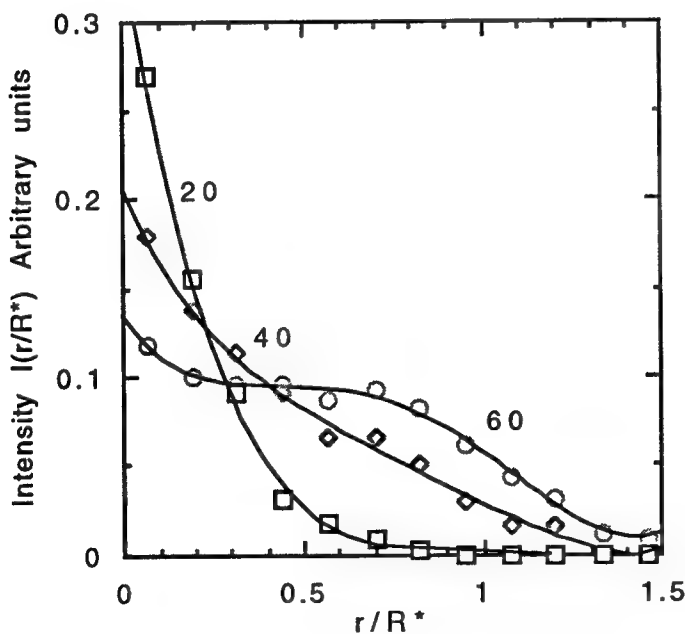


Fig. 1 Relative distribution of arc discharge path summed over a 20, 40, and 60 inch length from the anode.  $r$  denotes the distance from the longitudinal axis.  $R^*$  is the throat radius.

In compiling the intensity distribution shown in Fig. 1, we assumed that film records at the slits were representative of the first, the middle, and the last section of

the heater respectively. Thus, in calculating the intensity distributions at 40 and 60 inches we factored in the distributions of intensity in the preceding sections of the heater. It was also assumed that equal segments of the track on the film data had equal intensity. These assumptions are quite coarse but they suffice to demonstrate that the distribution of Joule heating is quite different depending on the distance from the anode. The expected intensity distribution at ~60 inches shows a square-like profile, justifying our choice for integration profile of  $H(r)$ . The square profile simulated a central heated core and a colder wall layer. The integration profile worked well and appeared appropriate for our problem. Actually, a square profile with a variable boundary layer at the heater wall shows physical merit and points to some interesting limits on the design of arc heaters. This topic will be presented in detail elsewhere.<sup>3</sup>

Film data showed that an arc becomes unstable at some length  $l_r$  in the center section of the heater. The discharge path wanders randomly in the center core of the heater but it is stabilized downstream by the tangential injection of mass, and becomes partially confined to an area the size of the throat diameter  $D^*$  in the last section of the heater.<sup>2</sup> Since the integration procedure for  $H(r)$  and  $\sigma(r, H, P)$ , ignored variability with length, we have to account for it in definition of  $P_i$  parameters.

Let us consider how we could account for a longitudinal distribution of heat input through definition of a  $P_i$  parameter. Since we have no information on plasma conditions giving rise to the instability length  $l_r$ , we could not build  $l_r$  into our formulation of a  $P_i$  parameter. However, let us examine the ratio of heat input into the air versus Joule heating. This is expressed by the gross efficiency ratio:

$$m'H_0/VI$$

The arc's intensity should provide a measure of the power input  $VI$ , while the length of the column of air passing through the arc's path should be proportional to  $m'H_0$ , the rate of heat input into the air. We already assumed in the integration of  $\sigma(r,H,P)$  that Joule heating was distributed uniformly throughout the arc's path. We also ignored the variability of  $H(r)$  with length. This leaves us with  $m'$  to account for the longitudinal dependence in  $m'H/VI$ . Mass flow output is constant in an arc heater else the continuity equation would not be satisfied. However, the effective length of air column passing through an element of arc depends on arc motion.

To compute the effective length of heated air column  $L_a$ , we used film records discussed above. We assumed that lateral excursions of arc in  $x$  and  $y$  directions were equally likely. We also assumed that turbulence effects and heat dispersal was the same on the average for a stationary and for a moving element of arc. Under those assumptions, we consider the flow of air through an infinitesimal element of arc representative of each section of the heater.

Let  $z$  denote the longitudinal axis of the heater. A stationary volume element of arc  $dxdydz$  would have a column of air  $dxdyv\Delta\tau$  passing through it. The element would heat a mass  $dm = (dxdy)(v\rho\Delta\tau)$ , where  $v=m'/(D^2\rho)$ .  $\rho$  denotes the density of air, and  $\Delta\tau (L/v)$  is the average time for transit of air through the heater. For a moving arc, the column would have a length  $(v_a)\Delta\tau$ , where  $v_a$  is the average speed of the arc element relative to the air stream. All other effects average out as in a stationary arc, except for this motion.

Arc elements have some average speed  $|v_x|$  and  $|v_y|$  depending on their distance from the anode. A record of the arc's position on a moving strip of film gives a measure of  $|v_x|$ . Using  $|v_x|$  determined from film data we define the effective length of air column for a moving arc versus a stationary arc as the ratio of relative speeds:

$$L_a/L = (2|v_x|^2 + v^2)^{1/2}/v.$$

We evaluate this ratio for a typical value of  $m' = 3 \text{ kg/s}$ ,  $D^* = 2.29 \text{ cm}$ , and  $P = 80 \text{ Atm}$ , and calculate  $L_a/L$  for 8.6, 30, and 51 inch distance from the anode. Fig. 2 shows the dependence of the effective length of air column  $L_a$  as a function of the distance from the anode.

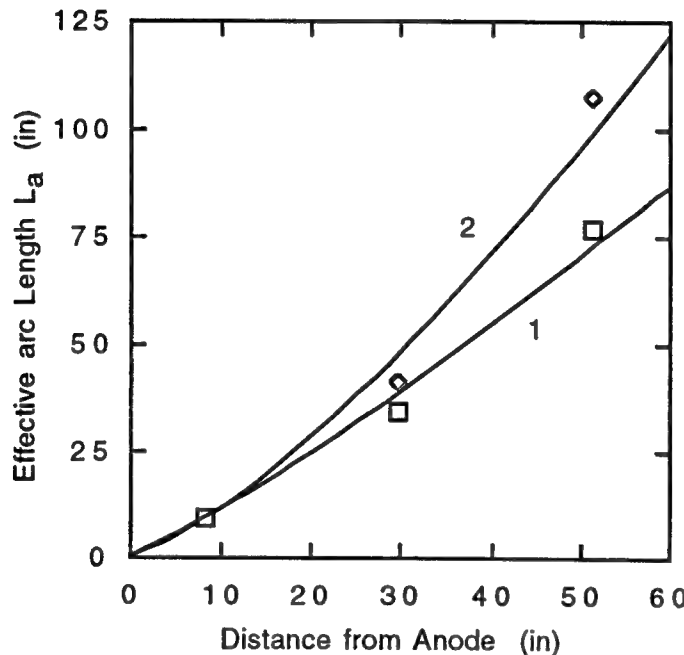


Fig.2 In two dimensions

$$1) (|v_x|^2 + v^2)^{1/2}/v \text{ gives}$$

$$L_a = 0.7L^{1.17}$$

In three dimensions:

$$2) (2|v_x|^2 + v^2)^{1/2}/v \text{ gives}$$

$$L_a = 0.48L^{1.35}$$

The best functional fit for  $L_a$  was given by  $L_a = 0.48L^{1.35}$  inches. Subsequently, we specified  $L_a/L$  as a length dependent Pi parameter that accounts for longitudinal non uniformity of heaters. We note that for short heaters,  $L_a \sim L$ , while for long heaters  $L_a$  is considerably greater than  $L$ .

We now consider our second observation, that arcs stabilize inside a cylindrical column the size of the throat diameter because of the tangential mass injection. This effect can be seen from plots of the arc's position at the three slit locations, as illustrated in Fig. 3.

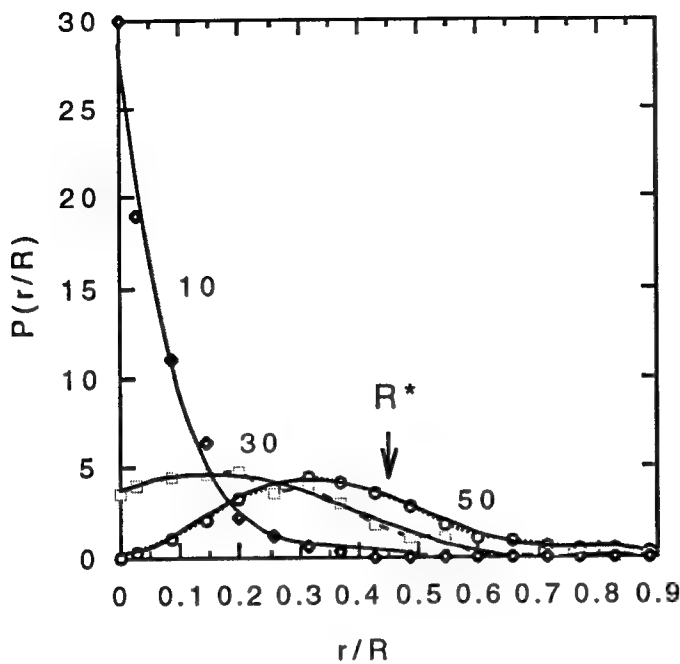


Fig. 3 Position of arc discharge path at 10, 30, and 50 inches from the anode in a 64 inch long arc heater. The heater had a radius  $R = 1.0$  inches, and throat radius  $R^* = 0.45$  inches.  $P(r/R)$  is the probability density.

Fig. 3 shows the radial probability density for the lateral position of the arc in a 64 inch heater. The distribution was derived under the assumption that  $P(x)=P(y)$ , and that  $\sum P(x)P(y)\Delta x\Delta y = P(r)2\pi r\Delta r$  over a ring shaped area of constant radius  $r$  and width  $\Delta r$ . A rough sum for this equality was performed by dividing each  $(2\pi r\Delta r/4)$  quadrant into four sections.

The downstream discharge path shown in Fig. 3, appears generally confined to the throat diameter although occasionally it does wander outside of the throat region. To test the anticipated significance of  $D^*$  and  $L_a$  in analytical description of heaters, and in particular their efficiency, we performed extensive correlation between various  $\Pi$  terms and physical variables. In particular, we examined closely the correlations for  $m'H_0/Vl$  since this ratio was fundamental in our formulation of  $L_a$ .

#### Results and discussion:

We ran extensive correlation for  $m'H_0/Vl$  in terms of:  $L$ ,  $D$ ,  $D^*$ ,  $D^*2/L$ ,  $D^2/L$ ,  $D^*2L$ ,  $D^2L$ ,  $m'$ ,  $T$ ,  $L_a$ , etc. The results showed clearly that the most significant

correlation was given by a "core ratio" specified by  $D^*2/L^{1.2}$ . The correlation between  $m'H_O/VI$  and  $D^*2/L^{1.2}$  was given (with r.m.s. error of 8%) by:

$$m'H_O/VI = 3 (D^*2/L^{1.2})^{0.3}$$

Oddly enough, the correlation picks  $D^*$  and possibly  $L_a$  as the fundamental variables.

Addition of other parameters did not improve this result significantly. Other choices of physical parameters such as  $L/D$  and  $D^2/L$  produced relatively poor results. For instance heater volume and  $m'H_O/VI$  produced a correlation of 27%, and  $D^2/L$  gave a correlation of 21%. We note that  $L^{1.2}$  in the above correlation resembles the effective length  $L_a$ .

In terms of non dimensional parameters, the best correlation for  $m'H_O/VI$  was provided by:

$$m'H_O/VI = 11.2 (L/D^*)^{-0.56} (L_a/L)^{0.7} (P/\rho H_O)^{0.58} \quad (7.12\%)$$

where  $L_a = 0.48L^{1.35}$  inches. However a simpler two-parameter expression for the gross efficiency works almost as well and is given by:

$$m'H_O/VI = 5.31(L/D^*)^{-0.62}(L_a/L)^{0.78} \quad (8\%)$$

This ratio gives a measure of the efficiency of the arc heater if one neglects the relatively small enthalpy of cold air. It is seen from the immediately preceding equation that the efficiency of a heater can be related strictly to  $L_a/L$ , that accounts for the motion of the arc, and  $L/D^*$ , which expresses the aspect ratio for arc confinement.

We now consider the general operation of arc heaters. Our basic problem can be stated as follows: given an operating pressure  $P$  and a desired heat output  $H_O$ , find  $V$  and  $I$  and vice versa.

From the above correlations we see that for any given pressure  $P$  and bulk enthalpy  $H_O$ , we can find  $m'$  from the sonic flow parameter according to:

$$m' = PD^*2/(1.67H_O^{1/2} (P/\rho H_O)^{0.4})$$

and determine the needed power input  $VI$  from:

$$VI = m'H_O/(5.31(L/D^*)^{-0.62}(L_a/L)^{0.78})$$

To separate V and I, we need  $\sigma$ , and R. However, the average electrical conductivity is unknown a priori. To find  $\sigma$ , we devise an internal Pi parameter  $H_c/H_o$ , since for any  $H_c$  we can determine  $\sigma$ , and given heater dimensions find R. In essence, a correlation for  $H_c/H_o$  gives us a general relationship between the implicit and the explicit variables of a heater. From our extensive search, we found two correlations for  $H_c/H_o$ .

For air we have:

$$H_c/H_o = 6.94(D^*/D)^{.44}(H_r/H_o)^{.64}(L/D^*)^{.16}(L_a/L)^{-.844} \quad (6.1\%)$$

This relation allowed us to find  $\sigma$  for any  $H_o$  and determine  $R=4L/\pi\sigma D^2$ . Having R, we can write the equations for I and V, as follows:

$$I = \{m'H_o/(5.3(L/D^*)^{-.62}(L_a/L)^{.78}R)\}^{1/2} \quad (3.5\%)$$

$$V = \{m'H_o R/(5.3(L/D^*)^{-.62}(L_a/L)^{.78})\}^{1/2} \quad (3.3\%)$$

The equations yield voltages and currents that correlate very well with the actual voltages and currents. However, to truly test the validity of the above expressions for V and I, we need to regenerate the data base from a randomized set of data points. The results for data regeneration are shown in the table 1.

Before we examine Table 1, we write down the general Pi equation representing operation of arc heaters in terms of strictly non-dimensional terms which should hold independent of specific gas, we have:

$$(H_c/H_o) = 201.2 \left\{ (D^*/D)^{.46} \left( \frac{P}{\rho_o H_o} \right)^{2.56} (L/D^*)^{.067} (L_a/L)^{-.71} \right\}$$

Pi1                    Pi2                    Pi3                    Pi4                    Pi5

This equation is good to an accuracy of 7.4%. It relates the unknown Pi parameter  $H_c/H_o$  with Pi parameters describing heater geometry, their operating pressure and enthalpy output, arc confinement, and longitudinal non uniformity.

Table 1

Parameter	I (Amps)	V (Volts)	m' (lbm/s)	m'Ho/VI
Combined data set	10.5%	8.6%	2.2%	8.5%
Data set 1	11.7%	6.5%	2.7%	8.1%
Data set 2	9.2%	10.2%	1.5%	9.1%

## Comparison of Data Base with Data regenerated from Dimensional Analysis

Table 1 shows good overall agreement between regenerated and the actual values of V, I, m' and gross efficiency m'Ho/VI.

In a further test of the predictive equations, we project an operating point for a heater by using runs that were not included in the data base. This is shown in Table 2.

Table 2

	Ho Btu/lbm	P Atm	V kilo Volts	I Amps	Power Meg Watts	m' lbm/s
Run 6/16/86 D*=0.9	3020	82.4	17.3	1180	20.4	4.19
	Predicted		16.8	1165	19.57	4.255
Run 10/16/85 D*=0.7	3470	53	11.1	944	10.5	1.5
	Predicted		12.1	791	12.2	1.56
Run 10/23/85 D*=1.16	2840	54.2	15.8	1230	19.4	4.32
	Predicted		14.4	1231	17.9	4.76

---

Table 2 shows a comparison of the experimental results with predicted values for three randomly picked runs that were not included the data base. The runs were made using a 64 inch long heater, 2 inches in diameter, and throat diameter  $D^*$  as indicated in table 2.

Conclusion:

We have shown that longitudinal non uniformity must be taken into account in analytical description of arc heaters. If it is not taken into account in  $\sigma$  and  $H(r)$  through a length dependence, then it must be expressed as a separate dependence through a  $\Pi$  parameter. Table 1 and 2 show good agreement between predictions made with correlations derived using dimensional analysis and the data base. The margin of error is largely determined by the statistical spread in the data base.  $L_a$  determined from experimental results produced excellent regenerated data tables. We thought this result fortuitous since the derivation of  $L_a/L$  was rough. However, variation of the discharge path length worsened the results in table 1 and 2.

It should be noted that the precise functional dependence of  $L_a/L$  does not make any difference in the accuracy of cross-correlations of  $\Pi$  parameters. The correlation procedure fits the parameters to within some constant and some power of a specified  $\Pi$  term. However, omission of a scaled length term that accounts for arc instability results in lack of any useful correlations for  $m'H_O/VI$ ,  $H_C/H_O$ . Thus the presented  $\Pi$  parameters and correlation equations appear necessary and well suited for predictive purposes in the operation and design of arc heaters.

Acknowledgments:

I would like to thank my mentor Dr. E. J. Felderman, and coworkers Mike Scott and Jack De Witt for their patience and indispensable help with programming. My thanks to John Felderman and Bill MacDermott for many discussions of the physics of arcs. I would also like to thank Dennis Horn and Walter Bruce for so generously sharing experimental information and data.

The Air Force Summer Faculty Program allowed me to participate in an experiment that could not be performed at my own institution, and has given me engineering experience and insight that will be most beneficial to my undergraduate engineering and physics students.

Finally, I would like to thank Rachel Killebrew and David Marlin for their help, and to say that the working conditions at Arnold Air Force Base were excellent, and that invariably, every person that I came in contact with was more than helpful.

References:

1. Glenn Murphy "Similitude in Engineering" The Ronald Press Company, New York, 1950.
2. Bruce W. E. III, and D. D. Horn "AEDC Arc Column Diagnostic Measurements" Proceedings of 38th International Instrumentation Symposium, paper N0. 92-0190, April 1992.
3. Paper submitted to 26th Plasmadynamics and Lasers conference held jointly by the American Institute of Aeronautics and Astronautics and Thermophysics Conference, June 19-22, 1995, San Diego California.

ULTRAVIOLET FLAT-FIELD RESPONSE  
OF AN INTENSIFIED CHARGE-COUPLED DEVICE (ICCD)  
CAMERA TO NANOSECOND LASER PULSES

John T. Tarvin  
Associate Professor  
Department of Physics and Astronomy

Samford University  
800 Lakeshore Drive  
Birmingham, AL 35229

Final Report for:  
Summer Faculty Research Program  
Arnold Engineering Development Center

Sponsored by:  
Air Force Office of Scientific Research  
Bolling Air Force Base, Washington, D.C.

and

Arnold Engineering Development Center

September 1994

ULTRAVIOLET FLAT-FIELD RESPONSE  
OF AN INTENSIFIED CHARGE-COUPLED DEVICE (ICCD)  
CAMERA TO NANOSECOND LASER PULSES

John T. Tarvin  
Associate Professor  
Department of Physics and Astronomy  
Samford University

ABSTRACT

The flat-field response of an intensified charge-coupled device (ICCD) camera to ultra-violet (uv) pulses from a Nd:YAG/dye laser system was determined. Intensifier gate-widths ranged from 50 ns to 200 us. The flat-field illumination was obtained in two different manners: 1) nitric oxide (NO) fluorescence from a static cell, and 2) fluorescence output from an integrating sphere. A third method, steady-state illumination of a diffusion screen with a deuterium lamp, was used to obtain a comparison of steady-state versus pulse illumination response. Measurements were obtained on two essentially identical camera systems; these cameras are to be used for dual-wavelength planar laser-induced fluorescence (PLIF) measurements of shock flows. Such measurements will allow temperature visualization within the flow. Results indicate that both camera systems have a non-linear signal versus energy response; the response is stable and can be corrected. A linear correction can be used for signals below 20% of the maximum camera response. There is also a smooth, correctable variation of response across the 578x384-pixel image. Corrected images are flat to within 10% or better.

ULTRAVIOLET FLAT-FIELD RESPONSE  
OF AN INTENSIFIED CHARGE-COUPLED DEVICE (ICCD)  
CAMERA TO NANOSECOND LASER PULSES

John T. Tarvin

INTRODUCTION

Planar laser-induced fluorescence (PLIF) has been used as a non-invasive technique for the visualization of flowfields (1-6). When used at two wavelengths, this technique will allow visualization of the flowfield temperature (4,6). The generated fluorescence is usually collected as a video image through the use of an intensified charge-coupled device (ICCD) camera (3-5). The response of the ICCD camera is of key importance to the accurate interpretation of the PLIF measurement. Previous work investigated the response of a ICCD camera system in the presence of continuous illumination (7). Since actual PLIF measurements use a short laser pulse (4) questions of possible camera response differences between continuous and pulsed illumination and their effects on image interpretation are relevant. For example, if camera response is "less flat" for continuous illumination than for pulsed illumination then pulsed images would be over corrected; such an over-correction could lead to an over-estimation of laser-beam absorption (8). The present work presents the findings of flat-field studies using a pulsed laser source.

## APPARATUS AND METHODOLOGY

The PLIF measurement system has been described previously (3,4). The primary difference between the present make-up of this system and that reported previously was the replacement of the PG-10 high-voltage pulser unit with the newer PG-50 unit (both by Princeton Instruments). The control program, CSMA (Princeton Instruments), has also been updated to version 2.3.

Although initial efforts were made to image an NO fluorescence signal using a camera lens, non-uniformity of the beam profile (and its correction) introduced an excessive amount of measurement uncertainty. Therefore, all reported measurements are for a lens-less ICCD camera system. Flat-field illumination was provided by three separate techniques: 1)NO fluorescence excited by 226 nm pulsed illumination (4), 2)a four-inch integrating sphere excited by the same pulsed laser system as in 1), and 3)a deuterium lamp reflected from a diffusion plate. Note that technique 3) differs from the other two in that it is a continuous, rather than a pulsed, source. In all cases, the ICCD camera was placed at a sufficient distance from the source that illumination variations due to geometrical placement were minimized. Pulse energy levels were monitored with either an energy meter (using a reflection from a steering prism face) or a PIN diode (Thorlabs). Energy variation was accomplished by either inserting neutral density filters in the beam path or by attenuating the beam diameter with an iris. All such beam modification was accomplished prior to the sheet-forming optics.

## RESULTS

Initial studies using NO fluorescence and neutral density filter for energy variation gave variable results: energy linearity was questionable. The major source of this variation appeared to be due to the neutral density filters. It was then decided to use an iris for the energy variation, along with a 4-inch integrating sphere with output down to 200 nm. Single-pulse energy was monitored using both a power meter (monitoring a beam reflection) and a PIN diode (staring into the integrating sphere). Both of these energy measurement techniques yielded reasonably linear results, as shown in Figure 1 (and Figure 3).

Surprisingly, signal level as a function of beam energy showed a non-linear variation for signals above about 20% of the maximum response of either 16383 or 65535, depending on the camera controller card used. Typical responses for both cameras are shown in Figure 2. Signal response is measured as the average of a 100x100-pixel region of the 384x578-pixel image. No flat-fielding correction has been applied to these averages; however, a relatively flat region of the image was chosen for the averaging region.

In order to further verify this non-linear response, half of the ICCD camera was covered with a neutral density (0.5) filter. Signal averages for each half of such an image are shown in Figure 3. It can be seen that the signal level of the unobscured side exhibits non-linear behavior before that of the

obscured side, suggesting that the non-linear behavior is indeed a function of the irradiance level and is a characteristic of the ICCD camera system.

The response of the ICCD camera system was also measured for the case of constant illumination. A deuterium lamp reflected off a diffusion plate was used as a source; the illumination level of the ICCD camera was varied by changing the distance of the camera from the plate. Results of this study are presented in Figure 4. Again, 100x100-pixel averages are used for the signal level. It can be seen that, above a high-voltage pulse width (the gate width for turning the ICCD intensifier plate ON) of about 20 microseconds, the signal varies linearly with gate width. This is the anticipated result. However, for shorter gate widths, the ICCD camera system again responds non-linearly.

In a related study, the timing of the laser pulse with respect to the gating pulse was found to be extremely critical, especially for short gate widths of 50 ns. This result is thought to be related to the finite time required for the intensifier plate to turn ON. For a laser pulse positioned (in time) near the start of the gating pulse, the ICCD image exhibits a "center-void" pattern; the periphery of the plate has turned ON but the center of the plate is still OFF. For a laser pulse positioned near the end of the gating pulse, a "golf-ball" image is seen; the periphery has now turned OFF but the center

is still ON. For placement at the center of the gating pulse the image was more uniform; the overall signal level was down slightly from that obtained with gate widths of 200 ns, however, suggesting that the plate may never be turning ON fully.

#### CONCLUSION

Flat-fielding of the ICCD camera system, as it presently exists, must involve a non-linear correct if the full signal range is to be used. For current PLIF work, however, a linear correction over the lower 20% of the signal range may suffice. This is based on the observed fact that, even at maximum intensifier gain, the PLIF signal in the flowfield region of interest is less than 20% of the maximum digitization range of the ICCD camera (8). Linear flat-fielding over this range results in a maximum image variation of 10% or less.

The source of the ICCD camera system non-linearity is intriguing, especially given the fact that this non-linearity was not evident when this system was examined a year ago (7). In particular, signal response as a function of gate width was linear to below 200 ns. The major difference in the system on which those measurements were performed and the present system is the replacement of the model PG-10 high-voltage pulser with the (newer) model PG-50. Additional studies of this new pulser unit, and its interaction with the rest of the ICCD camera system, need to be performed. In particular, the shape of the

high-voltage pulse at the ICCD camera needs to be monitored for "squareness". The shape of this pulse as a function of connecting cable length also needs to be investigated.

REFERENCES

1. McMillin, B.K., Seitzman, J.M. and Hanson, R.K., "Comparison of NO and OH PLIF Temperature Measurements in a SCRAMJET Model Flowfield", AIAA Paper 93-2035, AIAA/SAE/ASME/ASEE 29th Joint Propulsion Conference, Monterey, CA, June 28-30, 1993.
2. McMillin, B.K., Palmer, J.L. and Hanson, R.K., "Two-Dimensional Temperature Measurements of Shock Tube Flows Using Planar Laser-Induced Fluorescence Imaging of Nitric Oxide", AIAA Paper 91-1670, AIAA 22th Fluid Dynamics, Plasma Dynamics & Lasers Conference, Honolulu, HI, June 24-26, 1991.
3. Havener, A.G., and Smith, M.S., "Holographic and PLIF Measurements of Free-flight Hypervelocity Flows in the AEDC Range G Facility", AIAA Paper 92-3935, AIAA 17th Aerospace Ground Testing Conference, Nashville, TN, July 6-8, 1992.
4. Smith, M.S., Williams, W.D., Price, L.L., and Jones, J.H., "Shocktube Planar Laser Induced Fluorescence Measurements in Support of the AEDC Impulse Facility", AIAA Paper 94-2649, AIAA 18th Aerospace Ground Testing Conference, Colorado Springs, CO, June 20-23, 1994.

5. Ruyten, W., Heltsley, F., and Williams, W.D., "Computational Flow Imaging for Planar Laser Induced Fluorescence Applications (CFI-PLIF)", AIAA Paper 94-2621, AIAA 18th Aerospace Ground Testing Conference, Colorado Springs, CO, June 20-23, 1994.
6. Palmer, J.L., McMillin, B.K., and Hanson, R.K., "Planar Laser-Induced Fluorescence Imaging of Velocity and Temperature in Shock Tunnel Free Jet Flow", AIAA Paper 92-0762, AIAA 30th Aerospace Sciences Meeting, Reno, NV, January 6-9, 1992.
7. Tarvin, J.T., "Characterization of an Intensified Charge-Coupled Device (ICCD) camera used in Planar Laser-Induced Fluorescence (PLIF) Studies", Final Report for Summer Faculty Research Program, Arnold Engineering Development Center, August, 1993.
8. Ruyten, W., private communication.

## Diode vs. Energy Linearity (uv laser pulse into integ. sphere)

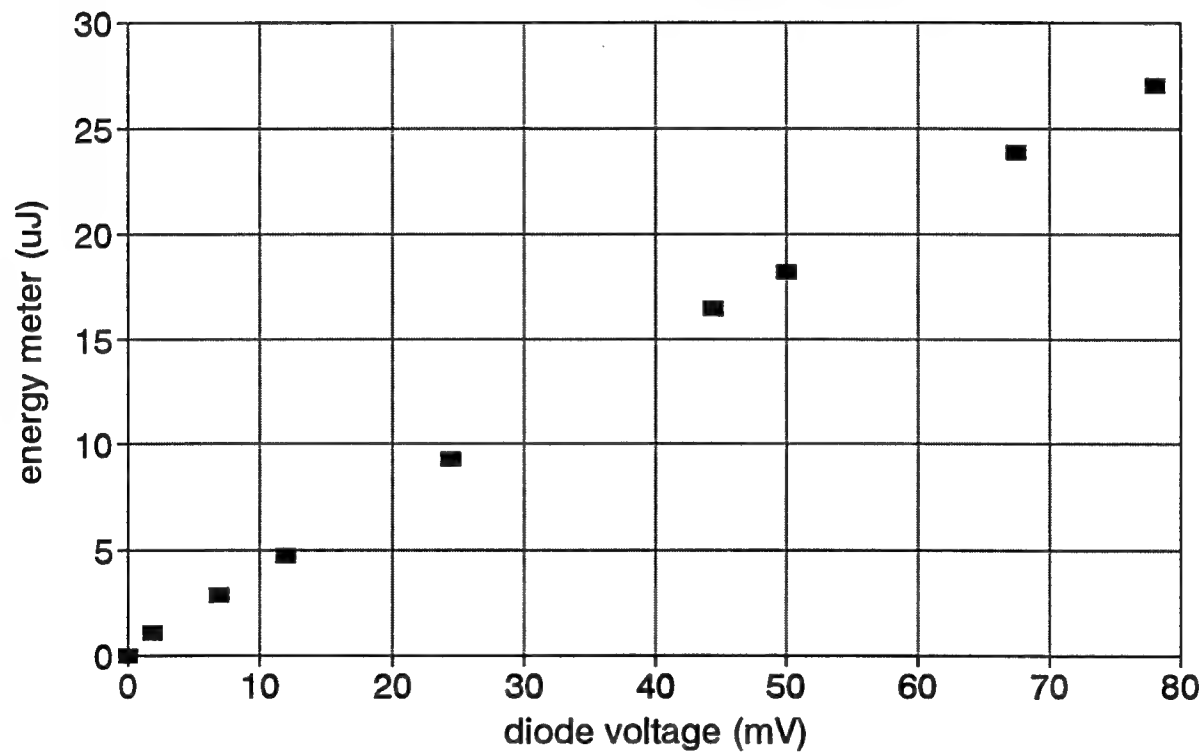


Figure 1.

## Linearity of Camera Signal Response (integ. sphere / laser / iris / diode)

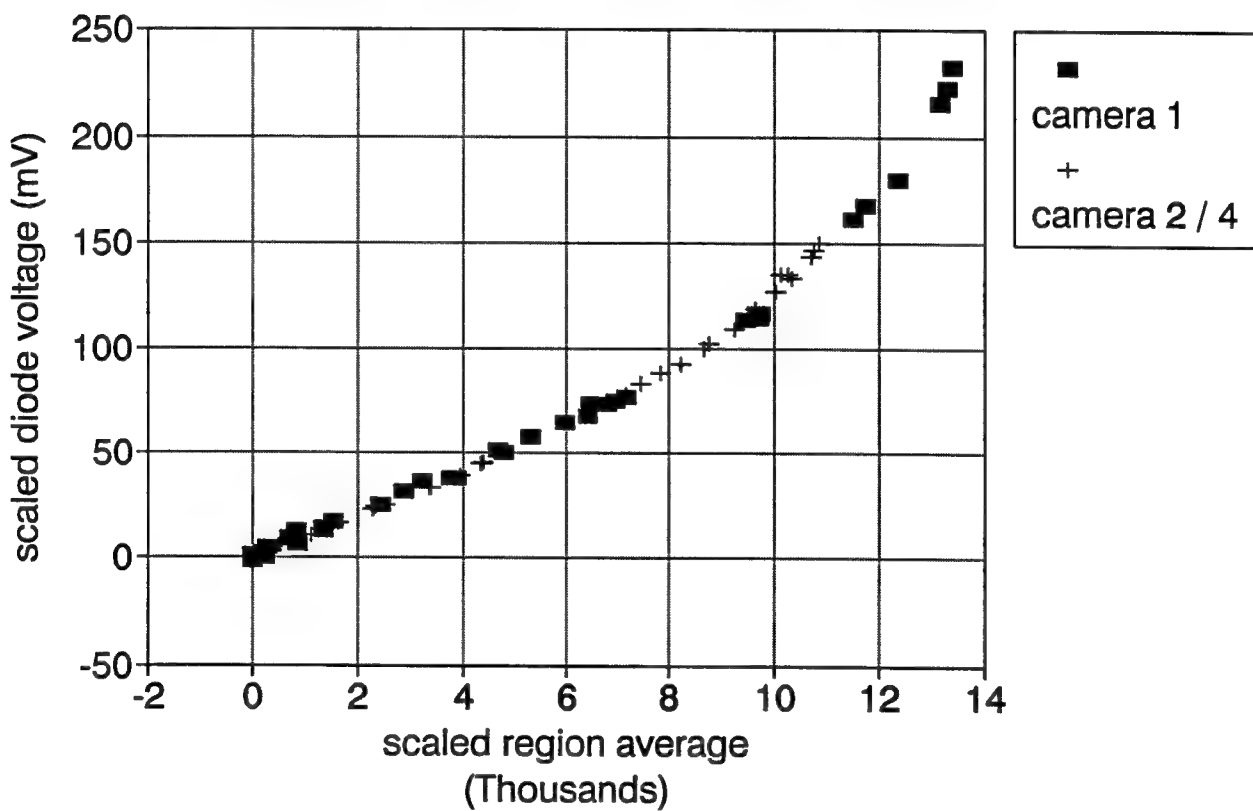


Figure 2.

## Linearity Test Using Partial Blockage

camera 2 / 200 us gate / iris / 0.5 ND

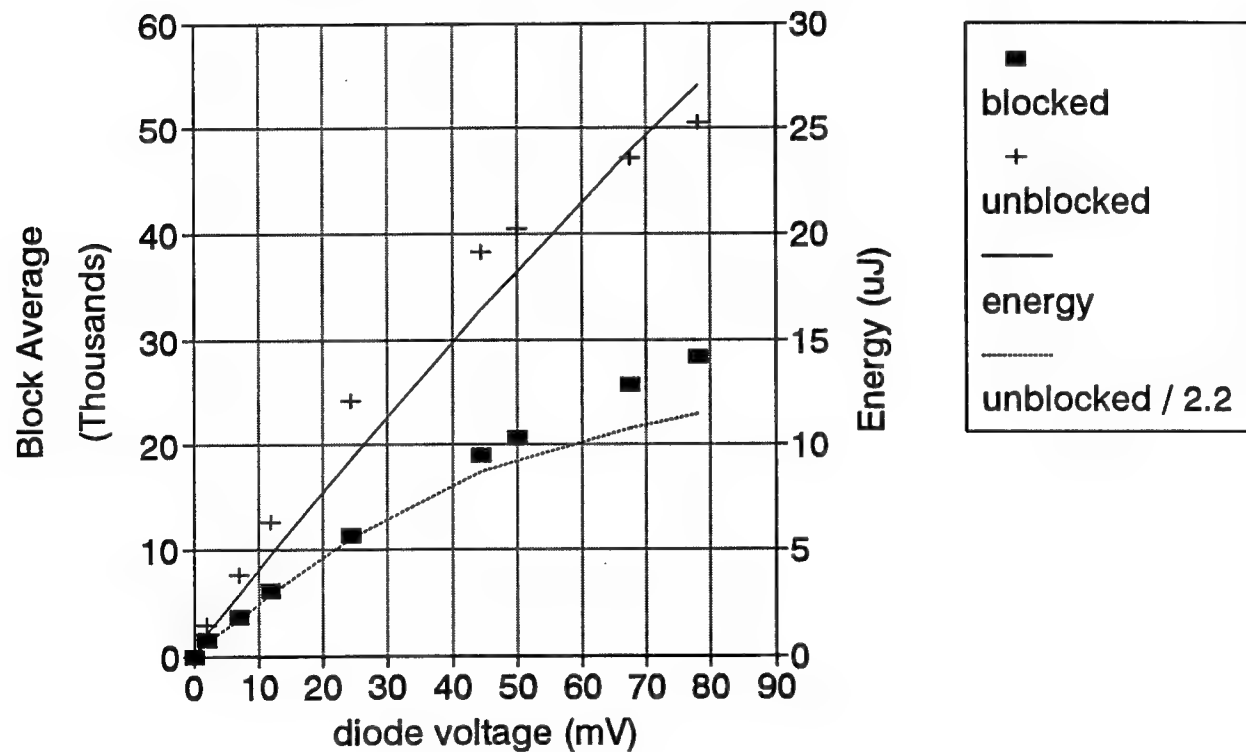


Figure 3.

## Camera 2 Gate Linearity

diffusing plate / D2-lamp

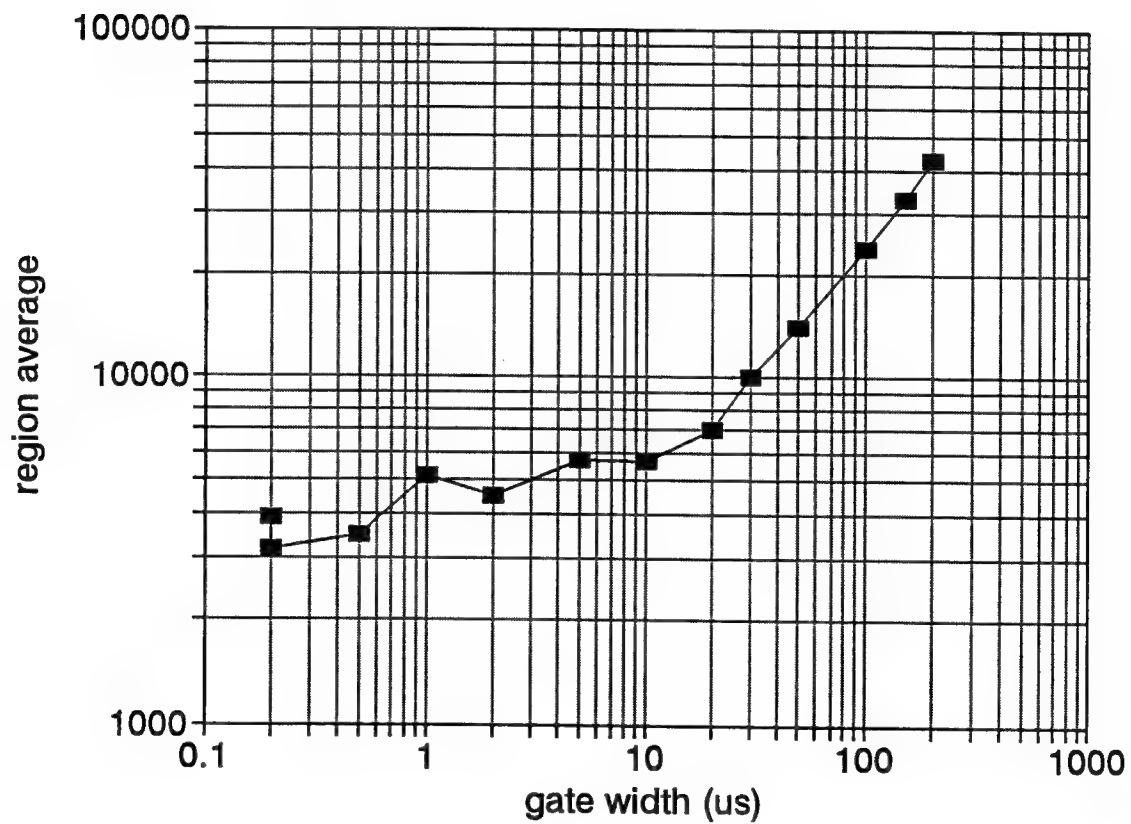


Figure 4.

**DR. GENE O. CARLISLE**

**REPORT**

**UNAVAILABLE**

Fundamental Studies on the  
Solution and Adsorption Properties  
of  
Block Copolymers

John R. Dorgan  
Assistant Professor  
Chemical Engineering and Petroleum Refining Department  
Colorado School of Mines  
Golden, CO 80401-1887

Final Report for:  
Summer Faculty Research Program  
Seiler Laboratory

Sponsored by:  
Air Force Office of Scientific Research  
Bolling Air Force Base, DC  
and  
Frank J. Seiler Research Laboratory

August 1994

# FUNDAMENTAL STUDIES ON THE SOLUTION AND ADSORPTION PROPERTIES OF BLOCK COPOLYMERS

John R. Dorgan  
Chemical Engineering and Petroleum Refining Department  
Colorado School of Mines  
Golden, CO 80401

## Abstract

Fundamental solution and adsorption properties of block copolymers have been investigated using Low Angle Laser Light Scattering (LALLS), Atomic Force Microscopy (AFM), and Ellipsometry (ELLI). Additionally, the solution properties of poly(vinyl caprolactam), a water soluble polymer used to inhibit hydrate growth in oil and gas pipelines, have been studied.

We report the first experimental results on the scaling characteristics of brush-forming middle-adsorbing triblocks. The triblocks used consist of relatively short poly(ethylene oxide) (PEO) middle blocks and much longer polystyrene (PS) end blocks. Adsorption takes place onto a well characterized silicon dioxide surface from toluene and ellipsometry is used to determine the adsorbed amount. We find that the surface density,  $\sigma$ , for each of the copolymers ( both those in the symmetric and asymmetric regimes ) scales according to the simple relationships proposed in the theory of Marques and Joanny ( i.e. in the symmetric to moderately symmetric regime,  $\sigma \propto N_A^{-1}$ , where  $N_A$  is the number of segments in the adsorbing PEO block and in the highly asymmetric regime,  $\sigma \propto \beta^{-2}$ , where  $\beta$  is the ratio of the size of the non-adsorbing block to the size of the adsorbing block ).

The scaling behavior of the radius of gyration of polystyrene homopolymers in toluene has been determined; it was found that  $R_g (\text{\AA}) = 1.76 N_{ps}^{0.597}$  for polymers with a molecular weight greater than 100,000 g/mol. For lower molecular weight polystyrene samples, we find  $R_g (\text{\AA}) = 7.16 N_{ps}^{0.401}$ . Finally, for poly(vinyl caprolactam) homopolymers in water, it was found that  $R_g (\text{\AA}) = 6.30 N_{pv-cap}^{0.56}$ . Based on this information it is possible to derive an engineering correlation for the overlap concentration, we find  $c^* (\text{mg / ml}) = 6315 MW_{pv-cap}^{-0.68}$  where  $MW_{pv-cap}$  is the polymer molecular weight.

## Copolymer Adsorption Studies

### Introduction:

Polymer coils at the solid-liquid interface are of technological interest. For example, they are used in the stabilization and flocculation of colloidal particles, to enhance biocompatibility of artificial implants, and for electrode modification.

Many studies have been made on diblock copolymers investigating their behavior at the solid-liquid interface.<sup>1</sup> Also, adsorption characteristics of end attaching triblocks have been studied.<sup>2</sup> Scaling laws have been verified for the different symmetry regimes of diblock copolymers proposed by Marques and Joanny.<sup>3</sup> This scaling theory is consistent with the results of the self consistent field theory of Scheutjens and Fleer.<sup>4</sup>

In this study, we report on the adsorption behavior of middle-attaching triblocks. The materials employed consist of relatively short poly(ethylene oxide) (PEO) middle-blocks capped by relatively long polystyrene (PS) end-blocks. The PEO block preferentially adsorbs to the surface whereas the PS block remains dangling in solution. Denoting the adsorbing block by A and the buoy block as B, these copolymers are of the B-A-B architecture. Adsorption takes place from toluene, a good solvent, onto a well characterized silicon oxide surface; this is a case of adsorption from a non-selective solvent onto a selective surface.

### Experimental

The copolymers used in this study have the characteristics shown in Table 1. The triblocks were synthesized at the Technical University of Istanbul by a procedure described earlier.<sup>5</sup> It is seen that the composition of the samples are such that the different regions of symmetry are covered (i.e. copolymers with  $\beta < N_A^{0.5}$  lie in the symmetric to moderately symmetric regime and polymers with  $\beta > N_A^{0.5}$  lie in the highly asymmetric regime). The silicon wafers are obtained from Silicon Source Inc. (Phoenix) and treated as described in previous work.<sup>2,6</sup> The film thickness of the oxide layer is independently determined prior to the adsorption run using

ellipsometry. HPLC grade toluene (Aldrich Chemicals) was used after filtering three times through 0.2 micron Whatman filters. The adsorption experiments are all conducted at solution concentrations of  $1.000 \pm 0.001$  mg/ml. Molecular weight distributions were characterized using gel permeation chromatography and were found to be relatively narrow ( $M_w / M_n < 3.0$  for all cases). Low angle laser light scattering (Wyatt Technologies DAWN B) was used to measure weight average molecular weight and the radii of gyration in solution; no evidence of micelle formation is present at the concentrations used in the experiments. A specially modified rotating analyzer ellipsometer (Gaertner Scientific) is used to measure the adsorbed amounts.<sup>7</sup>

#### Data Analysis:

The relationship of the measured ellipsometric angles ( $\Delta$  and  $\Psi$ ) to the film parameters of a multilayer stack can be expressed as:

$$e^{i\Delta} \tan \Psi = \frac{R_p}{R_s} = F(n_k, d_k) \quad (1)$$

where  $n_k$  and  $d_k$  refer to the indices of refraction and thicknesses of each layer present (denoted by the subscript  $k$ ). Measurement of the two independent quantities,  $\Delta$  and  $\Psi$ , allows for the solution of two unknowns, a layer thickness,  $d_1$ , and a refractive index,  $n_1$ . In this study, the adsorbed layer thickness and refractive index are determined assuming a homogeneous layer for the polymer thin film; the adsorbed amount is insensitive to the layer model assumed.<sup>6</sup> The adsorbed amount is calculated as:

$$A = d_1 c_1 = d_1 (n_1 - n_0) / \left( \frac{dn}{dc} \right)_0 \quad (2)$$

where  $n_1$  represents the refractive index of the adsorbed layer and  $d_1$  its thickness,  $n_0$  represents the refractive index of the copolymer solution and  $(dn/dc)_0$  is the change in refractive index of the solution with the concentration of the copolymer.

Knowing the adsorbed amount, the grafting density,  $\sigma$ , is calculated from Equation 3.

$$\sigma = \frac{A \text{ (mg/m}^2\text{)}}{M_w \text{ (mg/mol.)}} N_A \text{ (chains/mol.)} 10^{-18} \text{ (m}^2/\text{nm}^2\text{)} \quad (3)$$

which is the inverse of the area per chain. Accordingly, the interchain spacing is found from  $D = (1 / \sigma)^{1/2}$ . Further, the chain spacing at which coils on the surface first begin to touch is taken as

$$D_{\text{over}} = (\pi R_{\text{ps}}^2)^{1/2} \quad (4)$$

where  $R_{\text{ps}}$  represents the radius of gyration of the polystyrene blocks in solution. Another important variable in the scaling description of the copolymer adsorption is the asymmetry ratio,  $\beta$ .

$$\beta = \frac{R_{\text{ps}}}{R_{\text{peo}}} = \frac{a_B N_B^{3/5}}{a_A N_A^{3/5}} \quad (5)$$

where the ratio of the size of a single polystyrene segment to a single poly(ethylene oxide) segment is taken as 0.87 ( $a_B / a_A = 0.87$ ).

### Results and Discussion:

Results from the study are given in Table 1. It is clearly seen that the ratio of the interchain spacings to the overlap spacings are less than unity demonstrating that the triblock materials must be stretched away from the adsorbing surface. To our knowledge, this is the first report of brush formation in copolymers of the B-A-B architecture.

Table 1: Triblocks studied and chain spacings.

Copolymer	$N_B$	$N_A$	$N_A^{0.5}$	$\beta$	$D_{\text{int}} (\text{\AA})$	$D_{\text{int}} / D_{\text{over}}$
PS(233)-PEO(49)-PS(233)	4484	1227	35.0	1.97	298	0.56
PS(59)-PEO(1)-PS(59)	1134	22	4.7	9.16	139	0.32
PS(22)-PEO(1)-PS(22)	423	22	4.7	5.07	68	0.19
PS(127)-PEO(1)-PS(127)	2442	22	4.7	14.51	206	0.46
PS(107)-PEO(20)-PS(107)	2058	454	21.3	2.13	147	0.29
PS(305)-PEO(20)-PS(304)	5865	454	21.3	3.99	248	0.39
PS(168)-PEO(10)-PS(168)	3241	225	15.0	4.26	196	0.32
PS(1045)-PEO(10)-PS(1045)	20097	225	15.0	12.74	440	0.35

Figure 1 shows that the grafting density of the symmetric to moderately symmetric triblocks scale with the reciprocal of the adsorbing block size ( $1 / N_A$ ). For highly asymmetric triblocks, the surface density scales with the reciprocal of the square of the asymmetry ratio ( $\beta^{-2}$ ) as shown in Figure 2. Both of these results are consistent with the predictions of the scaling theory of Marques and Joanny for *A-B diblock adsorption*.<sup>3</sup> The B-A-B triblock materials are thus seen to behave the same as diblock materials as far as the effect of chain composition on the structure of the adsorbed layer is concerned.

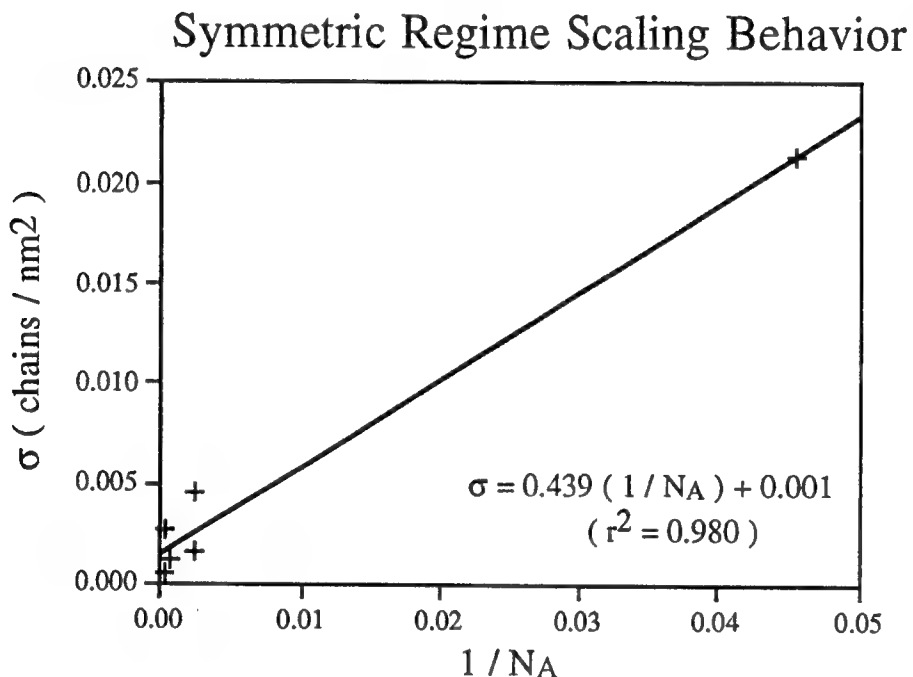


**Figure 1:** Scaling behavior of the grafting density for B-A-B triblocks falling in the symmetric regime ( $\beta < N_A^{0.5}$ ).

### Conclusions:

It is seen from the ( $D_{int} / D_{over}$ ) values in Table 1 that the B-A-B triblocks are stretched and hence it can be concluded that middle-adsorbing triblock materials can form a brush structure. Such materials should therefore be as effective as A-B diblock materials in steric stabilization applications.

It can be concluded that the middle-adsorbing triblock materials behave very similar to diblock materials. The change in composition of the B-A-B copolymers produces similar changes in the structure of the adsorbed layer as in A-B diblock layers. The surface density for the symmetric to moderately symmetric triblocks scale with the reciprocal of the head size ( $\sigma \propto N_A^{-1}$ ). For highly asymmetric triblocks, we find that the surface density scales with the reciprocal of the square of the asymmetry ratio ( $\sigma \propto \beta^{-2}$ ). The B-A-B architecture shares an important feature with the A-B diblock, namely attachment at a single location along the chain. This is in contrast to the A-B-A architecture where the chains may attach at two different locations; this later case may produce distinctly different behavior.<sup>2</sup>

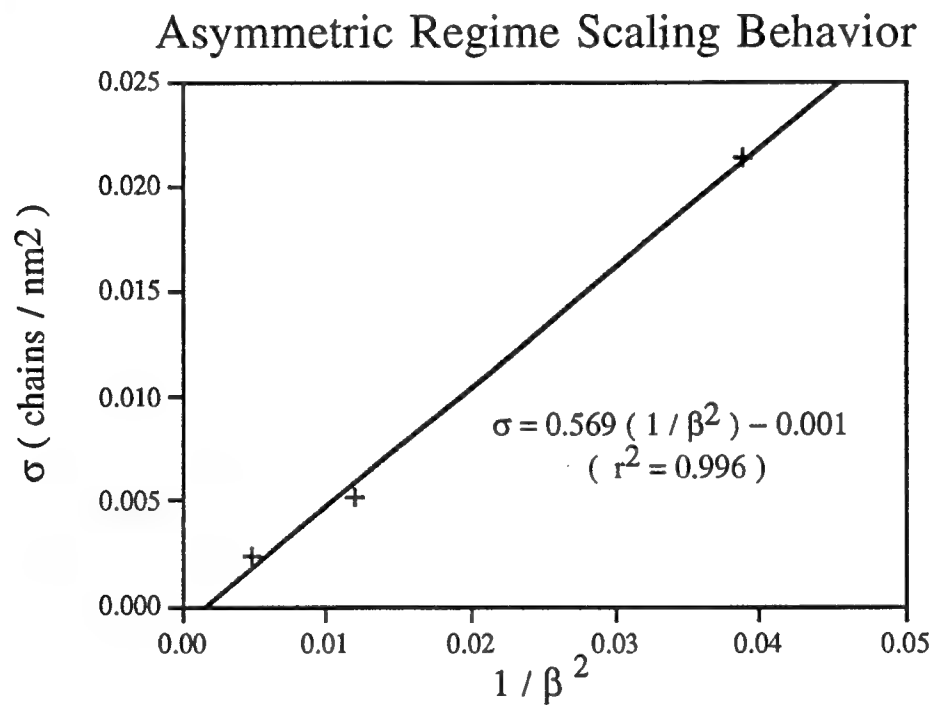


**Figure 2:** Scaling behavior of the grafting density for B-A-B triblocks falling in the asymmetric regime ( $\beta > N_A^{0.5}$ ).

## Homopolymer Solution Properties

### Introduction:

Understanding solution properties of polymers is a fundamental problem in polymer science. Solution properties must be understood in order to characterize polymeric materials and are essential in understanding the thermodynamic behavior of polymers.

In this section, results for two homopolymers in different solvents are described. The first system is polystyrene in toluene and the second is poly( vinyl caprolactam ) in water. Before presenting the results a brief background on solution properties is in order; a more detailed treatment may be found in the literature.

The *Radius of Gyration*,  $R_g$ , is an average measure of the radius of a polymer coil. It is defined as the average of the distance from a segment to the chain's center of mass; that is,

$$R_g^2 = \frac{1}{n+1} \sum_{i=0}^n (r_i - r_{c.o.m.})^2 \quad (6)$$

where  $n$  is the number of segments and,

$$r_{c.o.m.} = \frac{1}{n+1} \sum_{i=0}^n r_i$$

The value of the radius of gyration depends on molecular weight and the chemical environment of the molecule.

Theoretically, the relationship between the radius of gyration,  $R_g$ , and the number of repeat units in the polymer chain,  $N$ , should follow Equation 7.

$$R_g = a N^v \quad (7)$$

Here,  $a$  represents an effective segment size and  $v$  is an excluded volume parameter. This latter parameter takes on a value of 0.5 for athermal solutions and 0.6 for good solvents. Polymers expand under good solvent conditions and contract in poor solvents, in the melt state a polymer is under athermal conditions and  $R_g$  increases with the square root of the molecular weight.

The thermodynamics of polymer solutions may be described by the Flory-Huggins theory which yields the following expression for the Free Energy of Mixing:

$$\Delta \underline{G}_{\text{MIX}} = kT[n_1 \ln \varphi_1 + n_2 \ln \varphi_2 + n_1 \varphi_2 \chi] \quad (8)$$

where  $n_i$  represents the number of molecule  $i$  and  $\varphi_i$  its volume fraction. This free energy of mixing is a Helmholtz free energy because the derivation is based on a lattice model and is therefore restricted to constant volume. Flory-Huggins theory allows for a non-zero enthalpy of mixing through the introduction of a simple mixing parameter,  $\chi$ . The extensive enthalpy of mixing may be expressed as:

$$\Delta \underline{H}_{\text{MIX}} = kTn_1\varphi_2\chi \quad (9)$$

Within the framework of Flory-Huggins theory, once the  $\chi$  parameter is known, the phase diagram may be calculated. The theory as outlined here is capable only of predicting Upper Critical Solution Temperature (UCST) phase diagrams; in such systems the material phase separates upon cooling. While this behavior is often observed, other types of phase envelopes are known. These include LCST in which phase separation occurs upon heating, combined systems, hour glass shaped two phase regions and closed loop systems. In order to describe such behavior, the energetics parameter  $\chi$  must be determined as a function of temperature and composition.

### Experimental

LALLS (Low Angle Laser Light Scattering) is a powerful technique for studying solution properties because it provides measurements of the weight average molecular weight ( $M_w$ ), the radius of gyration ( $R_g$ ), and the Flory energetics parameter ( $\chi$ ), simultaneously. In LALLS, the intensity of light scattered is measured as a function of the angle from the incident beam (typically in the range from  $20^\circ$  to  $140^\circ$ ). Data analysis is based on the relationship expressed in Equation 10.

$$\frac{K^* c}{R_\theta} = \frac{1}{M_w} \left\{ 1 + \frac{16\pi^2}{3\lambda^2} \langle R_g^2 \rangle \sin^2 \left( \frac{\theta}{2} \right) \right\} + 2A_2 c + \dots \quad (10)$$

Here,  $\theta$  is the scattering angle,  $\lambda$  is the wavelength of the laser light,  $c$  is concentration,  $A_2$  is the

second virial coefficient,  $R_g$  is the Rayleigh Ratio, and  $K^*$  is a constant given by,

$$K^* = 4 \pi^2 n_o^2 \left( \frac{dn}{dc} \right)^2 \lambda^4 N_{Av}^{-1}$$

in which  $n$  is the index of refraction of the solvent and  $N_{Av}$  is Avagadro's number.

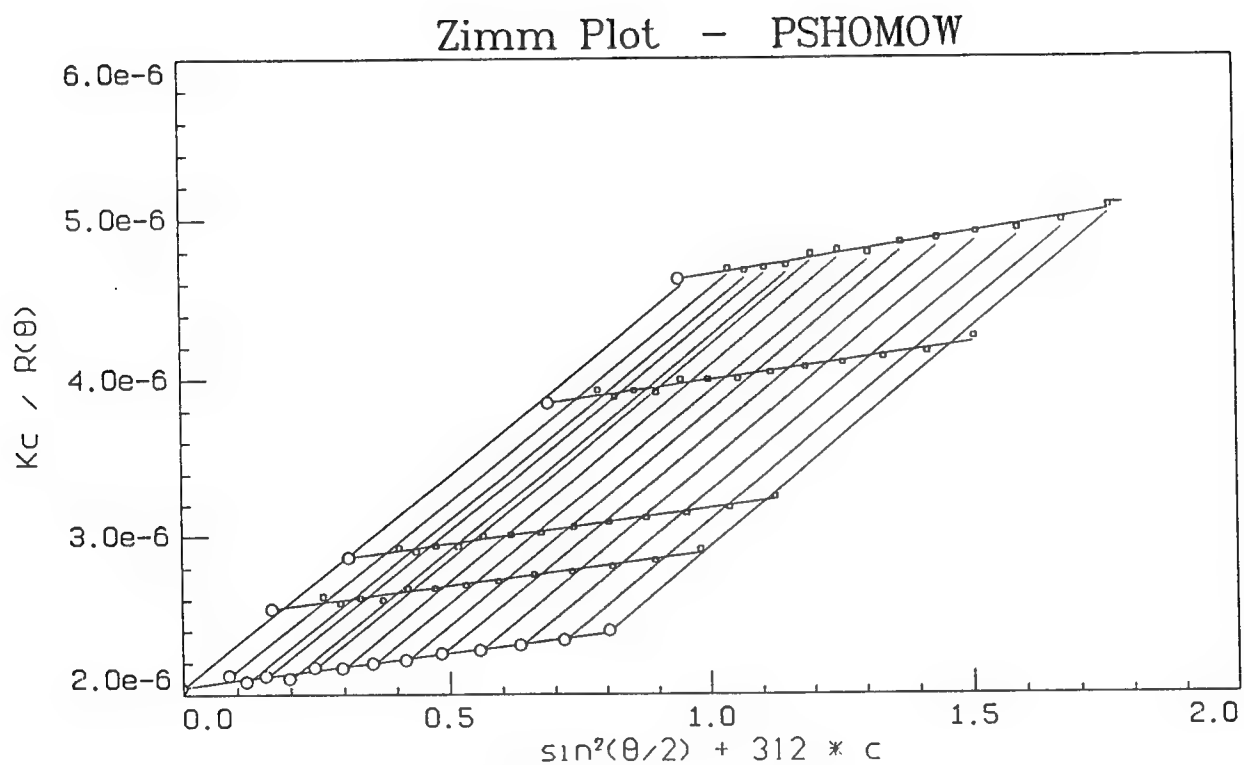
The second virial coefficient is related to the  $\chi$ -parameter by,

$$A_2 = \frac{v_p^2}{\bar{V}_s} \left( \frac{1}{2} - \chi \right) \quad (11)$$

in which  $\bar{V}_s$  is the partial molar volume of the solvent and  $v_p$  is the specific volume of the polymer.

The experimental quantities  $M_w$ ,  $R_g$ , and  $A_2$ , are usually deduced through the use of a so-called Zimm Plot, an example of which is shown in Figure 3. In this plot, the light scattering data from several concentrations are plotted as a function of the scattering angle. Each concentration is extrapolated to zero scattering angle and for each detection angle, the data is extrapolated to zero concentration. The Zimm Plot is thus based on different limits of Equation 10; the slope of the extrapolated zero concentration line gives  $R_g$ , the slope of the extrapolated zero angle line gives  $A_2$ , and the intercept of the two extrapolated lines with the y-axis yields  $M_w$ .

For all of the LALLS experiments samples were prepared in the same way. First, a scintillation vile was rinsed with acetone and allowed to dry. The polymer sample, in dry powdered form, was massed into the vile. Next, a high precision syringe was used to add 15.0 +/- 0.1 ml of solvent to the scintillation vile. The sample was capped using aluminum foil as a barrier against diffusional losses. Low heat, administrated via a hot plate, was used to speed the dissolution of the polymer in the solvent. Once dissolved, the solutions were filtered 3-5 times through a Whatman 0.2  $\mu\text{m}$  Polytetrafluoroethylene filter.



DATE: Mon Jul 18 11:14:48 1994

RMS Radius :  $26.5 \pm 0.7 \text{ nm}$

MW :  $(4.89 \pm 0.1) \times 10^5 \text{ g/mol}$

A2 :  $(4.17 \pm 0.2) \times 10^{-4} \text{ mol ml/g}$

**Figure 3:** A Zimm plot for polystyrene in toluene collected using a Wyatt Technologies DAWN model B low angle laser light scattering apparatus.

### Results and Discussion:

Figure 4 shows a  $\log R_g$  versus  $\log N$  plot for samples of polystyrene in toluene having a molecular weights greater than 100,000 g / mol. Based on the linear regression curve shown, the following specific form of Equation 7 is found,

$$R_g (\text{\AA}) = 1.76 N_{ps}^{0.597} \quad (12)$$

the closeness of the exponent to 0.600 demonstrates that toluene is a good solvent for polystyrene and is consistent with values found in the literature.

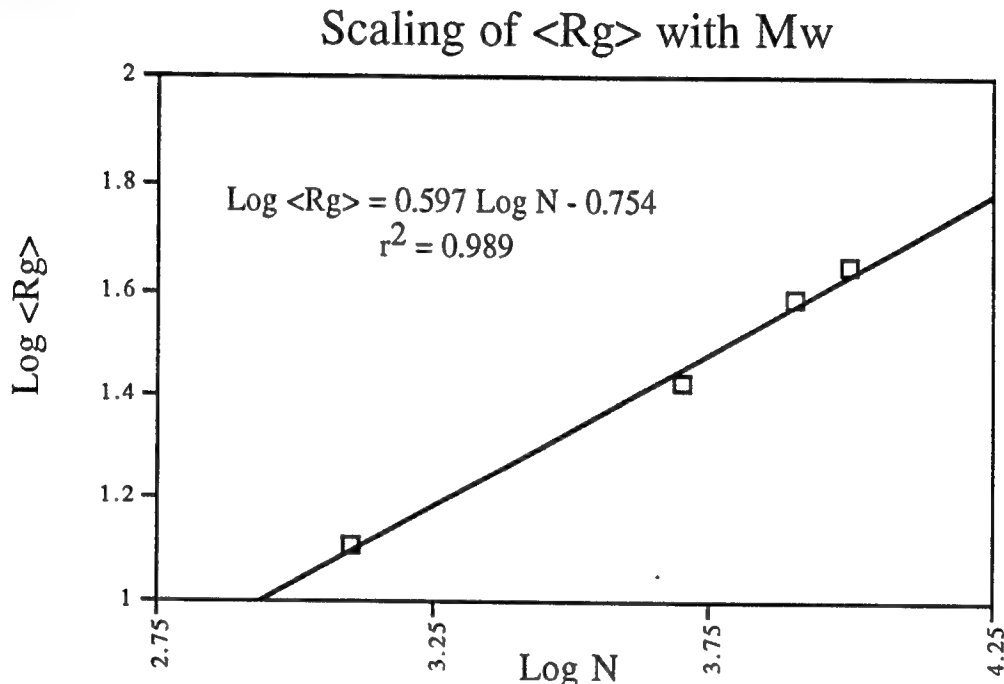


**Figure 4:**  $R_g$  against number of segments for high  $M_w$  polystyrenes in toluene.

For polystyrenes having lower molecular weights, a different scaling relationship is found. Figure 5 shows a  $\log R_g$  versus  $\log N$  plot for samples of polystyrene in toluene having molecular weights less than 100,000 g / mol. Based on the linear regression curve shown, the following specific form of Equation 7 is found,

$$R_g (\text{\AA}) = 7.16 N_{ps}^{0.401} \quad (13)$$

This finding, of having a lower valued scaling exponent for lower molecular weight samples, has appeared in the polymer literature previously but is generally unappreciated. This deviation from the expected 0.600 exponent may have to do with a lack of Gaussian statistics associated with lower molecular weight polymers.

The behavior of poly(vinyl caprolactam) in water produces another scaling relationship between the radius of gyration and the molecular weight. For this system, no previous reports are available in the literature because the synthesis of this polymer is a recent development, as such this information represents a *fundamental contribution to the knowledge base on polymeric materials*.

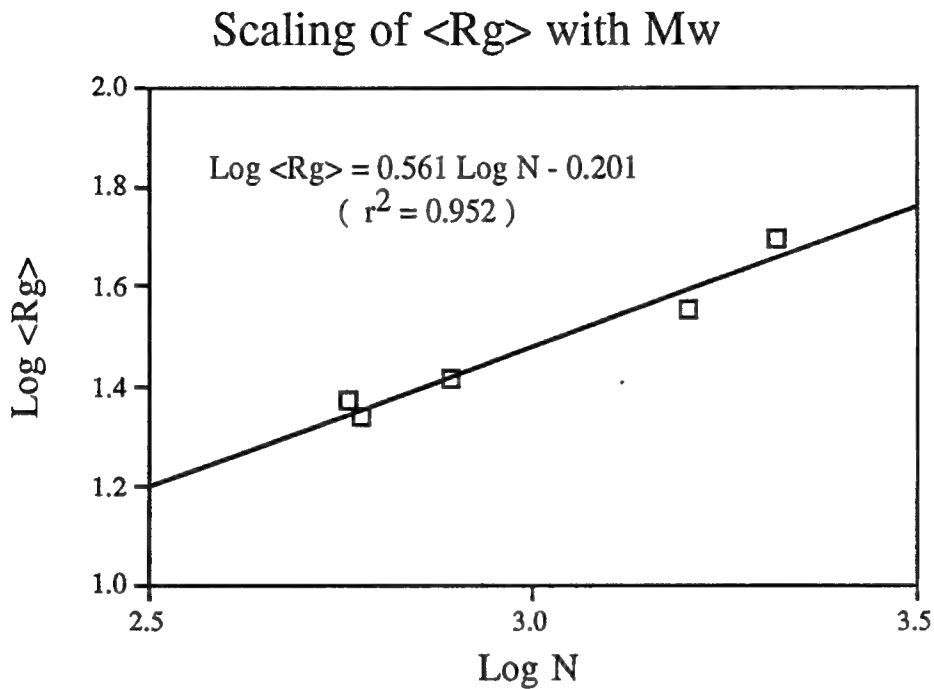


**Figure 5:**  $R_g$  against number of segments for low  $M_w$  polystyrenes in toluene.

Figure 6 shows the  $\log R_g$  versus  $\log N$  plot for samples of poly(vinyl caprolactam) in water, from this graph the following relationship is determined,

$$R_g (\text{\AA}) = 6.30 N_{\text{pv-cap}}^{0.561} \quad (14)$$

Equation 14 may be used to find  $c^*$ , the overlap concentration. This is the concentration at which a polymer solution makes the transition from the dilute regime (where individual coils are isolated in solution) to the semi-dilute regime (where polymer coils overlap and interdigitate). The overlap concentration is given by,

$$c^* (\text{mg / ml}) = 6315 \text{ MW}^{-0.68} \quad (15)$$

where MW is the molecular weight of the poly( vinyl caprolactam ). So, for aqueous solutions of this homopolymer with MW = 10k (g/mol),  $c^* = 12.03$  (mg/ml) or about 1.2 wt%, for a

homopolymer solution with MW = 100k (g/mol),  $c^* = 2.51$  (mg/ml) or about 0.25 wt%, and for a homopolymer solution with MW = 1,000k (g/mol),  $c^* = 0.52$  (mg/ml) or about 0.05 wt%.

Trial studies, performed in the laboratory of Professor Dendy Sloan at the Colorado School of Mines, on the inhibition of gas hydrate growth under conditions mimicking North Sea pipeline conditions have found poly( vinyl caprolactam ) to be an effective inhibiting agent. Specifically, for samples having molecular weights in the range of 100,000 g/mol concentrations of 0.5 wt % are needed. For such samples, concentrations of 0.25 wt% were found to be ineffective. It thus appears that the mechanism of inhibition is space filling by polymer coils, requiring concentrations in excess of  $c^*$ . As a result the engineering correlation ( Equation 15 ) developed in this work will have immense practical utility in oil and gas production!

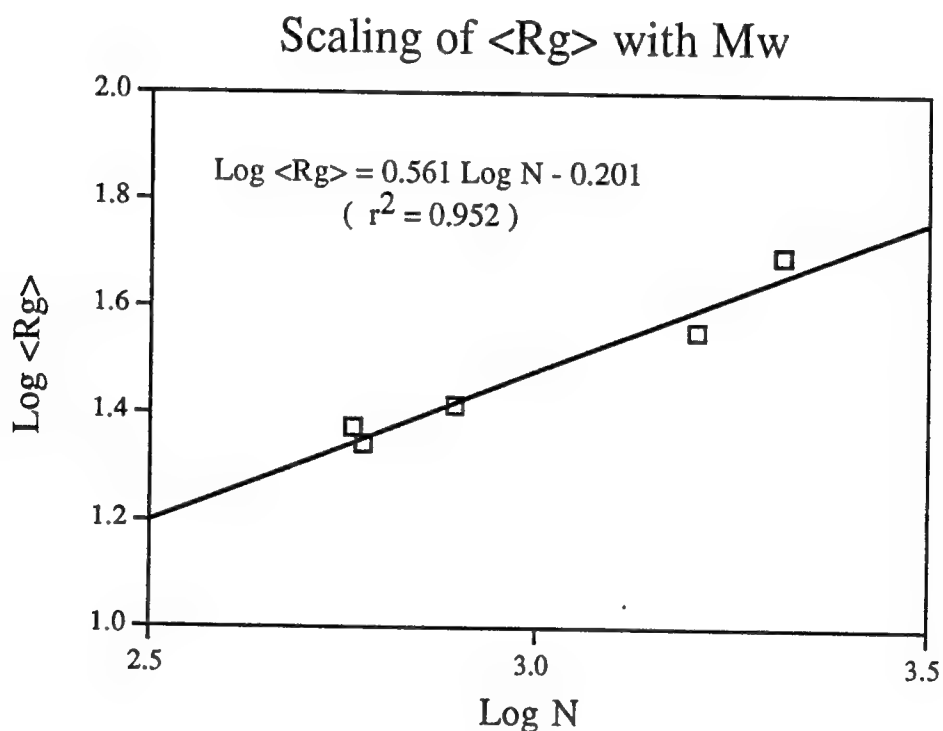


**Figure 6:**  $R_g$  against number of segments for poly( vinyl caprolactam ) in water.

### Conclusions:

The scaling behavior of the radius of gyration of polystyrene homopolymers in toluene has been determined; it was found that  $R_g (\text{\AA}) = 1.76 N_{ps}^{0.597}$  for polymers with a molecular weight greater than 100,000 g/mol. For lower molecular weight polystyrene samples, we find  $R_g (\text{\AA}) = 7.16 N_{ps}^{0.401}$ . Finally, for poly(vinyl caprolactam) homopolymers in water, it was found that  $R_g (\text{\AA}) = 6.30 N_{pv\text{-}cap}^{0.56}$ . Based on this information it is possible to derive an engineering correlation for the overlap concentration, we find  $c^* (\text{mg / ml}) = 6315 MW_{pv\text{-}cap}^{-0.68}$  where  $MW_{pv\text{-}cap}$  is the polymer molecular weight.

### References:

1. Halperin, A.; Tirrell, M.; Lodge, T. P. *Adv. Poly. Sci.*, 100, 31, 1992.
2. Dorgan, J. R.; Stamm, M.; Toprakcioglu, C. *Macromolecules*, 26(20), 5321, 1993.
3. Marques, C. M.; Joanny, J. F. *Macromolecules*, 22, 1454, 1989.
4. Fleer, G. J.; Scheutjens, J. M. H. M. *Coll. and Surf.*, 51, 281, 1990.
5. Uyanik, N; Baysal, B. M. *J. Appl. Poly. Sci.*, 41, 1981, 1990.
6. Motschmann, H.; Stamm, M; Toprakcioglu, C. *Macromolecules*, 24, 3681, 1991.
7. Pai-Panandiker, R. S.; Dorgan, J. R. , submitted to *Rev. Sci. Inst.*, 1994.

NON-LINEAR OPTICAL PROPERTIES  
OF A SERIES OF LINEAR TRIACETYLENES

Mary Ann Jungbauer  
Professor of Chemistry  
Department of Physical Sciences

Barry University  
11300 N. E. Second Avenue  
Miami Shores FL 33161

Final Report for  
Summer Faculty Research Program  
Frank J. Seiler Research Laboratory  
Materials Chemistry Division

Sponsored by:  
Air Force Office of Scientific Research  
Bolling Air Force Base, D. C.

and

Frank J. Seiler Research Laboratory  
United States Air Force Academy, CO

September, 1994

NON-LINEAR OPTICAL PROPERTIES  
OF A SERIES OF LINEAR TRIACETYLENES

Mary Ann Jungbauer  
Professor of Chemistry  
Department of Physical Sciences  
Barry University

Abstract

Frequency dependent polarizabilities ( $\alpha$ ), first hyperpolarizabilities ( $\beta$ ), and second hyperpolarizabilities ( $\gamma$ ) were calculated for a series of linear triacetylenes: triacetylene; monosubstituted fluoro, cyano, nitro, amino, and planar amino triacetylene; disubstituted fluoro/amino, cyano/amino, and nitro/amino triacetylene, for both the planar and non-planar amine group. For each of the disubstituted nitro compounds, with the planar and the non-planar amino group, two conformations were studied. Calculations were made for the static (zero frequency) state and for  $E = 1.16527$  eV (1064 nm). Statistical comparison of the 1064 nm data with the static data reveal linear relationships between the static values of  $\alpha$ ,  $\beta$ , and  $\gamma$  and the respective 1064 nm values for the polarizability,  $\alpha$ ; Second Harmonic Generation,  $\beta(a)$ ; Electro-Optic Pockels Effect,  $\beta(EOPE)$ ; Optical Rectification,  $\beta(OR)$ ; Third Harmonic Generation,  $\gamma(THG)$ ; Electric Field Induced Second Harmonic Generation,  $\gamma(EFISH)$ ; Intensity Dependent Refractive Index,  $\gamma(IDIR)$ ; and the Optical Kerr Effect,  $\gamma(OKE)$ . Semiempirical calculations were made using MOPAC 93.

## NON-LINEAR OPTICAL PROPERTIES OF A SERIES OF LINEAR TRIACETYLENES

Mary Ann Jungbauer

### Introduction

Linear optical properties have long been studied and include the familiar measurable properties of transmission, absorption, index of refraction, etc. In recent years, the availability of intense laser light of single frequency and wavelength, such as the 1064 nm (Nd:YAG laser) light of this study, has revealed that interaction of this intense light with matter can change these linear properties, and, in the process, change the light itself in a nonlinear way (1). Also, availability of intense laser light has made observable and useful the weak polarizability and hyperpolarizability properties of certain materials (2). The incident light can be doubled and tripled; if the incident light contains more than one frequency, sums and differences of frequencies can be observed (1). At the molecular level, the polarization (P) is related to the electric field strength (E) and can be expanded in a Taylor type series by:

$$P = \alpha E + \beta E^2 + \gamma E^3 + \dots$$

From the molecular to bulk level, these coefficients are proportional to the electric susceptibility ( $\chi$ ):

$$\alpha \propto \chi^{(1)}, \quad \beta \propto \chi^{(2)}, \quad \gamma \propto \chi^{(3)},$$

where  $\alpha$  indicates the extent of the polarizability,  $\beta$  the first hyperpolarizability, and  $\gamma$  the second hyperpolarizability (2).

Marder has shown the relationship between linear and nonlinear properties of linear conjugated molecules, and predicts that understanding of the relation between molecular structure and  $\beta$  and  $\gamma$  will progress to the point where measurements can themselves be used to provide detailed insight into chemical structure (3). Dagani, interpreting Marder, explains that as the field strength (E) increases the higher nonlinear contributions such as  $\beta$  and  $\gamma$  become important. In some molecules, and this is reflected in the present study of triacetylenes (1,3,5-hexatriynes) polarization occurs more in one direction than the other.  $\beta$  is a measure, in part, of this polarization asymmetry (4). The polarization P (that is, the

separation of charges in a molecule) will give rise to optical properties of molecules in bulk, and to the electric susceptibility ( $\chi$ ) as shown in the equations above (2).

Matsuzawa and Dixon compared calculated and experimental values for a series of donor-acceptor molecules including a series of mono and disubstituted benzenes, disubstituted biphenyls and fluorenes, disubstituted styrenes, and substituted stilbenes (5). They report good correlation for static hyperpolarizabilities ( $\beta$  and  $\gamma$ ) between semiempirical calculations and experiment. Since their calculations reproduced the dependence of  $\beta$  and  $\gamma$  on the strength of donor and acceptor molecules, and reproduced the increase of  $\beta$  and  $\gamma$  by charge transfer, they conclude that semiempirical methods should be a good scouting tool to aid in the search for new and novel NLO materials. Also, they point out that conformational averaging needs to be taken into account when comparing calculated and experimental values. In this study of triacetylenes we include conformers.

In two related articles, Cheng *et al.* present a systematic experimental investigation of organic molecular NLO polarizabilities of benzene and stilbene derivatives using light at 1.91  $\mu\text{m}$  (1910 nm to compare to this triacetylenes study at 1064 nm) (6, 7). They found geometric factors to be more important in some cases than the donor/acceptor properties of the substituent groups.

NLO properties of materials convert the laser light into new colors that are mathematically related to the original laser light. They are commonly used to double or triple the incident light enabling NLO materials to be used in novel ways. (2) NLO materials are being used, at present, as eye protection shields, wave guides, parametric converters, in the manufacture of weapons, communications, avionics, and survival techniques such as sensor protection etc. (2) However, currently identified NLO materials do not fulfill user needs for frequency agile laser sources, fast optical switching and computation, and available, affordable, and processable materials. Also, third order harmonic effects in currently available NLO materials are still far away from practical applications (8).

NLO materials being studied include polymers, conjugated polymers, crystals, polyurethanes, stilbenes, thiophenes, Langmuir-Blodgett films, other thin films, liquid crystals, etc. (4, 8). With respect to this study, the most important compounds being characterized are unsaturated organic compounds.  $\pi$  conjugated organic NLO materials represent a major advance for integrated optoelectronic circuits, high

speed fiber optics, and advanced packaging (9). Unsaturated organic materials with their associated  $\pi$  electrons, in many cases delocalized, give rise to large NLO activities. By simply considering  $\pi$  to  $\pi^*$  transitions, a two level perturbation theory model provides an adequate description of  $\beta$  response (10).

A goal of this Laboratory is to understand the fundamental cause of NLO properties at a molecular level. This study of the NLO properties of triacetylenes contributes to that goal. There is still a dearth of systematic theoretical data and another goal of this Laboratory is to address this need (2, 10). A detailed *ab initio* study of substituted linear diacetylenes has been completed to see the effect of substituents on the NLO properties of the parent diacetylene (11). This study of triacetylenes is a partial extension of that study. Another goal is to find underlying causes that lead to the observed linear relationships between static and dynamic (at 1064 nm)  $\alpha$ ,  $\beta$ , and  $\gamma$ . Data generated in this study should provide background material for achieving that goal (10).

### Methodology

Twelve different linear triacetylenes were studied. For two of the disubstituted molecules a second conformer was added, bringing the total number of molecules studied to fourteen. Triacetylene,  $C_6H_2$ , ( $D_{\infty h}$ ), the monofluoro,  $C_6HF$ , and the monocyano,  $C_6HCN$ , molecules, (both  $C_{\infty v}$ ) are linear. Planar aminotriacetylene,  $C_6HNH_2$ , planar aminofluoro triacetylene,  $C_6FNH_2$ , planar aminocyanotriacetylene,  $C_6CNNH_2$ , and nitrotriacetylene,  $C_6HNO_2$ , are planar ( $C_{2v}$ ). Aminotriacetylene,  $C_6HNH_2$ , aminofluorotriacetylene,  $C_6FNH_2$ , and aminocyanotriacetylene,  $C_6CNNH_2$ , are nonplanar molecules with a single plane of symmetry ( $C_s$ ).

The planar and non-planar amino nitro compounds, however, can be considered in two extreme orientations. In the more stable conformer (as indicated by the  $\Delta H^\circ_f$  values of the planar  $C_{2v}$  structure), the  $NO_2$  group is coplanar with the  $NH_2$  group. In the less stable conformer (also  $C_{2v}$ ) the plane of the  $NO_2$  group bisects the  $HNH$  angle. For  $H_2NC_6NO_2$  (nonplanar  $NH_2$ ) the two extreme orientations are the more stable conformer ( $C_s$ ) where the plane of the  $NO_2$  group is above the plane of the  $NH_2$  group, and the conformer, also ( $C_s$ ), where the plane of the  $NO_2$  group bisects the  $HNH$  angle. These are illustrated below.

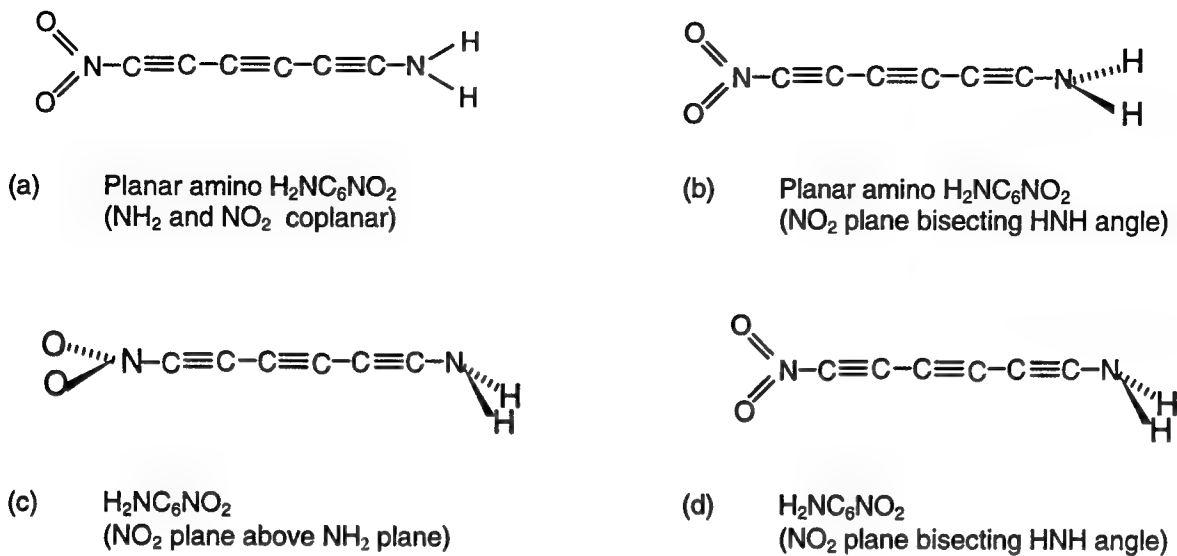


Figure I. Structures of conformers of  $\text{H}_2\text{NC}_6\text{NO}_2$ . (a) Planar  $\text{NH}_2$  coplanar with  $\text{NO}_2$  (b)  $\text{NO}_2$  plane bisecting  $\text{HNH}$  angle (c)  $\text{NO}_2$  plane above  $\text{NH}_2$  plane (d)  $\text{NO}_2$  plane bisecting  $\text{HNH}$  angle

Semiempirical frequency dependent polarizabilities ( $\alpha$ ), first hyperpolarizabilities ( $\beta$ ), and second hyperpolarizabilities ( $\gamma$ ) were calculated using MOPAC 93 (14). One of the lasers that has been a laboratory tool for twenty years is the Nd:YAG laser, which emits light of  $1.064 \mu\text{m}$  or  $1064 \text{ nm}$ . (12). To correlate with experiments (2), calculations were performed for the static  $\alpha$ ,  $\beta$ , and  $\gamma$  ( $E = 0$ ), and for  $E = 1.16527 \text{ eV}$  ( $1064 \text{ nm}$ ) for the Polarizability,  $\alpha$ ; Second Harmonic Generation,  $\beta(\text{SHG})$ ; Electro-Optic Pockels Effect,  $\beta(\text{EOPE})$ ; Optical Rectification,  $\beta(\text{OR})$ ; Third Harmonic Generation,  $\gamma(\text{THG})$ ; Electric Field Induced Second Harmonic generation,  $\gamma(\text{EFISH})$ ; Intensity Dependent Refractive Index,  $\gamma(\text{IDIR})$ ; and the Optical Kerr Effect,  $\gamma(\text{OKE})$ .

The data set for each calculation followed published guidelines (10, 14, 15). The PM3 Hamiltonian was used for all calculations. At least three MOPAC 93 runs were made for each of the fourteen molecules. All calculations achieved self consistent field, SCF. The first, to obtain general information, used the keywords PM3, EF, LOCAL, PRECISE, VECTORS. Symmetry was also imposed for the molecules containing amino and/or groups. The second was a FORCE calculation to obtain harmonic vibrational frequencies; all symmetry definitions are ignored in a FORCE calculation. The third

was a POLAR calculation to obtain the various  $\alpha$ ,  $\beta$  and  $\gamma$  values. To obtain all the values needed for  $\beta$ , several sections of the MOPAC 93 program had to be used, and the POLAR calculation repeated, to obtain consistent values for  $\beta$ (EOPE) and  $\beta$ (OR). Geometry was at a stationary point for all molecules except those involving the planar amino group, and the unstable conformer of  $\text{H}_2\text{NC}_6\text{NO}_2$  where the  $\text{NO}_2$  plane bisects the HNH angle (illustrated in Figure 1d). For these a LET DDMIN=0.0 was added and the calculations repeated.

Regressional analysis was performed on the fourteen values for each of these eight parameters. Statistical comparison of the 1064 nm data with the static data reveal linear relationships between the static values of  $\alpha$ ,  $\beta$ , and  $\gamma$  and the respective 1064 nm values for  $\alpha$ ,  $\beta$ (SHG),  $\beta$ (EOPE),  $\beta$ (OR),  $\gamma$ (THG),  $\gamma$ (EFISH),  $\gamma$ (IDIR), and  $\gamma$ (OKE). Values and graphical presentations are given in the Results and Discussion sections below.

## Results

Average values for the static state the 1064 nm state for  $\alpha$ ,  $\beta$ (SHG) and  $\gamma$ (THG) are given in Table I below. Two different options, in different parts of MOPAC 93, were used to calculate each static value. For comparisons involving 1064 nm  $\alpha$ ,  $\beta$ (SHG), and  $\gamma$ (THG), the static values generated with them were used. For comparisons involving 1064 nm  $\beta$ (EOPE),  $\beta$ (OR),  $\gamma$ (EFISH),  $\gamma$ (IDIR), and  $\gamma$ (OKE) the second set of static values generated with them were used.

In Table II below the order of the static values for the fourteen molecules are given for  $\alpha$ ,  $\beta$ , and  $\gamma$ . All the graphs in the following sections follow this order along the X-axis or static value axis for  $\alpha$ ,  $\beta$ , or  $\gamma$ . In Table III below is a detailed report for  $\alpha$ . Similar detailed values were generated for  $\beta$  and  $\gamma$ , but are not reported here. Data and graphs for 1064 nm values vs. static values are integrated into the Discussion section below.

Table I. Average Values for Various (Hyper) Polarizabilities

MOLECULE	$\langle\alpha(0)\rangle$	$\langle\beta(0)\rangle$	$\langle\gamma(0)\rangle$	$\langle\alpha(1064)\rangle$	$\langle\beta(1064)\rangle$ ( $\beta(\text{SHG})$ )	$\langle\gamma(1064)\rangle$ ( $\gamma(\text{THG})$ )
$\text{C}_6\text{H}_2$	60.576	0.00	10249.7	62.836	0.00	19717.7
$\text{C}_6\text{HF}$	63.923	51.41	12188.9	66.411	58.00	24091.3
$\text{C}_6\text{HCN}$	89.470	172.54	26981.3	93.483	251.48	63945.9
$\text{C}_6\text{HNO}_2$	81.833	103.43	22485.6	85.114	192.64	50224.2
$\text{C}_6\text{HNH}_2^*$	79.092	694.57	25448.1	82.887	1118.84	123739.9
$\text{C}_6\text{HNH}_2$	76.871	534.56	24753.2	80.294	795.77	78071.9
$\text{C}_6\text{FNH}_2^*$	83.145	702.20	29345.9	87.289	1184.04	161246.8
$\text{C}_6\text{FNH}_2$	80.776	525.53	28407.8	84.518	826.09	94961.7
$\text{C}_6\text{CNNH}_2^*$	112.410	1386.52	64239.7	118.632	2415.31	587934.3
$\text{C}_6\text{CNNH}_2$	109.048	1060.94	58896.8	114.671	1705.57	241448.6
$\text{C}_6\text{NO}_2\text{NH}_2^*\text{copl}$	105.147	1435.07	62638.8	110.813	2727.77	1177420.4
$\text{C}_6\text{NO}_2\text{NH}_2^*\text{perp}$	103.147	1113.01	45364.4	109.062	2727.77	320659.1
$\text{C}_6\text{NO}_2\text{NH}_2\text{paral}$	101.502	1082.62	54578.4	106.498	1872.93	313937.7
$\text{C}_6\text{NO}_2\text{NH}_2\text{perp}$	100.746	904.57	44635.0	105.579	1467.74	161896.6

Table II. Order of Static Values ( $\text{NH}_2^*$  indicates planar amino group)

Order of Increasing Alpha (Static) (a.u.)	Order of Increasing Beta (Static) (a.u.)	Order of Increasing Gamma (Static) (a.u.)
$\text{C}_6\text{H}_2$	60.576	$\text{C}_6\text{H}_2$
$\text{C}_6\text{HF}$	63.923	$\text{C}_6\text{HF}$
$\text{C}_6\text{HNH}_2$	76.871	$\text{C}_6\text{HNO}_2$
$\text{C}_6\text{HNH}_2^*$	79.092	$\text{C}_6\text{HCN}$
$\text{C}_6\text{FNH}_2$	80.776	$\text{C}_6\text{FNH}_2$
$\text{C}_6\text{HNO}_2$	81.833	$\text{C}_6\text{HNH}_2$
$\text{C}_6\text{FNH}_2^*$	83.145	$\text{C}_6\text{HNH}_2^*$
$\text{C}_6\text{HCN}$	89.471	$\text{C}_6\text{FNH}_2^*$
$\text{C}_6\text{NO}_2\text{NH}_2\text{perp}$	100.746	$\text{C}_6\text{NO}_2\text{NH}_2\text{perp}$
$\text{C}_6\text{NO}_2\text{NH}_2\text{paral}$	101.502	$\text{C}_6\text{CNNH}_2$
$\text{C}_6\text{NO}_2\text{NH}_2^*\text{perp}$	103.701	$\text{C}_6\text{NO}_2\text{NH}_2\text{paral}$
$\text{C}_6\text{NO}_2\text{NH}_2^*\text{copl}$	105.147	$\text{C}_6\text{NO}_2\text{NH}_2^*\text{perp}$
$\text{C}_6\text{CNNH}_2$	109.048	$\text{C}_6\text{CNNH}_2^*$
$\text{C}_6\text{CNNH}_2^*$	112.411	$\text{C}_6\text{NO}_2\text{NH}_2^*\text{copl}$
		1435.07

Table III. Detailed Report for Polarizability,  $\alpha$

MOLECULE	$\alpha_{xx}(0)$	$\alpha_{yy}(0)$	$\alpha_{xy}(0)$	$\alpha_{zz}(0)$	$\langle \alpha(0) \rangle$	$\alpha_{xx}(1064)$	$\alpha_{yy}(1064)$	$\alpha_{xy}$ or $\alpha_{yx}$	$\alpha_{zz}(1064)$	$\langle \alpha(1064) \rangle$
C <sub>6</sub> H <sub>2</sub>	167.625	7.051	0.000	7.051	60.576	174.249	7.129	0	7.129	62.836
C <sub>6</sub> HF	178.220	6.774	0.000	6.774	63.923	185.516	6.859	0	6.859	66.411
C <sub>6</sub> HCN	247.722	10.344	0.000	10.344	89.470	259.194	10.508	-0.00001	10.508	93.483
C <sub>6</sub> HNO <sub>2</sub>	207.187	30.063	0.000	8.249	81.833	216.231	30.774	0	8.337	85.114
C <sub>6</sub> HNH <sub>2</sub> *	214.870	12.309	0.000	10.097	79.092	225.737	12.454	0	10.470	82.887
C <sub>6</sub> HNH <sub>2</sub>	207.457	13.461	0.000	9.695	76.871	217.384	13.653	0	9.846	80.298
C <sub>6</sub> FNH <sub>2</sub> *	227.574	12.034	0.000	9.826	83.145	239.481	12.186	0	10.201	87.290
C <sub>6</sub> FNH <sub>2</sub>	219.728	13.172	0.000	9.427	80.776	230.597	13.370	0	9.586	84.518
C <sub>6</sub> CNNH <sub>2</sub> *	308.399	15.555	0.000	13.278	112.410	326.397	15.783	0	13.713	118.631
C <sub>6</sub> CNNH <sub>2</sub>	297.500	16.675	0.000	12.968	109.048	313.857	16.951	0	13.207	114.671
C <sub>6</sub> NO <sub>2</sub> NH <sub>2</sub> *copl	35.053	269.292	0.000	11.095	105.147	35.821	285.177	0	11.440	110.813
C <sub>6</sub> NO <sub>2</sub> NH <sub>2</sub> *perp	35.053	264.938	0.000	11.095	103.147	13.601	279.842	0	33.744	109.062
C <sub>6</sub> NO <sub>2</sub> NH <sub>2</sub> paral	257.429	36.216	0.000	10.86	101.502	271.433	37.030	0	11.030	106.498
C <sub>6</sub> NO <sub>2</sub> NH <sub>2</sub> perp	255.112	32.597	-0.462	14.531	100.746	286.621	33.386	-0.644	14.729	105.579

### Discussion

The structures of linear triacetylene (1,3,5-hexatriyne) and the substituted linear triacetylenes of this study are described on pages 13-5 and 13-6. For the NH<sub>2</sub> (sp<sup>3</sup>) amino compounds the distance, angle, and dihedral were all three optimized for the first of the two hydrogens. None were optimized for the second hydrogen; through symmetry relationships its bond distance and bond angle were made equal to those of the first hydrogen, and its dihedral angle equal to but opposite in sign. For the planar NH<sub>2</sub> (sp<sup>2</sup>) amino compounds the distance and angle were optimized, but not the dihedral for the first hydrogen. For the second hydrogen, none were optimized but through symmetry relations the two N-H distances and angles were made equal and the dihedral angles differed by 180°.

Stable molecules are minima on the potential energy surface and all vibrational frequencies are positive. For unstable molecules, one negative (imaginary) frequency is expected indicating a transition state. These include all of the planar amino molecules and the conformer of H<sub>2</sub>NC<sub>6</sub>NO<sub>2</sub> where the NO<sub>2</sub> plane bisects the HNH angle (Figure 1d). For this last molecule two negative frequencies were obtained indicating a higher order saddle point. Table IV below is a summary of negative (imaginary) frequencies obtained for triacetylenes, XC<sub>6</sub>Y.

Table IV. Data for Unstable Amino Compounds.  $\text{NH}_2^*$  is Planar ( $\text{sp}^2$ ) Amino.

X	Y	Figure No.	Point Group	No. of Negative Frequencies	Symmetry
$\text{NH}_2^*$	Hydrogen		$C_{2v}$	1	$B_1$
$\text{NH}_2^*$	Fluoro		$C_{2v}$	1	$B_1$
$\text{NH}_2^*$	Cyano		$C_{2v}$	1	$B_1$
$\text{NH}_2^*$	Nitro (Coplanar)	Ia	$C_{2v}$	1	$B_1$
$\text{NH}_2^*$	Nitro (Bisecting)	Ib	$C_{2v}$	2	$B_1$ & $A_2$
$\text{NH}_2$	Nitro (Bisecting)	Id	$C_s$	1	$A''$

Eight parameters were studied, one  $\alpha$ , three  $\beta$ , and four  $\gamma$ . Their symbols are listed in Table V below. The Sum-over-States (SOS) approach to calculations has its basis in a perturbation theory method developed by J. Ward in 1965 and gives the following basic equations for  $\alpha$ ,  $\beta$ (SHG) and  $\gamma$ (THG) (1):

$$\alpha(\omega) = \sum_n \frac{e^2}{\hbar} \left( \frac{r_{gn} r_{ng}}{\omega - \omega_{ng}} + \frac{r_{gn} r_{ng}}{\omega + \omega_{ng}} \right)$$

$$\beta(-2\omega; \omega, \omega) = p \sum_{n_1, n_2} \left( \frac{e^3}{2\hbar^2} \right) \frac{r_{gn_2} r_{n_2 n_1} r_{n_1 g}}{(\omega - \omega_{n_1 g})(2\omega - \omega_{n_2 g})}$$

$$\gamma(-3\omega; \omega, \omega, \omega) = p \sum_{n_1, n_2, n_3} \left( \frac{e^4}{4\hbar^3} \right) \frac{r_{gn_3} r_{n_3 n_2} r_{n_2 n_1} r_{n_1 g}}{(\omega - \omega_{n_3 g})(2\omega - \omega_{n_2 g})(3\omega - \omega_{n_1 g})}$$

where  $\alpha$ ,  $\beta$ , and  $\gamma$  are the (hyper)polarizabilities;  $\omega$  is the frequency of the incident light,  $e$  is the charge on the electron,  $g$  and  $n_n$  refer to the ground and excited states, and  $r$  is a coordinate associated with the position of the electrons. For compounds such as acetylenes and polyacetylenes the important electronic transitions are expected to be  $\pi$  to  $\pi^*$  transitions. For such systems a two level model, developed by J. L. Oudar and D. S. Chemla in 1977, works fairly well (1, 10). This model was the first one to take into account the contribution of charge-transfer resonances within a molecule to the first hyperpolarizability ( $\beta$ ).

This model can be reduced to an approximate equation for  $\beta$ , showing that when  $\omega$  or  $2\omega$  is close to the absorption band,  $\beta$  is enhanced (1):

$$\beta(-2\omega; \omega, \omega) \approx \frac{3e^2}{2\hbar m} \frac{\omega_{eg} f \Delta\mu}{(\omega_{eg}^2 - \omega^2)(\omega_{eg}^2 - 4\omega^2)}$$

where  $m$  is the mass of the electron,  $f$  is the oscillator strength,  $\omega_{eg}$  is the frequency of the optical transition, and  $\Delta\mu$  is the difference between the ground- and excited-state dipole moment. To calculate values for  $\gamma$ , a third level can be added to the model. The free-electron model has yielded useful equations for  $\gamma$  (1), including the technique of degenerate four-wave mixing (DFWM). The expression for  $\gamma$  measured by DFWM with all parallel polarization is (1):

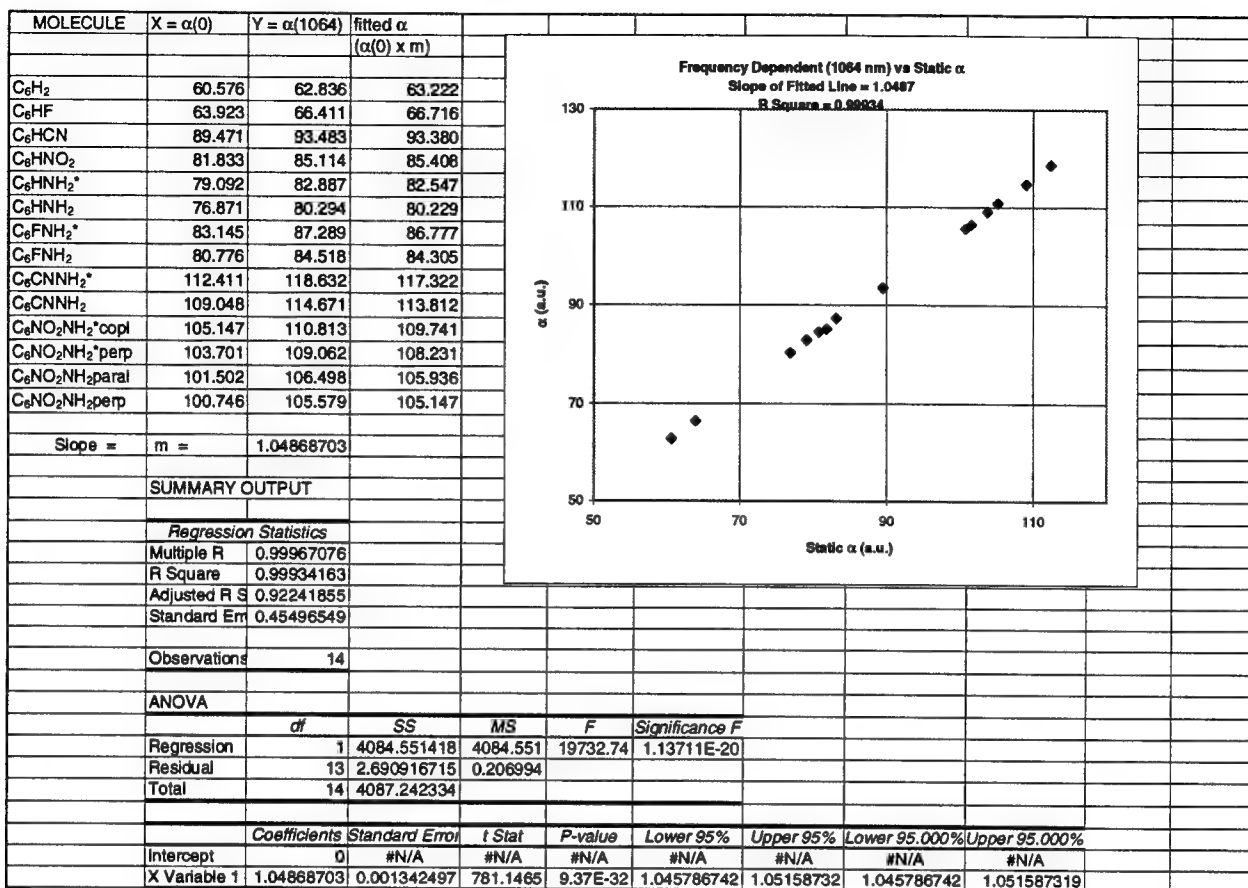
$$\gamma_{\text{orientation}} = \frac{1}{135} kT \left[ (\alpha_{11} - \alpha_{22})^2 + (\alpha_{22} - \alpha_{33})^2 + (\alpha_{11} - \alpha_{33})^2 \right]$$

where  $k$  is Boltzmann's constant,  $T$  the Kelvin temperature, and  $\alpha_{ii}$  are components of the linear polarizability tensor.

Table V. Symbols and Definitions. ( $\omega$  is the incident frequency).

$\alpha$	Frequency Dependent Polarizability	$\alpha(-\omega; \omega)$
$\beta(\text{SHG})$	Second Harmonic Generation	$\beta(-2\omega; \omega, \omega)$
$\beta(\text{EOPE})$	Electrooptic Pockels Effect	$\beta(-\omega; 0, \omega)$
$\beta(\text{OR})$	Optical Rectification	$\beta(0; -\omega, \omega)$
$\gamma(\text{THG})$	Third Harmonic Generation	$\gamma(-3\omega; \omega, \omega, \omega)$
$\gamma(\text{EFISH})$	DC-EFISH	$\gamma(-2\omega; \omega, \omega, 0)$
$\gamma(\text{IDIR})$	Intensity Dependent Index of Refraction	$\gamma(-\omega; \omega, -\omega, \omega)$
$\gamma(\text{OR})$	Optical Kerr Effect	$\gamma(-\omega; 0, 0, \omega) \equiv \gamma(0; 0, -\omega, \omega)$

Table VI. Static and 1064 nm Data for Polarizability ( $\alpha$ ), Statistical Data, and Graph.



NLO data, statistical data, and a graph for polarizability ( $\alpha$ ) are presented in Table VI. The relationship between  $\alpha(1064 \text{ nm})$  and static  $\alpha$  is almost perfectly linear; R Square is 0.999. In the monosubstituted series,  $\alpha$  follows the relationship (see Table II for actual values)



which agrees with the linear diacetylene order. The disubstituted groups follows the relationship



which again is the same as the diacetylene order (11). The polarizability changes very little from the static value to the 1064 nm value, and the values themselves are low.

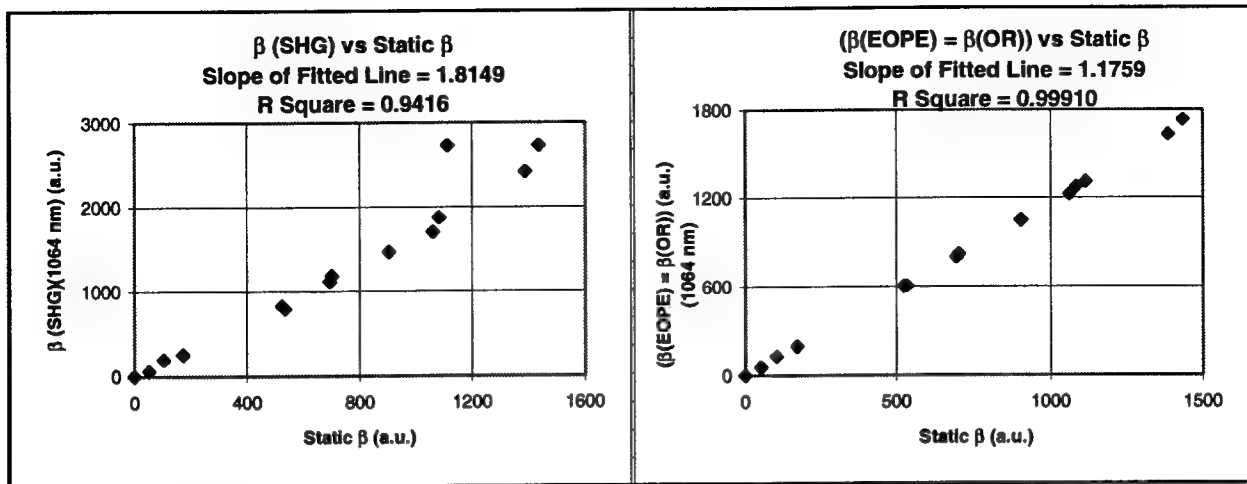


Figure 2. Comparison of  $\beta$  data.  $\beta(\text{SHG})(1064 \text{ nm})$  Vs Static  $\beta$  and  $(\beta(\text{EOPE}) = \beta(\text{OR}))$  Vs Static Beta.

Table VII. Static and 1064 nm Data for Second Hyperpolarizability  $\gamma(\text{SHG})$ , Statistical Data, and Graph.

MOLECULE	$\gamma$ STATIC	$\gamma$ (1064 nm)	fitted $\gamma$	$\gamma(0) \times m$	$\gamma(\text{THG})$	$\gamma(\text{THG}) (1064 \text{ nm})$			
	$\gamma(0)$	$\gamma(\text{THG})$							
$\text{C}_2\text{H}_2$	10249.7	19717.7	80568.6						
$\text{C}_2\text{HF}$	12188.9	24091.3	95811.9						
$\text{C}_2\text{HCN}$	26981.3	63945.9	212088.8						
$\text{C}_2\text{HNO}_2$	22485.6	50224.2	176749.9						
$\text{C}_2\text{HNH}_2^*$	25448.1	123739.9	200036.9						
$\text{C}_2\text{HNH}_2$	24753.2	78071.9	194574.6						
$\text{C}_2\text{FNH}_2^*$	29345.9	161248.8	230675.9						
$\text{C}_2\text{FNH}_2$	28407.8	94961.7	223301.9						
$\text{C}_2\text{CNNH}_2^*$	64239.7	587934.3	504961.5						
$\text{C}_2\text{CNNH}_2$	58896.8	241448.6	462963.2						
$\text{C}_2\text{NO}_2\text{NH}_2^*$ copl	62638.8	1177420.4	492377.5						
$\text{C}_2\text{NO}_2\text{NH}_2^*$ perp	45364.4	320659.1	356590.6						
$\text{C}_2\text{NO}_2\text{NH}_2$ paral	54578.4	313937.7	429018.1						
$\text{C}_2\text{NO}_2\text{NH}_2$ perp	44635.0	161896.6	350857.1						
Slope =	$m =$	7.86058331							
	SUMMARY OUTPUT								
	Regression Statistics								
	Multiple R	0.68428928							
	R Square	0.46825182							
	Adjusted R S	0.39132875							
	Standard Err	225825.847							
	Observations	14							
	ANOVA								
	<i>df</i>	<i>SS</i>	<i>MS</i>	<i>F</i>	<i>Significance F</i>				
Regression	1	5.838E+11	5.84E+11	11.44766	0.005433498				
Residual	13	6.62965E+11	5.1E+10						
Total	14	1.24677E+12							
	<i>Coefficients</i>	<i>Standard Error</i>	<i>t Stat</i>	<i>P-value</i>	<i>Lower 95%</i>	<i>Upper 95%</i>	<i>Lower 95.000%</i>	<i>Upper 95.000%</i>	
Intercept	0	#N/A	#N/A	#N/A	#N/A	#N/A	#N/A	#N/A	
X Variable 1	7.86058331	1.490220356	5.274779	0.00015	4.641158584	11.080008	4.641158584	11.08000804	

In Figure 2 is presented a graph relating 1064 nm data with static values for the first hyperpolarizability  $\beta$ (SHG), and, for comparison, 1064 nm data of (identical values) for  $\beta$ (EPOE) and  $\beta$ (OR) Vs static values. The R Square value for the  $\beta$ (SHG) graph is 0.942; the  $\beta$ (EPOE) =  $\beta$ (OR) is essentially linear (R Square = 0.9991). Note that the point for the  $\text{NH}_2\text{C}_6\text{NO}_2$  with  $\text{NH}_2$  coplanar with  $\text{NO}_2$ , ( $X = 1113$  a.u.) is out of line for the  $\beta$ (SHG) graph, but in line on the ( $\beta$ (EPOE) =  $\beta$ (OKE)) graph. The monosubstituted linear triacetylenes give static  $\beta$  values of  $\text{H} < \text{F} < \text{NO}_2 < \text{CN} < \text{NH}_2 < \text{NH}_2^*$  which differs from the order found in an *ab initio* study of linear diacetylenes (11).

Table VIII. Static and 1064 nm Data for  $\gamma$ (EFISH), Statistical Data and Graph.

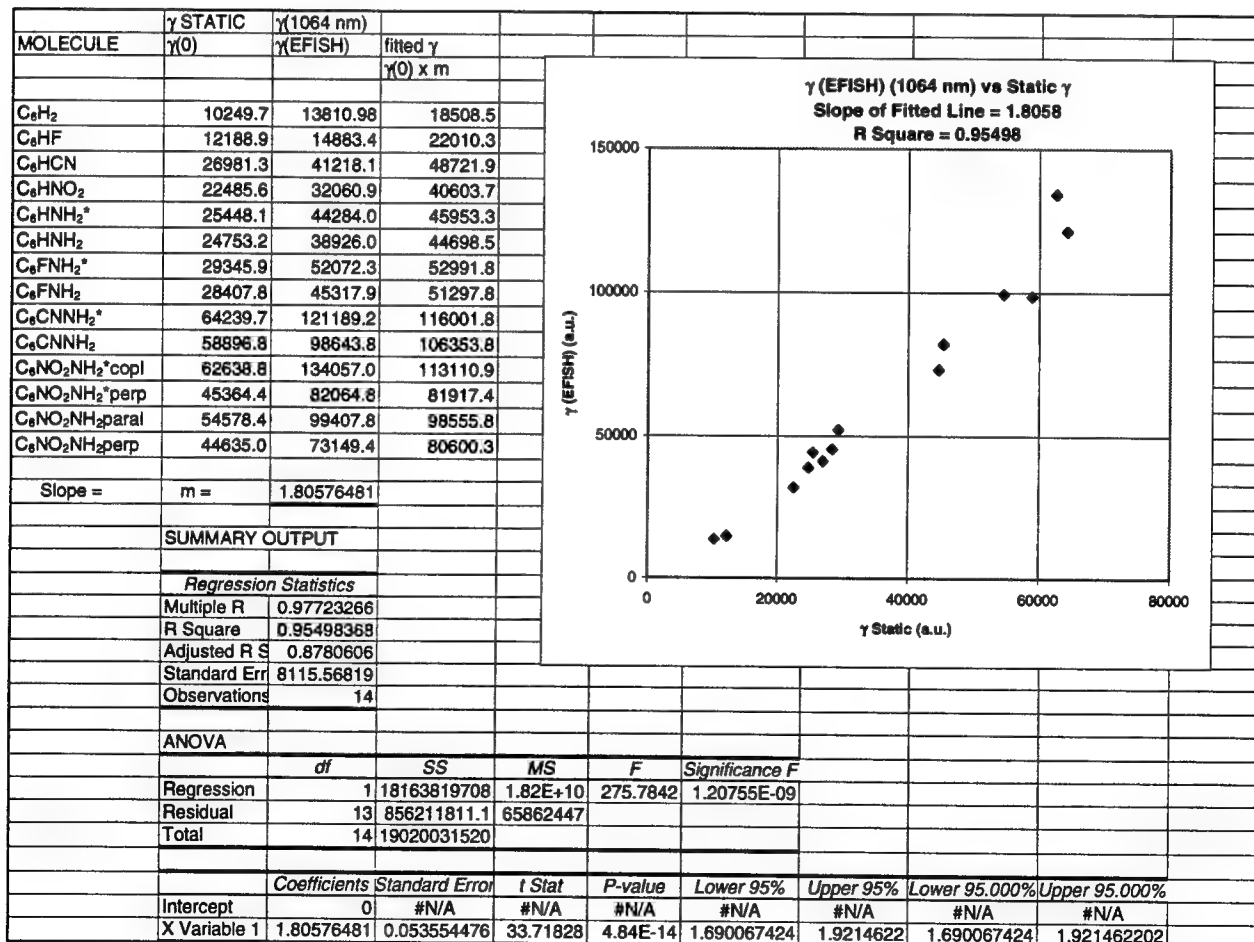
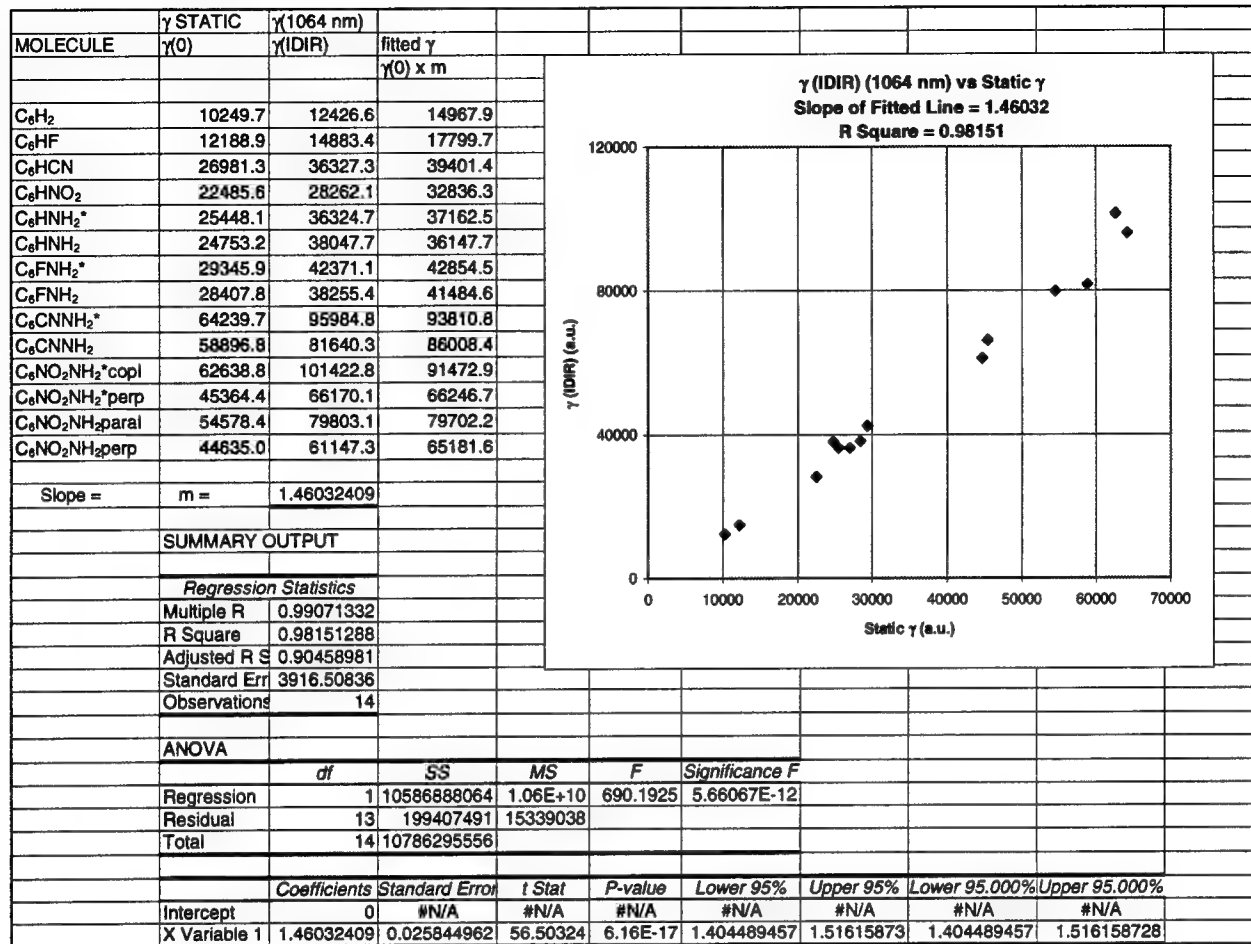


Table IX. Static and 1064 Data for g(IDIR), Statistical Data, and Graph.



In Tables VII, VIII, IX, and XI are given static  $\gamma$  and 1064 nm values for  $\gamma$ (SHG),  $\gamma$ (EFISH),  $\gamma$ (IDIR), and  $\gamma$ (OKE). The order of the static  $\gamma$  values for the monosubstituted compounds is



All of the disubstituted compounds have higher values than the monosubstituted compounds and follow the order



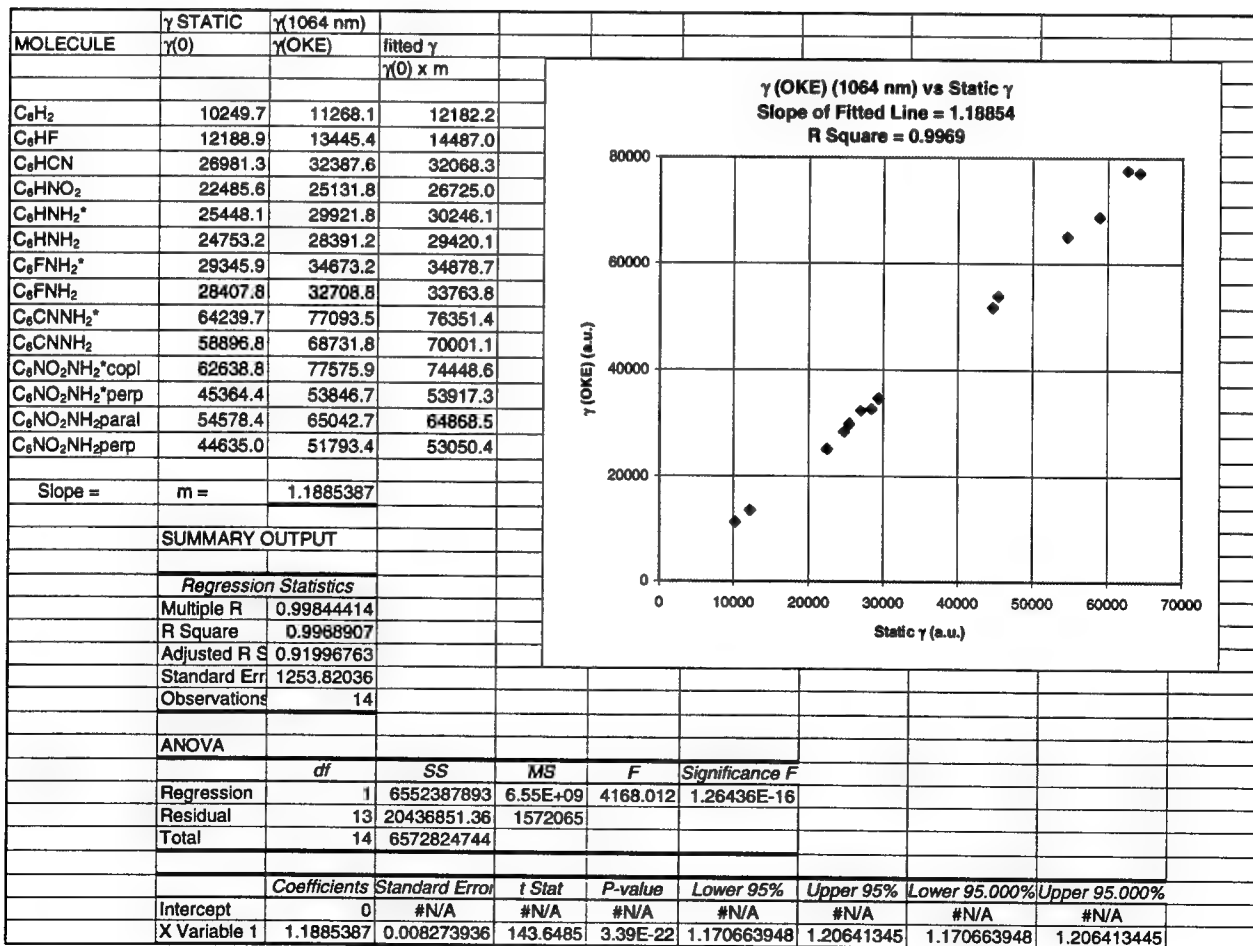
with the exception of planar  $NH_2C_6NO_2$ , which has the second highest value for static  $\gamma$ . The  $\gamma$  values also compare well with the diacetylene study (11). The most scattered line is the  $\gamma$ (THG) because of

resonance effects (1). The other three graphs are closer to linearity, with R Square values closer to one as can be seen in Table X below.

Table X. Statistical data for  $\gamma$  (1064 nm) Vs static  $\gamma$ . R Square = 0.468 and Slope = 7.86,

	R Square	Slope of Fitted Line
$\gamma$ (THG)	0.468	7.861
$\gamma$ (EFISH)	0.956	1.806
$\gamma$ (IDIR)	0.981	1.460
$\gamma$ (OKE)	0.997	1.189

Table X. Static and 1064 nm Data for  $\gamma$ (OKE), Statistical Data, and Graph.



## Conclusions

Linear triacetylenes (1,3,5-hexatriynes) show linear relationships between the 1064 nm data for the first ( $\alpha$ ), second ( $\beta$ ), and third ( $\gamma$ ) polarizabilities and the respective static  $\alpha$ ,  $\beta$  and  $\gamma$  data. This had been observed earlier in this Laboratory for linear diacetylenes (2, 11). These linear relationships among the NLO properties of  $\alpha$ ,  $\beta$ , and  $\gamma$  indicate that simple models can be derived for understanding NLO properties, and suggest the need for additional systematic study of related compounds (2, 10).

A consequence of this study was the discovery of a bug in the section of code which generates the NLO properties for MOPAC 93. One of the methods for determining the NLO properties was found to give erroneous values for all the different  $\beta$  processes. This information has since been communicated to the developers.

The  $\beta$ (EOPE) and  $\beta$ (OR) values were identical, and gave better linear fit than the  $\beta$ (SHG) values, R Square = .9991 Vs R Square = 0.9416. The difference is due primarily to the out-of-line  $\beta$ (SHG) point for planar amino  $\text{H}_2\text{NC}_6\text{NO}_2$ , illustrated in Figure 1b, which becomes in-line for either the EOPE or the OR process. Similarly, in comparing the data for the second hyperpolarizability ( $\gamma$ ), the  $\gamma$ (THG) graph has scattered points, R Square = 0.4683, while  $\gamma$ (EFISH),  $\gamma$ (IDIR) and  $\gamma$ (OKE) give good linear relationships of R Square = 0.9550, 0.9815, and 0.9969 respectively. This result, that  $\beta$ (SHG) and  $\gamma$ (THG) each deviate from linearity, is due to resonance effects. Both  $\beta$ (SHG) and  $\gamma$ (THG) would be complex near a resonance (1).

The graphical relationships of this semiempirical study of triacetylenes show behavior very similar to the *ab initio* study of linear diacetylenes (11) done in this Laboratory. It also shows the feasibility of future studies to provide theoretical data toward gaining a fundamental understanding of the mechanism of NLO activity (11).

This study focused on the polarizabilities ( $\alpha$ ) and the first ( $\beta$ ) and second ( $\gamma$ ) hyperpolarizabilities. However, the semiempirical calculations generated much additional data worthy of future study including thermodynamic properties, frequencies, moments of inertia, tensor values, etc.

Acknowledgment

This writer is very grateful to the Air Force Office of Scientific Research and to the Frank J. Seiler Research Laboratory and its Materials Chemistry Division, United States Air Force Academy for this appointment. She is also grateful to LTC Robert A. Hildreth who served as focal point and to CPT Walter J. Lauderdale who directed the research. She acknowledges particularly Captain Lauderdale's generosity of ideas, expertise and time throughout the project.

## References

- ( 1) Prasad, P. N.; Williams, D. J. *Introduction to Nonlinear Optical Effects in Molecules and Polymers*; John Wiley & Sons: New York, 1991.
- ( 2) Hildreth, R.; Rakowsky, M.; Lauderdale, W. *Materials Chemistry Research: AFOSR Task Review*; Frank J. Seiler Research Laboratory, USAFA, CO, Feb. 1994.
- ( 3) Marder, S. R.; Gorman, C. B.; Meyers, F.; Perry, J. W.; Bourhill, G.; Bredas, J. Pierce, B. M. *Science* **1994**, *265*, 632-635.
- ( 4) Dagani, R. *Chemical and Engineering News* August 15, **1994**, 34-36.
- ( 5) Matsuzawa, N.; Dixon, D. A. *J. Phys. Chem.* **1992**, *96*, 6232-6241.
- ( 6) Cheng, L.; Tam, W.; Stevenson, S. H.; Meredith, G. R. *J. Phys. Chem.* **1991**, *95*, 10631-10643.
- ( 7) Cheng, L.; Tam, W. *J. Phys. Chem.* **1991**, *95*, 10643-10652.
- ( 8) Garito, A.; Shi, R. F.; Wu, M. *Physics Today* **1994**, *47*, 51-57.
- ( 9) Messier, J.; Kajzar, F.; Prasad P. *Organic Molecules for Nonlinear Optics and Photonics*; Kluwer Academic: Boston, 1991.
- (10) Lauderdale, W. J. *private communication*, Frank J. Seiler Research Laboratory, USAFA, CO, Sept. 1994.
- (11) Lauderdale, W. J.; M. B. *Basis Set Effects on the Non-Linear Optical Properties of Selected Linear Diacetylenes*; Unpublished Paper, Frank J. Seiler Research Laboratory, USAFA, Colorado, 1994.
- (12) Fejer, M. M. *Physics Today* **1994**, *47*, 25-32.
- (13) Garmire, E. *Physics Today* **1994**, *47*, 23-24.
- (14) Stewart, J. J. P. *MOPAC 93 Manual*; Fujitsu Limited: Tokyo, Japan, 1993.
- (15) Dennington, II, R. D.; Healy, E. F. *Ampac Manual A General Molecular Orbital Package*, University of Texas: Austin, 1989.

CATALYTIC GASIFICATION OF PITCH CARBON FIBERS WITH SILVER,  
CERIUM OXIDE, AND PRECIOUS-METAL-DOPED CERIUM OXIDE

Larry Murrell  
Senior Scientist  
Materials Research Laboratory  
Pennsylvania State University

ABB Lummus-Crest Inc.  
1515 Broad Street  
Bloomfield, N.J.  
07003-3096

Final Report for:  
Summer Faculty Research Program  
F.J. Seiler Research Laboratory

Sponsored by:  
Air Force Office of Scientific Research  
Bolling Air Force Base, DC

and  
F.J. Seiler Research Laboratory

August 1994

CATALYTIC GASIFICATION OF PITCH CARBON FIBERS WITH SILVER,  
CERIUM OXIDE, AND PRECIOUS-METAL-DOPED CERIUM OXIDE

Larry Murrell

Senior Scientist

Materials Research Laboratory  
Pennsylvania State University

Abstract

Pitch carbon fibers have been gasified with silver metal as the catalyst to produce large geometric-shaped cavities which extend well into the fiber structure. The presence of large cavities was confirmed by: 1) Atomic Force Microscopy of the gasified fibers, 2) nitrogen adsorption to determine the surface area, 3) absence of macro-sized pores as determined by mercury porosimetry, and 4) adsorption of a colloidal oxide sol into the fiber structure. The failure of silver to generate the desired smaller sized pores for the fibers investigated was determined to be due to silver agglomeration to form large particles. Extensive silver agglomeration was even established for the case when a silver sol was deposited onto the fiber surface. The gasification of pitch fibers was also investigated in the case where cerium oxide was adsorbed onto the fiber surface in the form of a sol of ca. 4 nm diameter. Although this oxide was less active than silver in the gasification reaction, the oxide structure would make agglomeration on the fiber surface less likely than the problem identified with silver. It was discovered that by doping the cerium oxide, or ceria, surface with silver, platinum, or rhodium, that the gasification was enhanced. This enhancement is due to the modification of the redox properties of the ceria surface itself due to the precious metal oxide redox contribution. In contrast, palladium doped onto the ceria surface showed no enhanced catalytic function over that of ceria. The fact that the gasification temperature was lowered by 150°C compared to ceria in the case of silver-doped ceria suggests that there is a strong possibility of modification of the pore structure formed by the ceria versus the silver-doped ceria particles acting as the gasification catalyst. The comparison of the pores formed within the fibers from these two novel gasification catalysts will be determined in future work.

## CATALYTIC GASIFICATION OF PITCH CARBON FIBERS WITH SILVER, CERIUM OXIDE, AND PRECIOUS-METAL-DOPED CERIUM OXIDE

Larry L. Murrell

### Introduction

The use of silver to catalytically gasify carbon fibers has been investigated in recent work by Hoffman et. al.<sup>{1}</sup> where the goal was to remove only a small fraction of the carbon surface for use in composite materials. The evidence from detailed microscopy of these samples suggests that silver can channel across the carbon surface thereby removing material to form shallow troughs on the fiber surface. In earlier work Harris et. al.<sup>{2}</sup> and Baker et. al.<sup>{3,4}</sup> showed that silver could, in addition to channeling across the surface, attack successive layers of the graphite basal plane forming pits or "flower-pot" structures into the graphite sample. The use of silver, or another catalyst, that could produce cavities controllably of from 20 to 100 nm diameter would provide a novel conducting support which could be used for various application, including electrochemistry as micro electrodes with controlled porosity. Another novel application of these porous fibers would be to grow oxide or zeolite crystals under the influence of a static or an alternating charge on the surface of the pore walls of the fiber.

### Methodology

The carbon fibers used in this work were obtained from Amoco Oil Company and were designated as unsized high pitch carbon fibers, K1100X. These high pitch fibers were reported by Amoco to have a B.E.T. surface area of ca. 0.4 m<sup>2</sup>/g. This agrees with the surface area determined by ABB

Lummus-Crest Inc. to be 0.29 m<sup>2</sup>/g. The calculated surface area, based on the size of the fibers being uniformly 12 micron diameter, is 0.15 m<sup>2</sup>/g. The low surface area of the fibers dictated that the silver catalyst precursor be deposited by either evaporation of an aqueous or a non-aqueous solution of the silver nitrate salt. The carbon fibers were cut into 2 inch long segments and placed parallel in the bottom along one side of a beaker to which the silver salt was added. The fibers were not easily wet by either water or acetone. The fibers were continuously immersed and separated from one another in the impregnating liquid for a 15 minute period, and then the beaker was placed in a drying oven set at 120°C for one hour in the case of an aqueous impregnation or allowed to evaporate overnight in a hood in the case of an acetone impregnation. Following drying, the initial investigations of the gasification were carried out by placing the samples in ceramic boats directly into a muffle furnace at the gasification temperature of interest or pretreated at 200 or 400°C. The extent of gasification was monitored by periodic removal of the samples from the furnace. The fibers were weighed by placing the fibers on weighing boats made of aluminum foil which allowed for rapid cooling of the fibers. Rapid cooling of the fibers lead to consistent determinations of the relative extent of fiber gasification. Subsequent gasification of the fibers were done in a glass tube reactor placed in a horizontal tube furnace where the air flow rate was maintained at 300cc/min. The temperature was monitored by a thermocouple within the reactor in close proximity to the fibers which were either in a ceramic boat, or directly

placed in the reactor. Large quantities of fiber were gasified by placing the fibers in the reactor itself. The amount of gasification was usually in the range of from 10 to 40 wt % of the fiber in order to generate significant pore voids or pore volume within the fiber. Following gasification, the fibers were examined either by AFM or by optical microscopy to determine how attack had occurred on the exterior surface of the fiber.

A 0.14 wt% silver sol of size range from 20-50 nm diameter was adsorbed onto the carbon fibers. The silver sol had to be diluted by a factor of 100. The adsorption was done in a darkroom and the slurry after thorough mixing with the fibers for 15 min. was evaporated to dryness at 120°C. The, as prepared, and the gasified fiber were analyzed by optical microscopy in order to see if any large structures could be detected.

A cerium oxide or ceria sol(CS) of 4 nm diameter was obtained from P.Q. Corporation as a 20 wt.% slurry based on CeO<sub>2</sub>. The sol was diluted to make a slurry such that 0.1 wt.% CeO<sub>2</sub> would be adsorbed from 5-10 cc of the slurry onto the carbon fibers. This weight of ceria would be ca. 1 % coverage of the carbon fiber surface. The sol was shown to adsorb onto the carbon fibers by observing the gasification activity of the fibers where the sol slurry was decanted from the fibers after a 15 min. contacting period. Gasification of the fibers showed that the CS had been adsorbed onto the surface of the fibers. In subsequent preparations, after a 15 min. contacting period with the CS or precious-metal-doped CS the sol-fiber mixture was allowed to evaporate to dryness at 120°C so as to ensure uniformity in comparison on a weight basis of one sample to another. The preparations of the precious-metal-doped ceria samples involved dropwise addition of solutions of the nitrate salts of silver, rhodium, and palladium and the ammine nitrate salt of platinum to the rapidly stirred ceria slurry. After the addition of the metal salts the slurries were protected from light as the silver-sol slurry was found to be light sensitive.

In a special case the ceria sol was deposited onto the fibers and then dried at 120°C. In a second step the silver nitrate was deposited to give a sample with 5 wt.% silver on the basis of the ceria present on the carbon fiber surface. This amount of silver is very small compared to that employed to gasify the fibers when silver was employed as the catalyst itself. The silver was undoubtably localized on the ceria sol particles as evidenced by a very high gasification activity.

#### Results and Discussion.

##### A. Carbon Fiber Gasification with Silver From a Silver Nitrate Precursor

In the initial investigation of K1100X carbon fiber(CF) gasification with a silver catalyst 1 wt% silver as the metal was deposited from an acetone solution of silver nitrate. The sample was found to be completely gasified after an overnight treatment(16 hrs) in air at 500°C. In contrast, a sample of the fibers with no silver showed no weight loss

after this same treatment period. Chris Levan at Amoco confirmed that pitch fibers show no appreciable gasification when calcined at such low temperatures in air. After a 700°C calcination the CF with no catalyst present exhibited a few percent weight loss after a one hour treatment in air, as a reference point.

Because of the complete gasification of the 1 wt.% silver/CF sample an analogous sample was investigated for a 500°C calcination where the gasification was monitored as a function of time in minutes. The cumulative weight loss was 12.9, 20.4, 29.6 after a 1, 2, and 3 min. period, respectively. The rate of gasification is approximately linear with time. This linear gasification rate was confirmed for a second sample prepared in a similar fashion. The AFM micrographs of these catalytically oxidized CF samples showed that very large cavities had been formed in the surface of the fiber. In these images large interconnected sections of the fiber had been removed, often leaving regular shapes such as squares and triangles terminating the edges of the cavities. In other regions, regular squares or rectangles were commonly observed on the order of 100 to 170 nm length of the segments removed. The main conclusion from this investigation is that the desired small 20 to 100 nm dimension pores were not observed in the exterior carbon fiber surface. The reason that large geometric sections of the fiber are removed could be explained by the fact that once basal plane attack has occurred then the silver particles channel across the surface producing the removal of the large geometric sections observed. Another explanation for the gasified structures produced in the fiber exterior surface is that the silver particles are very large and attack large segments of the external surface of the fiber due to their large size. This would leave open the possibility that smaller pore structures are produced in the interior of the fiber not visible by AFM. Subsequent nitrogen surface area and mercury pore distribution analysis showed conclusively that this is not the case--large cavity structures are produced throughout the fiber structure. In an attempt to produce smaller pore openings in the fibers the gasification was investigated for 0.1 and 0.01 wt% silver loadings on the fibers. Again, the gasification was carried out at 500°C. For both of these samples about 1 % gasification occurred after 1 minute and then ceased after 10 min. in the case of the 0.1 % sample and after 2 min. in the case of the 0.01 % sample. The AFM micrographs showed no evidence for either of these samples that small pore structures were formed at the surface of the gasified CF. Only the presence of large geometric cavities could be detected at the exterior of the fiber surface. In subsequent work, a 0.1 % silver catalyst was found to maintain gasification activity at 550°C which lead to the large cavity structures similar to those formed by the 1 % silver gasified sample previously discussed. It is not at all clear why the lower silver content samples failed to maintain activity at 500°C. However, it is very clear from the results obtained that low silver loading levels on the CF using our acetone deposition technique probably do not produce a uniformly roughened surface as apparently observed in the Hoffman work{1}. Rather, the silver at these surface concentrations on the fibers either agglomerates to form large cavity structures prior to gasification, or attacks the carbon surface by channeling in a fairly small percent coverage of the fiber surface leading to the isolated and large cavities observed by AFM.

Another strategy which was investigated to form smaller cavities or pores within the fibers was to carryout the gasification reaction at lower temperatures. For a 1 wt.% silver on the CF, 2.3% gasification was obtained at 450°C, and 0.9% at 475°C. This same sample showed an additional 1.3% weight loss upon taking the sample to 500°C, whereupon the activity ceased. Therefore, it must be concluded that the pretreatment steps at 400°C and 450°C were effective in deactivating the silver catalyst that was responsible for generation of the large cavities within the fibers observed in previous experiments. This result may well be due to the conversion of a silver oxide or silver suboxide to the metal at a temperature of ca. 400°C{5}. If the temperature was increase to 550°C then rather slow gasification ensued. The weight loss was 12 and 15.6% after a 15 and a 30 min. reaction period. These results indicate a rapid initial gasification process which then slows markedly at increasing time. Two separate samples of 1 wt.% silver on CF were pretreated at 200°C and 400°C. The sample treated at 400°C showed almost no gasification activity when calcined at 500°C, whereas the sample treated at the lower temperature exhibited the same activity as that observed previously with no pretreatment. This result confirms that silver gasification of CF is strongly impacted by pretreatment at a temperature of about 400°C, and that there is no impact on silver gasification by treatment in air at a temperature of 200°C, or below.

#### B. Carbon Fiber Gasification with Silver From a Silver Sol Precursor

In an attempt to obtain CF gasification without formation of the undesired large, geometric-shaped pores , silver was deposited onto the fibers from a colloidal silver sol precursor. The silver sol was obtained from EY Laboratories, Inc. of San Mateo, Ca. and contained particle of size ranging from 20-50 nm diameter. Two silver loading levels were investigated, 0.1 and 1 wt.%. The 1% siver-sol/CF sample exhibited sluggish gasification compared to the sample prepared from silver nitrate where the nitrate salt was rapidly decomposed at the gasification temperature of 500°C. This would tend to confirm that silver may be a less effective catalyst than a silver oxide or silver suboxide particle of similar size range. For the 1% silver-sol/CF sample the cumulative weight loss was 5.1 and 10.3% after 10 and 20 min., respectively. The 0.1% silver-sol/CF sample showed no gasification activity at 500°C or 550°C. By increasing the temperature to 600°C gasification of this 0.1%Ag/CF commenced with 5.6 and 11.1 % weight loss after 10 and 20min., respectively. In comparison, a 0.1% silver/CF sample made by adsorption from acetone solution had a 20 % weight loss when treated at 550°C for 60 min. The remarkably lower CF gasification activity exhibited by a silver catalyst made from a silver sol compared to the analogous sample made from silver nitrate decomposition is probably not related to a major difference in the particle size of the active phase since rapid nucleation of silver is anticipated from the rapid decomposition of the silver nitrate at 500°C. The difference in catalytic activity is probably due to the lower activity of silver metal compared to an oxide or a suboxide particle of silver. The lower gasification activity of the CF when silver sol is employed is consistent with the greatly suppressed activity observed for the case where a silver nitrate/ CF sample is pretreated at a temperature where conversion of silver nitrate to silver metal is probably extensive{5}

Optical microscopy showed extensive pitting of the exterior surface of the CF after gasification at 500°C for the 1% silver-sol/CF sample. Optical microscopy also revealed that silver particle were clearly visible for both the 0.1 and the 1% silver-sol/CF sample prior to gasification. These samples had been dried at 120°C for 1hr. prior to investigation by optical microscopy. Apparently, it is very difficult to obtain a dispersed silver phase on the carbon fibers investigated in this research program using either a silver nitrate, or a silver metal sol as the precursor of the active catalyst.

#### C. Carbon Fiber Gasification with Ceria Particles and Precious-Metal-Doped Ceria Particles Obtained From a Sol Precursor

Ceria has been used extensively in the automotive industry as a promoter of the three way automotive catalyst{5}. Ceria has also been suggested to be an interactive phase for stabilization of precious metals under automotive catalyst application conditions{6-10}. Recent work of Murrell et. al.{11} brings into serious question if ceria particles function to retain any precious metals associated with the ceria phase under cyclic reducing-oxidizing conditions, which is the basis of operation of the currently used three way catalysts. Since fiber gasification may well involve an oxidation-reduction cycle at the surface of the catalyst it is speculative if metals doped onto the ceria particles can retain catalytic function under fiber oxidation conditions. Nevertheless, it has been shown that low levels of platinum on ceria have CO oxidation activity at ambient temperature conditions{12}. Therefore, it was decided to explore the possibility of carbon fiber gasification with ceria itself acting as a catalyst, and then to progress to precious-metal-doped ceria. The seminal idea of this research thrust was that ceria particles, being unreduceable to the metal, would be less prone than silver to agglomerate under the temperature window required for fiber gasification. If ceria was found to act as a catalyst for fiber gasification, then precious-metal-doped ceria particles would be explored to determine if the gasification reaction could be carried out at sufficiently low temperatures compared to ceria itself that the structure of the fibers from the different catalysts would be different. It was found that ceria adsorbed onto the fibers from a 4 nm diameter sol precursor was indeed a fairly active catalyst for gasification of pitch fibers. The first experiments that were done involved contacting the fibers with sufficient ceria sol to give a loading level of 0.1 wt.% on the fibers. This corresponds to ca. 1% coverage of the fiber surface by ceria sol particles. In an attempt to ascertain if the ceria had indeed adsorbed on the fiber surface the following procedure was used. After a 15 min. contacting period with thorough mixing of the fibers with the sol slurry the excess solution was decanted from the fibers. After drying for 1 hr. at 120°C the sample was investigated for fiber gasification. It was discovered that significant gasification ensued at 550°C. The analogous preparation was carried where the solution was not decanted from the fibers. For this modified preparation procedure the gasification was shown to be essentially identical to that for the sample prepared where the solution had been decanted. These combined results strongly suggest that the ceria sol has completely adsorbed onto the fibers in a 15 min. period, and that essentially no ceria remains in the slurry phase. The preparation was repeated and scaled-up for ca. a 0.6 gram

preparation of the fibers where the solution was removed by drying at 120°C. The rate of fiber gasification was essentially identical for the larger sample size. For this sample the gasification was done for sufficient time that about 20% gasification had occurred (ca. 40 hrs.). The nitrogen BET surface area was determined to be 2.4 m<sup>2</sup>/g. This strongly suggests that despite using a very different catalyst than silver very large cavities are produced in the gasified fibers when ceria is the gasification agent. This result is especially surprising in that very low levels of ceria were deposited onto the fiber surface prior to carrying out the gasification reaction. Because of this negative result of failing to produce a high surface area carbon support using ceria as the catalytic agent we proceed to investigate the case where the oxidation activity of the ceria was enhanced by doping the surface with precious metal/metal oxides. Recent work has shown great enhancement in the oxidation activity of the ceria when low levels of platinum, or other metals are doped onto the ceria surface{12}. The hope is to use the ceria particle formed on the fiber surface from the sol to anchor the precious metal/metal oxide so that they could serve to attack the basal planes of the carbon fibers to generate holes or "flower-pot" structures into the fiber. The results in Table 1 show that doping the ceria surface does indeed serve to enhance the rate of fiber gasification. The major surprise from the research thrust was that silver on the ceria surface was superior to an of the other metal/metal oxides investigated, i.e., rhodium, platinum, and palladium. The surface of ceria has a very substantial ability to oxidize metals to the corresponding oxides under oxidizing conditions due to a Strong Oxide Support Interaction{12}. The level of metal to which the ceria can strongly interact corresponds to 5 wt.% platinum. Five % platinum corresponds to 2.36 wt.% silver. It can be seen in Table 1 that silver is effective in enhancing the activity of ceria in fiber gasification at a critical window of concentration on the ceria surface. Silver shows a slight enhancement below the 2.36% level where silver oxide is expected to be present exclusively as a strongly interacting surface AgO complex. The enhancement in activity becomes very large at ca. twice that of the level where AgO is expected to be present. At still higher levels the catalyst reverts to that of ceria itself or slightly lower. It is tempting to speculate that at the higher silver levels that silver becomes encapsulated into the bulk of the ceria due to restructuring of the sol as has been observed by Murrell for platinum on ceria when made from a very small and reactive sol phase{13}. However, it is also possible that at the higher silver levels that silver converts to the metal which is able to interact strongly with the redox centers which are required for fiber gasification, and thereby serve to deactivate these redox centers. Developments in Raman spectroscopy suggest that by employing *in situ* Raman techniques that it may be possible to resolve the issue of how the fiber gasification is so markedly impacted by silver concentration on the ceria surface. The closest analogy to the enhancement of the ceria gasification activity by silver on the ceria surface comes from work where rhenium segregated to the surface of tungsten particles was found to be a highly active catalyst for graphite gasification under oxidizing conditions{14}.

### Conclusions

Silver is an active catalyst for pitch fiber gasification leading to removal of large geometric segments within the fiber. Decomposition of silver nitrate to form the active catalytic species at the gasification temperature of the fibers

leads to a more active catalyst than formed from a silver sol precursor. Pretreatment of silver nitrate on the fibers at a temperature where silver metal formation is likely leads to greatly impaired activity compared to the silver nitrate directly decomposed to the active catalyst. The surface area of the silver gasified fibers was  $1.6 \text{ m}^2/\text{g}$  compared to  $0.3 \text{ m}^2/\text{g}$  for the untreated fibers. Ceria was found to be a less active catalyst than silver, but has the advantage that it could be adsorbed onto the fibers as a colloidal or sol phase. The surface area of the ceria gasified fibers was  $2.4 \text{ m}^2/\text{g}$  which suggests that a similar gasification mechanism may be operative as that for the more active silver catalyst. The mechanism may be surface channeling which would accounts for the inability to generate a substantial surface area for the catalytically gasified fibers to date. The substantially higher activity for silver-doped ceria compared to either silver or ceria holds the hope that the desired high surface area may be achieved for the catalytically gasified fibers in ongoing experiments.

### References

1. W.P. Hoffman, in Extended Abstracts, 19th Biennial Conference on Carbon, State College, Pennsylvania, June, 1989, p. 80.
2. P.S. Harris, F.S. Feates, and B.G. Reuben, Carbon, **12**, 189 (1974).
3. R.T.K. Baker and P. Skiba Jr., Carbon, **15**, 233 (1977).
4. R.T.K. Baker in "Carbon and Coal Gasification" eds J.L. Figueiredo and J.A. Moulijn, Elsevier, p. 241, (1986).
5. B. Pettinger, X. Bao, I. Wilcock, M. Muhler, R. Schlogl, and G. Ertl, Angew. Chem. Int. Ed. Engl. **33**, 85 (1994).
6. H.C. Yao, H.S. Gandhi, and M. Shelef In "Metal Support and Metal-Additive Effects in Catalysis," ed. B. Imelik, Elsevier, Amsterdam (1992) and references therein.
7. J.T. Kummer, Y. Yao, and D. McKee, SASE Paper No. 760143 (1976).
8. J.C. Summers and S. Ausen, J. Catal. **58**, 131 (1979).
9. H.C. Yao and Y. F. Yu-Yao, J. Catal. **86**, 256 (1984).
10. E.C. Su and W.G. Rothschild, J. Catal. **99**, 502 (1986).
11. L.L. Murrell, S.J. Tauster, and D.R. Anderson, in "Catalysis and Automotive Pollution Control II," ed. A. Cracq, Elsevier, Amsterdam, Netherlands, p. 275 (1991).
12. L.L. Murrell, unpublished results.
13. L.L. Murrell, in press.
14. R. T.K. Baker, J.J. Chludzinski, Jr., N.C. Dispenziere, and L.L. Murrell, Carbon **21**, 579 (1983).

CHARGE TRANSPORT AND SECOND HARMONIC GENERATION  
IN GLASS WAVEGUIDES

David Statman  
Associate Professor  
Departments of Physics and Chemistry

Allegheny College  
Meadville, PA 16335

Final Report for:  
Summer Faculty Research Program  
F.J. Seiler Research Laboratory

Sponsored by:  
Air Force Office of Scientific Research  
Bolling Air Force Base, DC

and

F.J. Seiler Research Laboratory

CHARGE TRANSPORT AND SECOND HARMONIC GENERATION  
IN GLASS WAVEGUIDES

David Statman  
Associate Professor  
Departments of Physics and Chemistry

Allegheny College  
Meadville, PA 16335

Abstract

Second harmonic generation of laser light in glass films was studied. Laser light from a Nd:YAG ( $\lambda = 1.06 \mu\text{m}$ ) laser was coupled into a  $2\mu\text{m}$  thick glass film. Second harmonic signal was detected when either an external electric field was applied across the waveguide, or when the film was seeded with second harmonic light overlapping the fundamental radiation. Experimental results demonstrate that when an external field is applied, the second harmonic signal is proportional to the square of the applied field. However, this signal decays to some steady state value, indicating a screening of the applied field within the waveguide. When second harmonic signal is film generated, the growth of the signal can be slow, and in some cases oscillatory. It has been proposed that this growth is the result of an asymmetric current within the film. Modeling of charge transport within glass films suggest that when the carrier lifetime is longer than the diffusion time, oscillations in the film generated dc field, hence in the second harmonic signal, can be expected.

# CHARGE TRANSPORT AND SECOND HARMONIC GENERATION IN GLASS WAVEGUIDES

David Statman

## 1. Introduction

The generation of second harmonic signal from glass fibers, waveguides, as well as bulk glass has been well documented<sup>1</sup>. When, for example, infrared light from a Nd:YAG laser ( $\lambda = 1.064 \mu\text{m}$ ) is coupled into a glass waveguide, green light of half the wavelength of the IR pump ( $\lambda = 0.532 \mu\text{m}$ ) may be generated. This is observed either when there is already available some seed green light, or when the infrared intensity is great enough that there is sufficient spontaneously scattered green light to allow self seeding. At first glance, this phenomenon is enigmatic. By symmetry considerations, materials with a second order susceptibility, allowing the second harmonic generation of light, are not allowed to have a center of inversion and cannot be amorphous. Glass as a fiber, film, or in the bulk defies this description. It has, however, been proposed that second harmonic generation in glass is a third order process in which the third order susceptibility,  $\chi^{(3)}$ , operates on an internal DC electric field to produce an *effective* second order susceptibility<sup>2</sup>, i.e.;

$$\chi^{(3)}_{\text{eff}} = \chi^{(3)} \cdot E_{\text{DC}} \quad (1).$$

If this DC electric field has a spatial periodicity corresponding to the phase mismatch of the pump and signal beams;

$$E_{\text{DC}} \propto \cos(\Delta\beta z), \quad \Delta\beta = \beta_{2\omega} - 2\beta_{\omega} \quad (2),$$

where  $\beta_{\omega}$  and  $\beta_{2\omega}$  are the propagation components of the fundamental and second harmonic in the waveguide and  $z$  is the direction of propagation, then the effective second order susceptibility is exactly phase matched for efficient second harmonic generation.

This possibility has been demonstrated by Weitzman, Kester, and Osterberg<sup>3</sup>. When an external field with a spatial dependence given by Eq. 2 was applied to a glass film using interdigitated electrodes, second harmonic signal was observed. The signal was found to be proportional to the square of the applied electric field. This is exactly what is expected from Eq. 1. This raises the question as to what the source of this DC electric field is. It has been proposed that this DC field is the result of charge migration<sup>4</sup>. It is a space charge field. In order for such a space charge field to be generated, an asymmetric photocurrent has been postulated which drives the charge migration<sup>5</sup>.

In this report, second harmonic generation in glass films is studied. Experiments were conducted to investigate

the time dependence of the generation of second harmonic signal. Models using an asymmetric photocurrent were employed to try to explain experimental results. In section 2, the experiment will be outlined. In section 3 results will be given. Modeling of the dynamics of the space charge field will be presented in section 4, and conclusions presented in section 5.

## 2. Experiment.

A Nd:YAG laser was mode-locked and Q-switched. The output of the laser ( $\lambda = 1.064\mu\text{m}$ ) was sent through a frequency doubling crystal to generate green light ( $\lambda = 532\text{ nm}$ ). With the use of dichroic mirrors, the two wavelengths were separated and prism coupled into the glass film waveguide (see Fig. 1). The input beams could be angle tuned to couple into any of the desired waveguiding modes. In these experiments, only the zero mode was studied. Care was taken to make sure beam overlap was maximized within the waveguide. Measurements were made with a photomultiplier. Shutters were placed in the path of the green beam and in front of the photomultiplier. Interdigitated electrodes with a spacing of  $19\mu\text{m}$  were placed up against the glass film. The electrodes were rotated until second harmonic generation in the absence of green seed was maximized. This angle was  $3.1^\circ$ , corresponding to a spacing of  $2\pi/\Delta\beta = 19.03\mu\text{m} \approx 19\mu\text{m}$ . The acquisition of data was automated with the use of a MacIntosh computer and Labview. Measurements were completed studying the growth of second harmonic in the presence of seed on one film, and the dynamics of second harmonic in electric field induced second harmonic (EFISH) in another film. Attempts were also made at measuring currents in the film when the second harmonic signal was seed generated.

## 3. Results.

In the presence of an applied electric field with a periodicity of about  $19\mu\text{m}$ , second harmonic light could be generated from the fundamental IR pump in the absence of green seed light. The EFISH signal was observed immediately after the application of a voltage across the interdigitated electrodes. The initial signal intensity was found to be proportional to the square of the applied electric field, as expected from Eq. 1. This is shown in Fig. 2, where the second harmonic intensity is shown as a function of applied voltage. The voltages were varied from 0 to 50 V, corresponding to applied electric fields ranging from 0 to  $250\text{ kV/cm}$ . It was observed, however, that the EFISH signal decayed to a steady state value within a few seconds. This is shown in Fig. 3. This steady state value was not zero. There appeared to always be some second harmonic generation in the presence of an applied electric field. This suggests that some process occurs in which an electric field is established to oppose or screen the applied field. The fact that there was still some second harmonic signal at steady state indicates that this screening is not complete. To test this, the applied field was turned off. As seen in Fig. 3, upon the switching off of the applied field, the second harmonic signal immediately increased, and then decayed to zero. The amount of the increase in signal was that expected from an electric field equal to the amount screened. This was done several times with different applied voltages, and pump

intensities.

There are a number of possible explanations for this screening effect. One is that of charge transport within the bulk material. Charges may drift in the presence of the applied field establishing a secondary field to screen the applied field. Screening may not be 100% because it is dependent of the number of charges available for screening. The conductivity, however, of glass is quite low, and it is expected that it would take minutes rather than seconds for this process to occur. Even the presence of green light (EFISH signal) where there is expected to be some two photon excitation of electrons into the conduction band, hence an increase in conductivity, cannot account for the rate at which this screening takes place. The second possibility is dipole relaxation within the glass film. As in the first possibility of charge migration or charge transport, this is a bulk effect in which there may only be partial screening of the applied electric field. This explanation, too, is not without its problems. While the relaxation time for charge transport within glass is slow and expected to be on the order of minutes, dipole relaxation is expected to be much faster than the observed screening dynamics. A third possibility is that the applied field is screened by surface charges on the electrodes or the film itself. While this possibility is consistent with the measured relaxation times, one would expect that surface charges can screen 100%. Thus the screening of the applied field still remains an open question.

In a second set of measurements, the growth of seed generated second harmonic, also referred to as film generated second harmonic (but not to be confused with self seeding), was measured. Previous unreported results had shown that sometimes the growth of second harmonic was not exactly quadratic, as expected from some modeling. Instead, the second harmonic signal oscillated in time as it grew to its steady state value. This observation had been reported in the literature as well<sup>6</sup>. In this experiment, similar results were observed. The second harmonic signal was initially observed to oscillate. This oscillation was damped. However, as the oscillation was decaying, the signal began to grow quadratically, as expected. This is shown in Fig. 4. A possible explanation of this transient phenomenon is that when the carrier lifetime is longer than the carrier diffusion time, the carriers drift in the presence of any driving fields or forces. The current density in the film oscillates. On the other hand, when the carrier lifetime is less than the diffusion time, then the carriers are effectively site hopping. Any oscillatory behavior is overdamped. The oscillations may be an indication that the carrier lifetime is, indeed, longer than the diffusion time. This will be explored in more detail in the next section.

#### 4. Model.

As was discussed in the introduction, it is likely that second harmonic generation in glass is the result of the third order susceptibility operating on an electric field grating with a periodicity satisfying phase matching conditions. In this section, the dynamics of grating formation is discussed. Others have proposed that grating formation is the result of two processes. The first process involves the excitation of electrons into the conduction band. The band gap in glass is about 4.5 eV. Therefore, excitation may occur with two photons of green light, one photon of green light and two

photons of infrared light, or four photons of infrared light. It is assumed here that electrons are excited with two photons of green light. With the availability of electrons in the conduction band, the conductivity of the glass increases. The second process involves the proposal of an asymmetric photoconductivity. In this model, the current density from the asymmetric photoconductivity is proportional to the product of the square of the optical field of the fundamental wavelength and the complex conjugate of the optical field of the second harmonic wavelength, plus the complex conjugate;

$$J_p = \sigma^3 (E_0^2 E_{2\omega}^* + \text{c.c.}) \quad (3).$$

$\sigma^3$  is the asymmetric photoconductivity. Calculations based on this model have had some success. Clearly, some of the gross features of frequency doubling in glass waveguides result. However, some of the other experimental observations, such as oscillations in the second harmonic intensity cannot be predicted by this model.

In order to improve on the model, two extra terms were included. For the first process of two photon excitation, the process of recombination and trapping was included. Thus, the process of excitation and recombination could be described by

$$dn/dt = [(s/h\nu) I_{2\omega}]^2 (N_D - n + \rho/e) - \gamma n (n - \rho/e + N_A) \quad (4).$$

$n$  is the carrier density,  $\rho$  is the charge density,  $e$  is the electronic charge,  $N_D$  and  $N_A$  are the donor and trap densities, respectively,  $s$  is the cross section for two photon excitation of green ( $\lambda = 532$  nm) light, and  $\gamma$  is the recombination and trapping rate constant. Since it is not generally the case that the recombination rate constant is the same as the trapping rate constant, the trap density,  $N_A$ , is actually a renormalized trap density.

The second addition was to the current density. In addition to the Ohm's law term, relating current density to an applied DC electric field via the conductivity, and the asymmetric photocurrent (c.f. Eq. 3), is a diffusion term. Thus, the current density is given by

$$J = \sigma E_{DC} + \sigma^3 (E_0^2 E_{2\omega}^* + E_0^* E_{2\omega}) - eD\nabla n \quad (5).$$

$\sigma$  is the conductivity, and  $D$  is the carrier diffusion coefficient. From continuity, the time rate of change of the charge density is given by

$$dp/dt = -\nabla J \quad (6).$$

Since the conductivity,  $\sigma$ , is proportional to the number of carriers, it is also proposed here that the asymmetric conductivity is also proportional to the number of carriers. This is based on results from nonlinear susceptibilities in

plasmas. In addition, if the asymmetric conductivity were independent of carrier density then the asymmetrically induced electric field grating would decrease in amplitude with increasing carrier density. This is not the case. Hence

$$\sigma = \mu en ; \sigma^3 = \mu^3 en \quad (7)$$

$\mu$  is the linear mobility and  $\mu^3$  is the asymmetric mobility.

In order to solve Eqs. 4 - 7, the transverse profile of the waveguiding modes must be known. Using normal mode analysis for the fundamental beam 1 and the second harmonic beam 2, the transverse electric field components for the TM modes  $j$  and  $k$  propagating in the  $z$  direction are given by<sup>7</sup>

$$E_{1j}(x,t) = (1/2) A_{1j}(z) \phi_{1j}(y) \theta_{1j}(x,z) \exp[i(\beta_{1j} z - \omega_1 t)] \quad (8)$$

$$E_{2k}(x,t) = (1/2) A_{2k}(z) \phi_{2k}(y) \theta_{2k}(x,z) \exp[i(\beta_{2k} z - \omega_2 t)] \quad (9)$$

where the field distribution in the  $y$  direction (perpendicular to the plane of the waveguide) and  $x,z$  plane, respectively, within the waveguide is

$$\phi_{ij}(y) = C \cos[(n_i^2 k_i^2 - \beta_{ij}^2)^{1/2} y - \delta_i] \quad (10)$$

$$\theta_{ij}(x,z) = [1 + (2i z / \beta_{ij} w_{ij}^2)]^{1/2} \exp\{-x^2 / [w_{ij}^2 + (2i z / \beta_{ij})]\} \quad (11).$$

$k_i = \omega/c$  is the free space wave number,  $n_i$  is the refractive index for the fundamental ( $i = 1$ ) or the second harmonic ( $i = 2$ ),  $C$  is determined from boundary conditions, and  $w_{ij}$  is the waist of the beam in the  $x$  direction at  $z = 0$ .

With these input modes into the waveguide, the DC electric field grating is given by

$$E_{DC} = [E_{02}(t) \psi_{2k}(y) \theta_{2k}(x,z) + E_{0,1+2}(t) \psi_{1+2jk}(y) \theta_{1j} \theta_{2k} + E_{0,1-2} \psi_{1-2jk}(y) \theta_{1j}^2 \theta_{2k}^{*2} + c.c.] \cos(\Delta\beta z) \quad (12)$$

$$\psi_{2k}(y) = \exp\{i[(n_2^2 k_2^2 - \beta_{2k}^2)^{1/2} y - \delta_2]\}$$

$$\psi_{1+2jk}(y) = \exp\{i\{[(n_2^2 k_2^2 - \beta_{2k}^2)^{1/2} + 2(n_1^2 k_1^2 - \beta_{1j}^2)^{1/2}]y - \delta_2 - 2\delta_1\}\}$$

$$\psi_{1-2jk}(y) = \exp\{i\{[(n_2^2 k_2^2 - \beta_{2k}^2)^{1/2} - 2(n_1^2 k_1^2 - \beta_{1j}^2)^{1/2}]y - \delta_2 + 2\delta_1\}\},$$

where  $E_{DC}$  is related to the charge density  $\rho$  via Poisson's Equation

$$\nabla \cdot \epsilon \epsilon_0 E_{dc} = \rho. \quad (13)$$

From Eqs. 12 and 13, the space charge field and the charge density grating can be treated as 3 separate gratings with transverse spatial frequencies  $K_2 = (n_2^2 k_z^2 - \beta_{2k}^2)^{1/2}$ ,  $K_{1+2} = [(n_2^2 k_z^2 - \beta_{2k}^2)^{1/2} + 2(n_1^2 k_z^2 - \beta_{1k}^2)^{1/2}]$ , and  $K_{1-2} = [(n_2^2 k_z^2 - \beta_{2k}^2)^{1/2} - 2(n_1^2 k_z^2 - \beta_{1k}^2)^{1/2}]$ . The dynamics of the space charge field can be found in the solution to the time dependent amplitudes.

With Eqs. 12 and 13, Eqs. 4 - 7 can be linearized and simplified. Separating the charge density and carrier density,  $\rho$  and  $n$ , respectively, into their transverse components, their time dependent amplitudes are found as the solutions to

$$dn_2/dt = -n_2/\tau_R + \rho_2/\tau_i - n_2^*/\tau_N + \rho_2^*/\tau_N$$

$$d\rho_2/dt = -l_b^2 K_2^2 n_2/\tau_a - \rho_2/\tau_a - i K_2 E_N$$

$$dn_{1+2}/dt = -n_{1+2}/\tau_R + \rho_{1+2}/\tau_i - n_{1+2}^*/\tau_N + \rho_{1+2}^*/\tau_N$$

$$d\rho_{1+2}/dt = -l_b^2 K_{1+2}^2 n_{1+2}/\tau_a - \rho_{1+2}/\tau_a - i K_{1+2} E_N$$

$$dn_{1-2}/dt = -n_{1-2}/\tau_R + \rho_{1-2}/\tau_i - n_{1-2}^*/\tau_N + \rho_{1-2}^*/\tau_N$$

$$d\rho_{1-2}/dt = -l_b^2 K_{1-2}^2 n_{1-2}/\tau_a - \rho_{1-2}/\tau_a - i K_{1-2} E_N \quad (14)$$

where  $E_N = \sigma^3 n_0 I(2\omega) I(\omega)^2/32$ . In Eqs. 14, the carrier lifetime,  $\tau_R$ , charge lifetime,  $\tau_b$ , cross relaxation time,  $\tau_N$ , and dielectric relaxation time,  $\tau_a$ , are given by

$$\tau_R = 1/[f_0 + \gamma (N_A + n_0)]$$

$$\tau_i = 1/(f_0 + \gamma n_0)$$

$$\tau_N = 3/(4f_0)$$

$$\tau_a = \epsilon \epsilon_0 / (e \mu n_0),$$

$$f_0 = [(s/hv) \langle I_{2\omega} \rangle]^2$$

where  $n_0$  is the mean carrier density. It too is time dependent, and is given by

$$n_0 = n_{0i} [ n_{0i} - n_{0\infty} - (n_{0i}/n_{0\infty})(n_{0i} - n_{0\infty}) \exp(-\kappa t) ] / [ n_{0i} - n_{0\infty} - (n_{0i} - n_{0\infty}) \exp(-\kappa t) ]$$

where

$$\kappa = [ (f_0 + \gamma N_A)^2 + 4 \gamma f_0 N_D ]^{1/2}$$

$$n_{0i} = (\kappa - f_0 + \gamma N_A) / 2\gamma$$

$$n_{0\infty} = (-\kappa - f_0 + \gamma N_A) / 2\gamma$$

and  $n_{0i}$  is the initial mean carrier density. The Debye screening length in Eqs. 14 is given by

$$l_D^2 = D\tau_d = \epsilon\epsilon_0 k_B T / e^2 n_0$$

where  $D$  is the carrier diffusion coefficient.

One of the problems in solving Eqs. 14 is that the lifetimes and even the Debye screening length are also time dependent. However, in order to understand the qualitative behavior of the space charge field, and hence the time dependence of the second harmonic signal, it is assumed that the mean carrier density,  $n_0$ , is already at its steady state value. Another problem in solving Eqs. 14 is that the values for such parameters as mobilities, recombination rate constants, and cross sections are not known. Therefore, the various lifetimes are also not known. In order to get around this problem, Eqs. 14 were scaled to the dielectric relaxation time. With such scaling, general statements about the expected behavior of the space charge field can be made with respect to relative lifetimes. This has an advantage in that future experiments can be better defined regarding the relative values of these parameters. In the calculations, the dielectric relaxation time was estimated from a resistivity of about  $10^7 \Omega \text{ cm}$ , giving a dielectric relaxation time of about 330 s. While this value is reasonable, because of scaling, it is not important.

Eqs. 14 is solved as an eigenvalue problem with three pairs of eigenvalues. Each pair is associated with one of the three gratings and is the dominant pair of eigenvalues for that grating. The  $K_2$  grating is not coupled to the other two gratings, and is therefore independent of them. It only has one pair of eigenvalues. On the other hand, the  $K_{1+2}$  and  $K_{1-2}$  gratings are coupled, and therefore each grating has both of the two remaining pairs of eigenvalues. But, each

grating will have mutually exclusive dominant eigenvalues. If any pair of eigenvalues are complex conjugates of each other, then the space charge field will be oscillatory as it relaxes to its steady state value. If any of those pairs of complex conjugates do not have a real component, then the oscillation will persist indefinitely.

The question to raise, then, is whether there are conditions under which the eigenvalues are complex or imaginary. It turns out the answer is yes. This can be seen by taking the time derivative of Eqs. 14. When this is done, it is clear that the charge and carrier dynamics behave like coupled harmonic oscillators. When the product of the diffusion time,  $\tau_{\text{diff}} = \tau_{\text{c}}/(K^2 l_D^2)$ , and the charge lifetime is less than the square of the carrier lifetime, the space charge field oscillates. Carriers move in a harmonic well, hence damped oscillatory dynamics can be expected. On the other hand, when that product is greater than the dielectric relaxation time, the oscillators are overdamped. The carriers are in a "site-hopping" mode.

This was explored by varying the intensity of the seed green light in the calculations. By doing so, the ratio of the carrier lifetime to the diffusion time was also varied. It was found that at higher intensities, all three pairs of eigenvalues were real and negative. In this case the diffusion time was much greater than the carrier lifetime. Each grating relaxes to its steady state value multiexponentially. This is shown in Fig. 5. In Fig. 6, the resulting second harmonic intensity is shown, when it is assumed that the intensity is proportional to the square of the amplitude of the space charge field. As the intensity was decreased so that the ratio of carrier lifetime to diffusion time was greater than unity, each pair of eigenvalues became complex conjugates. This is shown in Figs. 7 and 8. Clearly the amplitude of the space charge field, and hence the intensity of second harmonic light oscillate as they relax to their steady state value. These figures, should be compared with Fig 4. It is important to note, however, that each pair of eigenvalues did not become complex at the same intensity. There were a range of intensities where only one or two of the three gratings had complex eigenvalues. This is expected, considering that the diffusion time is dependent on the transverse spatial frequency of the grating.

These results can be summarized by a simplified statement (perhaps oversimplified). When the carrier lifetime is longer than the diffusion time, the carriers are in a diffusion mode and are seen to demonstrate the damped oscillatory behavior seen in a potential well. This behavior is expected at low intensity levels of green light. When the carrier lifetime is shorter than the diffusion time, the carriers are in a site hopping mode and they exhibit overdamped dynamics. This behavior is expected at higher intensities of the green light.

## 5. Conclusions

The second harmonic generation of light in glass films was studied. It was confirmed that this process can be facilitated by applying an electric field grating across the waveguide, although the appearance of partial screening is still enigmatic. Additional experimental evidence was obtained to demonstrate that the film generated second harmonic light is the result of a space charge field, although the asymmetric photocurrent is still elusive. An interesting result was the

observation of oscillations in the intensity of the film generated second harmonic light. It was shown that this is expected for low levels of seed green light, because at those levels the carrier lifetime is much longer than the diffusion time of the carriers.

These results demonstrate the need for more experimental work. It is clear that the model presented above needs additional verification by determining the values of the charge mobility and photoexcitation cross sections, etc. By varying the intensity of the seed green light, the existence of the diffusion and site hopping regimes can be verified.

#### References.

1. U. Osterberg and W. Margulis, Opt. Lett., 11, 516 (1986), J.J. Kester, P.J. Wolf, and W.R. White, Opt. Lett., 17, 1779 (1992), N.M. Lawandy and M.D. Selker, Opt. Commun., 77, 339 (1990).
2. R.H. Stolen and H.W.K. Tom, Opt. Lett., 12, 585 (1987).
3. P. Weitzmann, J.J. Kester, and U. Osterberg, Electron. Lett., 30, 697 (1994).
4. M.L. Brauer and I. Dajani, (to be submitted).
5. B. Ya Zel'dovich and A.N. Chudinov, JETP Lett., 50, 439 (1989), E.M. Dianov, P.G. Kazansky, and D. Yu Stepanov, Sov. J. Quant. Electron., 19, 575 (1990), D.Z. Anderson, V. Mizrahi, and J.E. Sipe, Opt. Lett., 16, 796 (1991).
6. J.K. Lucek, R. Kashayap, S.P. Davey, and D.O. Williams, J. Mod. Opt., 37, 533 (1990).
7. I. Dajani (to be submitted).

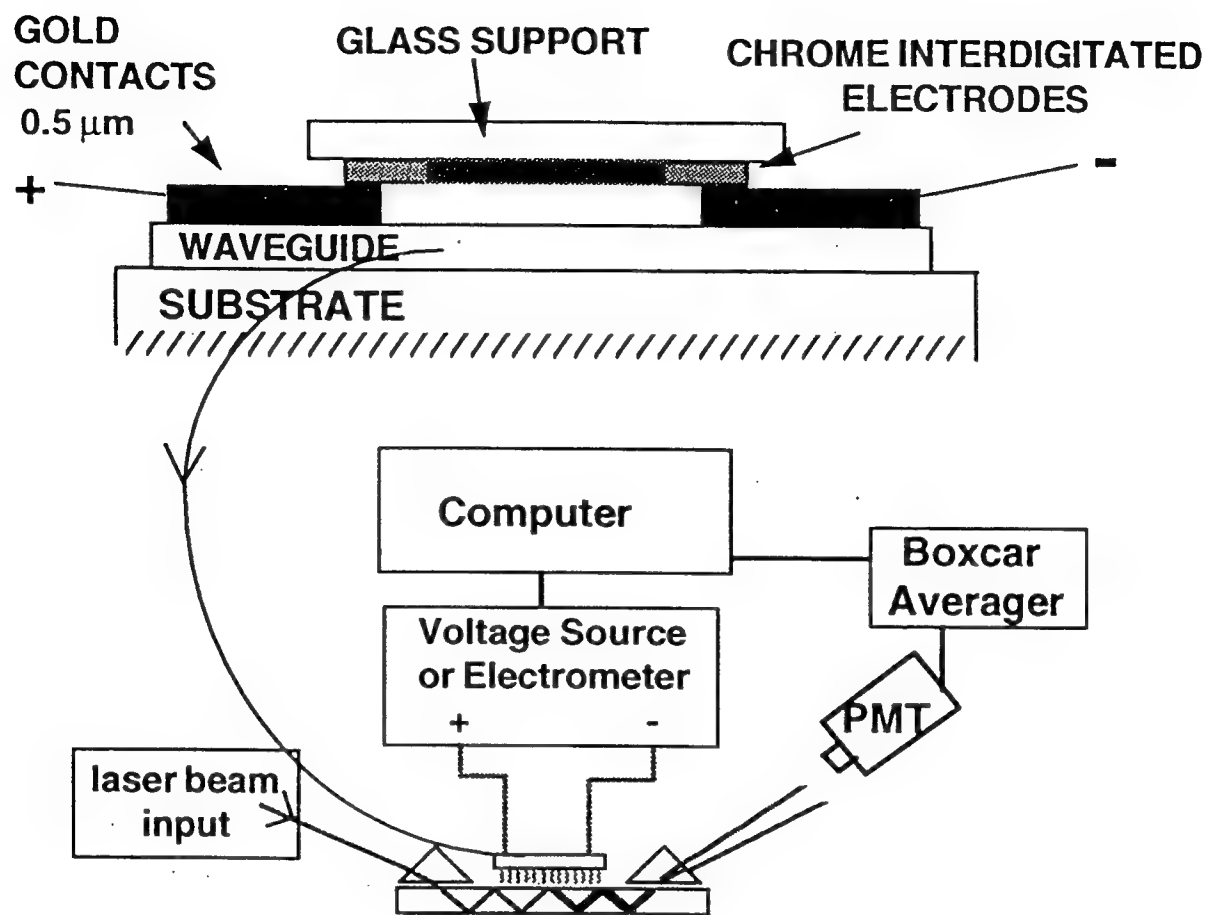


Fig 1: Experimental Set-Up

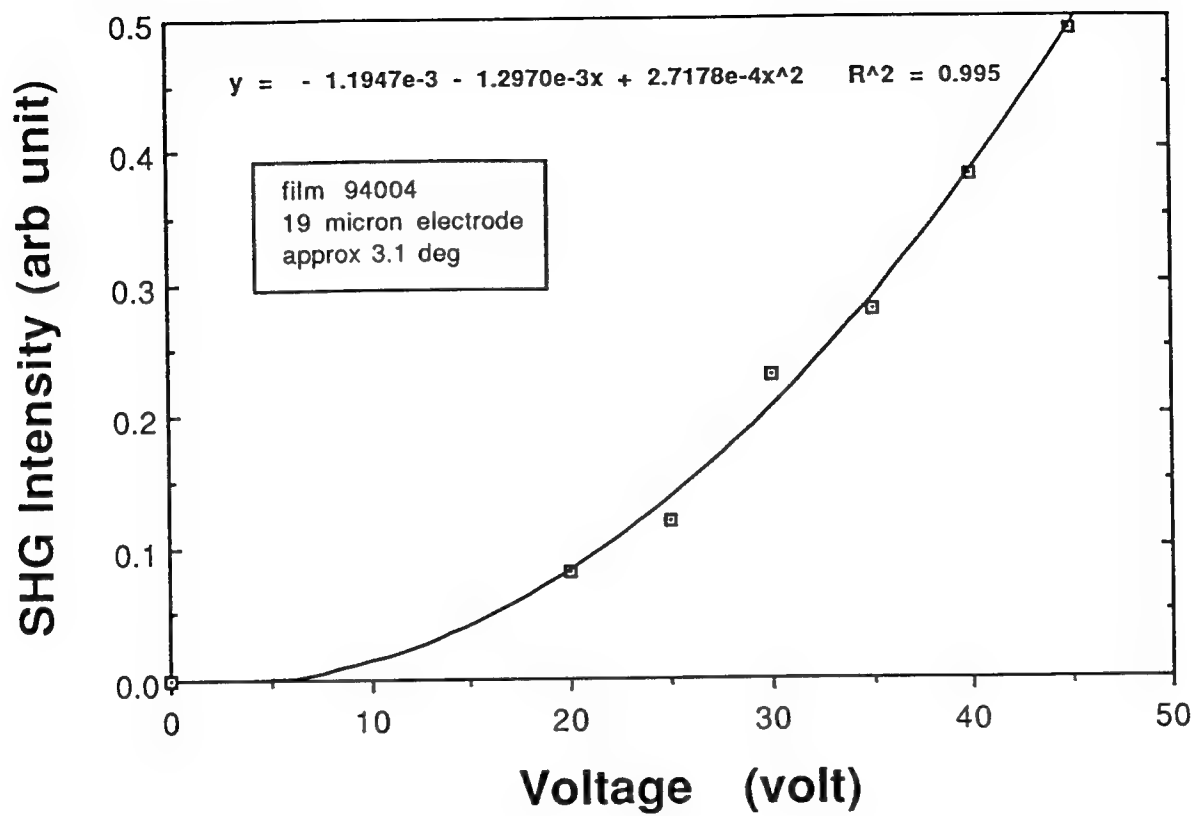


Fig 2: Second Harmonic Intensity versus Applied Voltage

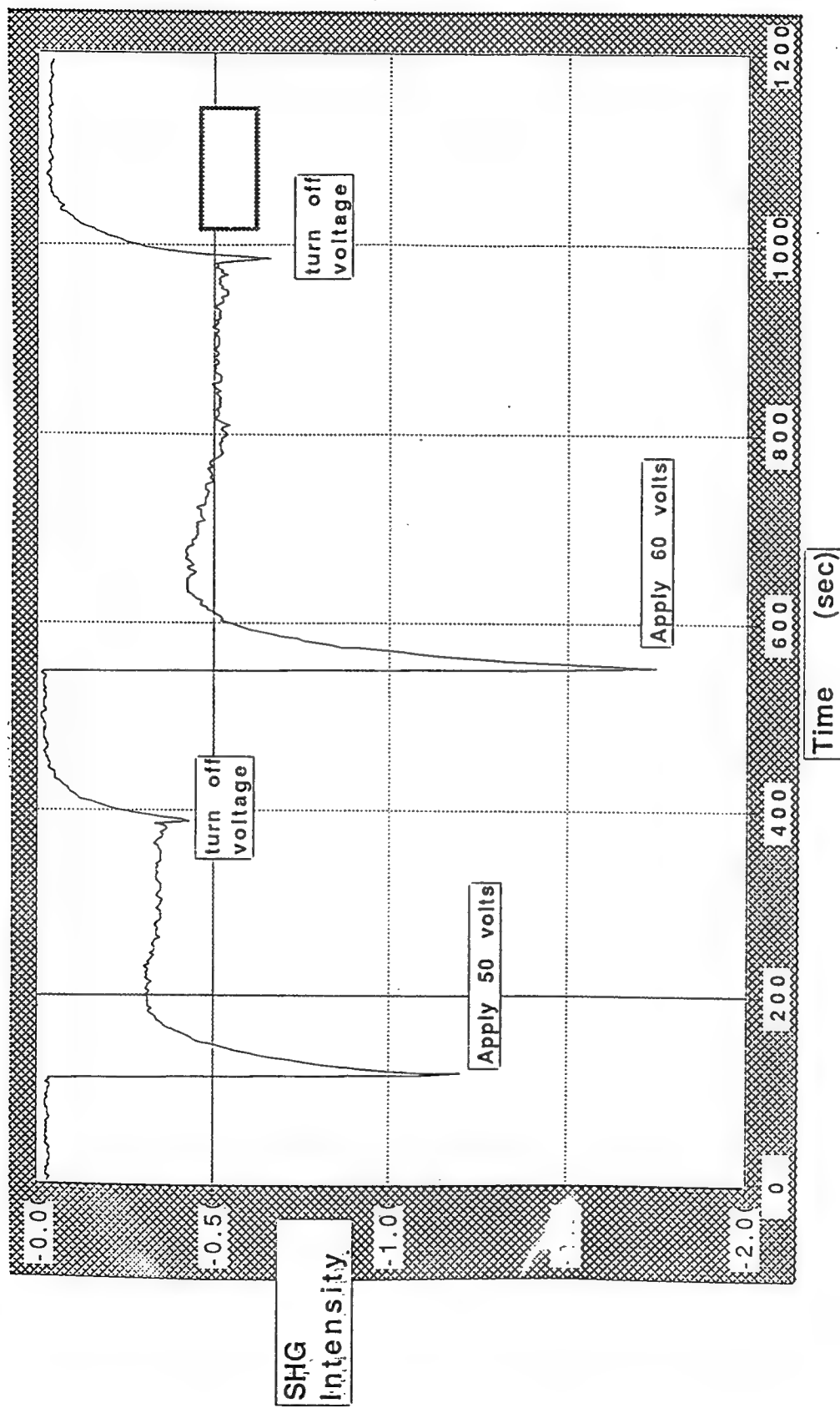


Fig 3: Electric Field Induced SHG versus Time

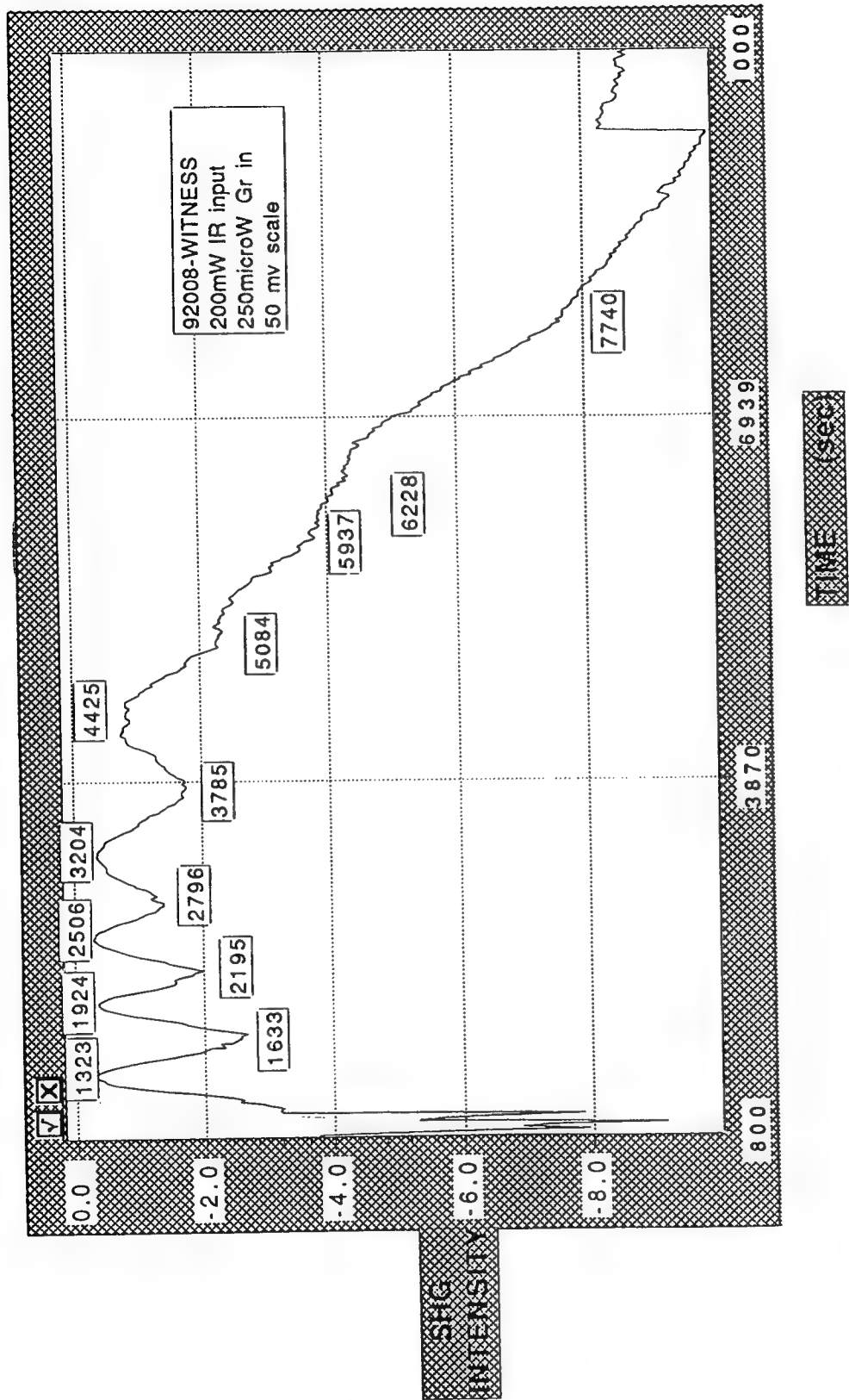


Fig 4: Second Harmonic Intensity versus Time

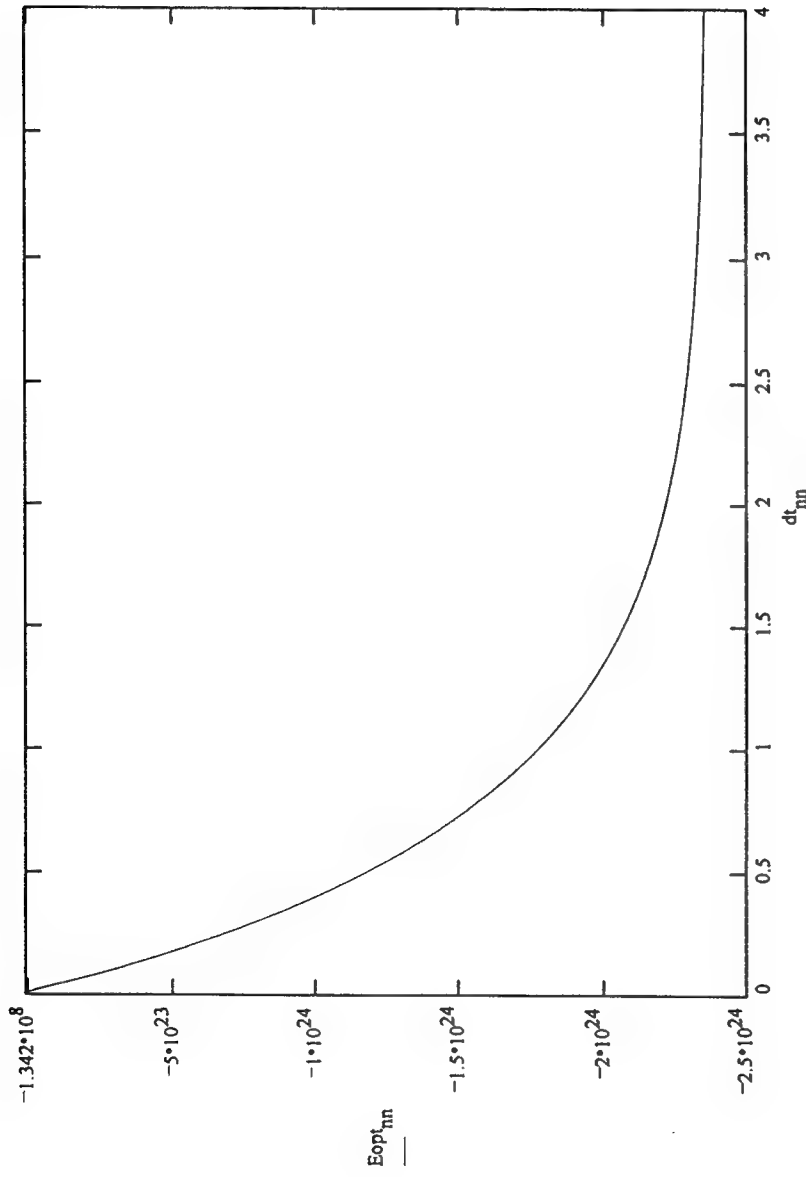


Fig 5: Space Charge Electric Field versus Time-High Seed Intensity

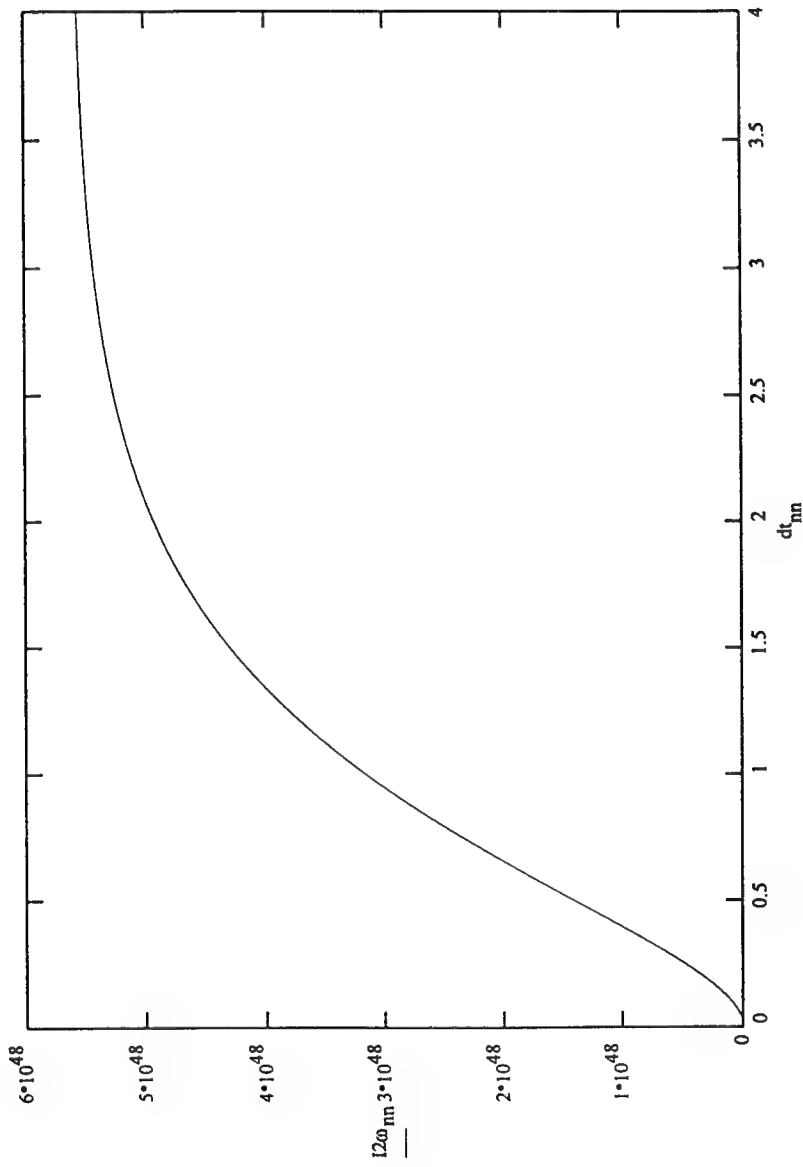


Fig 6: Second Harmonic Intensity versus Time--High Seed Intensity

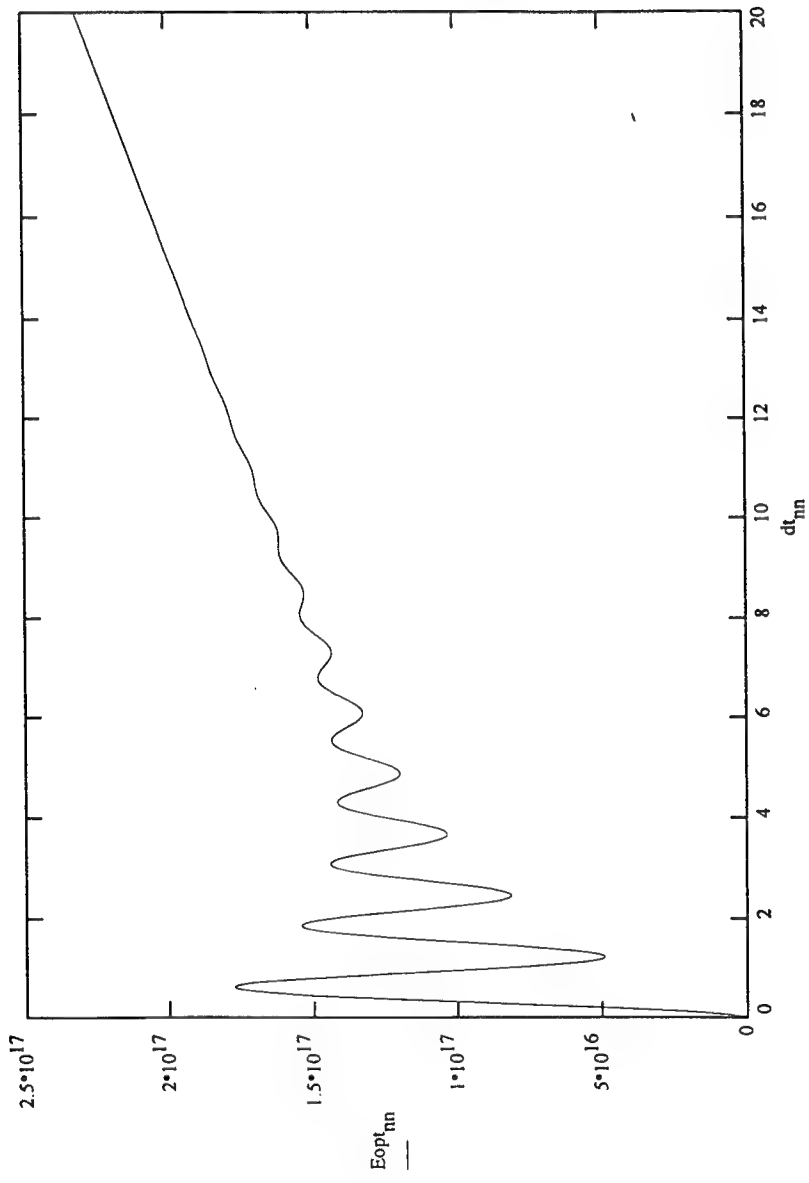


Fig 7: Space Charge Electric Field versus Time--Low Seed Intensity

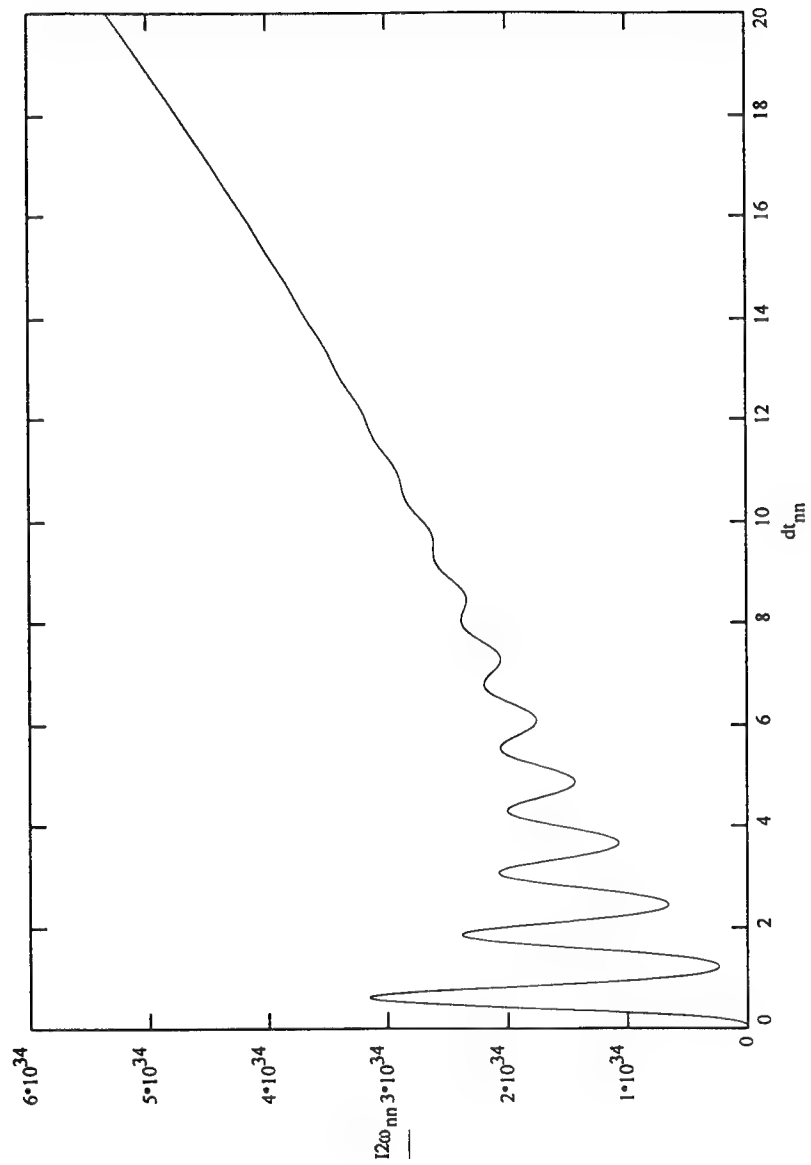


Fig 8: Second Harmonic Intensity versus Time-Low Seed Intensity

---

EFFECTS OF TEMPERATURE ON VARIOUS  
HEMATOLOGICAL PARAMETERS.

W. Drost-Hansen  
Professor of Chemistry

University of Miami  
Coral Gables, FL 33124

Final Report for:  
Summer Faculty Research Program  
Clinical Investigation Directorate  
Wilford Hall Medical Center  
Lackland AFB, San Antonio, TX

Sponsored by:  
Air Force Office of Scientific Research  
Boling Air Force Base, DC

and

Wilford Hall Medical Center

September 1994

## Effects of Temperature on various Hematological Parameters

W. Drost-Hansen, Department of Chemistry, University of Miami.  
and Student Co-investigator, Ramu Tummala, School of Medicine,  
University of Alabama.

### ABSTRACT

Using human blood samples, we have determined the effects of temperature on the following hematological parameters: Erythrocyte Sedimentation Rate (ESR), Mean Red Cell Volumes (MCV), Mean Platelet Volumes (MPV) and the sodium/potassium ratio in the plasma of heat-treated whole blood. As described in previous Reports, ESR data obtained over the range from about 30 °C and up to approx. 52 °C show distinct, abrupt and frequently dramatic changes near 45 °C and somewhat similar changes are observed at this temperature in the measured volume properties (MCV and MPV) and ion-distribution data. The temperature range from 44 ° to 46 °C is known to be a critical temperature range for all mammals and birds and is indeed the upper thermal limit for such organisms. As stressed in our earlier Reports, the dramatic effects near 45 °C undoubtedly reflect the transition at the third vicinal water thermal transition temperature ( $T_{k=3}$ ) which is known to affect a large number of parameters of the cell-associated water [see papers by Drost-Hansen et al.]. Some measurements of the same parameters have also been made at lower temperatures, for instance from 8 ° to 25 °C and from 20 ° to 37 °C. Some indications of anomalies near 15 ° and 30 °C have been seen (corresponding to the lower, critical thermal transition temperatures for vicinal water,  $T_{k=1}$  and  $T_{k=2}$ ) but the anomalies at these temperatures are far less pronounced than the 45 °C anomaly. To insure the best resolution practical, measurements have been made over the different temperature intervals at increments of 0.6 ° to 0.9 °C using our Temperature Gradient Incubator (TGI or "Polythermostat") which allows for simultaneous measurements at 30 different, constant temperatures. Earlier we have proposed that the distinct changes near 45 °C ( $T_{k=3}$ ) may play an important role in hyperthermia treatment of malignancies. While the findings in the current study do not prove this supposition, the data are consistent with this proposal: dramatic changes appear to take place at this critical temperature in such parameters as the ESR (probably reflecting reduced Red Cell-aggregation and/or rheological changes in the blood, likely related to vicinal hydration changes of the proteins present), and/or intracellular ion or solvent activities, and possibly changes in the stability of critical membrane-associated proteins or enzyme activities. Such changes may indeed preferentially affect the thermal stability of malignant cells compared to normal cells if the relative abundance of vicinal water in malignant cells differs from that of normal cells. The latter proposition is likely true as it is well-known that malignant cells have notably elevated water contents compared to healthy cells. The excess water of the malignant cells more closely resembles "bulk water" (solvent) than vicinal water.

## INTRODUCTION

The Erythrocyte Sedimentation Rate (ESR) has a long and distinguished history as one of clinical medicine's most frequently used diagnostic indicators and in spite of its lack of specificity and the advent of highly sophisticated electronic Hematology Counters the test continues to be in common use. A great deal of research has been reported on various aspects of the fundamental processes underlying the ESR yet our understanding of the aggregation and sedimentation processes remains notably incomplete and in fact unsatisfactory. The present study was initiated about five years ago in an effort to contribute towards a more complete description of the ESR in terms of the underlying adsorption phenomena, transport processes, biochemistry and basic cell physiology. In this connection we have stressed the response of the ESR to temperature: a subject not frequently dealt with in the literature.

In the Clinical Laboratory the ESR is usually determined at room temperature [taken to be 25 °C in USA but probably closer to ca. 20 °C in other locations, say Northern Europe, and likely higher than 25 °C in many tropical, Third World Countries]. We have previously advocated that it may be useful, on a routine basis, to determine the ESR at two (or more) different temperatures, such as to obtain a temperature coefficient (i.e.  $d[ESR]/dt$ ). We continue to explore the possibility that such a temperature coefficient may contain valuable diagnostic information and in view of the ease and low cost of the ESR measurements such an approach may be well worth the extra effort. The great drawback of such measurements at this time is the lack of any historical data for the temperature coefficient but considering the temperature data obtained in the present study, including the enormous variability in the effects of temperature on the ESR, it is highly probable that  $d[ESR]/dt$  does indeed contain some important information. In view of the fact that the temperature coefficient is a differential quantity it is conceivable that it does not depend on some of the variables known to affect the ESR itself such as age of the patient or obesity.

## EXPERIMENTAL PROCEDURES

As in previous years under the aegis of the AFOSR Summer Faculty Research Program, ESR data have been obtained using Wintrobe tubes. The blood (usually 50 ml) was obtained from human volunteers by antecubital venipuncture. Unless otherwise stated, the blood was drawn in plastic syringes (60 ml capacity) to which had been added 1.0 ml 0.25 molar sodium EDTA solution as anticoagulant. Depending on the experiment the blood samples were either stored at room temperature before using, or, if measurements at higher temperatures were planned, at 36 °- 37 °C. Usually the blood was used within one after collection. Routine Hematology characterization was made on all blood samples immediately after collection using the Baker 9000 Hematology Counter. Such characterization of the blood was also made at the end of each series of ESR determinations; thus, in general 30 complete sets of blood characteristics were determined after completion of exposure of the blood samples to the various temperatures in the Temperature Gradient Incubator (TGI). In previous years we have demonstrated that after exposure to the various temperatures the observed volume changes of both erythrocytes and platelets remain nearly exactly unchanged for at least two hours (and

frequently longer) after removal of the blood samples from the TGI. Thus the relatively slight delay between removing the tubes from the TGI and the time the 30 samples could be run on the Hematology Counter is not likely to introduce spurious variations.

As in previous years we have used Wintrobe tubes exclusively for the ESR determinations; the reason for the choice of the Wintrobe tubes is purely by convenience: Westergren tubes do not fit into the constrained geometry of the sample wells in the TGI. With practice, each Wintrobe tubes could be filled with blood [using a Pasteur pipette] in about 20 - 30 sec, and the entire range of sample wells in the TGI filled in about 10 to 15 minutes. Readings of the sediment heights was subsequently performed at the same rate as the charging of the TGI bar and the entire experiment therefore constitutes essentially truly simultaneous measurements. With experience it is possible to read [or rather, to estimate] the sediment height to within (0.1 to) 0.2 mm insuring excellent precision (note the extremely small scatter in the ESR data shown in the Data Section of this Report).

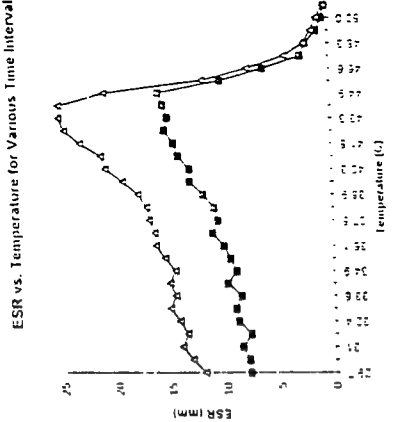
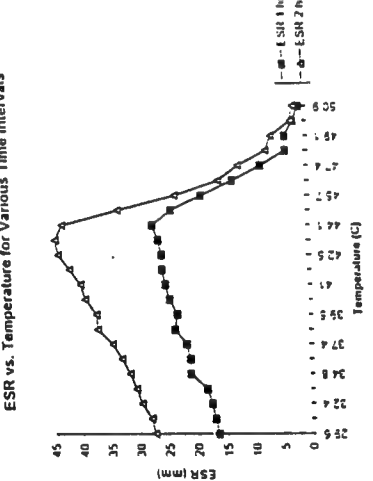
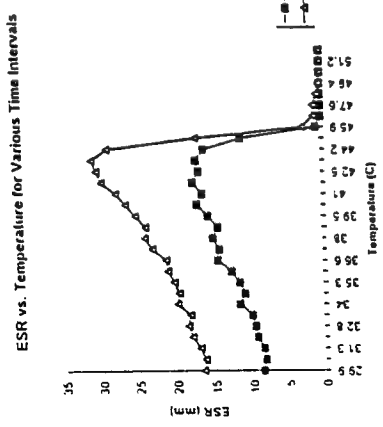
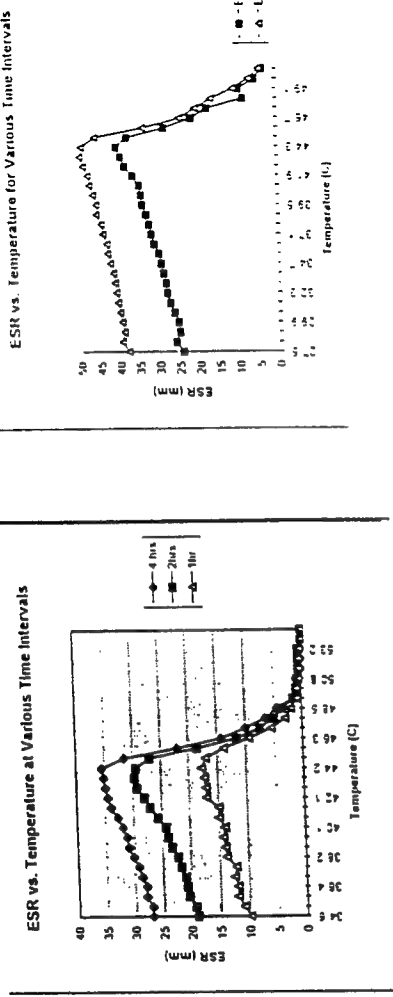
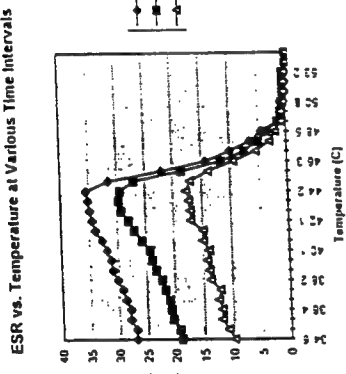
The Temperature Gradient Incubator (TGI or "Polythermostat") has been described in previous Reports; a brief summary is given in the Appendix. The TGI provides 30 different, constant temperatures; the temperature constancy in any given run (over two - three hours) is within 0.1 °C in each well - and sometimes notably better. The temperature gradient was obtained from readings using five or six different thermometers in different wells along the bar, using the second set of wells for the controls. The temperature readings were used on the computer to provide a least square best fit over the entire bar, usually to a second degree polynomial and frequently with extremely good correlation coefficients ( $R = 0.999+$ ). The difference in temperature between adjacent wells may readily be varied. In nearly all the runs described in this Report the temperature difference between samples has been 0.6 ° to 0.9 °C, thus providing excellent resolution in the temperature dependence of the different variables.

A number of sodium and potassium analyses were made on blood plasma after incubation of the whole blood for varying length of time. The ion analysis was made with a clinical ion-analyzer, based on ion-selective membranes. As most of the determinations were made on samples which were nearly identical except for their thermal history it is assumed that errors in absolute ion concentrations essentially cancel out. The samples were most often taken from the Wintrobe tubes after an ESR series of measurements. The Wintrobe tubes were spun down at      RPM for 10 minutes and the supernatant plasma removed with Pasteur pipettes and transferred to 1 ml sample vials for the measurement of the ion concentrations. In most all cases sodium, potassium and chloride ion concentrations were determined. Corrections were made to the sodium ion concentration to allow for the sodium added as anticoagulant ( $Na_4EDTA$ ).

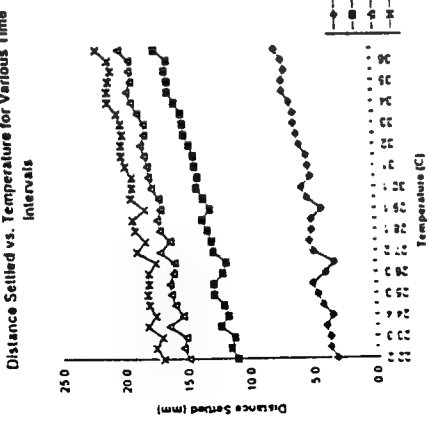
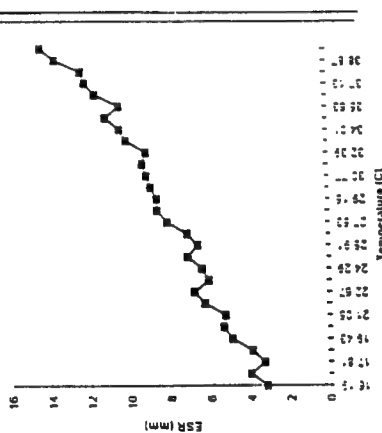
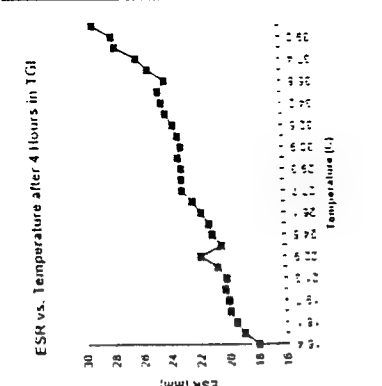
Dilutions:                    In some cases the whole blood was diluted using "Lactated Ringer's Solution", manufactured by Baxter; nominal (calculated) osmolarity: 273 mOsmol/liter, to which had been added 2.0 ml 0.25 Molar  $Na_4EDTA$  per 100 ml lactated Ringer.

**FIGURES 1 - 8**

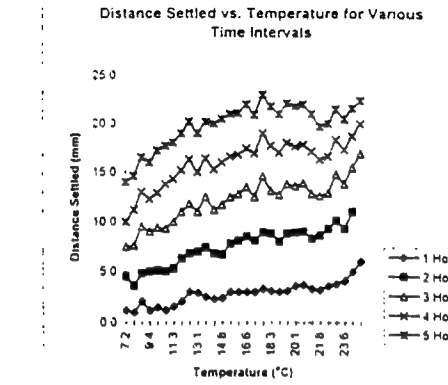
See Table at the end of this report  
for summary of time of incubation,  
type of experiment, donor code, age  
of donor and Hematocrit (Hct).



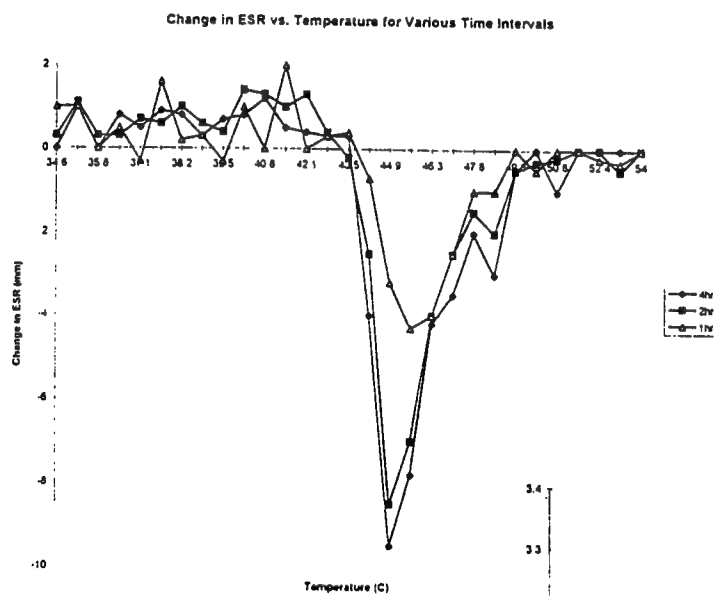
**EXPERIMENTAL RESULTS  
[SELECTED, TYPICAL DATA]**



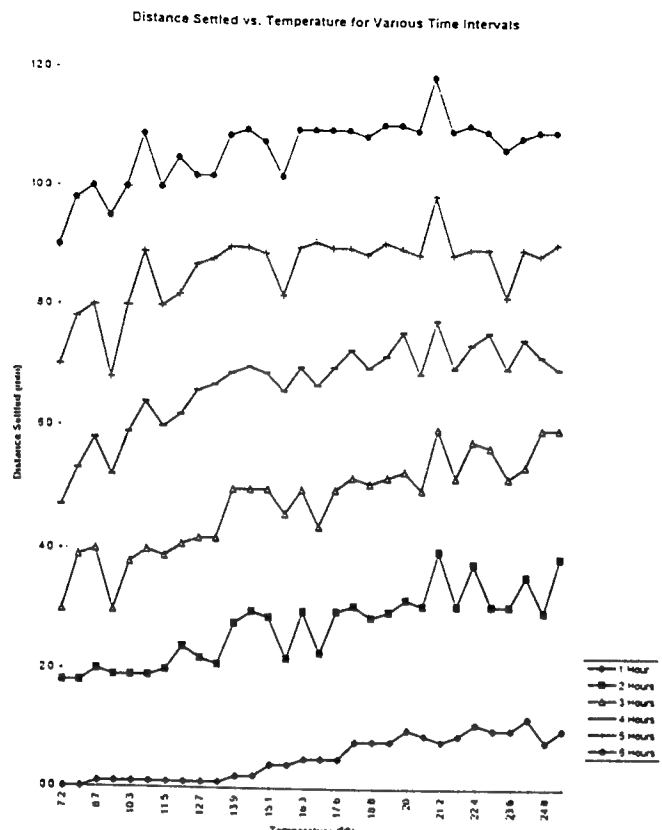
## FIGURES 9 - 12



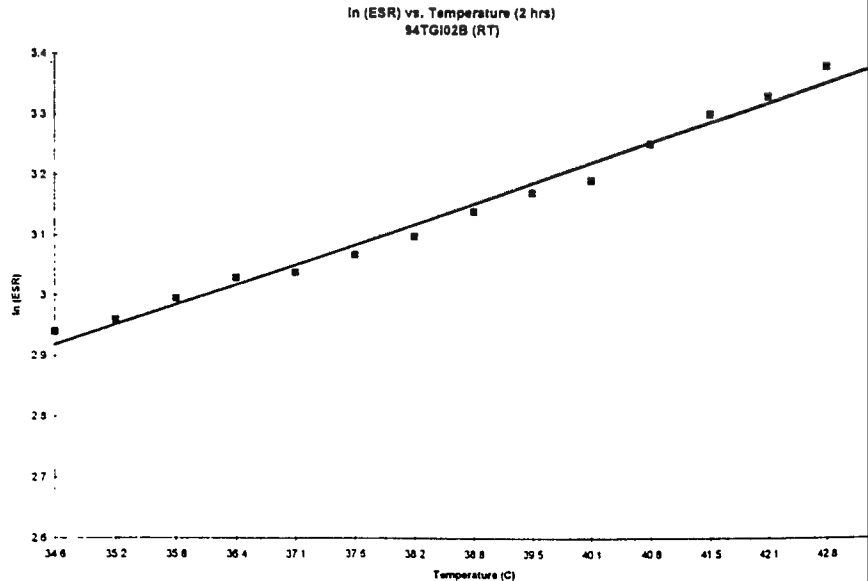
Change in ESR vs. Temperature for Various Time Intervals  
94TGI02B (RT)



Distance Settled vs. Temperature for Various Time Intervals  
94TGI19B (BD)

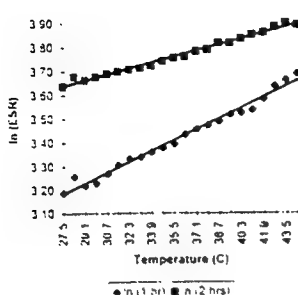


In (ESR) vs Temperature after Two Hours

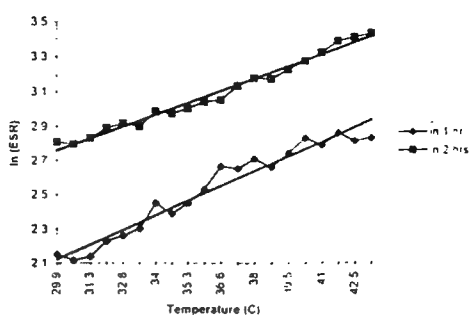


## FIGURES 13 - 20

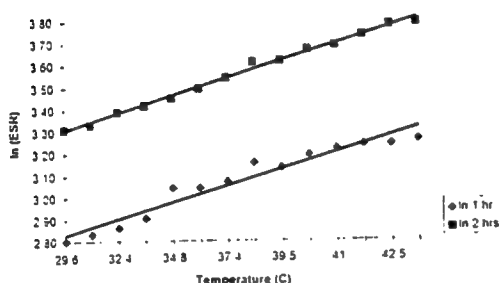
In (ESR) vs. Temperature for Various Time Intervals



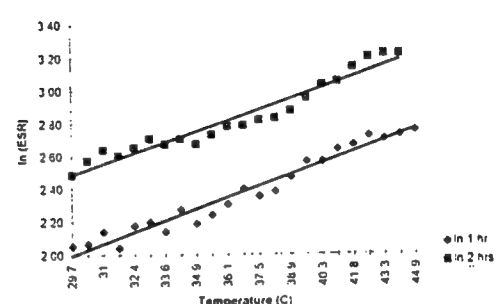
In (ESR) vs. Temperature for Various Time Intervals



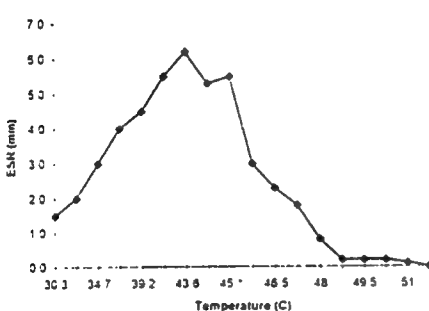
In (ESR) vs. Temperature for Various Time Intervals



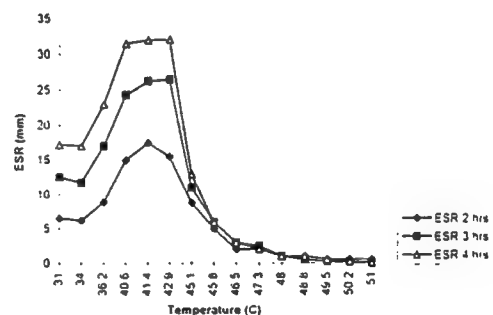
In (ESR) vs. Temperature for Various Time Intervals



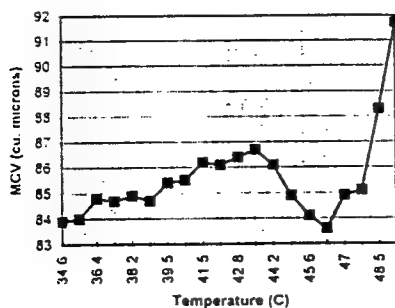
ESR vs. Temperature after 1 hour



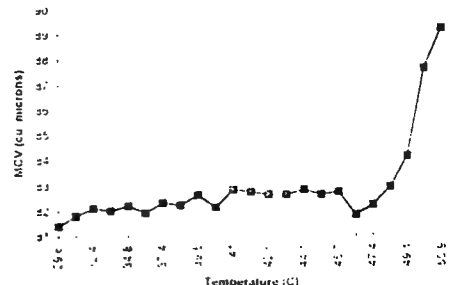
ESR vs. Temperature for Various Time Intervals



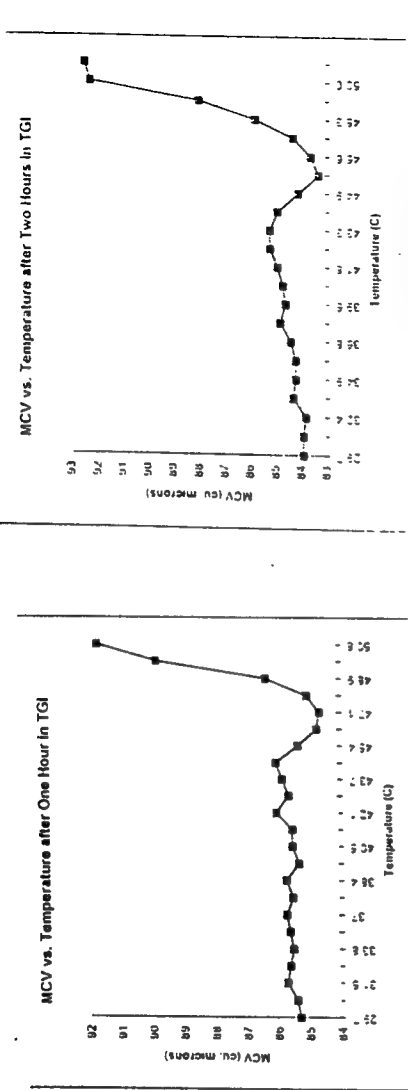
MCV vs. Temperature After Four Hours  
in TGI



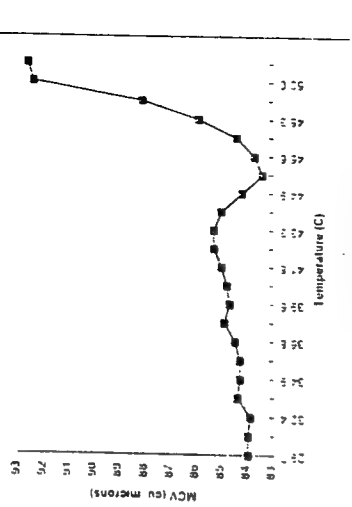
MCV vs. Temperature after Two Hours in TGI



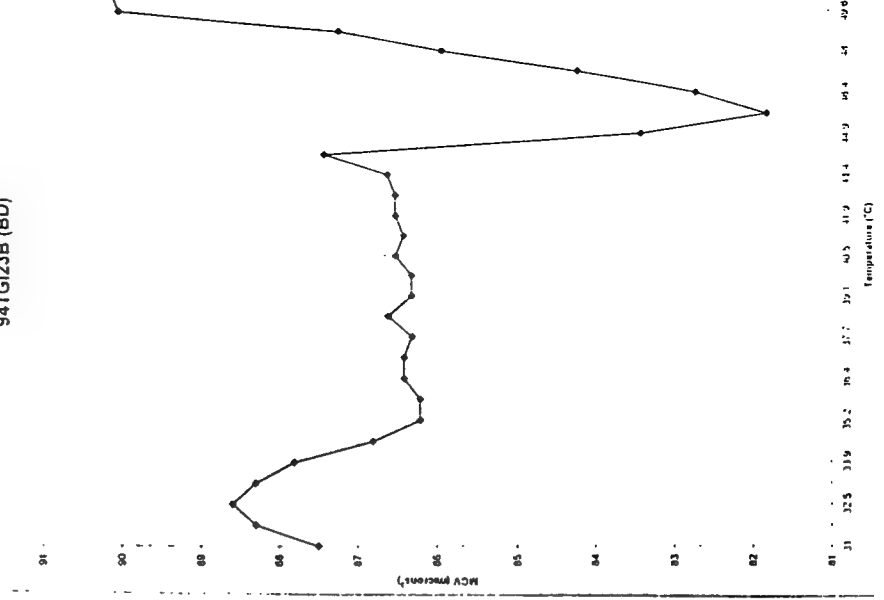
**FIGURES 21 - 26**



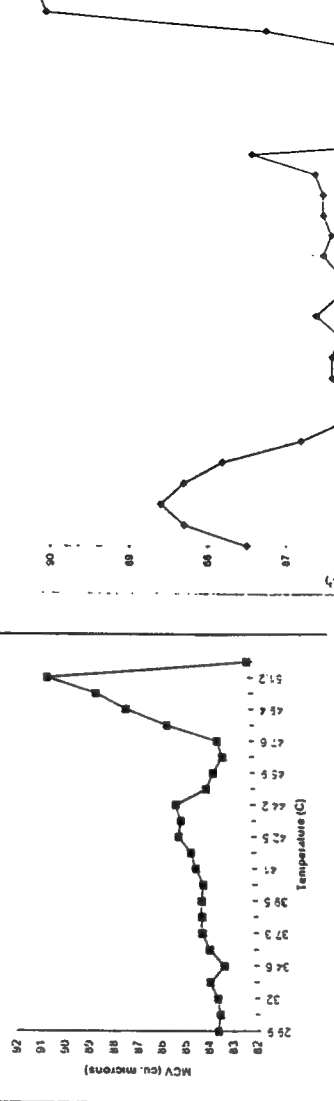
MCV vs. Temperature after Two Hours in TGI



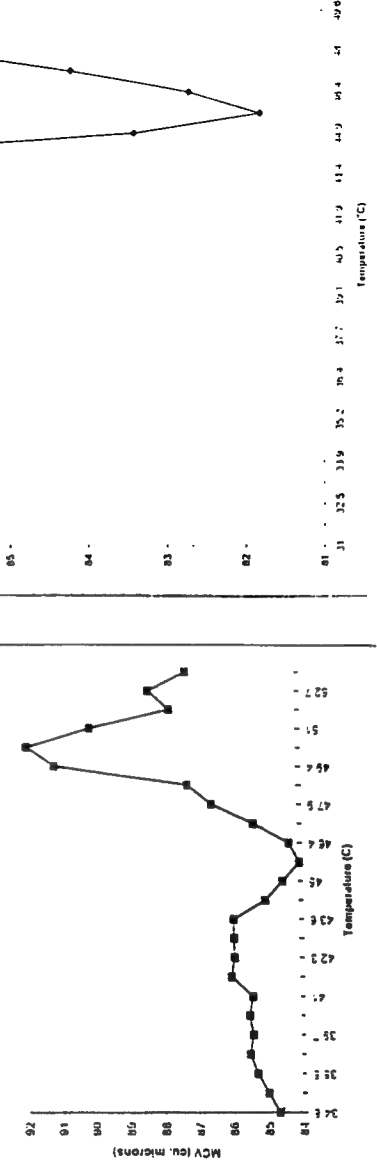
MCV of ESR Samples vs. Temperature after Three Hours in TGI



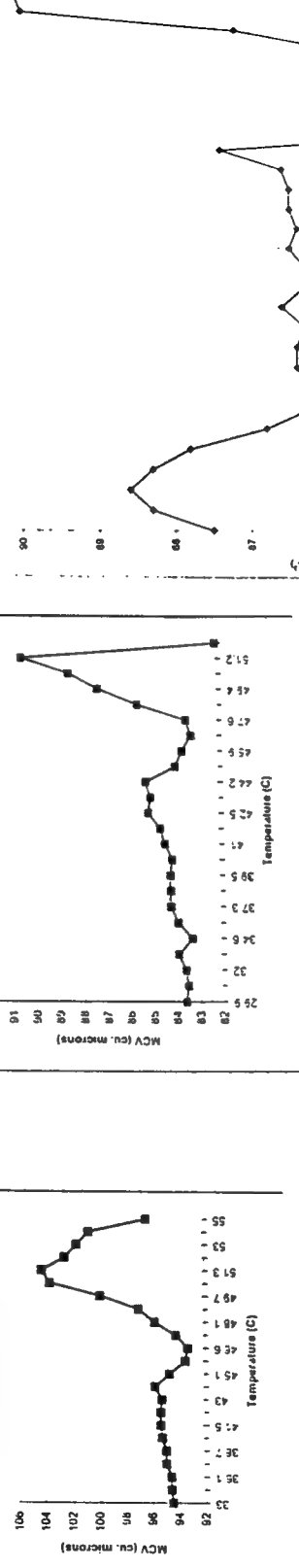
MCV vs. Temperature



MCV vs. Temperature after Two Hours in TGI

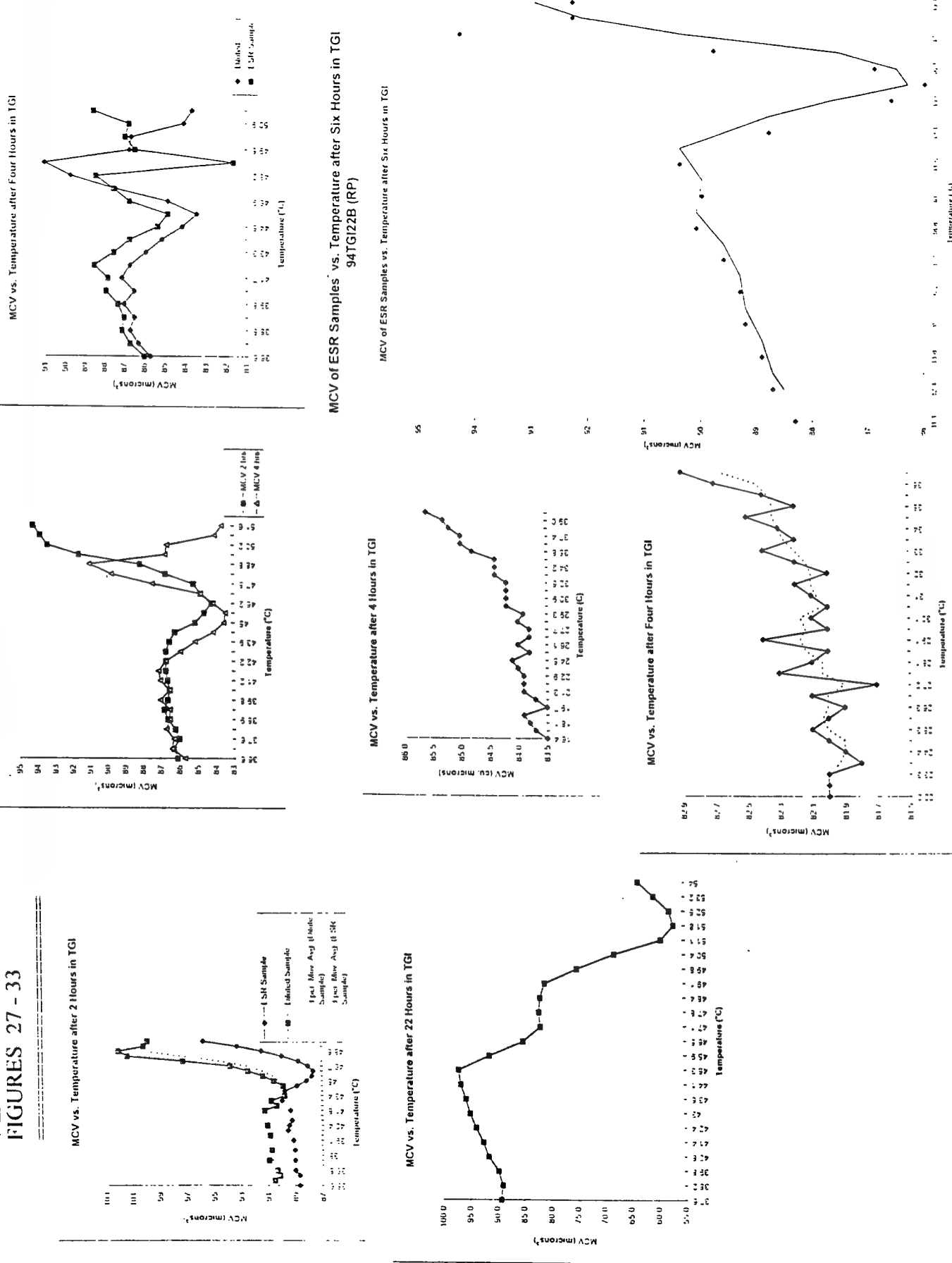


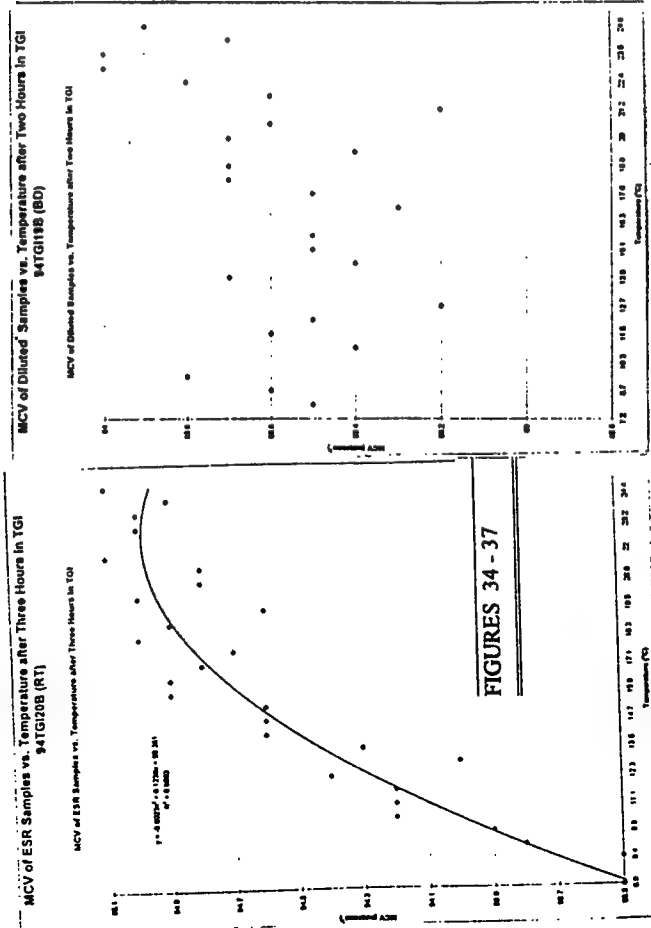
Mean Cell Volume vs. Temperature after Two Hours in TGI



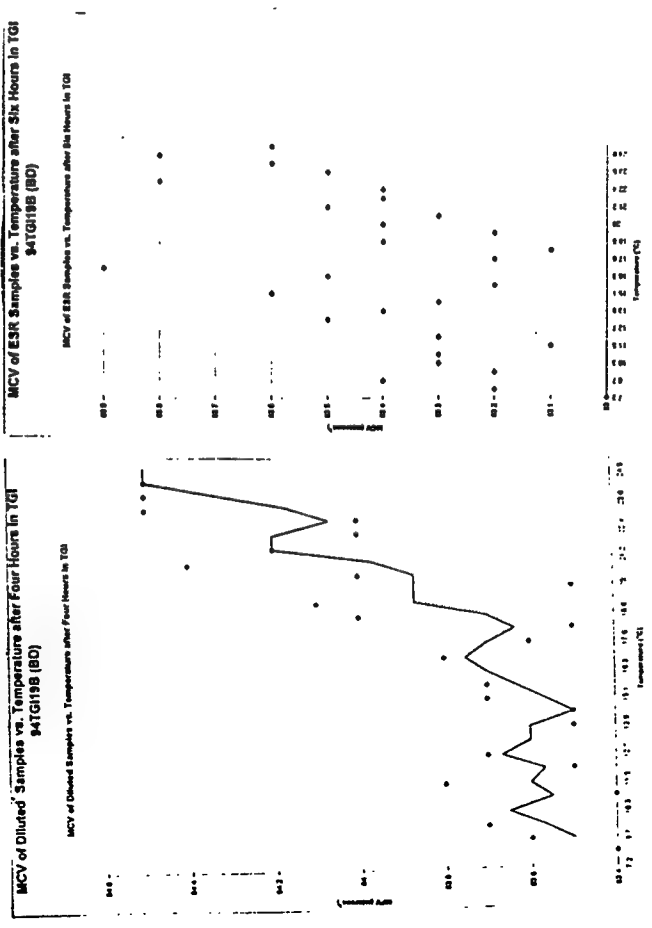
FIGURES 27 - 33

### MCV vs. Temperature for Various Time Intervals

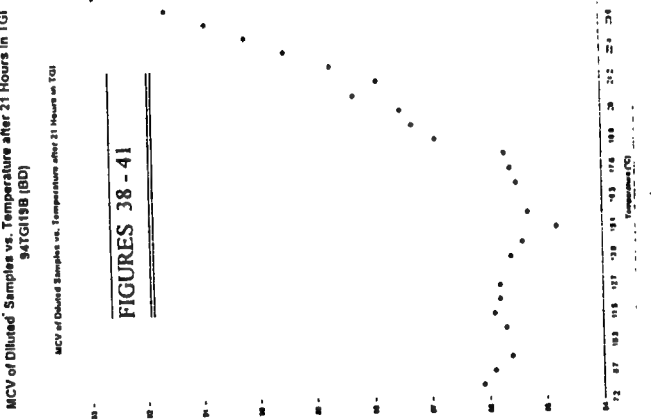




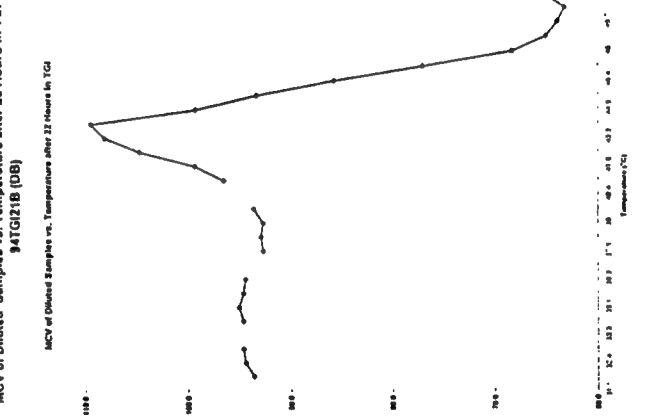
FIGURES 34 - 37



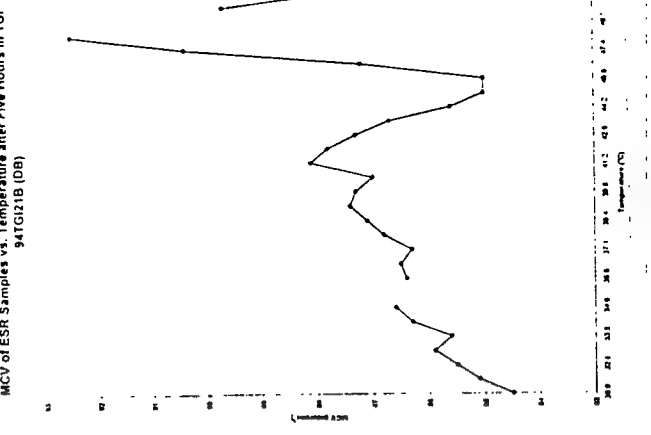
## FIGURES 38 - 41



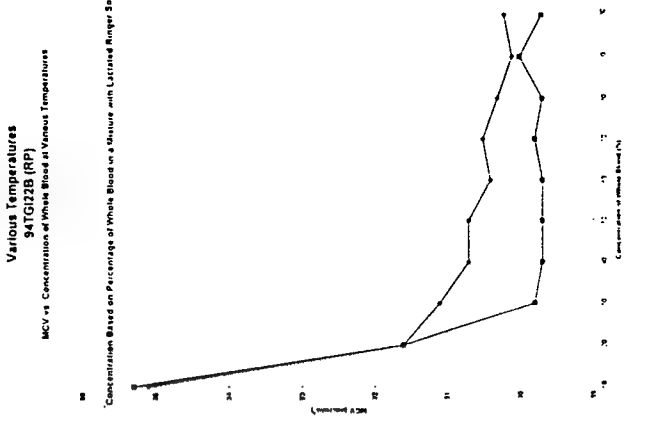
MCY of Fresh Services via Immersion after Six Hours in 100°



MCAT Practice Test 2018 (08) 94

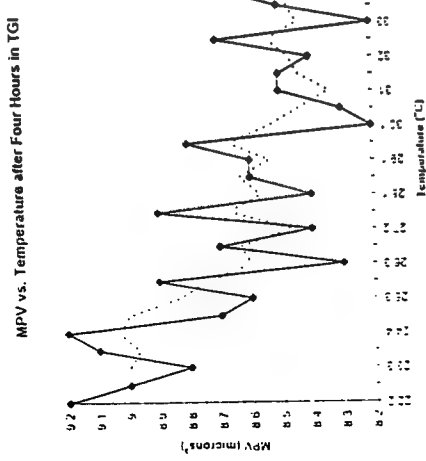
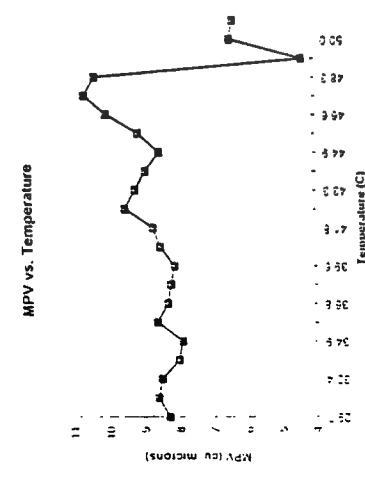
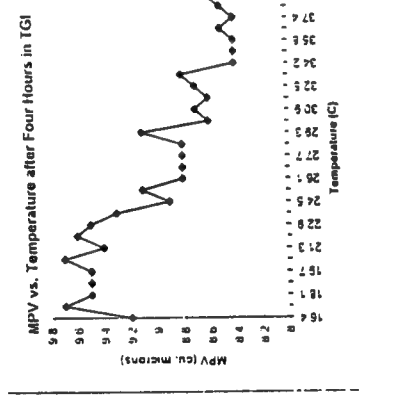
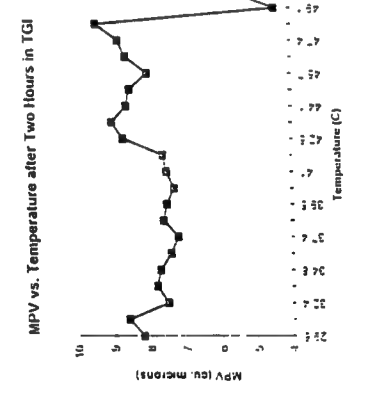
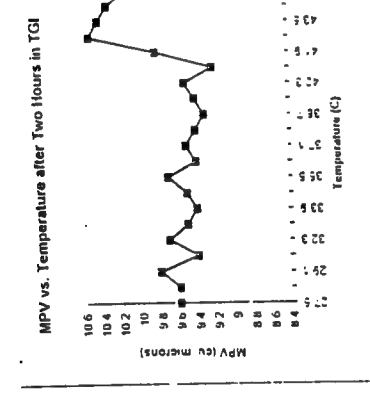
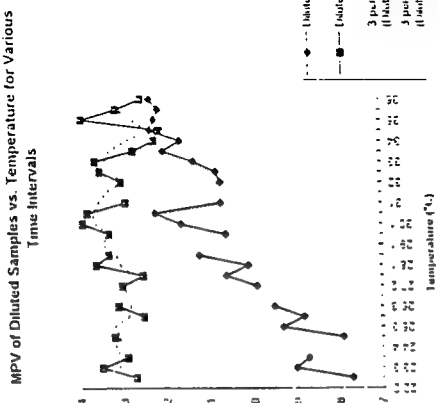
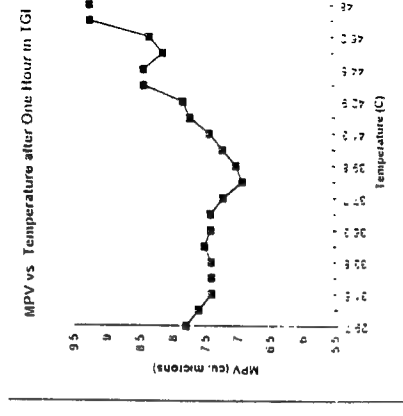
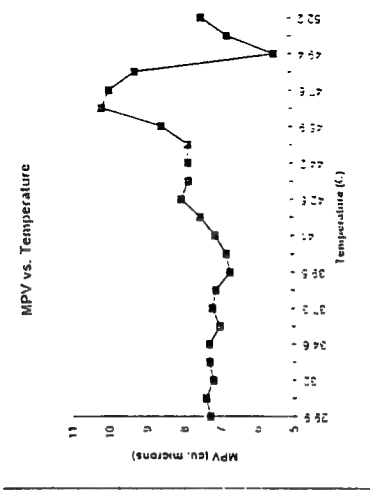


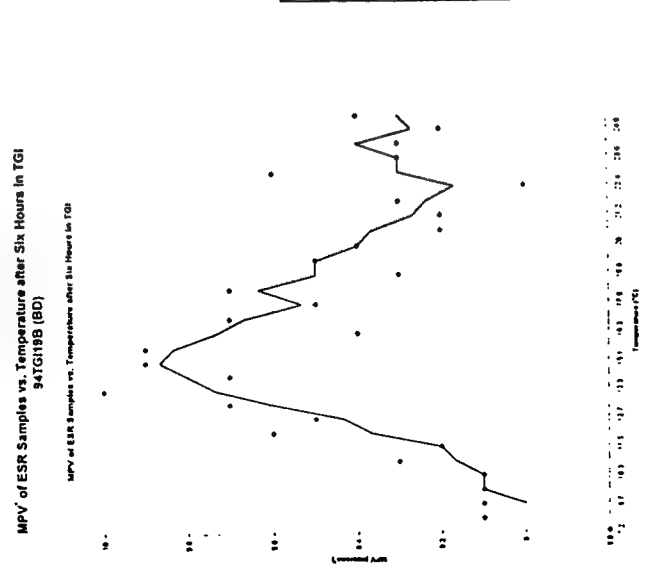
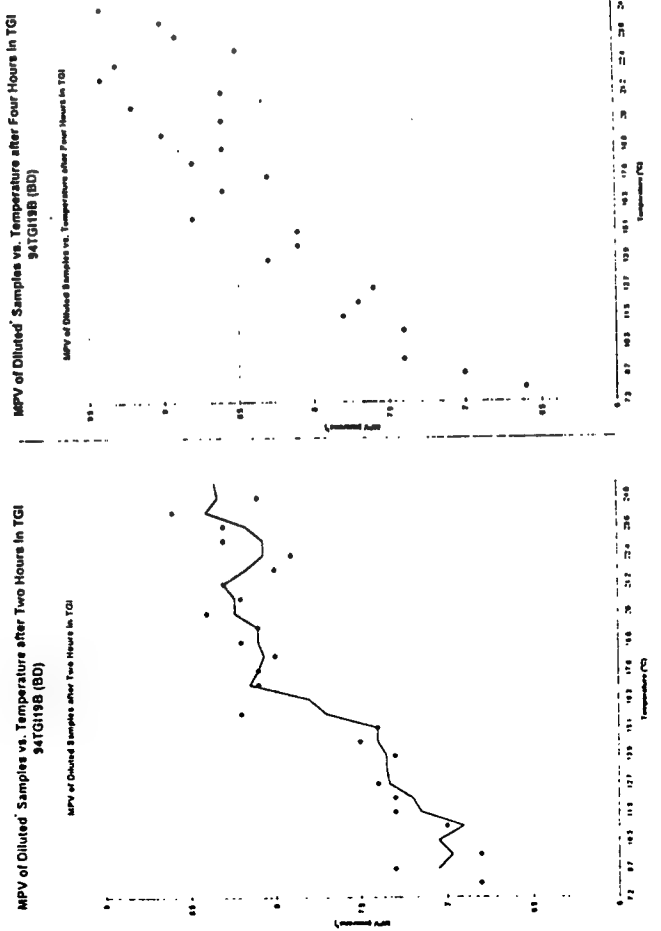
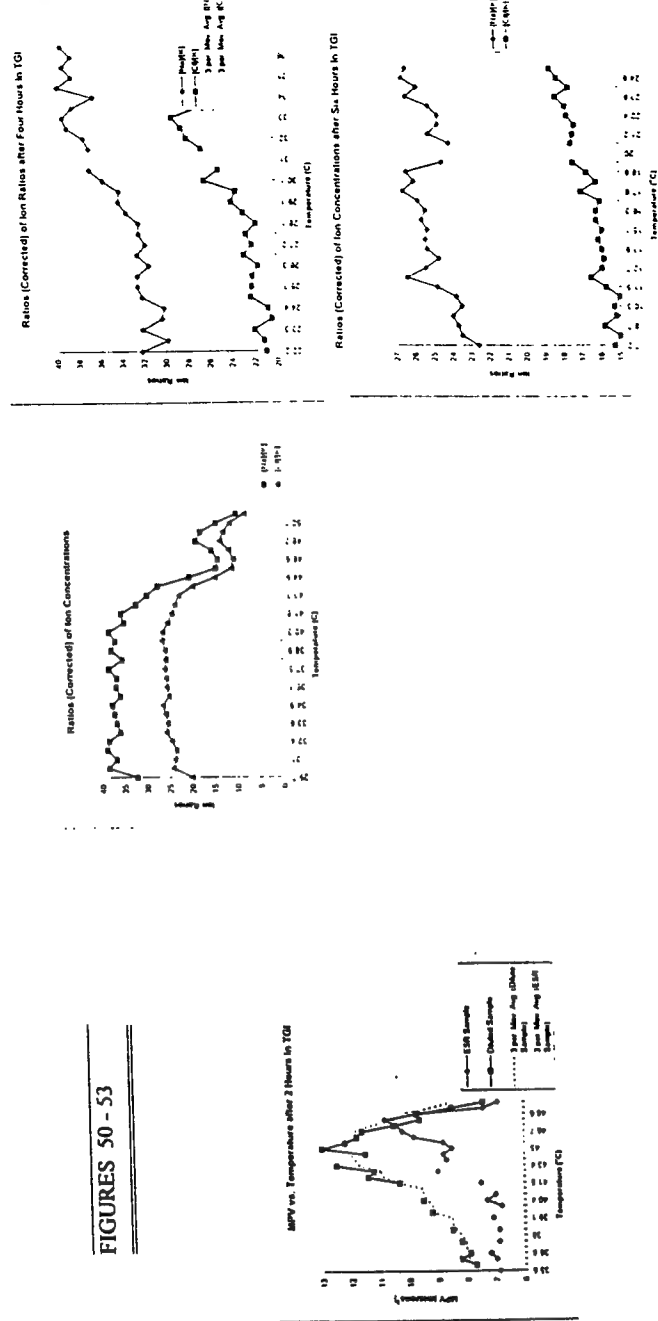
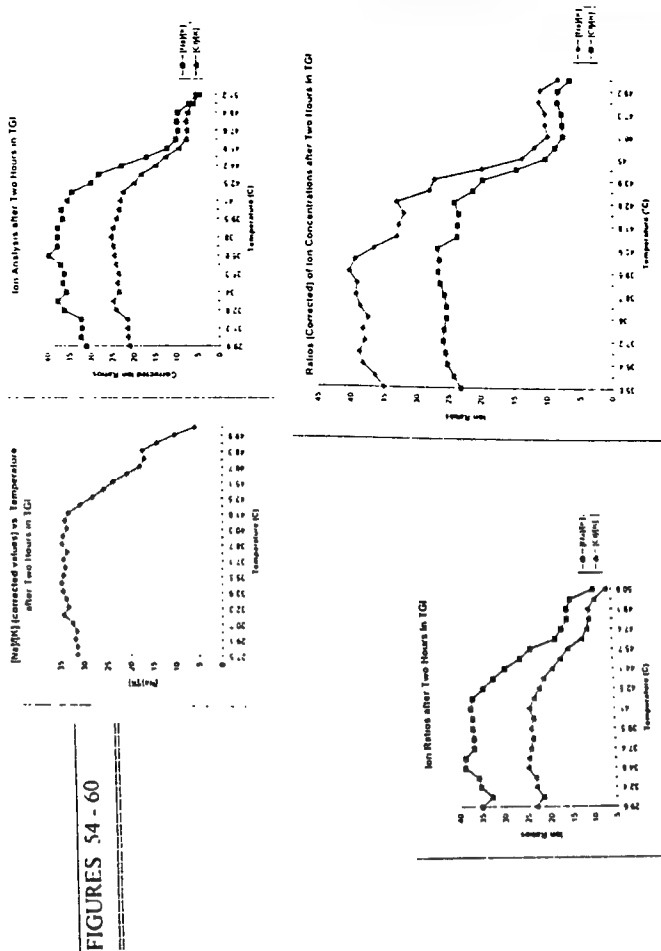
## Various Temperatures DATC110/98



### Various Temperatures 94°C (190°F)

FIGURES 42 - 49





## DATA ANALYSIS

### ERYTHROCYTE SEDIMENTATION RATE DATA

Figs. 1 - 5 show typical ESR curves as function of temperature (for various settling times) from approx. 30 to 54 °C. The curve-shape is characteristic: a general increase from approx. 30 °C to about 43 (to 44) °C, followed by a pronounced, sometimes dramatic, drop (to effectively zero settling velocity) at higher temperatures. The scatter in the curves is usually remarkably small; frequently deviations from a smooth curve being less than 0.2 - 0.3 mm (see for instance Fig. 2) while in other cases the scatter may occasionally be somewhat larger, say  $\pm$  1 mm (Figs. 3, 5). Between approx. 30 and 43 °C, the increase in the ESR is essentially exponential as illustrated in Figs. 12 - 16. The linearity of the log-plots is often very good (Fig. 12) but (weak) systematic variations may occur (compare for instance the data for two hours of settling as shown in Fig. 12 and in Fig. 16 - note that the blood samples came from different subjects). However, in general it appears fair to conclude that good linearity is observed. Over the temperature range investigated, the temperature in °C and the reciprocal of the absolute temperature (in Kelvin) are very roughly proportional (see the Appendix for a justification of this). In view of this, plots of  $\log[\text{ESR}]$  (or  $\ln[\text{ESR}]$ ) vs. temperature (in °C) are essentially Arrhenius graphs ["poor man's Arrhenius Graphs"]. Thus, a single straight line in such a graph suggests that only one rate-controlling process is involved and the slope of the line is essentially proportional to the apparent energy of activation ( $\Delta E_a$ ) for the rate-controlling process. In general we find  $\Delta E_a$  to be rather small, say of the order of 4 to 5 kcal/mole, suggesting that the rate controlling step may be a diffusion process or a viscous flow mechanism, for instance depending on the viscosity of whole blood or of the plasma. As the settling progresses, the slopes of the  $\log [\text{ESR}]$ -vs-temp. curves tend to become smaller (and of course ultimately close to zero in those experiments where a final sedimentation height has almost been reached). We return to the question of the slopes of the settling graphs and their possible diagnostic value in the Discussion Section.

The abruptness of the change near the critical maximum temperature is particularly easily seen in Fig. 11 in which the ESR curve has been numerically differentiated. Note in this graph the abrupt drop for temperatures above 43.5 °C and the sharp minimum observed after two or more hours of sedimentation, centered near 44.9 °C - i.e. quite precisely the 45 °C for the third Drost-Hansen Thermal Transition Temperature, ( $T_k$ ).

A number of measurements have been carried out also at lower temperatures. Such measurements were made because ESR measurements in the Clinical Laboratory are usually made at Room Temperature, i.e., generally 22 °to 25 °C. In other series of measurements we have also determined the ESR over temperature ranges including 15 ° and 30 °C as these temperatures represent two other Thermal Transition Temperatures ( $T_1$  and  $T_2$ , respectively) for vicinal water.

In Fig. 6 the settling was followed for 4 hours but no evidence is found for an anomaly near 30 °C. Likewise, neither Figs. 7 nor 8 offer any evidence of a transition near  $T_2$ ; on the other hand, in previous ESR measurement at CID in 1989 and 1991 anomalies were indeed seen near 30 °C. We have no immediate explanation for this variability.

Professor Glaser and co-workers in Berlin have published convincing data to show anomalies in the ESR (of *resuspended* RBCs) near 21 - 23°C. Only occasionally have we observed indications of such an anomaly in the ESR but from time to time we have seen a suggestion of an anomaly at this temperature range in *other* properties of the blood. In all probability the 22 ° anomaly is unrelated to the vicinal water structure; instead it most likely reflects a phase transition in a cell membrane lipid. Note that the two curves in Fig. 7 and 8 do not appear to increase in similar manners with temperature and may indeed not be well represented by an exponential curve.

A few measurements have also been made at lower temperatures. Thus Figs. 9 and 10 show the erythrocyte settling over a range of temperatures from 7 to 24 °C. At these low temperatures the rate of settling is notably less than at the higher temperatures as would be expected if the viscosity of whole blood (or the blood plasma) exerts a rate controlling role. Similarly, the rates of other processes influencing the settling rate will also be affected, for instance the rate of rouleaux formation is likely also decreased at the lower temperatures. Because of the lower rates of settling, measurements were possible over longer time intervals; as an example settling data were obtained over a six hour period in experiment 94TGI19B. Unfortunately the scatter seen in both Figs. 9 and 10 makes it impossible to determine if an anomaly (due to vicinal water) exists near 15 °C (due to the vicinal water) or near 21 - 23 °C (due to a membrane lipid transition) as suggested by Glaser's data.

#### CELL VOLUME DATA

A large number of Cell Volume Data have been collected, both on RBCs as well as on Platelets, over a wide range of temperatures and in some instances after dilution of the samples with lactated Ringer solution and incubating at various temperatures over different time intervals. [All cell volumes expressed in cubic microns:  $(\mu\text{m})^3 = 10^{-12} \text{ ml} = \text{a femtoliter (fl); } 10^{-15} \text{ liter}$ ].

#### MEAN ERYTHROCYTE VOLUMES (MCV).

A) Figures 19 through 26 show MCV data obtained on erythrocytes from whole blood after incubation at various temperatures for different lengths of time. Overall the data resemble quite precisely the volume data we have collected in previous years. The typical variation in the MCV as a function of temperature is a relatively small, gradual increase over the range ca. 30 °C to about 43 ° to 44°C; the increase is usually 1 to 2 % (with one exception; see Fig. 26); note the rather small variations from a smooth curve, suggesting excellent reproducibility of the volumes as determined with the Baker Model 9000 Hematology Counter. Characteristically, the gradual increase up to nearly 44 °C is

followed by a distinct and sometimes dramatic drop over the range of temperature from about 44 ° to about 46.5 (+/- 0.5) °C. The minimum at this temperature is frequently very sharp, followed by a large, abrupt increase in the MCV up to about 51 °- 52 °C. Above this temperature range the MCV again drops and again the change may be quite dramatic (!) - see for instance Figs. 24 and 25. Note that in all cases observed (in this study as well as in those data collected in previous years on both human blood and blood from about a dozen different mammals) the MCV values near the relative maximum around 51.5 °C are much larger than the values below the 45 °C anomaly.

B) Measurements of MCV has been made also on RBCs from whole blood diluted with lactated Ringer solution; unless otherwise stated, the dilution is 5:1, -- Ringer:blood. [Undiluted samples are referred to as "ESR Samples" as these are the samples used for the ESR measurements].

In Fig. 27 is shown the MCV for whole, undiluted blood after 2 hours incubation in the TGI compared to the MCV of diluted samples after the same length in the TGI. The two curves are relatively similar but distinct differences do exist: a) over the whole range of temperatures the MCVs of the diluted samples are larger than for the undiluted samples. The difference in volumes below the thermal transition region [approximately around 42 ° (to 45 °)C] is 2%. This suggests that the lactated Ringer solution is not truly isotonic with the plasma in the whole blood. b) The variations with temperature of the RBC in the whole blood are typical of the general response of the MCV to temperature as discussed for Figs. 19 - 26. However, the drop in MCV at higher temperature for the diluted samples begins already at about 42 °C which is distinctly below the range generally observed, 44 ° - 45 °C; at this time we have no explanation for this behavior. c) The minimum in the MCV - vs - temp. curve for the diluted samples is centered around 44 °C, or ca. 2.5 ° below the value for the whole blood. d) the rise from the minimum to the maximum value of the MCV curve for the diluted samples is as steep as observed for the whole blood (the curves are essentially parallel), suggesting that the same mechanism may be responsible for the swelling in both the whole blood and the diluted samples (-hardly a surprising finding). e) The MCV curve for the diluted samples decreases sharply above the maximum temperature (although in the present example only two data points were obtained below the maximum). The presence of a sharp maximum is qualitatively identical to the behavior seen in whole blood but again the temperature of the maximum appears to be ca. 3 °C less than for the whole blood.

With increasing length of incubation at elevated temperatures, the volume curves for the diluted samples seem in general to be "down-shifted" as illustrated in Fig. 28. For the curve for 4 hours of incubation the minimum now occurs at about 45.5 °C. However, the differences between the volumes of the cells in whole blood and in the diluted samples are not always great as illustrated in Fig. 29. (Note in this Figure that the total changes in the observed MCV above and below the thermal transition temperature around 45 °C are not large).

Finally note in FIG. 30 the distinctly different behavior of the MCV upon long term exposure to elevated temperatures; the initial MCV below 45 °C was about 89 (mm)<sup>3</sup> while after 22 hours of incubation the MCV is about 90 - 95 (mm)<sup>3</sup>. Note also that the drop in MCV begins at about 45 °C but the minimum usually seen near 46.5 °C has been eliminated or, at best, reduced to an inflection point in the curve but followed by a distinct if relatively broad minimum near 52 °C.

A number of other runs have been made at lower temperatures. FIG. 34 shows the variation of MCV as a function of temperature from approx. 7 °C to 25 °C, [with a parabola fitted to the data]. There is no indication in this case of an anomaly near 15 °C, but note that the total variation in MCV over this 18 ° interval is only 1.5 % (after 2 hours of incubation).

As would be expected, the rate of change in the RBC volumes is low at the lower temperature range. FIGS. 35 through 38 shows the change in MCV, measured on a sample of blood diluted with lactated Ringer solution, over an interval of 21 hours. While no obvious trends exist in the data in FIG. 35, measured after 2 hours of incubation, a distinct effect of temperature is seen in FIG. 38 after 21 hours of incubation: below 15 °C the MCV is nearly constant (dropping about 1 % between 7 ° and 15 °C) but increasing notably above this critical temperature ( $T_{k=1}$ ). [The increase is 8 % over an 8 ° interval, or a temperature coefficient of 1% per degree!]

Another example of the effects of long term incubation on MCV of red cells in diluted samples of blood is shown in FIGS 39 and 40: In FIG. 39, after 5 hours of incubation, a distinct maximum is seen in the MCV near 41 °C, followed by a relatively sharp minimum near 45 °C and a subsequent very dramatic increase [9 % over a 3 ° interval!] followed by an equally decisive drop. On the other hand, after 22 hours of incubation, the overall features of the MCV curve have changed: the difference between the maximum observed value and the minimum observed value is nearly 50 %! Below 40 °C the effect of temperature on the MCV is minimal but above ca. 40 ° and up to 44 °C, the MCV increases only to drop very dramatically above this temperature.

Finally, in FIG 41 is shown the effects of dilution with lactated Ringer solution on the MCV, at two different temperatures: 25 ° and 37 °C. The abscissa is the percentage of whole blood in the final solution while the ordinate is the MCV (measured after three hours of incubation). Note the pronounced increase in MCV for blood concentrations less than ca. 20 % for both isotherms and the remarkable temperature independence of the MCV, measured at 37 °C, from 30 to 100 % blood. In other words: over the physiologically important range, extending the blood plasma with lactated Ringer solution at body temperature does not cause any change in the MCV.

## MEAN PLATELET VOLUMES (MPV)

Platelet volumes are as sensitive to temperature variations as RBC volumes, especially near the 45 °C anomaly of the cell-associated vicinal water, and vary strongly with temperature below the 30 °C anomaly.

A) In general, the MPV is relatively constant over the temperature interval from ca. 30 °C up to a range of transition temperatures extending from about 42 °C to about 48 °C (see FIGS. 42 through 46) but distinct variations occur even over this relatively narrow [12 °C] temperature interval and large differences between otherwise similar runs are seen in the transition range from ca. 42 °C to 48 °C. As will become evident from some of the following illustrations, part of the large variability may be due to changes with time.

The main variation in MPV appears to be an increase starting around 45 °C followed by an abrupt drop near 47 °C - 48 °C, leading to a sharp minimum and an equally abrupt increase at higher temperatures [see particularly FIGS. 43, 44 and 45]. A slight modification on this behavior is seen in FIG. 42, where the initial rise before the abrupt drop occurs at about 41 °C; the data in FIG. 46 suggests that a minimum exists near 38 °C but this may be the result of insufficient time for equilibration as these data were obtained after only 1 hour of incubation. Note that the abrupt drop seen in the previous FIGURES are also seen here, starting at 49 °C.

B) Measurements of MPV have also been made at lower temperatures as well as on samples of blood diluted with lactated Ringer solution. FIG. 47 shows the MPV after four hours of incubation in the range of temperatures from ca. 22 °C to 37 °C. The net effect is a 10 % drop in the MPV over this temperature interval (with possibly a levelling-off for temperatures above 30 °C [?]). See also FIG. 48 which shows essentially the same behavior. (In both Figures note the scale: it would be possible to draw a smooth, single curve through the majority of data points with all deviations being less than  $\pm 5\%$ . In view of the nature of the quantity measured this is certainly not an unreasonable degree of scatter).

The variation in MPV in blood diluted with lactated Ringer solution is rather surprising. While such dilution (at 37 °C) did not seem to alter drastically the MCV, the effect on the platelets is quite surprising. In FIG. 49 one observes a dramatic *increase* in MPV after 1 hour of incubation on going from 22 °C to 37 °C whereas the MPV values in whole blood dropped approx. 10 % over the same temperature interval (compare FIG. 47).

On the other hand, after 3 hours of incubation, the MPV appears to be essentially temperature independent over the temperature interval studied - but at notably larger volumes! In fact, the swelling of the platelets over a 2 hour interval at 22 °C is more than 50 %! This surely suggests that the lactated Ringer solution is not isotonic with the platelets at low temperatures and that the approach of the platelets to an "equilibrium"

volume is fairly slow. This is particularly surprising as the erythrocytes appear to change rather little upon dilution with the Ringer solution at room temperature (confer FIG. 41). Another example of changes with time in the MPV at even lower temperatures is shown in FIGS 50, 51 and 52. The temperature range (from ca. 7 ° to 25 °C) was chosen such as to place the vicinal water transition temperatures ( $T_{k=1}$ ) of 15 °C near the midpoint of the observed range. After two hours of incubation (FIG. 50) a small but significant increase occurs between 7 ° and ca. 16 °C while the rate of increase is distinctly less at the higher temperatures. After 4 hours of incubation (FIG. 51) the MPV values have, on the average, increased a little less than 10 %, and no evidence is seen of the possible thermal anomaly near 15 °C. However, after an additional two hours of incubation, the MPV values have not only increased dramatically (by about 25 to 35 %) but a distinct maximum is now seen at 15 °C.

C) Finally, a few experiments have been made in the high temperature range on diluted samples as a function of time. FIG. 53 shows the MPV after 2 hours of incubation of whole blood ("ESR Samples") and blood diluted with lactated Ringer solution. Below the thermal transition temperature range (44 ° - 46 °C) the platelet volumes in the diluted samples are decidedly larger than the volumes in the whole blood (by about 10 to 20 %) but above this critical temperature range the volumes appear to be comparable.

#### Na/K RATIOS IN WHOLE BLOOD PLASMA

At normal body temperature, the ion ratio, R, defined as  $[Na^+]/[K^+]$  in the plasma of whole blood, is approx. 35 (within 95% confidence level: 28 to 40. See Cogan, 1991). Any notable deviations from this range of values suggest the existence of some active ionic unbalance, generally requiring decisive clinical intervention. R is obviously related to the RBC volume control mechanisms, notably the sodium membrane pump.

We have made a series of measurements of R in blood plasma after incubation of whole blood at various temperatures for different lengths of time. Invariable, R decreases above a very broad maximum centered around a temperature not too far from the normal body temperature of 37 °C. The decrease in R above ca. 40 °C is often very substantial and as one approaches the critical thermal transition temperature of 45 °C, R may have dropped to half of the value near 37 °C. In other words, in the range of elevated temperatures such as seen in severe febrile states, R may differ very significantly from the normal range. Surely this must have important clinical implications (for instance for patients with high fevers, heat strokes, severe burns, or in hyperthermia therapy) but it is somewhat surprising that over the same range of temperatures the MCV only tends to increase a relatively small amount (see FIGS. 19 - 24). Thus it appears that different molecular mechanisms may be involved although traditional wisdom would anticipate a close correlation between cell volumes and  $Na^+/K^+$  ratios.

NOTE: All the blood samples used in the present study were collected in syringes to which  $Na_4EDTA$  had been added. The contribution of this sodium is taken account of in the calculations; hence the data are referred to as "Corrected".

A series of measurements of R have been made and some of the results obtained at high temperatures (ca. 27 ° through 51 °C) are shown in FIGS. 54 through 58. In these graphs are also shown, where available, the ratio of the chloride ion concentration to potassium concentration ( $[Cl^-]/[K^+] = J$ ). In general the J-curve follows the R-curve very closely.

It is of interest to note that in many instances, the R- and the J- curves appear to level out near 45 ° to 46 °C (see FIGS. 55 and 56), while in some cases (FIGS. 57 and 58) a new, distinct, relative maximum occurs near 48 ° or 49 °C [the J-curves behaving in a similar manner]. It is instructive to compare this finding with the MCV data in the same temperature range: an abrupt decrease is seen in some of the MCV data, for temperatures near or above 50 ° - 51 °C; see FIGS. 23, 24, 25 and 26. On the other hand, no unusual features are seen in the ESR curves in this temperature range in agreement with expectations [the ESR essentially becomes zero above, 47 ° or 48 °C].

Finally, we have made a number of R measurements at lower temperatures. Some typical results are shown in FIGS. 59 and 60. It is seen in both of these graphs that R is less than at normal body temperature and increases from a value of about 22 to the "normal" value, 35 (- 40), over the range of temperature from 7 °C to normal body temperature. Unfortunately not enough data have been obtained to allow a decision to be made whether or not anomalies exist near 15 ° and 30 °C. (Note: the data in FIGS. 59 and 60 should perhaps not be compared directly because of the different lengths of incubation). Note again, however, that the J-curve essentially follows the R-curve.

## APPENDIX

I) The standard Arrhenius graph is a plot of  $\log(\text{Rate})$  [or  $\ln(\text{Rate})$ ] as a function of reciprocal, absolute temperature ( $1/T$ ,  $K^{-1}$ ). However, from around 0° to about 30 ° or 40 °C, the temperature in °C is roughly proportional to  $1/T$ . This is easily seen from the expansion of  $1/T$  namely

$$1/T = 1/(273.2 + t) = 1/273.2[1 + t/273.2] = 1/273.2 - t/(273.2)^2$$

which is of the form  $1/T = a - bt$ . Thus,  $1/T$  is roughly proportional to  $t$ . This approximation is of course dependent on  $t <$  (or  $\ll$ ) than 273.2; as long as this approx. is approximately fulfilled, graphs of  $\log(\text{Rate})$  vs temperature in °C will resemble Arrhenius graphs.

II) The Temperature Gradient Incubator (TGI or "polythermostat") has been briefly described in previous reports and a detailed description given in one of our papers (Drost-Hansen, 1981). The device consists of a massive aluminum bar with wells drilled along the bar to accommodate test tubes, culture tubes or other small samples (such as Wintrobe tubes). The bar is thermally insulated on all sides; one end is maintained at a constant high temperature while the other end is maintained at a constant low temperature. A temperature gradient is thus established along the bar; in the present version the bar provides two sets of 30 different wells, each at a different, constant temperature. Hence, almost precisely simultaneous measurements may be made at 30 different constant temperatures. The total span of temperatures (and hence the difference in temperatures between subsequent wells) is easily adjusted. Temperature intervals of 0.6 ° to 0.9 °C between adjacent wells have been used throughout this study, providing great thermal resolution in the measured quantities.

### ABBREVIATIONS:

#### TEMPERATURE RANGES:

H	HIGH; APPROX. 30 ° - 52 °C	
M	MEDIUM	20 ° - 40 °C
L	LOW	7 ° - 23 °C
ROOM TEMPERATURE		24 ° - 26 °C

#### DILUTIONS:

Unless otherwise stated: whole blood (W)

W	WHOLE BLOOD
D	DILUTED (usually 5:1).

## CONCLUSIONS AND RECOMMENDATIONS

All the hematological parameters measured in this study (ESR, MCV, MPV and  $[Na]/[K]$  ratio) show anomalies at 45 °C, within one or two degrees, in complete agreement with our previous findings (1989, 1991, 1992). It seems an inescapable conclusion that this must be a manifestation of critical roles for the cell-associated, vicinal water in these systems. These findings are also consistent with a wealth of independent observations showing a critical role of vicinal water in nearly all aspects of cell physiology, ranging from determining multiple growth optima and minima for many micro-organisms to determining body temperatures of mammals and birds. In some cases, the effects of the thermal transitions begin to be manifested at temperatures as low as 42 ° to 43 °C and this may play an important role in a variety of processes in the hyperthermic state, for instance in patients with severe fevers or during hyperthermia therapy of malignancies.

That the thermal anomalies of vicinal water plays a crucial role in many biological systems is now beyond doubt; what remains far less well understood is the question of the "site of action" of such solvent structural transitions. We have recently proposed (Drost-Hansen and Singleton, 1995) that the effects of the structural transitions of the vicinal water may be in the hydration of the biomacromolecules present in the cellular systems. One such sensitive site may be the vicinal hydration structure of some protein, for instance partially imbedded in the cell-membrane, regulating ion transport across the membrane. If the transport mechanism depends on the extent of dimerization (or oligomerization) of such a protein, a sudden change in the vicinal hydration of that protein at  $T_k$  will surely affect the equilibrium constant for the dimerization equilibrium and may thus suddenly change the transmembrane transport of a crucial ion, for instance required in the regulation of the osmotic equilibria of the cell.

On the basis of this hypothesis for the criticality of the vicinal water control, it is possible to make some predictions which may be tested experimentally. Thus it would be of interest to study those cell processes for which it is known that dimerization (or oligomerization) of a protein or enzyme is required for the process to take place. The prediction is that for such processes the rate might change dramatically at least near one of the thermal transition temperatures,  $T_k$ . Because of the number and sizes of the subunits in, for instance, the ATPases these are likely candidates for distinct thermal anomalies in their rates as ion-translocators. In fact, because of the frequent involvement of associated proteins in the cell-membrane *all* cell transport processes may be influenced by the vicinal hydration of the protein subunits involved.

Another possibility is the tissue deterioration caused by various venoms; we particularly propose to study the rates of proteolysis caused by the venom from the brown recluse spider (*Loxosceles reclusa*) as a function of temperature near 45 °C. Our prediction is that near this critical temperature the venom activity may be lessened considerably - or indeed completely eliminated - while the surrounding tissue may be able to withstand the required hyperthermia stress without irreversible damage (or with minimal deleterious effect).

## ACKNOWLEDGEMENTS

The authors wish to thank the US Air Force, Office of Scientific Research, and the Clinical Investigation Directorate of Wilford Hall Medical Center for making this research possible and our sincerest thanks go as well to those at CID who so cheerfully and competently helped make this work much easier. Special thanks go to Dr. J. H. Cissik, (Col., USAF, ret.), Lt. Col. John Cody, Ph.D. and the Director, Col. E. S. Oertli, Ph.D., DVM, for their interest in this work and their continued encouragement. We also wish to thank those who so graciously volunteered to donate blood for this study. The efforts by RDL to facilitate the mechanics of this research opportunity is also appreciated.